Volume 53
Number 17
7 September 2024
Pages 8515–8950

Chem Soc Rev

Chemical Society Reviews

rsc.li/chem-soc-rev

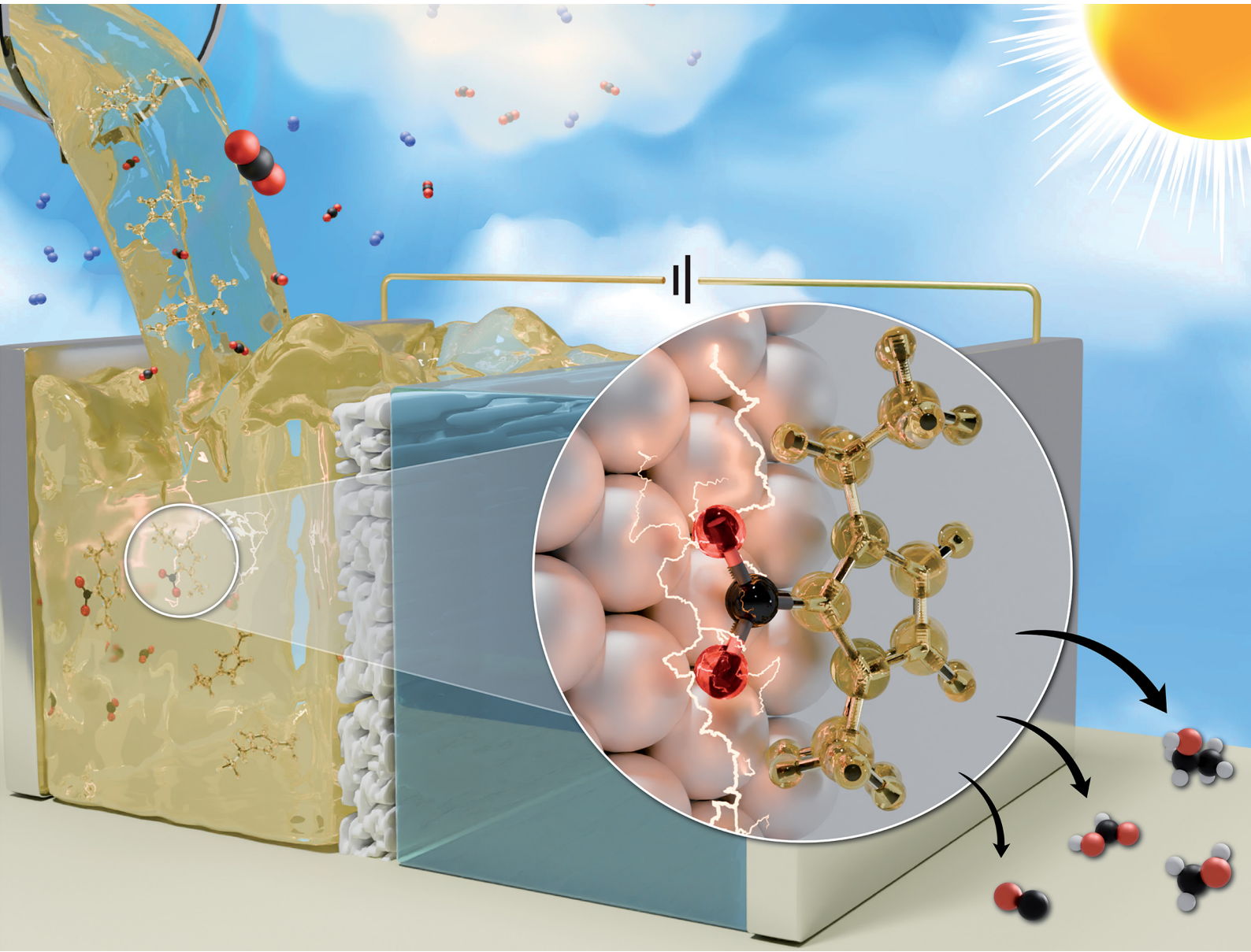

ISSN 0306-0012

ROYAL SOCIETY OF CHEMISTRY

REVIEW ARTICLE

Burcu Gurkan *et al.*

Reactive capture and electrochemical conversion of CO_2 with ionic liquids and deep eutectic solvents

Chem Soc Rev

REVIEW ARTICLE

View Article Online
View Journal | View Issue

Check for updates

Cite this: *Chem. Soc. Rev.*, 2024, **53**, 8563

Reactive capture and electrochemical conversion of CO_2 with ionic liquids and deep eutectic solvents

Saudagar Dongare, [a] Muhammad Zeeshan, [a] Ahmet Safa Aydogdu, [bc] Ruth Dikki, [a] Samira F. Kurtoğlu-Öztulum, [bcd] Oguz Kagan Coskun, [a] Miguel Muñoz, [a] Avishek Banerjee, [e] Manu Gautam, [f] R. Dominic Ross, [g] Jared S. Stanley, [h] Rowan S. Brower, [i] Baleeswaraiah Muchharla, [j] Robert L. Sacci, [k] Jesús M. Velázquez, [i] Bijandra Kumar, [j] Jenny Y. Yang, [h] Christopher Hahn, [g] Seda Keskin, [bc] Carlos G. Morales-Guio, [e] Alper Uzun, [bcl] Joshua M. Spurgeon [f] and Burcu Gurkan *[a]

Ionic liquids (ILs) and deep eutectic solvents (DESs) have tremendous potential for reactive capture and conversion (RCC) of CO_2 due to their wide electrochemical stability window, low volatility, and high CO_2 solubility. There is environmental and economic interest in the direct utilization of the captured CO_2 using electrified and modular processes that forgo the thermal- or pressure-swing regeneration steps to concentrate CO_2, eliminating the need to compress, transport, or store the gas. The conventional electrochemical conversion of CO_2 with aqueous electrolytes presents limited CO_2 solubility and high energy requirement to achieve industrially relevant products. Additionally, aqueous systems have competitive hydrogen evolution. In the past decade, there has been significant progress toward the design of ILs and DESs, and their composites to separate CO_2 from dilute streams. In parallel, but not necessarily in synergy, there have been studies focused on a few select ILs and DESs for electrochemical reduction of CO_2, often diluting them with aqueous or non-aqueous solvents. The resulting electrode–electrolyte interfaces present a complex speciation for RCC. In this review, we describe how the ILs and DESs are tuned for RCC and specifically address the CO_2 chemisorption and electroreduction mechanisms. Critical bulk and interfacial properties of ILs and DESs are discussed in the context of RCC, and the potential of these electrolytes are presented through a techno-economic evaluation.

Received 25th April 2024

DOI: 10.1039/d4cs00390j

rsc.li/chem-soc-rev

Open Access Article. Published on 24 June 2024. Downloaded on 1/17/2026 6:47:09 PM.
This article is licensed under a Creative Commons Attribution-NonCommercial 3.0 Unported Licence.

[a] *Chemical and Biomolecular Engineering, Case Western Reserve University, Cleveland, OH, 44106, USA. E-mail: beg23@case.edu*
[b] *Department of Chemical and Biological Engineering, Koç University, Rumelifeneri Yolu, Sariyer, 34450 Istanbul, Turkey*
[c] *Koç University TÜPRAŞ Energy Center (KUTEM), Koç University, Rumelifeneri Yolu, Sariyer, 34450 Istanbul, Turkey*
[d] *Department of Materials Science and Technology, Faculty of Science, Turkish-German University, Sahinkaya Cad., Beykoz, 34820 Istanbul, Turkey*
[e] *Department of Chemical and Biomolecular Engineering, University of California, Los Angeles, Los Angeles, CA 90095, USA*
[f] *Conn Center for Renewable Energy Research, University of Louisville, Louisville, KY 40292, USA*
[g] *Materials Science Division, Lawrence Livermore National Laboratory, Livermore, CA, 94550, USA*
[h] *Department of Chemistry, University of California, Irvine, Irvine, CA 92697, USA*
[i] *Department of Chemistry, University of California, Davis, Davis, CA 95616, USA*
[j] *Department of Mathematics, Computer Science, & Engineering Technology, Elizabeth City State University, 1704 Weeksville Road, Elizabeth City, NC 27909, USA*
[k] *Chemical Sciences Division, Oak Ridge National Laboratory, Oak Ridge, Tennessee 37830, USA*
[l] *Koç University Surface Science and Technology Center (KUYTAM), Koç University, Rumelifeneri Yolu, Sariyer, 34450 Istanbul, Turkey*

1. Introduction

The current carbon economy relies on fossil fuels for energy generation and the production of chemicals, resulting in record-high CO_2 emissions.[1,2] CO_2 is a greenhouse gas and therefore, it is environmentally desirable to capture CO_2 from the atmosphere and emission sources.[1] CO_2 capture from post-combustion flue gas and the atmosphere is critical for net-zero and net-negative emissions, respectively. To prevent further deleterious effects of CO_2 in the atmosphere on climate change, approximately 10 gigatons of CO_2/year needs to be removed to limit global warming to a maximum of 1.5 °C by 2050.[3–6] This goal is ambitious and requires a cooperative effort to simultaneously implement emission mitigation and negative emission technologies in parallel to decarbonization efforts toward a more sustainable future. To incentivize these implementations, technologies for capturing and converting CO_2 into higher value products need to become more energy efficient.[2]

Open Access Article. Published on 24 June 2024. Downloaded on 1/17/2026 6:47:09 PM. This article is licensed under a Creative Commons Attribution-NonCommercial 3.0 Unported Licence.

Currently, chemical separations make up 10–15% of all the energy consumed in the USA, according to the 2019 report by the National Academies of Sciences, Engineering and Medicine: "A Research Agenda for Transforming Separation Science".[3] In negative emission technologies,[4] such as CO_2 separation from direct air, achieving favorable energetics and practical gas–volume processability depends on our ability to design highly selective materials and interfaces.[5,6] Further, the reduction of the captured CO_2 to produce other carbon products such as fuels and commodity chemicals *via* chemical, thermal, biochemical, photochemical, and electrochemical reactions are possible.[7–9] However, the critical challenges are the requirement of substantial energy to activate CO_2, which is otherwise a very stable molecule, and the lack of highly selective catalysts. Therefore, materials that can multi-function for selective absorption and conversion with lower energy requirements have transformative potential for emission mitigation and negative emissions science, which are pressing societal needs.

Another challenge when converting CO_2 to fuels and feedstocks is the availability of CO_2. While CO_2 is present in many industrial waste streams, its concentration is typically low (Table 1), therefore it is necessary to concentrate CO_2 from these dilute sources.

Traditionally, CO_2 separation and concentration are achieved by thermal, moisture, or pressure-swing processes utilizing sorbents and have substantial energy requirements;[13] current capture approaches yield CO_2 at a cost of up to $200 per ton. The energetic and capital costs are largely due to low CO_2 concentration and sorbent regeneration. With decreasing partial pressure of CO_2 in the available stream, sorbents with higher capacity and selectivity are desired. For example, the direct air capture (DAC) of CO_2 is a critical technology platform for CO_2 removal (carbon dioxide removal, CDR) to achieve negative emissions technologies.[7,8] This goal necessitates the use of sorbents with high binding constants (*i.e.*, enthalpy) for highly selective CO_2 absorption at ambient temperature and pressures. Consequently, the CO_2 release in the concentration step

Burcu Gurkan

Burcu (Eksioglu) Gurkan is a Professor at Case Western Reserve University; she is the Associate Editor for ACS Applied Engineering Materials; she serves as the Deputy Director of BEES2 (Breakthrough Electrolytes for Energy Storage Systems) – a Department of Energy Frontier Research Center (EFRC) where she leads the effort in developing structured electrolytes for flow batteries and a Key Researcher in 4C (Center for Closing the Carbon Cycle) EFRC where her team develops functional electrolytes for capture and conversion of CO_2. Her team synthesizes and investigates deep eutectic solvents and ionic liquids for solving problems in separations, electrocatalysis, energy storage and conversion.

Saudagar Dongare

Saudagar Dongare is a Postdoctoral Researcher at Case Western Reserve University in the Gurkan group. He is a member of the 4C EFRC Energy Early Career Network. He received his PhD in Chemical Engineering from Thapar Institute of Engineering and Technology, India. His research interests include environmental electrocatalysis, developing electrode materials and electrolytes for electrochemical CO_2 reduction, and studying the electrode–electrolyte interfaces with in situ spectroscopy.

Left to Right (members of the Gurkan group at CWRU): Muhammad Zeeshan; Ruth Dikki; Miguel Muñoz; Oguz Kagan Coskun.

Dr Zeeshan is a postdoctoral researcher; he earned his PhD degree in Chemical Engineering from Koç University, Türkiye; his expertise is the development of composites for CO_2 separations.

Ruth Dikki is a PhD student; her thesis involves the synthesis and characterization of CO_2 capture solvents.

Miguel Muñoz is a PhD student and a member of the Student Research Organization of BEES2 EFRC; his thesis involves the understanding of transport and electron transfer reactions in structured electrolytes; he earned his MS degree in Chemical Science and Technology from the Autonomous University of Zacatecas, Mexico.

Oguz Kagan Coskun is a PhD student; his thesis involves the probing of interfaces in electrocatalysis through electroanalytical techniques; he earned his MS degree in Metallurgical and Materials Engineering from Istanbul Technical University, Türkiye.

 This journal is © The Royal Society of Chemistry 2024

Open Access Article. Published on 24 June 2024. Downloaded on 1/17/2026 6:47:09 PM. This article is licensed under a Creative Commons Attribution-NonCommercial 3.0 Unported Licence.

Table 1 Composition of available CO_2 sources[10–12]

	Contents (vol%)					
Stream	CO_2	N_2	O_2	H_2O	Other major gases	Trace contaminants
Biogas	30–50	0–1	0–1	15	CH_4	
Cement Plant	18	56.5	7.5	18.2	—	CO, NO_x, SO_2, HCl
Flue gas (coal)	11	76	6	10–18	Ar	NO_x, SO_2, Hg, Cd, other heavy metals
Flue gas (natural gas)	3	76	14	6	Ar	NO_x
Air	0.04	78	21	1	Ar	—

becomes more energy intensive. Further, the reactive contaminants in the CO_2 streams, if not removed, can degrade the sorbent in the capture process and poison the catalyst in the post CO_2 conversion process. Therefore, discovery of sorbents with high CO_2 capacity and selectivity, stability (*e.g.*, against humidity, thermal-swing, feed contaminants) and regenerability with minimal energy input remain a critical challenge.

The theoretical minimum energy cost for CO_2 capture and concentration (CCC) from flue gas ($\sim$5–15% CO_2 concentration) using the aqueous amine (*i.e.*, monoethanolamine, MEA) solvent, the benchmark, is calculated as 8.4 kJ mol^{-1}.[14] This requirement increases to 20 kJ mol^{-1} for DAC by earlier estimates and further increases to 30 kJ mol^{-1} when taking into account the irreversibility of practical sorbents.[15] While the CCC from flue gas and DAC processes are not alternatives to each other, the energetics of various processes are often compared to provide a perspective of the needs within a portfolio of solutions. Most common sorbents require thermal swing operation for regeneration and this step is the most energy intensive step in the processes. In addition, sorbents exposed to high temperatures during thermal swing

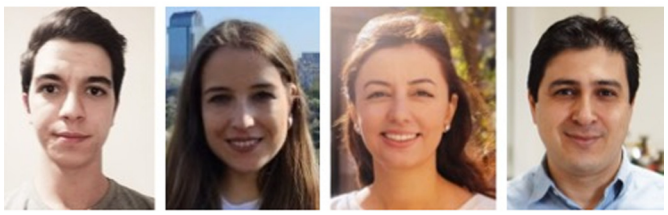

Left to Right (from Koç University): Ahmet Safa Aydogdu; Samira F. Kurtoğlu-Öztulum; Seda Kesin, Alper Uzun.

Ahmet Safa Aydogdu is a PhD student, co-advised by Prof. Seda Keskin and Prof. Alper Uzun in Chemical and Biological Engineering Department (CheBioEng) at Koç University (KU), Türkiye; his thesis focuses on ionic liquids and MOFs for CO_2 capture and separation.
Samira F. Kurtoğlu-Öztulum is an Assistant Professor at Turkish-German University; she got her PhD in CheBioEng from KU; her research focuses on catalysis for energy-related applications.
Seda Keskin is a Professor and the Director of the Nanomaterials, Energy, and Molecular Modeling Research Group; she completed her PhD at Georgia Institute of Technology; her group currently focuses on MOFs for energy applications.
Alper Uzun is a Professor and the Director of the UzunLab Materials for Energy Research Group at KU; previously he worked as an Associate Research Engineer at ConocoPhillips/Phillips66 Bartlesville Technology Center and completed postdoctoral training at the University of California, Berkeley after receiving his PhD from University of California, Davis.

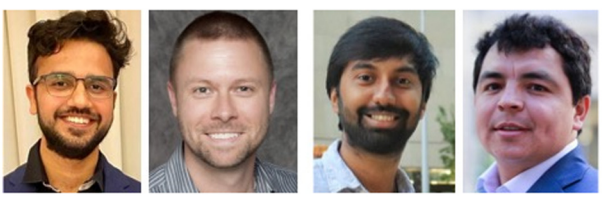

Left to Right (members of 4C EFRC): Manu Gautam; Joshua M. Spurgeon; Avishek Banerjee; Carlos G. Morales-Guio.

Manu Gautam is a postdoctoral researcher in the Spurgeon group at the University of Louisville; his research involves the examination of contaminants in electrochemical CO_2 reduction.
Joshua M. Spurgeon is the Theme Leader for Solar Fuels research at the Conn Center; he was previously the Project Lead for the Interface group and Processing, Materials, and Integration Team at JCAP (2013).
Avishek Banarjee is a PhD student in the Morales-Guio group at the University of California, Los Angeles working on CO_2 electrolyzes; he earned his MS at McGill University.
Carlos G. Morales-Guio is an Assistant Professor at the UCLA Samueli School of Engineering; he completed his postdoctoral training at Stanford University with a fellowship from the Swiss National Science Foundation; his group specializes in electrochemical engineering for catalytic processes.

Open Access Article. Published on 24 June 2024. Downloaded on 1/17/2026 6:47:09 PM.
This article is licensed under a Creative Commons Attribution-NonCommercial 3.0 Unported Licence.

undergo thermal degradation, thus necessitating material or solvent replacement. Pressure- and thermal-swings also require significant infrastructure, reducing their applicability with smaller point sources. For example, regeneration of the sorbent in DAC is currently estimated to consume 95% of the total energy consumption and requires 75% of the capital cost.[16,17] Combined capture and conversion bypasses the costly step of regeneration of the captured CO_2 from sorbents. It also provides for direct, low temperature utilization that minimizes sorbent degradation. By eliminating the biggest energetic and capital cost from CCC, direct reduction of captured CO_2 would make the largest difference in improving the overall efficiency from CO_2-source-to-products.[18] While pure CO_2 from current DAC methods are expected to cost more than \$200 per ton of CO_2, combined carbon capture and utilization (CCU) is estimated to achieve carbon negative processes at \$20–25 per ton of CO_2.[19]

The potential economic and energy intensity advantages have led to broad interest in CCU strategies. However, most research and development has focused on integration and intensification of CCU at the systems and process level. There has not been as significant focus on tailoring the integration of CCU at the molecular scale for efficient and selective capture with direct conversion of captured CO_2, or reactive capture of CO_2 (RCC). While there has been substantial research in the two separate areas – electrochemical CO_2 capture and concentration (eCCC)[20] and catalysts for electrolytic CO_2 reduction reactions (CO_2RR), these two disciplines have often not been discussed together. While the eCCC community has focused on selectivity, stability, and efficiency at scale, efforts in CO_2RR have primarily used pure CO_2 streams to improve rate, selectivity, and durability. The unique metrics defined for successful eCCC and CO_2RR do not necessarily translate to RCC. Fig. 1 illustrates the concepts of eCCC, CO_2RR, and RCC.

In this review, we focus on materials and electrolytes that have the potential for the advancements in RCC. Specifically, the recent developments, key considerations, and current specific challenges in RCC with multifunctional solvents such as ionic liquids (ILs), deep eutectic solvents (DESs), and more generally electrolytes with IL and DES components are presented.

ILs are salts that melt below 100 °C, an arbitrary temperature chosen to differentiate ILs from molten salts.[21] ILs are typically based on an organic bulky cation and an organic or inorganic anion. Since the review article[22] by Welton published in 1999, interest in ILs has grown tremendously and they have been proposed for numerous applications such as catalysis, separations, energy storage, sensors, and drug delivery.[23–28] Their versatility is associated with their tunability for specific applications through the immense structural diversity and combination of ions. ILs present lack of flammability, negligible vapor pressures, and generally high thermal stability, hence they are regarded as green solvents. The specific relation of ILs to RCC is their multifunctionality in synergizing the capture and conversion processes. More specifically, ILs have high CO_2 absorption capacity and selectivity, with tunable absorption reaction enthalpy. Further, ILs are ionically conductive and can serve as the electrolyte in electrochemical conversion reactions in addition to serving as the liquid sorbent for the capture process. Since the functionalized ILs complex with CO_2, they provide large availability of the reactants for the electrocatalytic conversion reaction (as long as the chemisorption complex is electrochemically active), thus enhancing their utility for RCC.

As alternatives to ILs, DESs are easier to obtain as they are mixtures of two or more components where the resulting liquid demonstrates significantly depressed melting point compared to the parent compounds (lower than the ideal liquid mixture).[29] There are different classes of DESs as first introduced by Abbott.[30,31] However, DESs that have been studied for CO_2 capture and conversion are mostly those formed from mixtures of hydrogen bond acceptor (HBA) such as a halide salt and hydrogen bond donor (HBD) compounds such as urea

Left to Right (members of 4C EFRC). Top row: Baleeswaraiah Muchharla; Bijandra Kumar; Jared S. Stanley; Jenny Y. Yang. Bottom Row: Rowan S. Brower; Jesús M. Velázquez; Robert L. Sacci; R. Dominic Ross; Christopher Hahn.

Baleeswaraiah Muchharla is a postdoctoral researcher in the Kumar group;
Bijandra Kumar is an Associate Professor at the Elizabeth City State University researching CO_2 reduction, energy storage, and sensors.
Jared S. Stanley is a PhD student in the Yang group developing molecular catalysts;
Jenny Yang is a Professor and Chancellor's Fellow at the University of California, Irvine; she is the Director of 4C EFRC.
Rowan S. Brower is a PhD student in the Velázquez group developing catalysts;
Jesús M. Velázquez is an Associate Professor at the University of California, Davis.
Robert L. Sacci is the Interim Group Leader of the Energy Storage & Conversion Group at Oak Ridge National Laboratory; his group images solid–liquid interfaces.
R. Dominic Ross is a postdoctoral researcher under the supervision of Christopher Hahn who is the Deputy Group Leader of the materials for Energy and Climate Security at Lawrence Livermore National Laboratory and the Deputy Director of 4C EFRC.

 This journal is © The Royal Society of Chemistry 2024

Open Access Article. Published on 24 June 2024. Downloaded on 1/17/2026 6:47:09 PM.
This article is licensed under a Creative Commons Attribution-NonCommercial 3.0 Unported Licence.

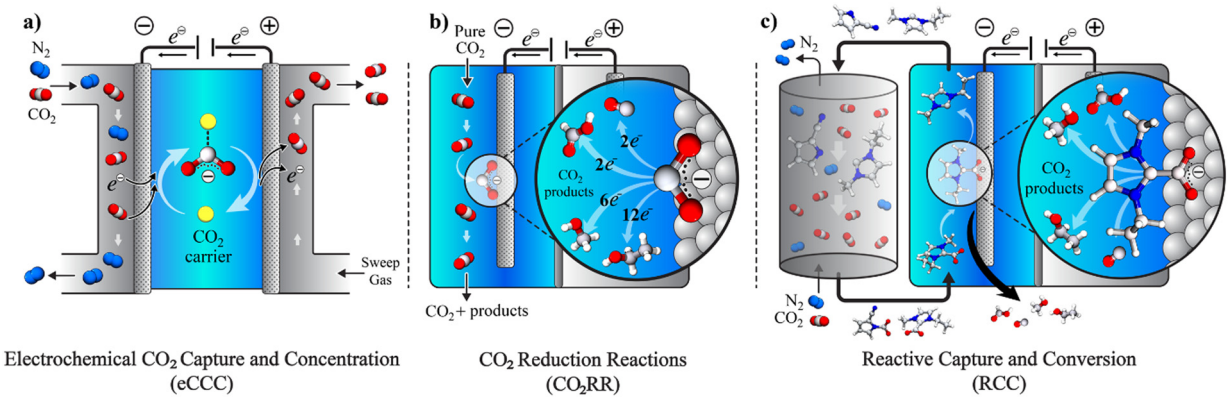

Fig. 1 Schematic illustration of eCCC, CO_2RR, and RCC processes. (a) A redox active carrier (represented by yellow sphere) binds with CO_2 upon reduction (generating a nucleophile) at the cathode, which is a gas diffusion electrode in contact with feed gas, and the carrier releases the CO_2 upon oxidation at the anode, thereby pumping CO_2 from the feed to the effluent side in an eCCC process. (b) The CO_2 that is physisorbed by the electrolyte is reduced to $CO_2^{\bullet-}$ at the cathode (also the catalyst) in a CO_2RR process and this intermediate then undergoes hydrogenation in the availability of a proton source, or C–C coupling at the cathode/catalyst surface, thus achieving heterogenous electrocatalytic conversion of CO_2. (c) The electron is injected from the electrode to the chemisorbed CO_2 either through a molecular catalyst or a functionalized electrolyte component, thus RCC achieves direct conversion of the chemisorbed CO_2.

and glycerol.[32] DESs present similar advantages as ILs including low vapor pressures, high CO_2 solubilities, high ionic conductivities, and generally tunable physical properties. As emphasized by Coutinho and colleagues,[33] 'deep eutectic' behavior of these solvents is what distinguishes them from simple mixtures or eutectic mixtures. However, as DESs are adapted and further tuned for specific applications, the confirmation of the phase behavior gets overlooked and many simple mixtures are referred as DESs.[33] As is the case, for DES applications in both CO_2 capture and electrochemical conversion where the formulations for tuning viscosity, conductivity, solubility, polarity, and electrochemical stability for RCC yield mixtures that loose this classification identity. Further, it is often difficult to measure the melting point of these mixtures and often only a glass transition temperature is seen. Therefore, these solvents are also referred as low-transition-temperature mixtures (LTTMs).[34] Nevertheless, these mixtures still offer some of the advantageous properties such as low volatility and high solubilities.[35] Example structures for ILs and DESs developed or utilized for CO_2 capture and electrochemical conversion are shown in Fig. 2.

While the focus of this review is RCC with electrolytes based on ILs and DESs, state-of-the-art solvents, electrolytes, and materials are introduced to provide a background and a perspective of the field. In particular ILs, DESs, and the related composite materials for CO_2 capture are reviewed with critical evaluations of their adaptability in electrochemical conversion approaches of CO_2. As a more conventional approach, efforts on the thermal conversion of CO_2 involving ILs are also summarized. A focused review on the mechanisms, thermodynamics, and kinetics of CO_2RR and RCC, as governed by the microenvironment created by ILs and DESs is presented with an emphasis on the topics of debate and recent findings. Further, a list of critical properties and key factors specific to IL and DES electrolytes for the combined capture and conversion processes are provided with the aim of better integration of the two fields toward the advancement of IL/DES systems for electrocatalysis in general. Specific takeaways from the techno-economic analysis of CO_2 electrolyzers are summarized as they relate to RCC with ILs. Finally, conclusion with a brief outlook are presented.

2. Functional solvents as capture media

2.1 Overview of sorption

Significant advances have been made in the development of sorbents both for CO_2 capture from point source of emissions (*e.g.*, flue gas streams) and DAC of CO_2 (at concentrations as low as 0.4 vol% of CO_2). These sorbents are categorized as liquid solvents (*e.g.*, amines, ILs, DESs, and alkaline solutions) and solid sorbents (*e.g.*, activated carbons, metal organic frameworks (MOFs), covalent organic frameworks (COFs), zeolites, silicas, porous organic polymers, carbon nanotubes, and particularly amine-modified porous supports). CO_2 is typically captured by liquid solvents *via* chemisorption, whereas in solid sorbents, CO_2 can either be chemisorbed or physisorbed onto the sorbent surface. The weak, reversible interactions of the physisorption process enable efficient desorption at moderate temperatures (40–60 °C), promoting energy conservation during regeneration. Moreover, rapid sorption and desorption kinetics associated with the physisorption contribute to fast sorbent cycling. However, the limited CO_2 capacity and low capture efficiency of such sorbents specifically for the capture from dilute streams pose challenges for RCC.

Among the carbon capture technologies, benchmark of industrial processes for CO_2 capture is absorption by aqueous alkanolamines and aqueous hydroxide solutions. Amines have many advantages such as excellent CO_2 capacity, high efficiency, and they are relatively inexpensive. However, CO_2 binds chemically with amines, hence, considerable amount of energy

Open Access Article. Published on 24 June 2024. Downloaded on 1/17/2026 6:47:09 PM.
This article is licensed under a Creative Commons Attribution-NonCommercial 3.0 Unported Licence.

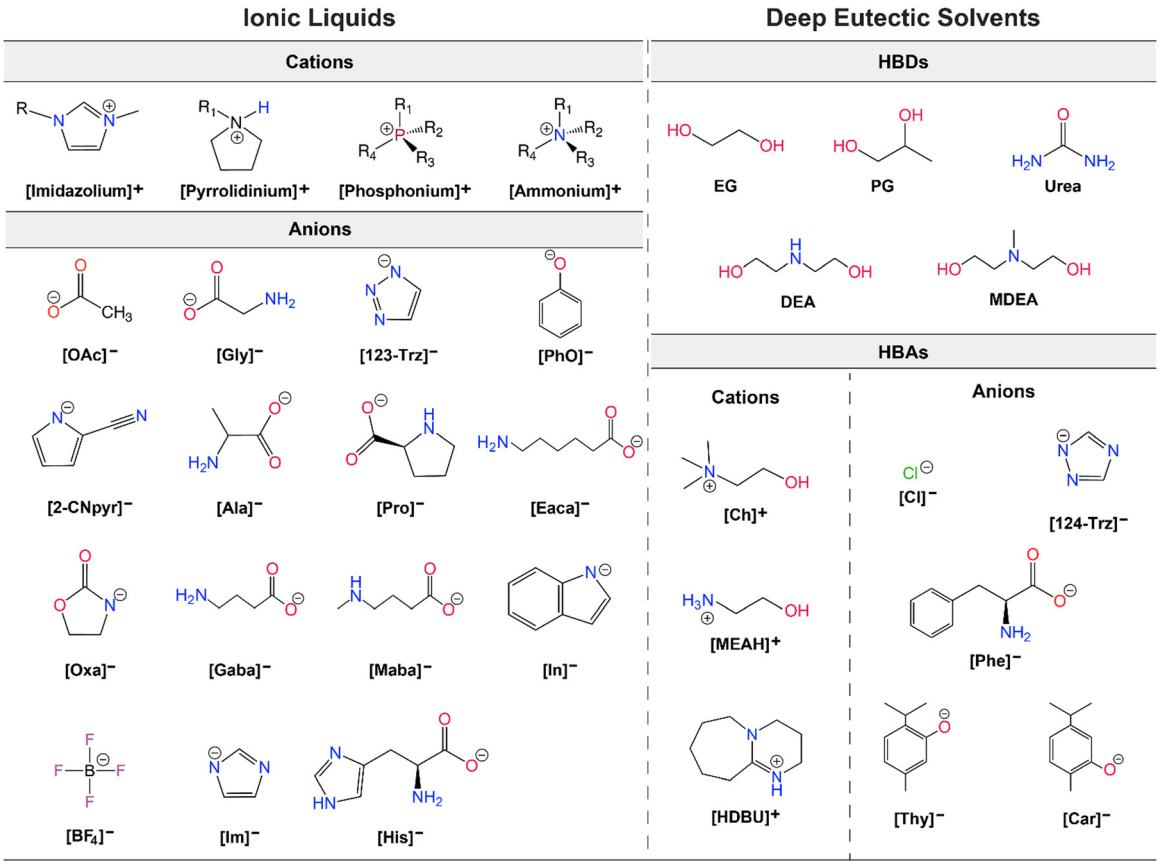

Fig. 2 Example structures of ILs (left) and DESs (right) studied for CO_2 capture and electrochemical conversion.

(−60 to −100 kJ mol^{-1} or 4–6 GJ per ton CO_2) is required to regenerate the solvent for the next cycle, which significantly lowers the efficacy of the overall process.[36,37] Furthermore, regeneration of sorbents at relatively high temperatures (*e.g.*, $CaCO_3$ requires higher than 800 °C for regeneration during DAC process) results in evaporation and susceptibility to thermal degradation of solvents. Other problems include corrosivity, toxicity, and oxidative degradation of the amine. Compared to liquid solvents, solid-based sorbents have shown promising potential to capture CO_2 from flue gas in terms of selective sorption capacity and lower energy for regeneration. Particularly, MOFs have received a lot of attention for CO_2 capture owing to their structural tunability,[38,39] as well as their high surface areas, high CO_2 capacities, and lower isosteric heat of adsorption (−20 to −30 kJ mol^{-1}) than the traditional sorbents such as zeolites,[40] activated carbons,[41] and silicas (−30 to −40 kJ mol^{-1}).[42]

Once CO_2 is captured from a gas mixture, it can be released either by an increase in temperature (temperature-swing) or through a reduction in pressure (pressure-swing). In temperature-swing adsorption/absorption technique, the temperature of the sorbent is increased to release the weakly bound CO_2, driven by the increasing kinetic energy of the molecules. High temperatures directly break the chemical bonds between CO_2 and functional groups of the sorbent, releasing the captured gas. Although this approach is effective, it is energy-intensive, and the sorbents are prone to degradation at elevated temperatures. Alternatively, pressure-swing adsorption/absorption lowers the pressure to release the captured CO_2. In the last decade, researchers have reported moisture-swing,[43–45] electro-swing,[46–48] and microwave-assisted (dielectric heating)[49–51] regeneration methods to desorb CO_2, which are comparatively more effective than conventional thermal heating owing to targeted heating, rapid desorption, and suppression of sorbent degradation. As a follow-up to these CCC processes where CO_2 is released during regeneration, conversion of the concentrated CO_2 *via* CO_2RR provides higher-value products, such as fuels and commodity chemicals. Better yet, if the CCC process is replaced by employing an RCC approach where the captured CO_2 is directly utilized for fuel production, it would, in theory, be a cost-effective solution. Chemisorption, characterized by chemical bond formation between the solvent components and CO_2, facilitates higher CO_2 capacities particularly at low partial pressures, making chemisorbing solvents interesting for achieving large-scale CO_2 conversion, specifically directly from CO_2 emission sources. However, not all of the capture sorbents are adaptable for RCC. Here, we present the insights to each of the capture media and provide a perspective on their adaptability for RCC.

2.2 Solvent types

2.2.1 Amines. Amines play a pivotal role in CO_2 absorption processes, particularly in the context of alkanolamines serving as well-established solvents.[52] These compounds, featuring

 This journal is © The Royal Society of Chemistry 2024

Open Access Article. Published on 24 June 2024. Downloaded on 1/17/2026 6:47:09 PM.
This article is licensed under a Creative Commons Attribution-NonCommercial 3.0 Unported Licence.

hydroxyl (–OH) and amino (–NH_2, –NHR, and –NR_2) functional groups on an alkane group, have been extensively studied in terms of their chemistry, kinetics, and thermodynamics in CO_2 capture.[53,54] Primary and secondary amines undergo a two-step process with CO_2, which includes direct reaction with CO_2 to generate zwitterionic species followed by the formation of carbamates upon protonation of the amine as shown as in Scheme 1.[55] The rapid reaction rates of primary and secondary amines contribute to the efficient mass transfer. However, carbamates are highly stable, requiring significant energy (-60 to -100 kJ mol^{-1})[56] to break the CO_2-amine bonds and release the captured CO_2 during regeneration.[57] In contrast, tertiary amines are incapable of directly reacting with CO_2 and require water to generate bicarbonate and a protonated amine through a zwitterionic intermediate as shown in Scheme 1.[58] The weaker C–O bonds in bicarbonates and carbonates, in comparison to the C–N bonds in carbamates, make CO_2 removal from tertiary amine solvents less energy-demanding. Yet, CO_2 absorption in tertiary amines is impeded by a slow absorption rate.[54] Hence, there are limitations related to the kinetics, energy usage, and equipment deterioration of amines as they tend to be corrosive.[59]

Because CO_2 is an acidic gas, a key feature in an organic sorbent is its basicity. Aqueous amines and aqueous alkali bases have been studied for CO_2 capture for decades in pressure-swing and temperature-swing absorption–desorption processes for point sources.[60–62] The CO_2 cyclic absorption capacities are found to be enhanced by increased basicity and the heat of absorption was reported to follow an order of primary/secondary > tertiary, with few exceptions as seen in Fig. 3.[63] Regeneration of amines, is an energy-intensive process because of high binding energy of amine with CO_2, in the order of -80 kJ mol^{-1}.[64] Thus, innovative heat integration schemes have been carried out to reduce the parasitic energy consumption of CO_2 capture technologies. Another challenge is fugitive emission of the solvent vapor, which must be re-condensed to prevent loss of active material, leading to an even greater energy penalty.[65] Nevertheless, these materials have been employed for post-combustion flue gas and direct air capture owing to their availability.[1]

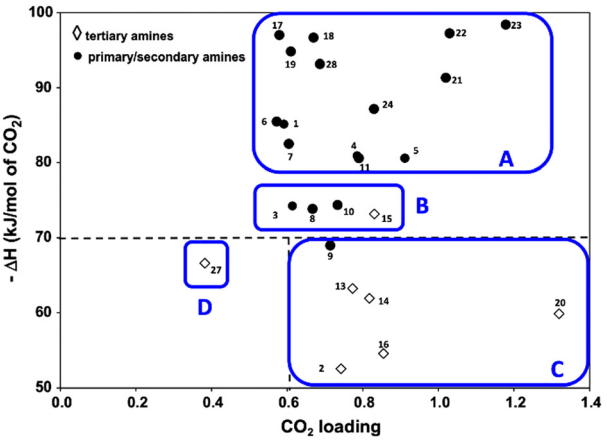

Fig. 3 Heat of absorption of aqueous amine solutions (primary, secondary, and tertiary amines). Classes A, B, and C are organized as high, moderate, and low ΔH. Class D (tertiary) is also with low ΔH but has very low CO_2 capacity. Reprinted with permission from ref. 63 Copyright 2017, Elsevier.

Recently, there has been interesting studies utilizing amines in RCC with the aim of replacing the conventional amine recovery unit in commercially available amine-based CO_2 capture processes with CO_2 electrolysis.[66–68] This approach can substitute the most energy-intensive step in industrial amine scrubbing processes while concurrently providing a pathway for CO_2 utilization.[69] As depicted in Scheme 1, the carbamate and bicarbonate are the primary CO_2 species and the concentration of free dissolved CO_2 is negligible. However, during the CO_2 electrolysis in amine solutions, there has not been direct evidence showing the conversion of the amine complexed CO_2 (*i.e.*, carbamate and bicarbonate species) on the electrode surface. For instance, despite the high CO_2 capture capacity of MEA, Chen *et al.*[70] observed dominance of the hydrogen evolution reaction (HER) (>80% faradaic efficiency, FE) and negligible CO_2 conversion rates and CO selectivities over smooth surfaces of Bi, Pb, Pd, Ag, Cu, and Zn in CO_2-saturated 30% (w/w) aqueous MEA solution containing 0.1% (w/w) cetrimonium bromide. These findings suggest that free dissolved CO_2 primarily serves as the active species during CO_2 electrolysis. Subsequently, Gallent *et al.*[66] proposed a process wherein CO_2 must be liberated from amine solutions before undergoing reduction to form various products. In this method, a CO_2-rich propylene carbonate solvent with 1 M 2-amino-2-methyl-1-propanol (AMP) and 0.7 M tetraethylammonium chloride is introduced into the cathodic side of an electrochemical reactor operated at approximately 75 °C. Here, the captured CO_2 is desorbed in close proximity to the cathode electrode surface and subsequently electrochemically converted into formate (giving up to 50% FE) and some oxalate and glycolate over a Pb surface. Further, other studies also highlighted the issues related to electrochemical instability, high volatility, and the corrosive nature of the amine towards the

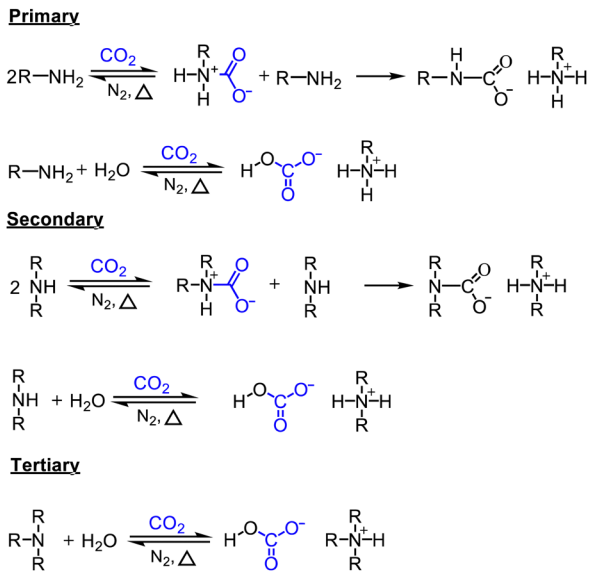

Scheme 1 CO_2 absorption by aqueous amines.

Open Access Article. Published on 24 June 2024. Downloaded on 1/17/2026 6:47:09 PM.
This article is licensed under a Creative Commons Attribution-NonCommercial 3.0 Unported Licence.

metal electrodes commonly used in RCC such as copper.[71,72] Achieving long-term stability in RCC requires selecting the right electrode material, electrolyte composition, and understanding the fundamental processes both in the bulk and at the electrode–electrolyte interfaces so that bottom-up approaches can be developed. Functional ILs are considered as alternatives to aqueous amines for RCC due to their corrosion-resistant properties and higher CO_2 capacities.[73,74]

2.2.2 Ammonia solutions. Ammonia-based solvents present a compelling option for CO_2 absorption. These solvents are characterized by lower degradation in flue gas environments compared to amines,[75] and by minimal corrosion, facile regeneration, and high absorption capacity.[76] Additionally, the aqueous ammonia based processes enable CO_2 stripping at elevated pressures, thereby mitigating the compression cost associated with the CO_2 capture. However, a significant challenge in the application of ammonia-based solvents lies in the potential escape of NH_3 due to its volatile nature,[77] which not only causes environmental issues, but also leads to a reduced NH_3 concentration in the solution, diminishing the overall CO_2 absorption capacity. Water washing, while recognized as an effective technology to inhibit NH_3 escape at the absorber outlet, requires substantial water consumption and generates wastewater, necessitating sophisticated post-processing measures.[78] Alternatively, acids such as sulfuric acid, hydrochloric acid, and hydrogen sulfide can be employed to absorb NH_3, offering advantages, such as minimized water usage and energy consumption, and the potential for processing the formed products into useful chemicals like fertilizers.[79] Hence, the choice of method is contingent upon a careful consideration of trade-offs between efficiency, environmental impact, and resource consumption.

The aqueous ammonia-based CO_2 capture yields ammonium bicarbonate (NH_4HCO_3) as a product. There has been reports of NH_4HCO_3 electrolysis for utilization of the captured CO_2 for integrated processes where the on-site generated NH_3 from nitrate can be used for RCC, thus generating formate.[80] Syngas production has also been reported for the direct electroreduction of NH_4HCO_3 on bromine-modified Ag electrocatalyst.[81] Separately, electrochemically driven C–N bond formation from NH_3 and CO_2 over a copper catalyst toward formamide and acetamide products is documented.[82] However, the desired product selectivities for these processes have heretofore remained very low.

2.2.3 Salt solutions. Salt solutions, such as carbonate/bicarbonate, hydroxides, and amino acid salts solutions, present a cost-effective and versatile family of chemical solvents utilized for CO_2 absorption.[1] These solutions, inherently salt-based, readily produce electrolyte solutions upon dissolution in water. Notably, their affordability, ease of regeneration, low toxicity, and high stability are the key characteristics. Potassium and sodium carbonates are the most popular chemical CO_2 absorption methods among salt solutions. While the reaction of CO_2 with carbonate is exothermic, the process is known for its slow absorption rate.[83] However, carbonates are superior to amines thanks to their lower heat of absorption. To enhance efficiency, promoters or activators, categorized as organic or inorganic, are introduced.[84] Similar characteristics and behavior of sodium carbonate and potassium carbonate make them interchangeable in these applications. In addition to the traditional solvents, innovative approaches involve the use of amino acid salts as potential substitutes, showing promise in CO_2 capture studies.[85] Despite their potential for capture, these systems were not explored for RCC due to challenges associated with the precipitation of the amino acid salt upon sharp decrease in pH after CO_2 saturation.[86] Further, CO_2 absorbed by the alkali hydroxide solution in the form of carbonate or bicarbonate can be converted to commodity chemicals such as CO, formic acid, and C_2H_4 by CO_2RR.[87] However, challenges associated with HER due to water reduction make this process inefficient. Therefore, various strategies such as improving ionic conductivity of electrolyte and innovations in the electrode material and structure have been utilized to modify the local reaction environment for HER suppression.

2.2.4 Ionic liquids (ILs). The tunable nature of ILs, coupled with their negligible volatility, chemical and thermal stability, and appreciable CO_2 capacity and selectivity under low CO_2 partial pressures makes ILs desirable for carbon capture. ILs have the capability to capture CO_2 through chemisorption (chemical reaction with CO_2, functionalized ILs) and physisorption (physical dissolution of CO_2, conventional ILs) mechanisms.[88] Among them, functionalized ILs offer advantages such as high CO_2 selectivity by preferentially binding CO_2 over other gases (*i.e.*, N_2 and O_2), resulting in a pure captured CO_2 stream and higher sorption capacity compared to physical absorption. Owing to their ionic conductivity, ILs can multifunction as electrolytes. As discussed later, ILs are specifically well suited for CO_2RR and RCC as they have high CO_2 solubilities besides other advantages such as wide electrochemical stability, negligible volatility, and lack of flammability. ILs have also shown to be effective in eCCC approaches where the high solubility and stabilization offered by the IL toward the electrochemically generated nucleophiles (that bind and release CO_2 with electro-swing) were critical enabling factors.[89] Here, we briefly discuss the tunability of ILs for CO_2 capture and present in more detail the various types of functional ILs that have been developed primarily for CO_2 capture.

CO_2-reactive ILs typically contain a nucleophilic functional group such as hydroxyl (–OH), amine (–NH_2) or amino acids, that can participate in hydrogen bonding with CO_2, *via* a nucleophilic attack mechanism similar to amine-based sorbents. Initially, this functionalization comes in the form of alkyl chains containing a primary amine, usually attached to the cation. However, ILs can be functionalized by introducing strong nucleophilic alcohol and amine moieties that allows for the chemisorption of CO_2 through a Lewis type acid–base reaction. Functionalized ILs offer impressive CO_2 capacity particularly at low partial pressures through the formation of carbonates and carbamates. The study by Bates *et al.* in 2002 was the first to report amine functional ILs for CO_2 capture, namely the task specific ILs, where they were able to attain almost 0.5 mol of chemisorbed CO_2 per mol of IL at 1 bar CO_2 and room temperature, according to the scheme shown in Scheme 2.[90] Following studies demonstrated improved CO_2 capacities, as high as 2 mol CO_2 per mol IL for the ILs utilizing biofriendly, cheap, and readily available amino acids with

 This journal is © The Royal Society of Chemistry 2024

Open Access Article. Published on 24 June 2024. Downloaded on 1/17/2026 6:47:09 PM.
This article is licensed under a Creative Commons Attribution-NonCommercial 3.0 Unported Licence.

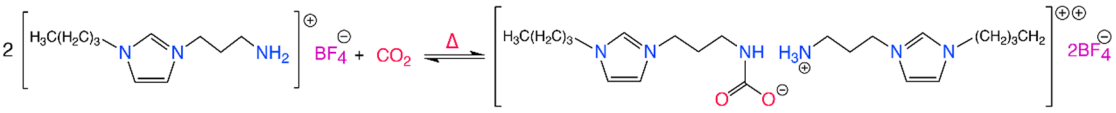

Scheme 2 The CO_2 chemisorption of a task specific IL where the imidazolium cation is functionalized with $-NH_2$ moiety. Adapted with permission from ref. 90 Copyright 2002, American Chemical Society.

nucleophilic amine groups for CO_2 chemisorption.[91,92] Similarly, Wang *et al.*,[93] investigated Lewis type acid–base interactions observed between CO_2 and the ILs, demonstrating the tunability of different aprotic trihexyl(tetradecyl)phosphonium cation-based ILs with varied anions. By varying the basicity of the anions in these solvents, the absorption enthalpy of CO_2 was varied, making it possible to tune the energy requirement for CO_2 desorption. For instance, the highly basic anion containing solvents, such as those containing the imidazolate anion, form high CO_2 capacity ILs with high CO_2–IL absorption enthalpies, making it harder to regenerate at elevated temperatures compared to the ILs containing the less basic triazolide anions.

Functionalized ILs demonstrate an increase in viscosity upon CO_2 complexation, associated with formation of intermolecular H-bonding.[94] For example, the viscosity of trihexyl(tetradecyl)-phosphonium isoleucinate ([P_{66614}][Iso]) increases over 200-fold after CO_2 absorption.[91] This limitation makes them less suitable for industrial CO_2 capture due to slow sorption rates driven by limitations in diffusion and mass transfer. Besides the ionic associations and H-bonding, this is in part due to the high molecular weight of the IL, which further translates to low CO_2 gravimetric capacities (<0.1 g CO_2 per g IL).[95] Therefore, the follow-up research focused on eliminating the increased H-bonding and reducing molecular weight as discussed later.[96]

Aside from aprotic ILs, protic ionic liquids (P-ILs), such as those formed from the combination of 1,8-diazabicyclo[5.4.0]undec-7-ene (DBU) superbase with weak acids such as imidazole, have shown great promise in the field of CO_2 separations.[97] CO_2 chemisorption in P-ILs, as shown in Scheme 3, is generally first induced by a proton transfer reaction from imidazole type molecules to the superbase, creating the electron rich imidazolate anion which is attractive for CO_2 chemisorption. However, the proton activities in P-ILs typically result in a decrease in their molar capacity in comparison to aprotic ILs, which potentially results from a decrease in the Coulombic interactions that aids in the absorption of CO_2. Additionally, to attain higher gravimetric capacities with ILs, Noorani and Mehrdad[98] studied the use of choline cation which has a relatively lower molecular mass when paired with different amino acids. However, choline–amino acid based ILs are known to be extremely viscous and typically require dilutants to improve their CO_2 absorption rates. The following sections provide an overview of different classes of functionalized ILs and discusses each type relevant to CO_2 capture with a perspective on their adaptability for RCC.

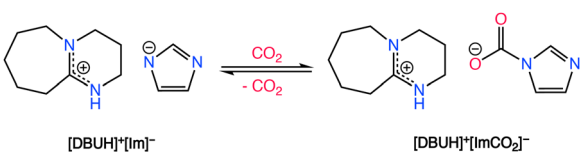

Scheme 3 CO_2 chemisorption by a DBU-based PIL. Adapted with permission from ref. 97 Copyright 2017, American Chemical Society.

2.3 Functionalized ILs

ILs are classified into several categories based on the combination of cations and anions, each exhibiting unique biological, physical, chemical, and thermal properties. Fig. 4 summarizes the category of functionalized ILs as discussed in this section. Task-specific ionic liquids (TS-ILs) are functionalized ILs that have received attention for their tunable properties achieved by altering cation–anion combinations, making them versatile for applications in organic synthesis, catalysis, and chiral compound synthesis.[99] Chiral ILs are useful for asymmetric inductions, having use in the liquid chiral chromatography, stereoselective polymerization, and chiral compound synthesis.[99] Switchable

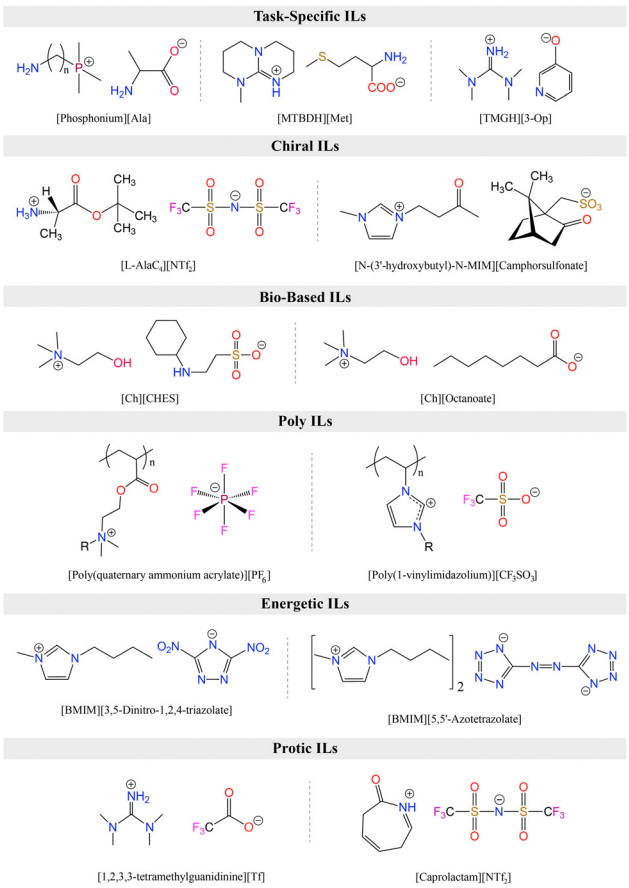

Fig. 4 Classes of ILs with representative structures.

Open Access Article. Published on 24 June 2024. Downloaded on 1/17/2026 6:47:09 PM. This article is licensed under a Creative Commons Attribution-NonCommercial 3.0 Unported Licence.

Polarity ILs (SPS-ILs) undergo polarity changes upon activation,[100] and bio-based ILs address the toxicity concerns by utilizing sustainable bio-precursors.[101] Polymerized ILs (poly-ILs) form repeating motifs and are utilized in diverse applications, including polymer electrolytes and sensors.[102] Energetic ILs offer advantages over conventional energetic compounds, such as 2,4,6-trinitrotoluene (TNT), 2,4,6,8,10,12-hexanitro-2,4,6,8,10,12-hexaazaisowurtzitane (HNIW), because of their higher density and thermal stability,[103] while neutral ILs exhibit weak electrostatic interactions and are used as inert solvents.[104] Protic ILs have redeemable Brønsted acidic protons,[105] and metallic ILs involve metal salts with specific counter anions,[106] showcasing a wide array of applications across various scientific and industrial domains.

Among different types of ILs, TS-ILs received a considerable amount of attention for CO_2 capture.[107] Such ILs are modified by the incorporation of various functional groups, such as amino,[54] carboxyl,[108] imidazolyl,[109] pyridyl,[110] alkoxyl,[111] and hydroxyl,[112] into their molecular structure. Introduction of these functional groups alters the physical and chemical properties of the ILs, enabling them to create additional or enhanced chemical interactions with CO_2.[113] This chemical reactivity significantly boosts the CO_2 absorption capacity, making TS-ILs crucial for achieving high absorption efficiency. Notably, as mentioned before, TS-ILs have demonstrated the ability to absorb equimolar or multi-molar amounts of CO_2, addressing the limitations of conventional ILs and offering a more effective solution for carbon capture in scenarios with low CO_2 partial pressures, such as post-combustion flue gas.[114]

2.3.1 Amino functionalized ILs. Amino functionalization on ILs by the incorporation of amino ($-NH_2$) groups has gained importance in CO_2 capture owing to their low cost, low environmental impact, biodegradability, and high biological activity. Pioneering work by Davis *et al.* introduced amino-functionalized ILs, exemplified by [APBIM][BF_4].[90] Their results demonstrated a notable capture capacity of 0.5 mole of CO_2 per mole of IL *via* a 2 : 1 carbamate mechanism (2 mol of amino: 1 mol of CO_2) at 1 bar, as in Scheme 2. This carbon capture capacity surpassed the performance of conventional alkanolamine aqueous solutions. However, a substantial increase in the viscosity upon complexation with CO_2 was observed. Similarly, Mehrdad *et al.* reported the impact of hydrogen bonding in their investigation of three amino acid ILs ([BMIM][Gly], [BMIM][Ala], and [BMIM][Val]) for CO_2 capture.[115] Their study explored both physical and chemical sorption mechanisms, revealing that the hydrogen bonding in these ILs led to elevated viscosity. Further exploration led to the synthesis of tetraalkylammonium amino acid ILs (AAILs) by Wu *et al.*, demonstrating low viscosity and high capture capacities approaching 0.5 mole of CO_2 per mole of IL for [N_{2222}][Ala], [N_{2222}][β-Ala], and [N_{2224}][Ala] at 1 bar and 40 °C.[116,117] Hence, these investigations highlight the nuanced approaches in tailoring amino-functionalized ILs for enhanced CO_2 absorption.

2.3.2 Carboxylate functionalized ILs. Functionalization of ILs with carboxylate groups has proven to be an efficient approach for enhancing their CO_2 absorption capabilities. Shiflett *et al.* examined the gas–liquid equilibria for CO_2 and

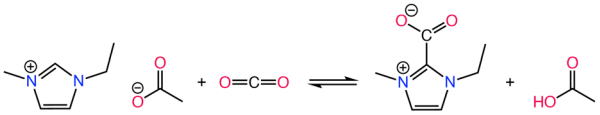

Scheme 4 Chemical reaction of CO_2 with carboxylate-functionalized ILs. Adapted with permission from ref. 125 Copyright 2022, Elsevier.

[BMIM][OAc], and reported significant CO_2 capacity of the IL.[118] They claimed chemisorption of CO_2 through the imidazolium carboxylate formation as evidenced by the spectroscopy and noted the acetic acid odor upon mixing of CO_2 and the IL. In a later study by the same group, a reversible formation of a chemical complex when CO_2 was bubbled through [EMIM][OAc] was reported.[119] Similarly, Maginn *et al.* examined carboxylate functionalized IL [BMIM][OAc] for CO_2 capture, and demonstrated a design strategy in the quest for effective CO_2-philic solvents.[120] Carboxylate-containing ILs have shown to be efficient in CO_2 capture through various chemisorption mechanisms as presented in Scheme 4. These mechanisms include deprotonation of the imidazolium C-2 position leading to the coupling of carbene with CO_2,[121] formation of non-volatile[118] or electron donor–acceptor (EDA) complexes confirmed by the ^{13}C high resolution magic angle spinning nuclear magnetic resonance (HRMAS NMR) spectra,[122,123] indicating the presence of multidentate binding between CO_2 and acetate, and carboxylate-induced ylide intermediates. *Ab initio* calculations have played a crucial role in understanding these interactions, as exemplified by the studies on [BMIM][OAc], where the presence of cooperative C–H···O interactions and Lewis acid–Lewis base interactions contribute to the enhanced stability of CO_2 complexes.[124] Hence, the functionalization of ILs with carboxylate moieties emerged as a promising venue for advancing environmentally friendly and efficient CO_2 capture solvents.

2.3.3 Azolate functionalized ILs. Azolate-functionalized ILs, also referred to as aprotic heterocyclic anion (AHA) based ILs were first discovered by Gurkan *et al.*[126] The design of these ILs were motivated by the need to control the viscosity of the solvent during CO_2 absorption and the reaction enthalpy; both factors are critical for practical applications in considering the operational costs of CO_2 absorption–desorption columns process. Later, derivatives featuring azoles like imidazole, pyrazole, trizole, and tetrazole have been reported.[127] Numerous studies investigating the CO_2 capture on different azolate functionalized protic and aprotic ILs demonstrated that the CO_2 reacts with the azolate anion, forming a new carbamate group.[97,127–129] Notably, anion-driven interactions play a pivotal role in this process, as highlighted by a study on super-base ILs, where reported CO_2 absorption capacities emphasize the importance of anion properties.[93] Basicity of the ILs, influenced by the pK_a values of the azoles, directly impacts the CO_2 absorption, with [P_{66614}][124-Trz] emerging as an exemplar IL owing to its favorable absorption enthalpy and high capacity.[130,131]

Effect of the basicity of the anion is further analyzed in various studies demonstrating different basicity on azolate anions can induce the extraction of an active hydrogen atom from the cation, leading to the formation of carbene or ylide

 This journal is © The Royal Society of Chemistry 2024

Open Access Article. Published on 24 June 2024. Downloaded on 1/17/2026 6:47:09 PM.
This article is licensed under a Creative Commons Attribution-NonCommercial 3.0 Unported Licence.

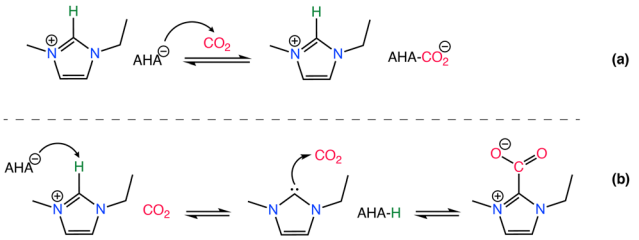

Scheme 5 CO_2 chemisorption by an AHA IL where the CO_2 binds to the nucleophilic anion (a) and to the imidazolium cation through the C2 position (b). Adapted with permission from ref. 132 Copyright 2019, American Chemical Society.

compounds that subsequently interact with CO_2 to create carbene–CO_2 or ylide–CO_2 complexes,[132–135] as in Scheme 5. The reversibility of CO_2 absorption on AHA ILs was further investigated with $[P_{2228}][2\text{-CNpyr}]$ and $[P_{2222}][BnIm]$, both in the absence and presence of water.[136] However, it is worth noting that the CO_2 absorption mechanism in moist conditions is different, thus often enhancing CO_2 absorption capacity.[136] However, the presence of co-adsorbed moisture necessitates increased thermal energy to regenerate the solvent due to the high heat capacity of water (4.2 J g^{-1} K^{-1}).[137] Bonilla *et al.*,[136] showed that in the presence of water, CO_2 capture mechanism includes an additional reaction pathway in AHA ILs. One pathway leads to the carbamate formation (expected reaction of the anion with CO_2) and the other pathway leads to the bicarbonate formation. Accordingly, the anion is protonated by water and CO_2 reacts with the hydroxide to form bicarbonate.

The versatility of the azolate ILs is underscored by their maintained viscosities without further increase, ease of regeneration (reaction enthalpies in the order of −50 kJ mol^{-1}),[138] and the potential formation of carbene and ylide complexes,[135,139,140] providing a rich landscape for designing tailored ILs for enhanced CO_2 capture efficiency. Further, some of the earlier works with ILs in CO_2RR and RCC are based on azolate ILs as discussed later.

2.3.4 Alkoxide and phenoxide functionalized ILs. In aqueous solutions of NaOH or KOH, CO_2 chemically reacts with hydroxide ions (OH^-) to form bicarbonate (HCO^{3-}) and carbonate (CO_3^{2-}) ions.[14,141] However, it is important to note that CO_2 sorption by OH^- is nearly irreversible.[142] The alkoxide is an anion, derived by removing a hydrogen atom from the –OH group of an alcohol. Hence, alkoxide-functionalized ILs can be formed by synthesizing switchable solvents, which are liquid mixtures of alcohol and a superbase. Moreover, a novel approach was presented by designing P-ILs by combining superbases with various weak proton donors, such as trifluoroethanol, utilizing their adjustable chemical reactivity towards CO_2, where superbases act as robust proton acceptors, creating a thermodynamic driving force for the formation of reactive P-ILs.[76] This method facilitated equimolar CO_2 capture under atmospheric pressure, with the ILs remaining in liquid form after the reaction. The P-ILs exhibited efficient CO_2 release at elevated temperatures and could be recycled without a significant loss in capacity. The lower viscosities of these superbase-derived P-ILs, compared to amino-functionalized ILs, further enhances their practical applicability for CO_2 capture. On the other hand, the protic nature of these ILs may induce HER in CO_2RR and RCC.

Similarly, phenol can be used to synthesize phenoxide based-functionalized ILs *via* the deprotonation of hydrogen atom from the –OH group of phenol to form phenolate anion. For example, a study investigated various phenolate ILs by modifying the phenolate anion structure with different substituents.[143] Performance measurements demonstrated that absorption capacities of these ILs varied with carbonyl-substituted phenolates.[144] The findings indicate that incorporation of a CHO group into the anion resulted in a notable increase in CO_2 capacity. Specifically, a molar increase of 0.2 was observed when comparing $[P_{66614}][PhO]$ and $[P_{66614}][4\text{-CHO-PhO}]$, with the CO_2 capacity rising from 0.81 to 1.01 mol CO_2 per mol IL.

Fluorinated phenolate ILs were also examined to have high CO_2 capacities. Specifically, a notable increase of approximately 20% in CO_2 capacity was observed for [DMAPAH][4F-PhO] and $[P_{4444}][4\text{-F-PhO}]$ in comparison to their respective counterparts [DMAPAH][2F-PhO] and $[P_{4444}][PhO]$.[145,146] The chemisorption mechanism for [DMAPAH][4F-PhO] is shown in Scheme 6. Additionally, phenoxides have no direct bond between the O atoms and the hydrogen atoms, hence, the absence of any intermolecular hydrogen bond interactions results in reduced viscosity.[144] Overall, the tunability of these functional groups highlights the potential of alkoxide and phenolate functionalized ILs in capturing CO_2, showcasing their role in environmentally relevant processes.

2.3.5 Other types of functionalized ILs. Various other functionalization have been explored to enhance the CO_2 capture of ILs, addressing the challenge of low CO_2 absorption capacity of non-reactive ILs. For instance, imide functionalized ILs, such as $[P_{4442}][Suc]$ and $[P_{4442}][DAA]$, were synthesized *via* a pre-organization approach to achieve a notable CO_2 capture efficiency.[147] Specifically, $[P_{4442}][Suc]$ demonstrated significant performance, capturing 1.9 mol CO_2 per mol IL through cooperative three-site, (O–N–O)–2–CO_2, interactions. Conversely, the N atom in neutral pyridine exhibited limited CO_2 capture ability, however, a study exploring hydroxypyridine-based functionalized ILs ($[P_{66614}][2\text{-Op}]$, $[P_{66614}][3\text{-Op}]$, $[P_{66614}][4\text{-Op}]$), reporting CO_2 capacities exceeding equimolar absorption thanks to the presence of cooperative N–CO_2 and O–CO_2 interactions.[110] Additionally, further investigation of hydroxypyridinate ILs with $[P_{4444}]^+$ cation showed 1.20 mol CO_2 absorption per mol of $[P_{4444}][2\text{-Op}]$ with a very low viscosity of 193 cP through anion–CO_2 interactions.[148] This study also demonstrated a polarity-induced viscosity model to

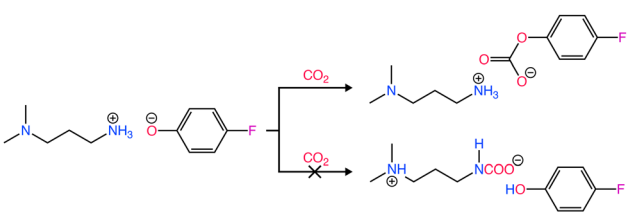

Scheme 6 CO_2 chemisorption by a phenoxide functionalized IL; CO_2 binding the hydroxy in the fluorine-substituted phenolic anion was favored. Adapted with permission from 146 Copyright 2018, Elsevier.

Open Access Article. Published on 24 June 2024. Downloaded on 1/17/2026 6:47:09 PM.
This article is licensed under a Creative Commons Attribution-NonCommercial 3.0 Unported Licence.

Table 2 CO_2 capture capacities (at 1 bar of CO_2 unless noted otherwise), viscosities, and the demonstrated regeneration temperatures for the functionalized ILs reported in literature in the last six years. T_A and T_D are the absorption and desorption temperatures, respectively

Ionic liquids	T_A (°C)	Capacity (mol CO_2 per kg solvent)	T_D (°C)	Viscosity at T_A (mPa s)
[Ch][Gly][149]	25	2.69	—	—
[Ch][βAla][149]		2.65	—	—
[Ch][Pro][149]		1.92	50	—
[Ch][Phe][149]		0.78	—	—
[HDBU][Im][150]	40.0	4.41	—	19
[HDBU][Ind][150]		3.02	—	—
[HDBU][124-Trz][150]		1.73	—	307
[HDBN][Im][151]	40.2	3.38		
		1.61 (0.1 bar)	80.2	8.3
[HDBN][Pyr][151]		3.38		
		1.30 (0.1 bar)	—	5.1
[HDBU][Pyr][151]		3.04		
		1.41 (0.1 bar)	—	9.7
[EMIM][OAc][152]	40.2	1.65	—	—
[EMIM][Ala][152]		1.89	—	34.5
[EMIM][Gly][152]		2.32	—	39.4
$[P_{66614}][3HMPz]$[153]	25.0	1.65	60.0	922.6
$[P_{66614}][5HMPz]$[153]		0.74	—	—
$[P_{66614}][1HDMPz]$[153]		1.16	—	—
$[P_{66614}][1HMPz]$[153]		1.43	—	—
$[N_{1111}][Eaca]$[154]	40.2	4.02		
		2.84 (0.1 bar)	80.2	85.5
$[N_{1111}][Maba]$[154]		4.05		
		2.79 (0.1 bar)	—	116.3
$[N_{1111}][Gaba]$[154]		3.29		
		2.55 (0.1 bar)	—	140.5
$[P_{66614}][MN]$[155]	25	1.53 (1 bar)		1235

elucidate the relationship between viscosity and linear interaction energy by performing quantum chemistry calculations for the first time. It was concluded that the viscosity differences in hydroxypyridine-based ILs and changes in viscosity after CO_2 absorption are primarily associated with varying distributions of negative charges within the anions. These examples highlight the diverse strategies for functionalizing ILs to optimize CO_2 capture across various conditions. Table 2 summarizes CO_2 absorption capacities of various types of functionalized ILs.

2.4 Deep eutectic solvents (DESs)

In the context of CO_2 capture, where it is essential to prioritize high selectivity, absorption capacity, low desorption energy, and stability, DESs stand out as effective contenders as capture media. Common examples of DESs for CO_2 capture include HBAs that are often ammonium or phosphonium salts and HBDs such as ethylene glycol, urea, or other organic compounds with functional groups such as the carboxylic acid, amide, alcohol, and thiol groups. A common characteristic of DESs is the significant depression in the melting point of the liquid at the deep eutectic composition compared to the individual constituents. Although earlier reports revealed advantageous properties, such as the formation of low viscous solvents with the highest conductivity at the eutectic composition, eutectic solvents formed at different HBA:HBD compositions in the vicinity of the eutectic point have also been of interest[35] because of the similar desirable properties they present for application in biotechnology, catalysis, and gas separations and conversion. Given the various degree of melting point depression obtained in different HBA:HBD compositions discussed here, these mixtures will be referred to as eutectic solvents for simplicity.

A common example of eutectic solvents includes reline, formed by mixing solid choline chloride salt ([Ch][Cl]) and urea (in a 1 : 2 molar ratio) which result in the formation of a room temperature liquid. Other examples of eutectic solvents include ethaline and glycine, both of which contain [Ch][Cl] as HBA, with ethylene glycol (EG) and glycerol (Gly) as HBDs, respectively. Ethaline contains about 1 : 4 molar ratio of [Ch][Cl] : EG, whereas glycine contains about 1 : 2 molar ratio of [Ch][Cl] : Gly, both of which have been studied for CO_2 capture and separation applications.[156,157] In these solvents, CO_2 absorption is mainly dominated by the physical absorption of CO_2 through the occupation of the entropic voids that are maximized at the deep eutectic composition.[32] While physisorbing eutectic solvents show appreciable CO_2 capacities at elevated pressures, they are less effective for low partial pressure CO_2 separations due to their low CO_2 selectivity and uptake. Through precise adjustment of the CO_2 affinities of the functional groups present in the HBAs and HBDs, eutectic solvents can be tuned to both physisorb and chemisorb CO_2. As such, introducing CO_2 reactive functional groups into eutectic solvent results in the formation of more suitable solvents for applications such as DAC, where CO_2 is captured from air with ultra-low CO_2 concentration (*i.e.*, 410 ppm).[158] Increasing the CO_2 affinity of the HBAs/HBDs typically involves incorporation of the nucleophilic moieties that allows formation of CO_2 reactive eutectic solvents with appreciable CO_2 capacity and selectivity even under CO_2 concentrations as low as 0.5% of the feed.[150,159,160] Commonly utilized eutectic solvents for the process of chemical absorption consist of ILs, amines, and alkanol amines *via* the creation of N–C, O–C, and C–C bonds.[125,161]

Earlier examples of DESs with CO_2 chemisorption include the addition of superbases to ethaline such as the one reported by Bhawna *et al.*,[162] where 1,5-diazabicyclo[4.3.0]non-5-ene (DBN) and 1,5,7-triazabicyclo[4.4.0]dec-5-ene (TBD) were the active components. Superbases participates in strong proton sharing interactions with ethaline, inducing the formation of electron rich (nucleophilic) moieties with high CO_2 affinity, which facilitates chemisorption as shown in Scheme 7.

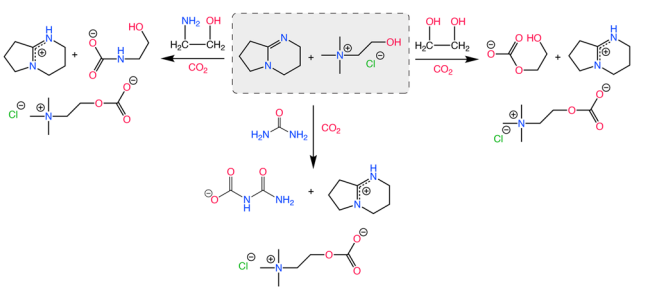

Scheme 7 CO_2 chemisorption in superbase-added [Ch][Cl] based eutectic solvent. Adapted with permission from ref. 162 Copyright 2017, John Wiley and Sons.

This journal is © The Royal Society of Chemistry 2024

Open Access Article. Published on 24 June 2024. Downloaded on 1/17/2026 6:47:09 PM. This article is licensed under a Creative Commons Attribution-NonCommercial 3.0 Unported Licence.

The strong proton sharing induced by the superbase results from their high proton affinity as strong Brønsted-Lowry bases. Several studies have further shown how the proton activities, influenced by the presence of strong Brønsted–Lowry bases, affect the CO_2 chemisorption in eutectic solvents. For instance, Cui *et al.*[159] showed the impact of phosphonium and ammonium based HBAs with imidazolate and triazolate conjugate base anions, both of which have high HBA ability, on the chemisorption of CO_2 to EG. The EG chemisorption was initiated by an induced proton sharing interaction due to the presence of the strong conjugate bases. These tetraethylphosphonium ($[P_{222}]^+$) and tetraethylammonium ($[N_{222}]^+$) based eutectic solvents, capable of absorbing almost 1 mol CO_2 per mol solvent at 1 bar CO_2 and at 25 °C were easily regenerable at 70 °C; with the $[P_{222}]^+$ and $[N_{222}]^+$ counterions showing very similar absorption behaviors. Similarly, Wang *et al.*[163] studied the impact of HBDs on CO_2 where both EG and triazole HBDs were used. While EG HBD systems were observed to show appreciable CO_2 capacities, the use of triazole HBDs in place of EG resulted in a sufficient decrease in the CO_2 chemisorbing ability of the eutectic solvents despite the buildup of electron density resulting from the proton sharing interactions, highlighting the complex interplay between components in eutectic solvents. Wang *et al.*[164] also observed the reactivity of EG in bio-phenol based eutectic solvents; however, changes in the HBD from EG to 4-methylimidazole was accompanied by a change in the chemisorption sites and CO_2 absorption mechanism. While eutectic solvents employing EG as the HBD exhibited primary chemisorption by EG itself, replacing EG with 4-methylimidazole HBD resulted in a shift, with bio-phenol derivatives becoming the predominant chemisorption sites. This potentially results from a combination of the changes in the proton activities present within these solvents, as well as the differences in the localization of electron density in the various binding sites.

Lee *et al.*[160] reported on the eutectic formation when [EMIM][2-CNpyr] IL was mixed with the common HBD ethylene glycol. Similar to previous reports, in the presence of a basic anion, EG was deprotonated neutralizing the pyrrolide that enabled CO_2 binding to EG, thus forming carbonate species in addition to the known CO_2 binding mechanism to the IL component itself. Scheme 8 illustrates the CO_2 absorption reaction by this reported eutectic solvent. Further, from the transition state calculations performed at the density functional theory (DFT) level, the authors showed the significantly reduced reaction energies for CO_2 binding to both the IL anion and the cation in the presence of EG due to the hydrogen bonding interactions. These interactions resulted in lowered energy requirements for the regeneration of the solvent where regeneration temperatures as low as 40 °C was possible for a cyclable working capacity of CO_2.

Dikki *et al.*[165] further demonstrated a very similar EG-CO_2 chemisorption behaviors in choline based eutectic solvents with EG as the HBD. By tuning the proton affinity of the conjugate base anions in the different eutectic solvent systems, they observed a change in the concentration of CO_2 chemisorbed by EG. For instance, the concentration of CO_2 bound to the eutectics was greatest in the imidazolate containing solvents with the highest proton affinity (pK_b of imidazolate in H_2O = −0.52), followed by those with triazolate anion-based solvent (pK_b of triazolate in H_2O = 4.03). Notably, EG-CO_2 chemisorption was non-detectable in the chloride-based eutectic solvent (pK_b of chloride in H_2O = ∼20), thus demonstrating the tunability of CO_2 capacity through modifying the proton activity.

Scheme 9 shows the representative proton sharing and the CO_2 binding in this reactive eutectic solvent. It was further observed that anions such as imidazolate, triazolate, and phenolate systems with electron density delocalization by resonance were less likely to interact with CO_2 compared to EG with a more localized electron density. Aside from its ability to participate in the CO_2 chemisorption process, studies have shown that EG can modulate proton activity in these mixtures.

As reported by Klemm *et al.*,[149] mixing EG with choline amino acid based salts (*i.e.*, [Ch][Pro]) resulted in an increase in the chemisorption of CO_2 to –NH_2 group present in $[Pro]^-$ in the eutectic solvents when compared to the neat [Ch][Pro]. Through a combination of experimental NMR spectroscopy and computational methods including molecular dynamics

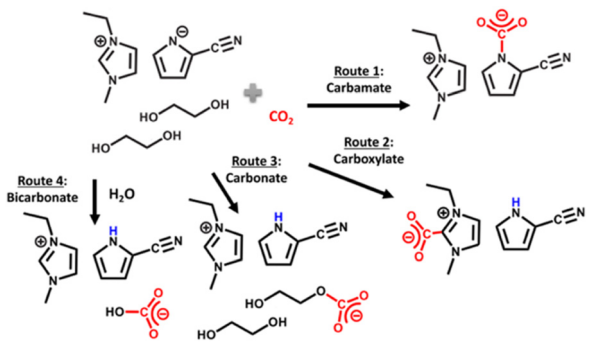

Scheme 8 CO_2 chemisorption in DES composed of [EMIM][2-CNpyr] and EG. Reprinted with permission from ref. 160 under CC-BY-NC-ND license.

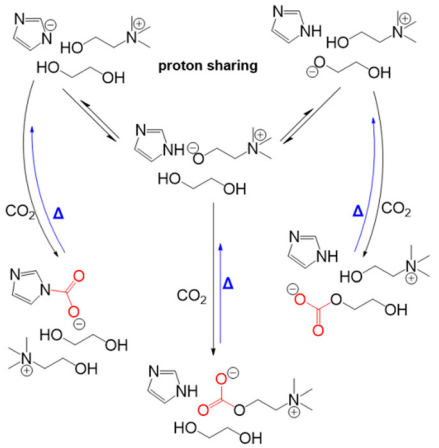

Scheme 9 CO_2 chemisorption in a eutectic solvent composed of choline imidazole and ethylene glycol. Reprinted from ref. 165 with permission from the Royal Society of Chemistry. Copyright 2024.

Open Access Article. Published on 24 June 2024. Downloaded on 1/17/2026 6:47:09 PM.
This article is licensed under a Creative Commons Attribution-NonCommercial 3.0 Unported Licence.

(MD) simulations and DFT calculations, authors elucidated CO_2 absorption mechanism. Analysis demonstrated that hydrogen bonding interactions facilitated by EG play a crucial role in preventing proton transfer between [Pro]–[Pro] species upon CO_2 binding to $[Pro]^-$. With the inclusion of EG, deactivation of CO_2 binding sites resulting from intermolecular proton transfer was prevented and higher CO_2 capacity was obtained with the eutectic solvent compared to neat [Ch][Pro].

While the chemical makeup of the eutectic mixtures can be tuned for CO_2 absorption, significant changes are also noted in physical properties including the basicity, polarity, thermal stability, density, and viscosity.[166] These properties are important when regenerating these solvents at elevated temperatures. Like ILs, different functional groups present in the HBAs and the HBDs influence the binding energies of the CO_2, which further translate to large variations in the amount of energy required to desorb the captured CO_2. For instance, among the studied choline-based eutectic solvents with imidazolate, triazolate, 2-cyanopyrilide, and phenolate, Dikki *et al.*,[165] found that the triazolate solvents were easily regenerated at 50 °C while the imidazolate eutectics required elevation up to 70 °C for regeneration for the same working capacity post absorption at 25 °C. This difference was in spite of having similar CO_2 binding sites in both systems, thus showing the tunability of the energy required to desorb the chemisorbed CO_2 in these solvents through the proton activity and the electrostatics induced by the hydrogen bonding network. Since it is desired to minimize water in these liquids to maintain a low energy requirement for regeneration, there has been some examples of hydrophobic DESs as well.[167] Table 3 summarizes the gravimetric capacities of different CO_2 reactive ILs and eutectic solvent systems reported in literature, along with the changes in viscosities post CO_2 saturation. Considering the target CO_2 loading quoted by DAC companies (*e.g.*, Climeworks) is 1 mmol CO_2 per g of sorbent, these results are very promising.

From Table 3, it can be gathered that the viscosity of the HBDs component primarily governs the viscosity of the resulting liquid mixture. It is also noticed that by replacing the hydroxyl

Table 3 CO_2 capture capacities (at 1 bar of CO_2), viscosities, and the regeneration temperatures for the functionalized eutectic solvents reported in literature within the last five years. T_A and T_D are the absorption and desorption temperatures, respectively

Eutectic solvents	T_A (°C)	Capacity (mol CO_2 per kg)	T_D (°C)	Viscosity at T_A (mPa s)	Viscosity with CO_2 at T_A (mPa s)
$Ch^{\pm}$ImH : EG (1 : 2)[165]	25	3.25	70	200	191
$Ch^{\pm}$PhOH : EG (1 : 2)[165]		2.49	50	356	185
[Ch][2-CNpyr] : EG (1 : 2)[165]		2.41		95	178
[Ch][124-Trz] : EG (1 : 2)[165]		2.36		171	157
$Ch^{\pm}$ImH : PG (1 : 2)[166]	25	2.75	70	369	430
$Ch^{\pm}$PhOH : PG (1 : 2)[166]		2.35	5	644	409
[Ch][2-CNpyr] : PG (1 : 2)[166]		1.67		170	340
[Ch][124-Trz] : PG (1 : 2)[166]		2.03		335	349
$Ch^{\pm}$ImH : MEA (1 : 2)[166]		4.60	—	128	—
$Ch^{\pm}$PhOH : MEA (1 : 2)[166]		3.13	—	182	—
[Ch][124-Trz] : MEA (1 : 2)[166]		4.92	60	121	—
$[N_{2222}]$[123-Trz] : :EG (1 : 2)[163]	25	2.48	60	—	—
$[P_{2222}]$[123-Trz] : EG (1 : 2)[159]	25	2.68	70	—	—
$[P_{2222}]$[Im] : EG (1 : 2)[159]		2.69	—	—	—
[EMIM][2-CNpyr] : EG (1 : 2)[160]	25	2.59	40	45	—
[Ch][Pro] : EG (1 : 2)[149]	25	2.10	50	—	—
[Ch][βAla] : EG (1 : 2)[149]		1.83		—	—
[Ch][Gly] : EG (1 : 2)[149]		1.69		—	—
[Ch][Phe] : EG (1 : 2)[149]		0.45		—	—
[HBDU][Im] : EG (7 : 3)[150]	40	3.20	70	31.48	166.51
[HBDU][Ind] : EG (7 : 3)[150]		2.66	—	36.99	114.18
[HBDU][123-Trz] : EG (7 : 3)[150]		2.45		197.72	205.26
[HBDU][Im] : EG EG (6 : 4)[150]		2.68		—	—
[HBDU][Im] : EG EG (5 : 5)[150]		2.48		—	—
[HBDU][Im] : EG EG (4 : 6)[150]		1.86		—	—
[Ch][Cl] : MEA (1 : 5)[168]	30	6.18	—	~25	—
[Ch][Cl] : DEA (1 : 6)[168]		3.89		~75	—
[Ch][Cl] : MDEA (1 : 7)[168]		1.39		~350	—
[HDBU][Car] : EG (1 : 2)[169]	25	2.27	70	389	—
[HDBU][Car] : EG (1 : 3)[169]		2.03	—	228	—
[HDBU][Car] : EG (1 : 4)[169]		1.80		166	—
[HDBU][Thy] : EG (1 : 2)[169]		2.27	70	477	—
[HDBU][Thy] : EG (1 : 3)[169]		2.03	—	263	—
[HDBU][Thy] : EG (1 : 4)[169]		1.82		179	—
[MEAH][Cl] : MDEA (1 : 3)[170]	25	2.64	80	262	~1500
[DEAH][Cl] : MDEA (1 : 3)[170]		2.46	—	~260	~1450
[MDEAH][Cl] : MDEA (1 : 3)[170]		1.34		~250	~420
[DBUH][4-F-PhO] : EG (1 : 5)[171]	25	1.74	75	87	—
$[N_{2222}]$[4-PyO] : DMSO (1 : 4)[172]	40	2.06	—	6.5	—
$[N_{2222}][CH(CN)_2]$: Eim (1 : 1)[173]	30	2.8	120	12.7	115

 This journal is © The Royal Society of Chemistry 2024

Open Access Article. Published on 24 June 2024. Downloaded on 1/17/2026 6:47:09 PM. This article is licensed under a Creative Commons Attribution-NonCommercial 3.0 Unported Licence.

functionalized HBAs with those with amine functionalized HBAs, viscosity of the eutectic solvent is reduced. However, the viscosities of these solvents are generally increased with CO_2 saturation and the starting viscosity range is one to two orders of magnitude higher compared to aqueous amines. Therefore, the advantages from their lowered regeneration energy and the disadvantage from their high viscosities should be analysed in a coupled manner to further improve the CO_2 capture and separation performance of DES sorbents.

2.5 Composite materials with ILs/DESs

Although ILs provide several advantages as sorbents, such as low volatility and high thermal stability at CO_2 capture conditions, they exhibit quite high viscosities, which can increase even more upon CO_2 saturation, reducing the mass transfer.[174] However, having a low viscosity is another prerequisite for a good sorbent.[126] To mitigate the negative effects arising from the high viscosities of ILs, they can be immobilized on porous materials. An increased contact area of the IL with the CO_2 gas increases the sorption rate.[175] Furthermore, this is a cost-efficient solution when considering the costs of the ILs.[176]

For CO_2 capture, several composites (Table 4) were considered by depositing ILs on high-surface-area supports, such as metal organic frameworks (MOFs),[175,177–181] covalent organic frameworks (COFs),[179,182,183] carbonaceous materials,[175,181,184–188] zeolites,[189,190] synthetic and natural clay minerals,[191–193] mesoporous and microporous silica and alumina,[175,194–196] and polymers.[197,198] ILs immobilized within the pores of these materials, improved several aspects of the CO_2 capture process, owing to the increased gas–liquid interface.[199] For example, Arellano *et al.* demonstrated a sevenfold higher CO_2 uptake for [EMIM][NTf_2]-zincate/SBA15 composite compared to the bulk IL.[200] Likewise, [BMIM][NTf_2]/MOF-808, with an IL thickness layer of 1.7 nm on the external MOF, provided a normalized CO_2 uptake of 38.7 mmol g^{-1} at 100 kPa and 25 °C; 1000 times higher than the bulk IL.[201]

Similar to IL-based hybrid composites, impregnation of DESs into porous materials has recently emerged as a promising strategy to design hybrid materials for CO_2 capture and separation. This approach aims to increase the affinity of the hybrid sorbents towards CO_2 for enhanced selectivities and to increase the CO_2-DES contact area for improved sorption rates. Furthermore, tunability of DES composition allows to tailor CO_2 interaction strength with the binding sites. Impregnation of porous materials including activated carbon,[234] silica,[235] and MOFs[236] with DESs also showed to be effective in terms of increasing the additional CO_2 binding sites in the composite, compared to the parent compounds.

Such composites of ILs or DESs with porous materials are synthesized by a variety of methods, either through *in situ* methods, such as ionothermal synthesis, or by post synthesis routes, like wet impregnation, incipient wetness impregnation, capillary action, ship-in-a-bottle, and grafting.[237] Wet impregnation, one of the most frequently used routes, results in a noncovalent interaction between the IL/DES and the surface of the porous material. On the other hand, methods, such as grafting, involve a covalent bond formation between the liquid and the surface,[229] which can offer advantages, such as maintaining the porosity of the host material and higher stability, in the expense of more complicated synthesis procedure. In this section, we focus on physically impregnated porous materials; more details on the CO_2 uptake and separation performance of composites obtained by grafting ILs on supports can be found in the review article by Zheng *et al.*[175]

One of the crucial properties of IL/porous material composites determining their applicability is their thermal stability limits. The thermogravimetric analysis data of a composite typically presents a two-step decomposition, associated with the decomposition

Table 4 CO_2 capacities of different IL-based porous composites reported in the literature

IL/porous composites	P (bar)	T_A (°C)	T_D (°C)	CO_2 uptake (mmol g^{-1})
[HEMIM][DCA]/ZIF-8[202]	1	25	125	0.42
[BMIM][SCN]/ZIF-8[203]	1	25	125	0.33
[BMIM][BF_4]/ZIF-8[177]	1	25	125	0.27
[BMIM][PF_6]/ZIF-8[204]	1	25	125	0.39
[BMIM][OAc]/ZIF-8[205]	1	30	80	1.03
[BMIM][$MeSO_3$]/ZIF-8[206]	1	25	125	0.39
[BMIM][CF_3SO_3]/ZIF-8[206]				0.37
[BMIM][$MeSO_4$]/ZIF-8[206]				0.41
[EMIM][OAc]/ZIF-8[207]	1	30	100	0.59
[EMIM][NTf_2]/ZIF-8[207]				0.43
[C_2OHMIM][NTf_2]/ZIF-8[207]				0.41
[C_{10}MIM][NTf_2]/ZIF-8[207]				0.45
[P_{66614}][NTf_2]/ZIF-8[208]	1	30	100	0.42
[C_6MIM][DCA]/ZIF-8[208]				0.43
[C_6MIM][$C(CN)_3$]/ZIF-8[208]				0.45
[C_6MIM][Cl]/ZIF-8[208]				0.43
[BMIM][$FeCl_4$]/ZIF-8[208]				0.41
[BMIM][OAc]/CuBTC[209]	1	30	80	1.90
[BMIM][NTf_2]/CuBTC[209]				2.1
PIL/CuBTC[210]	0.2	25	200	0.8
[EMIM][NTf_2]/MOF-808[201]	1	25	60	3.0
[DETA][OAc]/MIL-101(Cr)[211]	1	25	100	2.35
BUCT-C19[212]	1	25	150	1.88
AFIL-ZIF-8[213]	1	25	150	2.38
Ni-MOF/IL-3[214]	1	25	80	4.34
[BMIM][Cl]/SBA-15[215]	0.4	25	65	2.40
[BMIM][NTf_2]/alumina[216]	0.4	25	65	1.30
[C_4MIM][NTf_2]/Silica[216]				1.27
[BMIM][$MeSO_4$]/MIL-53(Al)[217]	1	25	110	0.89
[TETA][NO_3]/SBA-15[218]	0.15	40	150	2.12
[BMIM][OAc]/SBA-15[219]	0.04	25	120	0.93
[EMIM][OAc]SBA-15[220]	1	30	110	2.20
[EMIM][OAc]/MOF-177[221]	1	30	120	0.4
[EMIM][Gly]/activated carbon[222]	0.04	50	100	0.58
[EMIM][Gly]/PMMA[198]	0.023	30	150	0.88
[EMIM][Lys]/PMMA[198]				1.05
[N_{1111}][Gly]/PMMA[223]	0.023	30	100	2.14
[EMIM][Gly]/PMMA[224]	0.023	30	100	0.90
[EMIM][Lys]/MCM-41[225]	0.15	30	100	1.50
[N_{1111}][Gly]/silica[136]	1.5	30	80	0.65
[Vbtma][Gly]/activated carbon[187]	1	25	110	1.51
[TEA][Tau]/SBA-15[226]	0.1	25	110	1
[P_{4444}][2-Op]/silica[227]	0.15	50	120	1.49
[P_{66614}][124-Trz]/SBA-15[228]	1	20	50	0.70
[P_{4443}][Cl]/silica gel[229]	1	0	150	1.07
[P_{4443}][BF_4]/silica gel[229]				1.30
[$(EtO)_3SiP_{8883}$][NTf_2]/activated carbon[188]	2	25	80	0.87
[EMIM][Lys]/silica[230]	1	25	105	0.61
[DAMT][BF_4]/graphene[231]	1	25	120	0.88
[NAIm][Br]/ZIF-67[232]	0.15	25	200	0.68
[Et_4NBr]/Py-COF[233]	1	25	100	1.97

Open Access Article. Published on 24 June 2024. Downloaded on 1/17/2026 6:47:09 PM.
This article is licensed under a Creative Commons Attribution-NonCommercial 3.0 Unported Licence.

of the IL and the porous material separately.[238,239] However, if the porous material is highly stable, as in the case of metal oxides or zeolites, typically only one decomposition step, corresponding to the decomposition of the IL only, is observed.[240,241]

Interestingly, thermal stability limits of these composites are generally reported to be largely different than those of their individual components (the IL and the porous material),[238,240] representing the formation of a new hybrid material having different characteristics. These characteristics are mostly set by the molecular interactions between the IL molecules and the surface of the porous material. These interactions also play a major role in determining the gas sorption properties of the composite. For instance, Kinik *et al.* presented the results of a detailed infrared (IR) spectroscopy-based analysis by comparing the IR spectrum of [BMIM][PF_6] in the bulk state with that of the composite prepared by incorporating the same IL into the cages of ZIF-8.[204] Data showed that the IR bands belonging to the imidazolium ring of the IL blue-shifted when the IL was immobilized on the MOF, while the features associated with the $[PF_6]^-$ anion were red-shifting. The weakening of the P–F bond upon immobilizing the IL on ZIF-8 demonstrated an electron-sharing between the anion and the ZIF-8, which evidenced a direct interaction between MOF and the anion of the IL. The extend of such interactions, and their consequences on the gas sorption properties, depends significantly on the individual components of a composite, and hence different combinations of an IL with different porous materials offer significantly different performance measures.[237] The research has been directed towards tuning these interactions towards improved ability for separating CO_2 from different gas mixtures.

In one of the earliest reports introducing the potential of IL incorporated MOFs for CO_2 separation, Sezginel *et al.* immobilized [BMIM][BF_4] into Cu-BTC at IL loadings of 5, 20, and 30 wt% by impregnation.[242] Data showed that the ideal sorption selectivities, calculated as the ratio of adsorbed amounts of single-component gases, exhibited significant changes. For instance, the CO_2/H_2 selectivity was almost 1.5-times higher compared to that of the pristine CuBTC (Fig. 5a).[242] Similarly, when [BMIM][PF_6] was incorporated into ZIF-8, the CO_2/CH_4 and CO_2/N_2 selectivities were more than two-times higher than for that of pristine ZIF-8 at low pressures (up to 0.4 bar), because of the high CO_2 affinity of $[PF_6]^-$.[204] Even though up to 0.4 bar the CO_2 uptake in the composite increased in comparison to the pristine ZIF-8 owing to the newly created adsorption sites, CO_2 uptake measurements showed that the composite underperformed compared to pristine ZIF-8 above 0.4 bar.[204] This result was as expected, because the majority of the pore volume of the ZIF-8 was occupied by the IL molecules in the composite, largely reducing the available pore space for gas storage at relatively high pressures.

Investigating the structural factors controlling the separation performance of such composites, Zeeshan *et al.* demonstrated a direct influence of the size and electronic structure of the anion of the IL.[206] The composite formed by using the IL with a fluorinated anion ([BMIM][CF_3SO_3]/ZIF-8) provided a three-fold increase in CO_2/CH_4 selectivity compared to the composite formed with the non-fluorinated IL ([BMIM][$MeSO_3$]/ZIF-8) at 1 bar (Fig. 5b). On the other hand, the composite having an IL with a small-sized anion ([BMIM][$MeSO_4$]/ZIF-8) exhibited a CO_2/CH_4 selectivity 3.3-times higher at 1 bar compared to the selectivity of a similar composite having an IL with a bulkier anion ([BMIM][$OcSO_4$]/ZIF-8). Even though all composites led to decreased CO_2 capacities compared to the pristine ZIF-8, the composites were superior in terms of CO_2/CH_4 selectivity, controlled by the choice of the anion. Similarly, Nozari *et al.*[243] investigated that the methylation at the C2 position on the imidazolium ring ([BMMIM][PF_6] *vs.* [BMIM][PF_6]) effects the interaction between the IL and CuBTC in composites which had a direct influence on the CO_2 separation performance. The composite prepared by non-methylated IL ([BMIM][PF_6]/CuBTC) provided a higher CO_2/N_2 selectivity compared to the selectivity of the composite prepared by the methylated IL ([BMMIM][PF_6]/CuBTC) up to 200 mbar.[243]

The effect of IL structure on the CO_2 storage and separation performance of the composite was investigated by considering metal oxides as supports as well. Mirzaei *et al.* immobilized

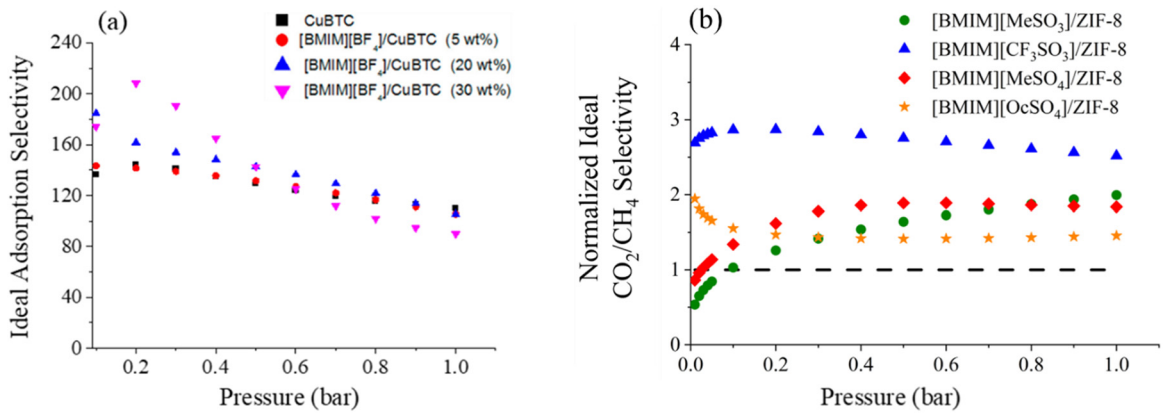

Fig. 5 Ideal adsorption selectivities of (a) CO_2/H_2 for IL-based CuBTC composite with various IL loadings. Reprinted with permission from ref. 242 Copyright 2016, American Chemical Society. (b) CO_2/CH_4 selectivity for IL-based ZIF-8 composite. Reprinted with permission from ref. 206 Copyright 2020, Elsevier.

 This journal is © The Royal Society of Chemistry 2024

Open Access Article. Published on 24 June 2024. Downloaded on 1/17/2026 6:47:09 PM. This article is licensed under a Creative Commons Attribution-NonCommercial 3.0 Unported Licence.

various imidazolium ILs ([BMIM][NO_3], [BMIM][SCN], [BMIM][HSO_4], and [BMIM][DCA]) on silica and investigated the CO_2 capacity of both bulk ILs and silica-supported ILs.[244] Among the bulk ILs, [BMIM][DCA] and among supported ILs, [BMIM][HSO_4]/SiO_2 provided the highest CO_2 capacities (0.42 and 0.53 mmol g^{-1}, respectively, at 25 °C and 1 bar). The CO_2 capacity of the composites was higher compared to the corresponding capacity of the bulk IL, which was attributed to the synergistic effects of silica and IL.

To investigate the extend of such synergistic effects between the IL molecules and the surface, pyridinium ILs with opposite hydrophobic characters (hydrophilic [BMPyr][DCA] and hydrophobic [BMPyr][PF_6]) were immobilized on the surface of reduced graphene aerogel (rGA), whose surface characteristics were tuned by simple heat treatments at different temperatures prior to deposition of the ILs.[184] Detailed characterization indicated that the heat treatment of GAs facilitates the partial removal of surface oxygen-containing groups and tunes the surface area by the formation of micropores.[186,245] Even though the CO_2 uptakes of the IL/rGA composites were outperformed by pristine rGA, a remarkable CO_2/CH_4 selectivity of 450.9 was obtained at 1 mbar and 25 °C for [BMPyr][PF_6] immobilized on GA reduced at 300 °C. Similar findings regarding the decreased uptake of CO_2 along with an increased CO_2 selectivity over other gases, such as N_2 and CH_4, with the immobilization of an IL to pristine porous materials were also observed for [BMIM][Cl]/SBA-15,[215] [BMIM][$MeSO_4$]/MIL-53(Al),[217] [BMIM][PF_6]/MIL-53(Al),[246] [BMIM][CF_3SO_3]/MIL-53(Al),[246] [BMIM][SbF_6]/MIL-53(Al),[246] [BMIM][NTf_2]/MIL-53(Al),[246] [BMIM][BF_4]/MIL-53(Al),[246] [BMIM][SCN]/ZIF-8,[203] 1,3-bis (3-trimethoxysilylpropyl) imidazolium chloride/MCM-41,[247] [BMIM][PF_6]/Cu-BTC,[248] [MPPyr][DCA]/MIL-101(Cr),[249] [EMIM][DEP]/Cu-BTC,[250] [BMIM][PF_6]/rGA,[186] and [BMIM][NTf_2]/CuBTC.[248] However, it is worth noting that several composites prepared by using conventional ILs, such as [BMIM][Cl]/montmorillonite,[193] [BMIM][Cl]/α-zirconium phosphate,[193] and [BMIM][Cl]/LAPONITE®,[192] can provide an enhanced CO_2 uptake compared to the pristine host material. This result was observed mostly when the porous material has very limited or no CO_2 uptake.[193]

2.5.1 Composites with functionalized ILs and DESs. As demonstrated by these examples, use of conventional ILs on porous materials offers broad opportunities, particularly towards boosting the CO_2 separation performance. Although the CO_2 uptake decreases because of the reduced pore volume upon immobilizing the IL in the porous material, the high affinity of many conventional ILs to CO_2 results in high CO_2 selectivities over other gases. Ideally, having composites which can simultaneously present high CO_2 selectivity and high CO_2 uptake is desired. This prospect can be achieved by means of functionalized ILs that provide chemisorption sites. One of the functional groups used to enhance the CO_2 uptake and selectivity is the carboxyl group. For example, an ordinary activated carbon was used as a host material for [BMIM][OAc] and the formed composite having 35 wt% IL loading provided an extraordinary CO_2/CH_4 selectivity of 688.3 at 1 bar and 25 °C, which was 3.3 for pristine activated carbon at identical conditions.[185] The presence of new chemisorption sites was attributed to the high CO_2 selectivity. In another example, Mohamedali *et al.* showed that when [BMIM][OAc] is incorporated into CuBTC at 5 wt% IL loading, the CO_2 capacity almost doubled compared to that of the pristine CuBTC at 30 °C and 0.15 bar.[209] On the contrary, the conventional IL, [PMIM][NTf_2], did not provide any improvement.[209] Mohamedali *et al.* also introduced [BMIM][OAc] into ZIF-8 and reported that the resulting composite provided up to seven-times higher CO_2 capacity compared to the pristine ZIF-8 at 0.2 bar and 30 °C.[205] It was further demonstrated that when [EMIM][OAc] was immobilized into ZIF-8, the selectivity of CO_2 over N_2 increased by approximately 18-times. The carbonyl group of the functionalized IL having a chemisorption interaction between CO_2 was reported to be responsible for this high selectivity and uptake.[205] Other examples showing the increase in CO_2 capacities by functionalized ILs with carboxyl groups include [EMIM][OAc]/polyethyleneimine-impregnated SBA-15,[220] [BMIM][OAc]/silica gel particles,[251] and [EMIM][OAc]/MOF-177[221] composites.

Amino- and amino acid-functionalized ILs were also used to prepare composites with porous materials[187,225] to obtain higher CO_2 capacities, owing to the chemisorption by the amine moiety.[74,90] For example, a composite obtained by immobilizing a polyamine-based P-IL on SBA-15 ([TEPA][NO_3]/SBA-15) provided a 7.8-fold CO_2 uptake enhancement upon IL incorporation into the mesoporous silica (Fig. 6a).[252] IR spectroscopy measurements performed on the composite after CO_2 uptake experiments confirmed that CO_2 is captured through the amine groups as new IR features associated with the carbamate moieties formed. The chemisorption of CO_2 was further confirmed by isosteric heat of adsorption measurements and DFT calculations.

Uehara *et al.* investigated the CO_2 uptake of various ILs having $[EMIM]^+$ and $[P_{4444}]^+$ cations, and amino acid based anions (glycine, L-lysine, L-histidine, L-alanine, β-alanine, L-arginine) immobilized on PMMA microspheres by impregnation.[198] Overall, the amino acid based ILs with $[P_{4444}]^+$ cation provided better CO_2 capacities. All composites reached their maximum uptake at an IL loading of 50 wt%, while PMMA itself provided almost no CO_2 capacity. Furthermore, the CO_2 adsorption on these amino acid-based IL/PMMA composites were determined as chemisorption. A comparison among anions showed that glycine and L-lysine anions having linear side chains with only one primary amino group provided higher CO_2 capacities, while the L-histidine and L-arginine having secondary or tertiary amino groups provided lower CO_2 capture although they have more amine groups. This difference was attributed to the presence of multiple amino groups blocking the pores of the supports and hindering the interaction with CO_2.[187,198] Similarly, Huang *et al.* immobilized an IL, 1-aminopropyl-3-methylimidazolium lysine ([APMIM][Lys]), having amino functional groups on both the cation and the anion, on PMMA and on pore expanded-SBA-15.[256] All prepared composites having varying IL loadings provided significantly higher CO_2 capacity than the pristine supports. Wu *et al.* showed that [C_2OHmim][Lys] incorporation on a porous polymer, (GDX-103 (Poly divinylbenzene porous beads)) provides six-times more CO_2 capacity than the pristine GDX-103 by using an IL loading of 60 wt%, at 1 bar and 40 °C.[197]

Open Access Article. Published on 24 June 2024. Downloaded on 1/17/2026 6:47:09 PM.
This article is licensed under a Creative Commons Attribution-NonCommercial 3.0 Unported Licence.

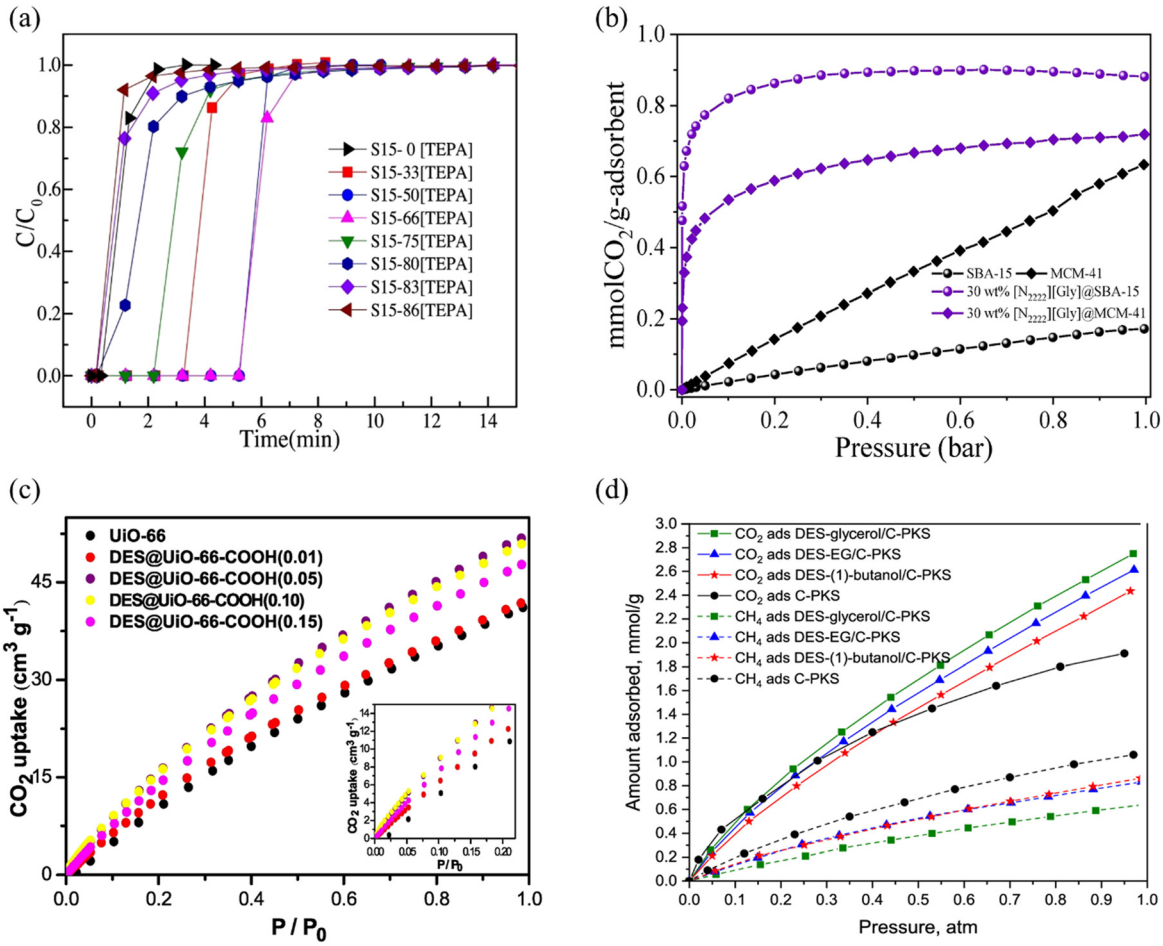

Fig. 6 (a) CO_2 breakthrough curves of SBA-15 and TEPA immobilized SBA-15 at 40 °C and 0.15 bar. Reprinted with permission from ref. 252 Copyright 2019, Elsevier. (b) CO_2 uptake of amino acid-functionalized IL composites with MCM-41 and SBA-15 at 40 °C. Adapted with permission from ref. 253 Copyright 2023, Elsevier. (c) CO_2 adsorption isotherms of DES@UiO-66 MOFs at 25 °C. Reprinted with permission from ref. 254 Copyright 2019, Elsevier. (d) Adsorption isotherms of CO_2 at 30 °C for DES-impregnated C-PKS. Reprinted with permission from ref. 255 under CC-BY-NC-ND 4.0 license.

One challenge in the field of CO_2 capture and separation is the removal of trace amount of CO_2. To mitigate this challenge, Zheng and coworkers immobilized an amino acid-functionalized IL, $[N_{2222}][Gly]$, by impregnation at different loadings on SBA-15 and MCM-41, where both a higher CO_2 capacity and a higher CO_2 selectivity were achieved compared to host materials.[253] $[N_{2222}][Gly]$/SBA-15 composite at an IL loading of 60 wt% provided an CO_2/N_2 selectivity of 11 545 at 0.005 bar and 15 °C, 288-times higher than that of the pristine SBA-15. Moreover, at 0.005 bar and 40 °C, 2200-times higher CO_2 capacity was achieved upon IL incorporation (Fig. 6b). This outstanding performance was associated with the chemisorption of CO_2 by the ILs and the newly formed ultra-micropores (smaller than 0.65 nm), especially with 60 wt% IL loading, which were not present in pristine SBA-15 (having a pore size distribution between 4.5 and 9.5 nm). As provided by these examples, amine functionalization is a promising approach to enhance the CO_2 uptake of IL/porous composites.

As an alternative to carboxyl-, amine-, and amino acid-functionalized ILs, Arellano *et al.* demonstrated the efficiency of impregnating a zinc-functionalized IL on microporous aluminosilicate,[257] non-porous nano-silica,[257] non-ordered mesoporous silica,[257] bio-templated mesoporous silica beads,[258] and ordered mesoporous silica.[200] It was shown that the zinc functionalized IL having a high viscosity could be effectively immobilized as a thin layer on the supports to make use of its interaction sites with CO_2 and to overcome the mass transport challenge due to high viscosity. The efficient wetting of the zinc functionalized IL ([EMIM][NTf_2] zincate) provided access to the pores of the porous host material. It has been shown that the zinc functionalized bulk IL, provided superior CO_2 uptake compared to its non-functionalized analogue ([EMIM][NTf_2]), owing to the additional sites for chemisorption.[257]

Similar to the IL/MOF composites, studies with DESs have also reported enhanced CO_2 capacity. Li *et al.*[254] showed that incorporation of reline into a UiO-66 framework not only increased the CO_2 capture capacity but also preserved the open metal sites within the MOF, offering additional binding sites for CO_2. Results showed that DES-incorporated UiO-66 had a CO_2 uptake of 2.35 mmol g^{-1} compared to 1.85 mmol g^{-1} of pristine UiO-66 at 25 °C and 1 bar, such increase in uptake capacity was attributed to the combination of physical and chemical adsorption *via* $-NH_2$ and –OH groups (Fig. 6c). Similarly, Mehrdad and

 This journal is © The Royal Society of Chemistry 2024

Open Access Article. Published on 24 June 2024. Downloaded on 1/17/2026 6:47:09 PM. This article is licensed under a Creative Commons Attribution-NonCommercial 3.0 Unported Licence.

co-workers[236] prepared NH_2-MIL-53(Al) incorporated DESs ([Ch][Cl] mixed with different amines) and reported two-fold improvement in the CO_2 uptake compared to the pristine MOF at 25 °C and 5 bar. This improvement in CO_2 capacity was ascribed to the dual-mode CO_2 capture mechanism within DES-impregnated NH_2-MIL-53(Al): it binds to the DES monolayer formed on the pore surfaces *via* hydrogen bonding, and secondly, it interacts with the residual DES confined within the pores. Additionally, the amine groups within the MOF structure also contributed to the overall CO_2 uptake.

Composites made up of DES-impregnated porous carbon and silica have also been demonstrated. For instance, Mukti *et al.*[259] extended this concept to modify porous carbon surface by impregnating with DES ([Ch][Cl]:Gly). Gas adsorption experiments showed that CO_2 uptake was increased from 1.85 mmol g^{-1} (pristine Carbon)[202] to 2.85 mmol g^{-1} (DES-modified carbon) at 30 °C and 1 bar. In another example, Hussin *et al.*[260] functionalized palm shell based activated carbon with 14 different combinations of DESs. Among the studied samples, DES-functionalized (choline hydroxide + urea, 1 : 05 mole ratio) activated carbon achieved the highest CO_2 uptake (0.85 mmol g^{-1}) compared to pristine carbon (0.15 mmol g^{-1}) at 25 °C and feed concentration of 10 vol% CO_2 in He. The same group studied three types of DES-functionalized activated carbon and reported that the combination of tetrabutylammonium bromide (TBAB) and triethylene glycol (TEG) (mole ratio 1 : 2) is the most effective, achieving a maximum CO_2 adsorption capacity of 0.37 mmol g^{-1} in the composite at 25 °C and 0.1 bar. Ariyanto *et al.*[255] explored the potential of porous carbon derived from the palm kernel shell (C-PKS) impregnated with a DESs, which were composed of a ChCl and the HBDs of 1-butanol, ethylene glycol, and glycerol. Adsorption isotherm revealed that CO_2 adsorption capacity in DES ([Ch][Cl]: glycerol)/C-PKS increased to 2.75 mmol g^{-1} in comparison to pristine C-PKS, which had a CO_2 adsorption capacity of 1.70 mmol g^{-1} at 30 °C and 1 bar (Fig. 6d). Ghazali *et al.*[235] investigated modification of mesoporous silica-gel with a mixture of [Ch][Cl], urea, and polyethyleneimine to prepare a hybrid material and reported a CO_2 capacity of 1.15 mmol g^{-1} at 25 °C and 1 bar for DES incorporated silica gel composite, which was 2.5 times higher than the CO_2 uptake of pristine silica gel.

2.5.2 Composites with alternative structures. Another important factor which can influence the CO_2 capture and separation performance of IL/porous material composites is the morphology of the composite and how ILs interact with the host material. Similar to the majority of the examples provided above, if the pore size and pore opening of the porous material are large enough to accommodate the IL, ILs are incorporated into the pores of the host material to produce the typical IL/porous material composites. However, if the kinetic diameter of the IL is larger than the pore opening of the porous host material, it can position itself as a sheath covering the external surface of the support creating a core–shell-like structure. For instance, in a pioneering study, Zeeshan *et al.* illustrated that when [HEMIM][DCA] is deposited on ZIF-8 at an IL loading of 40 wt% by simple impregnation, the IL layer covering the external surface of ZIF-8 particles acts as a smart gate to control the molecules going into the pores of the MOF (Fig. 7a). Another advantage of the core–shell type composites is that the original pore volume of the host material can be retained, which is crucial in maintaining a high CO_2 capacity and diffusivity. The core–shell type [HEMIM][DCA]/ZIF-8 composite provided 5.7 times higher CO_2 uptake accompanied by 45-times higher CO_2/CH_4 selectivity compared to those of the pristine MOF at 1 mbar and 25 °C (Fig. 7b). Separation performance can be further improved when a functionalized IL is used as the shell layer. For instance, Yang *et al.* used a functionalized IL, rich in amino groups with high CO_2 affinity, to synthesize a core–shell type composite with ZIF-8 (40 wt% IL).[212] At 0.03 bar and 25 °C, a superior CO_2/C_2H_2 selectivity of 246.5 was achieved, outperforming pristine ZIF-8 and several other reported composites. With an opposite approach to these samples, another core–shell type composite can be obtained when the core is the IL and the shell is the porous material, frequently referred as encapsulated ionic liquids (ENILs).[190] In this class of composites, the IL loading is typically higher than 50 wt%.[175] A detailed review of ENILs for CO_2 capture and separation can be found in a recent review article.[261]

For the core–shell type composites mentioned so far, IL loadings are restricted under the incipient wetness limit so that the composite remains in its powder form. When the incipient wetness is exceeded by a large extend, however, porous liquids (PLs) are obtained. The PLs are another novel concept that combines the intrinsic characteristics of porous materials with liquid solvents.[265] A recent review paper provides a comprehensive categorization of three distinct types of PLs based on their structures,[266] where type I presents intrinsic rigid porosity, type II is for porous materials dissolved in a sterically hindered solvent, and type III is where the porous material such as a MOF is dispersed in the solvent. Among these, type III PLs are synthesized by employing an excess amount of dispersive solvent that fails to permeate the pores of porous materials, hence preserving their liquid form.[267] The unique combination of high ionic conductivity, very low volatility, and high solubilities of ILs makes them promising candidates for the synthesis of type III PLs.[268] Commonly utilized porous materials for PL synthesis encompass zeolites, mesoporous silica, COFs, and MOFs. Among these, MOFs emerge as particularly promising porous materials for integration with ILs, facilitating the synthesis of highly stable porous ionic liquids (PoILs).[269] Additionally, PoILs exhibit significant potential for CO_2 capture, owing to the easily tunable structure of ILs.

Some examples of PoILs include $[P_{4444}][Lev]$ and $[C_6(BIm)_2][NTf_2]$ with ZIF-8 and ZIF-67, respectively.[262,270] When 5 wt% ZIF-8 was dispersed in $[P_{4444}][Lev]$, the resulting PoIL exhibited a CO_2 sorption capacity of 1.5 mmol CO_2 per g PoILs, approximately 20% higher than that of the bulk IL, at 30 °C and 2 bar. Moreover, 10 wt% ZIF-67 dispersed in $[C_6(BIm)_2][NTf_2]$ displayed a remarkable CO_2 capacity of 9.54 mmol CO_2 per g PoILs (Fig. 7c). This result represents a 55-fold increase compared to the bulk IL, observed at 25 °C and 1 bar. Various porous materials, including silicalite-1, (a type of ZSM-5) and ZIF-8, were also employed for the synthesis of PoILs dispersed

Open Access Article. Published on 24 June 2024. Downloaded on 1/17/2026 6:47:09 PM.
This article is licensed under a Creative Commons Attribution-NonCommercial 3.0 Unported Licence.

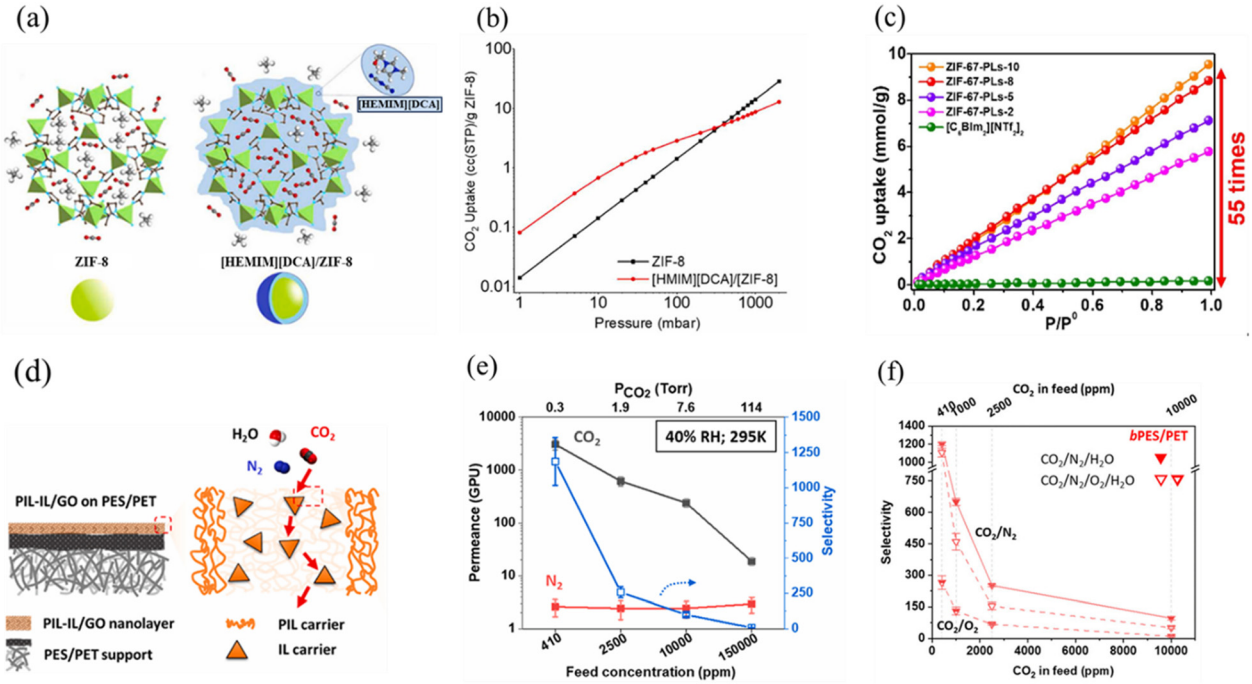

Fig. 7 (a) Schematic representation of the proposed core–shell type IL/MOF structure; (b) CO_2 uptake of ZIF-8 and IL/ZIF-8 composite at 25 °C. Reprinted with permission from ref. 202 Copyright 2018, American Chemical Society. (c) CO_2 adsorption isotherms of bulk IL and ZIF-67-PLs with different loadings at 25 °C. Reprinted with permission from ref. 262 Copyright 2021, Elsevier. (d) Schematics of the fabricated PIL-IL/GO membrane on PES/PET substrate; (e) Measured CO_2 and N_2 permeances PIL-IL/GO thin film composite membrane (right) as a function of CO_2 concentration in the feed at 22 °C and 40% relative humidity (RH). Reprinted with permission from ref. 263 Copyright 2021, Elsevier. (f) CO_2/N_2 and CO_2/O_2 selectivities of PIL–IL/GO on bPES/PET substrate at 22 °C and 40% RH. Reprinted from ref. 264 with permission from the Royal Society of Chemistry. Copyright 2022.

in [DBU-PEG][NTf_2].[271] The results revealed that the PoIL consists of 30 wt% ZIF-8 and remaining as [DBU-PEG][NTf_2] exhibited superior performance, approximately 4.7-times higher than the bulk IL. However, the effective application of type III PoILs for CO_2 capture is significantly constrained due to the requirement of bulky ILs (low gravimetric uptake) and porous materials with pore apertures sufficiently small to prevent the permeation of ILs into their pores.

As evidenced from these above-mentioned studies, hybrid materials, such as those obtained by confining ILs or functionalized ILs in the pores of porous supports, core–shell type composites, ENILs or PoILs provide opportunities towards reaching high CO_2 uptake and particularly high CO_2 selectivity over other gases, such as CH_4, N_2, C_2H_2, H_2. Hence, such composites can be used as fillers in polymer matrix to form mixed matrix membranes (MMMs) to boost the CO_2 separation performance. Alternatively, the ILs can be used in membrane-based gas separation in the form of supported ionic liquid membranes (SILMs),[272] where the IL is directly impregnated into the pores of the membrane. However, they have certain drawbacks such as swelling and IL-leaching.[273] IL polymer membranes (ILPMs), which are obtained by physically mixing the IL and polymer can be a potential solution to this problem, however, they lack mechanical strength, particularly when the IL loading is high.[237] Therefore, combining ILs with inorganic fillers in the polymer matrix to obtain MMMs is a promising approach. In this way, high selectivity obtained by IL/porous material samples can be used and the IL can offer a better compatibility between the inorganic filler and the polymer by acting as a wetting agent.

Several ILs have been tested to enhance the performance of MOFs and zeolites as fillers in MMMs.[274] For example, Habib *et al.* fabricated an IL/MOF/polymer MMM by using [MPPyr][DCA]/MIL-101(Cr) composite as a filler in Pebax.[275] [MPPyr][DCA]/MIL-101(Cr)/Pebax performed 45-times and 10-times higher CO_2/N_2 and CO_2/CH_4 selectivities, than pristine Pebax, respectively. Similarly, Mahboubi *et al.* synthesized [BMIM][OAc]/Al_2O_3 nanoparticles/Pebax-1657 MMM and demonstrated that the CO_2 permeability and selectivity of CO_2 over CH_4 improved compared to the Pebax membrane.[276]

Similar examples of confined ILs in membrane separations have been demonstrated. For example, Lee and Gurkan[263] fabricated a composite membrane where a functionalized IL was impregnated into a graphene oxide nanoframework that served as a micron-thick selective layer supported on an ultrafiltration membrane for separation of CO_2 from air (Fig. 7d). This study demonstrated the first facilitated transport membranes with a functionalized IL for separating CO_2 from air. Accordingly, a CO_2 permeance of 3090 GPU (1 GPU = 3.348×10^{-10} mol m^{-2} s^{-1} Pa^{-1}) and a CO_2/N_2 selectivity of 1180 were demonstrated at conditions relevant to direct air capture (295 K and 40% RH) (Fig. 7e). Later, they also demonstrated a CO_2/O_2 selectivity of 300 with a 410 ppm of CO_2 at 1 atm feed gas with helium sweeping on the permeate side (Fig. 7f).[264] They noted a significant reduction in the separation performance under higher transmembrane pressures. Thin membranes based on graphene

 This journal is © The Royal Society of Chemistry 2024

Open Access Article. Published on 24 June 2024. Downloaded on 1/17/2026 6:47:09 PM. This article is licensed under a Creative Commons Attribution-NonCommercial 3.0 Unported Licence.

oxide layers offer a very low resistance; however, they are also prone to defect formation under high transmembrane pressures. To enhance their durability and mechanical stability, reinforcement by poly ionic liquids and increased membrane thicknesses are viable strategies as demonstrated in the discussed examples but these types of membranes are currently difficult to adapt for roll-to-roll fabrication to assemble membrane modules.

2.5.3 Computational approaches in the composite design. There is almost an infinite number of possible IL–porous material combinations when considering the highly tunable nature of ILs and porous materials with wide range of varieties. For instance, for MOFs only, as of January 2024, the number of synthesized MOFs deposited into the Cambridge Structural Database (CSD)[277] is 123 457 based on our search of this data center using Conquest software.[278] Other host materials used, such as zeolites, mesoporous silica, or carbonaceous materials, also provide a substantial flexibility. In addition to this, when considering that the possible anion/cation combination for ILs is almost unlimited number, hence, it is impossible to synthesize every possible IL/porous material composite and test them for CO_2 capture and separation. Similarly, there is virtually unlimited possibilities of DES compositions with varying HBAs and HBDs. There has been a lot of progress in the prediction of ILs and DES bulk properties using machine learning (ML). For example, interpretable and explainable ML models to predict the solubility of CO_2 in chemically reactive DESs were demonstrated by integrating the quantum chemistry-derived Sigma σ-profiles.[279] Sigma profile is used to quantify the relative probability of a molecular surface segment having a screening charge density. By utilizing σ-profiles as inputs, the developed models capture the molecular interactions.[280] Among the investigated ML models, feed forward neural network (FFNN) showed the optimal performance on the CO_2 solubility predictions including DESs with chemisorption capability.[279] Therefore, molecular simulations and ML approaches are crucial to screen a large number of ILs/DESs and porous material combinations to determine the best candidates.

In this regard, for instance, Polat *et al.* used Grand Canonical Monte Carlo (GCMC) simulations to predict the CO_2 uptakes and selectivities over CH_4 and N_2 for various IL/CuBTC composites that have ILs with the same $[BMIM]^+$ cation but different anions, and compared their computational results with experimental measurements.[281] It was demonstrated that all of the IL/CuBTC composites yielded higher CO_2 selectivities than the pristine CuBTC and the predicted values agreed well with the experimental results. In another study,[282] high throughput molecular simulations were combined with experiments to analyze the CO_2/N_2 separation performances of IL/MOF composites. Experimentally, three IL/MOF composites, [BMIM][BF_4]/UiO-66, [BMIM][BF_4]/ZIF-8, and [BMIM][BF_4]/CuBTC, were synthesized and tested for CO_2 and N_2 uptakes and their CO_2/N_2 selectivities were determined to compare the experimental results with simulations to confirm the accuracy of the methodology. Thereafter, CO_2/N_2 selectivities of 1085 composites were predicted by using a single type of IL ([BMIM][BF_4]) in combination with various MOFs. Accordingly, 97.6% of the studied MOFs provided higher CO_2/N_2 selectivity and 82.8% of them provided an increased CO_2 working capacity.

Gulbalkan *et al.* employed a computational screening strategy by integrating conductor-like screening model for realistic solvents (COSMO-RS) calculations, GCMC and MD simulations, and DFT calculations to explore the capabilities of different IL/COF composites for CO_2/N_2 selectivity by considering adsorption and membrane-based separation methods.[283] The CO_2/N_2 selectivity of TpPa-1-F2 increased from 12 to 26 upon [BMPyrr][DCA] incorporation at VSA conditions. Yan *et al.* investigated the optimal IL loading in IL/COF composites by high-throughput computational screening and ML.[284] Instead of the frequently used gravimetric loading ratio (wt%), they proposed a new "volumetric loading (vol%)" descriptor, which was defined as the ratio of inserted IL molecules into the COF over the maximum number of ILs that can be loaded into the pore of the COF. Among 15 410 screened IL/COF composites, the highest CO_2/N_2 selectivity was reached when the volumetric IL loading was 35 vol%, showing that computational studies can also provide insights on the optimum IL loading for synthesis to achieve the best gas separation performance.

By combining various computational tools, including quantum chemical calculations (COSMO-RS- and DFT) and molecular simulations (GCMC), Zeeshan *et al.*[285] identified [BMPyrr][DCA] as the best pyrrolidinium IL based candidate to be combined with UiO-66 for obtaining superior CO_2 separation performance. The experimental data obtained on this composite demonstrated that the [BMPyrr][DCA]/UiO-66 offers practically infinite CO_2/N_2 selectivity owing to extremely poor solubility of N_2 and superior solubility of CO_2 in [BMPyrr][DCA]. These results demonstrated the great potential of computational efforts in the way of designing composites with exceptional CO_2 separation performance, especially when they are integrated in a hierarchical way.

3. CO_2 thermal conversion

Reduction of CO_2 *via* chemical, thermal, biochemical, photochemical, and electrochemical reactions have been reported.[7–9] The critical challenges are the requirement of substantial energy to activate CO_2 and the lack of highly selective catalysts. The conventional CO_2 conversion is thermal with an appropriate catalyst. Typical catalysts for the conversion of CO_2 are very broad; ranging from noble and non-noble metal-based homogeneous or heterogeneous catalysts to metal-free ones. Although noble metals, such as Pd, Pt, Ir, Rh, Ru, or Au, provide several advantages, including high CO_2 conversion performance, they are scarce and costly.[286] Thus, cost-effective non-noble metal-based catalysts such as Cu-, Ni-, and Fe-based ones, metal oxides, zeolites or ordered mesoporous silica,[287,288] and in particular metal-free catalysts, such as graphene and carbon nanotubes[289] or porous organic polymers, have gained significant attention for thermal, as well as photo- and electro-catalytic CO_2 conversion. This section provides an overview of the thermal catalysis of CO_2 as a point of reference for conversion processes utilizing ILs (Fig. 8).

ILs offer several advantages for their utilization in thermocatalytic conversion of CO_2, since they can be used as both the sorption media and catalytically active phase itself, enabling an

Open Access Article. Published on 24 June 2024. Downloaded on 1/17/2026 6:47:09 PM.
This article is licensed under a Creative Commons Attribution-NonCommercial 3.0 Unported Licence.

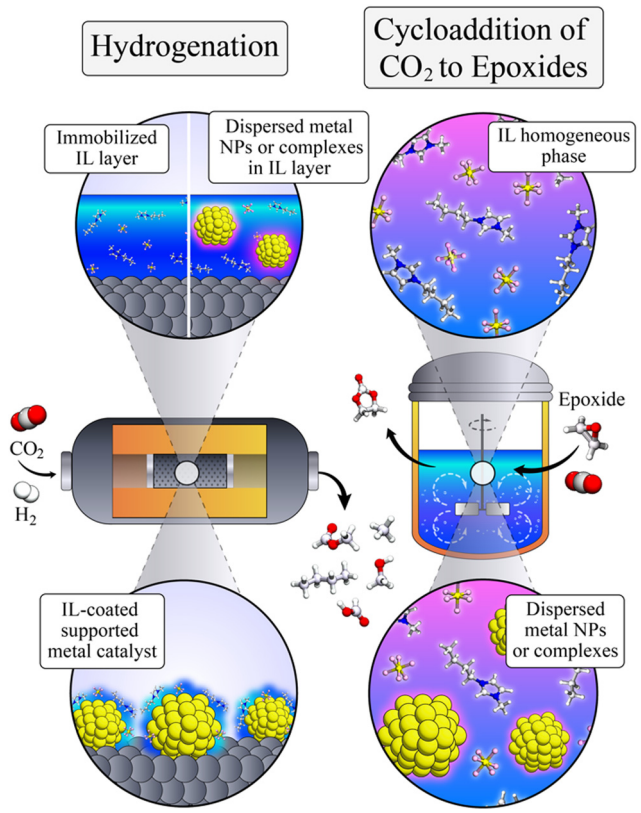

Fig. 8 Overview of CO_2 thermal catalysis by IL in a continuous flow reactor mostly used for hydrogenation of CO_2 (left) and a batch reactor mostly used of epoxidation of CO_2 (right). The zoomed-in panels for the flow reactor represent the possible configurations where an IL layer itself or with metal NPs serves as the catalyst surface (top) or the IL-coated metal NPs are decorated over the porous support (bottom). The zoomed-in panels for the batch reactor represent the cases of IL acting as the homogenous catalyst as well as the reaction media (top) and the NPs dispersed in the IL media (bottom).

integrated capture and conversion technology consisting of a metal-free catalyst.[290] Furthermore, they can also act as solvents for the reaction, where they can host externally added metal-based homogeneous or heterogeneous catalysts, or they can be themselves supported by high-surface area materials (supported ionic liquid phase catalysts, SILPs).[290] Advantages which further foster their utilization in thermal conversion of CO_2 are their relatively high stability at CO_2 conversion temperatures and pressures, and their low vapor pressures and low melting points. By pairing of specific anions and cations or by attaching functional groups depending on the active sites needed for a specific product by CO_2 conversion, ILs can be used in a very flexible way for CO_2 conversion.

The thermal conversion of CO_2 with systems involving ILs comprises mostly the following reactions: (i) cycloaddition of CO_2 to epoxides to produce cyclic carbonates[291] and the reaction of CO_2 and methanol to produce linear carbonates,[292] (ii) the hydrogenation of CO_2 to products, such as methane, methanol, formic acid, methyl formate, or long-chain hydrocarbons, (iii) the synthesis of nitrogen containing compounds, such as quinazoline-2,4(1*H*,3*H*)-dione,[293] and (iv) the synthesis of sulfur containing compounds, such as benzothiazole.[294] Detailed discussion on the latter two routes regarding the production of *N*- and *S*-containing compounds can be found elsewhere.[286] For the cycloaddition reaction of CO_2 to epoxides, ILs can act as the catalysts themselves without the addition of any co-catalyst or solvent, while the hydrogenation of CO_2 to products, such as methanol, methane, or long chain hydrocarbons, mostly necessitates the presence of other active sites of noble or non-noble metals. In the following sections, a summary of different kinds of approaches to convert CO_2 to valuable products in IL-containing systems is provided with a specific focus on the CO_2 cycloaddition to epoxides and CO_2 hydrogenation.

3.1 CO_2 conversion to cyclic carbonates

Cycloaddition of CO_2 to epoxides is one of the most widely studied routes for the thermal conversion of CO_2. Several ILs, SILPs, and ILs hosting metals have been considered for this reaction. For the cycloaddition reaction, the catalyst should involve multiple active sites which are crucial for the ring opening, CO_2 insertion, and ring closure steps.[295] A Lewis acid site or HBD is needed to polarize the epoxide.[237,295] This active site can be obtained by metal sites in conventional catalysts.[237] However, in IL-catalyzed systems, the cation, which provides hydrogen bonds, can act as a Lewis acid site.[290] The anion, on the other hand, acts as a nucleophile to induce the ring opening of the epoxide.[296] Thus, the selection of an IL is quite important as the cation and anion are the active sites for this reaction. Furthermore, the interaction of ILs dictates how available the anion and cation are for this reaction.[297]

There are several studies reporting the use of different classes of neat ILs for the reactions involving the cycloaddition reaction of CO_2 to epoxides to obtain cyclic carbonates. The very first demonstration of using ILs for solvent-free and metal-free cycloaddition reaction was by Peng *et al.*[298] A series of imidazolium and pyridinium ILs were used as catalysts in a batch reactor to produce propylene carbonate from propylene oxide and CO_2 at 2 MPa CO_2 pressure, where [BMIM][BF_4] was found as the best performing IL.[298] Then, it has been shown that the use of supercritical CO_2 is more effective for such reaction systems.[299] Several ILs,[299–302] P-ILs,[303–306] poly-ILs,[296,307–310] and dicationic ILs[311] have been further investigated as catalyst for the cycloaddition reaction. Scheme 10 illustrates a proposed reaction mechanism of the cycloaddition of CO_2 with epoxides.[300] Accordingly, the anion plays a crucial role in the nucleophilic ring opening of the epoxide, which is the rate-determining step for this reaction. For this reaction, P-ILs are specifically advantageous since it is easy to synthesize them at relatively low-cost.[303] Besides, poly-ILs can be also used as heterogeneous catalysts for the cycloaddition reaction. These ILs offer advantages in terms of ease of separation from the reaction medium, as opposed to ILs which are homogeneous catalysts.[102] Other catalysts reported were amino acid-based ILs,[312,313] and ILs having metals (metal ILs)[314] for the cycloaddition of CO_2 to epoxides.

To further improve the catalytic performance, several novel functionalized ILs,[315–320] functionalized poly-ILs,[292,307,321,322]

 This journal is © The Royal Society of Chemistry 2024

Open Access Article. Published on 24 June 2024. Downloaded on 1/17/2026 6:47:09 PM.
This article is licensed under a Creative Commons Attribution-NonCommercial 3.0 Unported Licence.

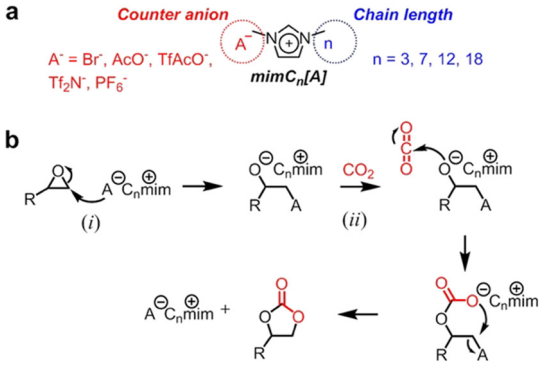

Scheme 10 Proposed mechanism for CO_2 cycloaddition reaction of CO_2 to epoxides to cyclic carbonates by imidazolium ILs. A^- is representing the anion and *n* in the cation ($mimC_n^+$) is representing the chain length on the imidazolium. Reprinted with permission from ref. 300. Copyright 2018, John Wiley and Sons.

and functionalized P-ILs[323] were tested for the cycloaddition reaction. Functionalization leads to an even higher flexibility of ILs and a control of active sites for the reaction allowing the synthesis of sites with desired nucleophilic and electrophilic character.[324] For example, hydroxyl (–OH) functionalization on imidazolium-based ILs offers an eased activation of the epoxide thanks to the hydrogen bonding with the oxygen atom on the epoxide.[319] In addition to –OH, other HBD moieties have been incorporated to ILs, such as –NH– and –COOH groups.[295] Although the introduction of such groups can polarize the epoxide and accelerate the slow step of the cycloaddition reaction, it can also result in an intramolecular hydrogen bonding between the HBD functional group and the anion of the IL itself (typically halides), which can cause a lowered catalytic activity.[325] Thus, controlling the position and number of HBD groups is crucial. To overcome this issue, Zhang *et al.*[325] synthesized a novel family of imidazolium based ILs with multiple weak HBD groups (*e.g.*, N–H and C–H groups) and obtained a high performance for the reaction between epichlorohydrin and CO_2. In another example demonstrating the use of functionalized ILs, the synergistic effect of pyridine and bromide anion sites in mesoporous pyridine-functionalized binuclear poly(ionic liquid) showed an excellent yield of 95% at 2 MPa and 100 °C for the cycloaddition of low-concentration CO_2 (15% CO_2, balance N_2) and epichlorohydrin without a co-solvent or co-catalyst.[322]

Multiple active sites for cycloaddition reaction can be obtained by synthesizing composites of ILs with porous materials, such as MOFs and COFs as heterogeneous catalysts.[237] These composites provide substantial flexibility, because both the IL structure and the porous material can be functionalized and combined to reach a high performance. IL/MOF,[326,327] IL/COF, IL/metal oxide,[328] IL/carbon,[329] IL/zeolite, IL/mesoporous silica[330,331] composites have been considered widely for the cycloaddition reaction.[237] For instance, a bi-functionalized IL ([HeMOEim][Br]) was impregnated on a MOF (MIL-53(Al)) and it reached a yield of 95.7% cyclopropyl carbonate for the low-CO_2 concentration cycloaddition reaction at 130 °C, 0.1 MPa, and using a catalyst dosage of 0.2 mol% without the addition of any solvent or co-catalyst.[332] The synergistic effect of the hydroxyl group of the IL and the Al sites of the MOF acted as Lewis acid sites to activate the epoxide, while the halide anion served as the nucleophile. Multiple functional sites could be obtained also by immobilizing a dicationic IL, having two imidazolium rings with COOH groups and two Br^- anions, on SBA-15.[333] A high yield (97.4%) and high selectivity (99.1%) of cyclic carbonates at a reaction temperature of 130 °C and at a CO_2 pressure of 2 MPa (50 mg catalyst) were achieved thanks to the presence of multiple active sites and the successful dispersion of the IL on the support.

Another CO_2 fixation approach through thermal catalysis is the reaction of CO_2 and alcohols to form linear carbonates.[334] For example, He *et al.*[292] demonstrated that ternary copolymerized bifunctional poly-ILs having hydroxyls, halogen anions, and tertiary N sites are effective catalysts for the solvent- and co-catalyst-free dimethyl carbonate production from CO_2 and methanol. In another example, Ding and coworkers[335] synthesized porous sulfonyl binuclear carbonate poly(ionic liquid)s for utilization as a catalyst in dimethyl carbonate production where a yield of 80% was achieved without any co-catalyst from the reaction between methanol and the low concentration CO_2, representing flue gas (15% CO_2 + 85% N_2).

3.2 CO_2 hydrogenation

CO_2 can be hydrogenated into a variety of products, such as formic acid, formaldehyde, methanol, methane, or long-chain hydrocarbons, by thermal catalysis. The most direct CO_2 conversion route is the CO_2 conversion to methanol, which can then be used as a platform molecule to produce several other chemicals.[336] In another route, CO_2 can be converted to CO by the reverse water gas shift reaction (RWGS). The produced syngas can further be converted to methanol, methane, and formaldehyde, or to long-chain hydrocarbons by Fischer–Tropsch synthesis. Another approach is the direct synthesis of hydrocarbons by Fischer–Tropsch from CO_2 and H_2, where RWGS reaction and the Fischer–Tropsch synthesis is performed simultaneously in a single-pass reactor, which needs sophisticated multifunctional catalyst design. In such a system, to shift the equilibrium to CO formation by the RWGS reaction (newly formed CO then enters the Fischer–Tropsch path to produce long-chain hydrocarbons), the co-formed water should be constantly removed.[290] This could be achieved by introducing a hydrophobic IL nearby the active site, to reduce the concentration of H_2O formed during the reaction.[337] In addition, when ILs cover the active sites, they can also control the effective CO_2 concentration. Choosing an IL having high CO_2 solubility can significantly enhance the performance. Therefore, the use of ILs has several advantageous functions in hydrogenation of CO_2 by thermal catalysis, when used as modifiers for the main active site or as solvents. These main active sites of the thermal CO_2 hydrogenation are often provided by another active phase of noble or non-noble metal catalyst.[338]

Melo *et al.*[339] used *in situ* prepared Ru nanoparticle catalysts in an imidazolium IL ([C_8MIM][NTf_2]) for CO_2 hydrogenation to

Open Access Article. Published on 24 June 2024. Downloaded on 1/17/2026 6:47:09 PM.
This article is licensed under a Creative Commons Attribution-NonCommercial 3.0 Unported Licence.

methane. A methane yield of 69% using 0.24 mol% catalyst at 40 bar and 150 °C was achieved through the ability of $[C_8MIM][NTf_2]$ to stabilize Ru nanoparticles (2.5 nm).[339] The yield could be improved further to 84% by conducting a systematic study revealing $[C_8mim][NfO]$ is a better IL to host the Ru nanoparticles.[340] Wang *et al.*, on the other hand, encapsulated Ru complexes into poly(ionic liquid)s and reached almost 100% CH_4 selectivity at 160 °C in a batch reactor by feeding H_2 at a pressure of 3 MPa and CO_2 at a pressure of 2 MPa with this catalyst.[341]

CO_2 can be thermally hydrogenated to obtain long-chain hydrocarbons as well. Qadir *et al.*[342] used RuFe alloy nanoparticles in two different ILs (in the hydrophobic $[BMIM][NTf_2]$ and the basic [BMIM][OAc]) for CO_2 hydrogenation. The reaction path depended on the IL structure: RuFe nanoparticles in $[BMIM][NTf_2]$ favored the long-chain hydrocarbon formation path, while RuFe nanoparticles in [BMIM][OAc] led to the production of formic acid. Hydrophobic $[BMIM][NTf_2]$ controlled the H_2O concentration near the active sites, shifting the equilibrium to the products. RuFe nanoparticles in $[BMIM][NTf_2]$ provided 12% CO_2 conversion and 10% selectivity towards the long-chain hydrocarbons (C_7–C_{21}) at a relatively mild temperature of 150 °C and reaction pressure of 8.5 bar ($CO_2:H_2$, 1 : 4). Qadir *et al.*[343] also investigated Ru/Ni core shell nanoparticles in the same hydrophobic IL, $[BMIM][NTf_2]$, and reached 30% conversion at 150 °C and at 8.5 bar ($CO_2:H_2$, 1 : 4) with 5% CH_4, 79% C_2^+ alkane, and 16% olefin selectivity, respectively. Further details regarding the CO_2 conversion in IL mediated catalytic systems can be found in a recent review article.[344]

Formic acid production by CO_2 hydrogenation is one of the most studied reactions in IL containing systems. Typically, bases are added to the reaction environment to consume the produced formic acid, so that the thermodynamic equilibrium shifts to the products.[345] This approach results in extra cost, as the produced waste (the formic acid salts produced because of the acid–base reaction) should be purified from the pure formic acid.[345] Several reports showed that using basic ILs as buffering agents is a promising approach to shift the equilibrium to the products. For example, Weilhard and coworkers[346] used a basic IL as a buffer ([BMMIM][OAc]) together with a Ru-based homogeneous catalyst (Ru pincer N-heterocyclic carbenes) and a Lewis acid catalyst to obtain comparable CO_2 hydrogenation performance to formic acid to base-containing systems. In several other reports, homogeneous catalysts consisting of metal complexes were used together with ILs and with or without a co-solvent to produce formic acid as an alternative to a reaction medium containing bases.[347–350]

Using ploy-ILs as support materials for noble metals, such as Pd, to obtain heterogeneous catalysts for formic acid production by CO_2 hydrogenation is another approach.[351,352] IL-mediated heterogeneous catalysts for formic acid production can also be obtained by SILP systems.[353] For example, Anandaraj and coworkers synthesized SILPs on SiO_2 using various imidazolium ILs with different anions, followed by the immobilization of Ru nanoparticles by impregnation on the SILP materials.[353] All Ru immobilized SILP catalysts with a high Ru dispersion (ranging between 0.8 ± 0.3 and 2.9 ± 0.8 nm) provided up to ten-times more catalytic performance towards formic acid production by CO_2 hydrogenation than a reference Ru/SiO_2 catalyst (1.5 ± 0.5 nm) despite their similar dispersions, emphasizing the importance of having ILs in close proximity to Ru as modifiers.

Few studies were reported involving the usage of ILs for the methanol synthesis by CO_2 and H_2. Generally, high pressures exceeding 2 MPa and temperatures above 200 °C are needed for the direct synthesis of methanol from CO_2 and H_2. The industrial methanol synthesis catalyst is $Cu/ZnO/Al_2O_3$ which remains superior to alternatives reported to date.[354] Several attempts were made to enhance the methanol synthesis performance of $Cu/ZnO/Al_2O_3$ by adding noble metals such as Pt, Au, Rh, and Pd or promoters such as Zr, Ga, and F.[354] Although these approaches increase the catalytic performance, they are not feasible from an economic point of view. In contrast, ILs can be used as cost-effective and metal-free modifiers for $Cu/ZnO/Al_2O_3$. They can act as sorbents for methanol, which eventually can shift the rection equilibrium to the products. For example, Zebarjad *et al.*[355] used $[EMIM][BF_4]$, in a membrane reactor. A CO_2 conversion of 42% was obtained at a temperature of 220 °C and pressure of 24 bar by using a commercial Cu-based methanol synthesis catalysts where a feed consisting of a mixture of CO_2, CO, H_2 and N_2, and a sweep liquid consisting of $[EMIM][BF_4]$ with a flow rate of 1 cc min^{-1} were the testing conditions. The obtained conversion value of 42% was even higher than the equilibrium conversion (35.5%) at that condition. It remained higher when compared to the conventional organic solvent tetraethylene glycol dimethyl ether (TGDE), where a conversion of 38.4% was obtained under the identical conditions (220 °C and 24 bar). The constant *in situ* removal of methanol from the system by $[EMIM][BF_4]$ was proven to be an efficient approach to shift the equilibrium towards the products. Therefore, Zebarjad and coworkers further investigated the CO_2 and methanol solubilities of $[EMIM][BF_4]$ at high pressure and temperature.[356] Their findings demonstrate that CO_2 has negligible solubility in $[EMIM][BF_4]$ under high temperature and pressure conditions. However, it was demonstrated that the solubility of methanol in $[EMIM][BF_4]$ was quite high, which is a desired property to obtain a high performing sweep liquid in processes involving methanol production. It was also found that the solubility of methanol in $[EMIM][BF_4]$ was higher than in a petroleum-based solvent, TGDE. Similarly, Reichert *et al.*[357] showed that adding a solution of $Li[NTf_2]$ doped $[P_{1444}][NTf_2]$ as a sorbent to the methanol synthesis reaction medium provided a yield of 63.3%. Using solely $[P_{1444}][NTf_2]$ resulted in no observed enhancement in product yield, indicating that addition of an alkali salt ($Li[NTf_2]$) is crucial because of its high-water sorption capacity which shifts the equilibrium drastically toward the products.

Other IL-modified CO_2 reduction routes include methyl formate production from CO_2 hydrogenation in the presence of alcohols, the hydroformylation of olefins with CO_2 and H_2 to yield aldehydes, and the alkoxycarbonylation of olefins with CO_2 and methanol to yield carboxylic esters. Further details can be found in related review articles.[286,290]

For most of the above mentioned examples comprising the IL-mediated CO_2 hydrogenation reactions, temperatures exceeding

 This journal is © The Royal Society of Chemistry 2024

Open Access Article. Published on 24 June 2024. Downloaded on 1/17/2026 6:47:09 PM.
This article is licensed under a Creative Commons Attribution-NonCommercial 3.0 Unported Licence.

150 °C are needed. This need comes with a challenge related with the limited thermal stabilities of ILs, which can vary significantly depending on the anion/cation pair.[240] These stability limits should be high enough to ensure stable operation at the desired conditions. Even if a certain IL has a sufficiently high thermal stability in the bulk state, its stability limits can deviate substantially when they are immobilized on high-surface area supports, such as on metal oxides[240,241] or MOFs.[238] This phenomenon should be taken into account when using the SILP phase for CO_2 conversion. In addition, it should also be noted that any co-catalysts present with ILs, such as metal nanoparticles, can also accelerate the catalytic decomposition of ILs at elevated temperatures. Besides, for the catalyst systems having ILs in direct contact with metal complexes or nanoparticles, ILs can donate or withdraw electrons to/from the metal, and the presence of such electronic interactions can potentially influence the electronic structure of the active sites.[358–360] This possibility should be taken into consideration when designing such catalysts; the structure–performance relationships should be investigated focusing particularly on characterizing these electronic interactions, and their consequences on the catalytic properties.

In the light of the temperature, pressure, and catalyst requirements of thermal conversions, electrochemical approaches provide a more benign alternative where the reactions can be driven by electricity under ambient conditions. ILs maintain their importance in electrochemical conversions as they discussed in the next section.

4. CO_2 electrocatalytic conversion

Electrochemical reduction of CO_2 is a 154-year-old, still unresolved challenge, which was first studied in 1870 by M. E. Royer[361] in Paris. Various CO_2 reaction pathways have been suggested based on the physicochemical features of the metal catalyst.[362–368] Hori *et al.*[369] showed conversion of CO_2 to other chemicals beyond CO, including gaseous C_2 products, and even tri-carbons can be achieved, specifically with a copper catalyst in aqueous electrolytes. Among the major challenges associated with CO_2RR are the large energy requirements, low efficiencies due to competition with the hydrogen evolution reaction (HER), and limited solubility of CO_2 in the liquid. On the other hand, electroreduction of CO_2 offers the potential to achieve higher conversion efficiency and product selectivity compared to other conversion methods.[370] Theoretically, the overall potentials of +0.2–0.6 V (*vs.* Normal Hydrogen Electrode, SHE) are sufficient to reduce CO_2 to CO, formic acid, methane, and other products in an aqueous solution (1 M electrolyte, pH = 7, 25 °C, 1 atm CO_2) as seen in Table 5. However, the thermodynamic potential values in nonaqueous electrolytes can be different.[371] Further, the overpotentials required for the formation of CO_2 reduction products are independent of the bulk electrolyte pH on an absolute potential scale.[372,373] In practice, very negative potentials must be applied to reduce CO_2 to intermediates. The first step in CO_2RR is the anion radical formation, $CO_2^{\bullet-}$, by one electron transfer from the electrode to the CO_2 on the electrode surface. This initial step involves an energetically unfavorable intermediate, which requires a potential of −1.9 V (*vs.* SHE).

Table 5 CO_2RR reaction steps to commonly reported products and the associated reaction potentials as summarized in ref. 374

Half reactions of electrochemical CO_2 reduction	Electrode potentials (*V vs.* SHE) at pH 7
$CO_{2(g)} + e^- \rightarrow CO_2^{\bullet-}$	−1.90
$CO_{2(g)} + 2H^+ + 2e^- \rightarrow HCOOH_{(l)}$	−0.61
$CO_{2(g)} + H_2O_{(l)} + 2e^- \rightarrow HCOO_{(aq)}^- + OH^-$	−0.43
$CO_{2(g)} + 2H^+ + 2e^- \rightarrow CO_{(g)} + H_2O_{(l)}$	−0.53
$CO_{2(g)} + 2H_2O_{(l)} + 2e^- \rightarrow CO_{(g)} + OH^-$	−0.52
$CO_{2(g)} + 4H^+ + 2e^- \rightarrow HCHO_{(l)} + H_2O_{(l)}$	−0.48
$CO_{2(g)} + 3H_2O_{(l)} + 4e^- \rightarrow HCHO_{(l)} + 4OH^-$	−0.89
$CO_{2(g)} + 6H^+ + 6e^- \rightarrow CH_3OH_{(l)} + H_2O_{(l)}$	−0.38
$CO_{2(g)} + 5H_2O_{(l)} + 6e^- \rightarrow CH_3OH_{(g)} + 6OH^-$	−0.81
$CO_{2(g)} + 8H^+ + 8e^- \rightarrow CH_{4(g)} + 2H_2O_{(l)}$	−0.24
$CO_{2(g)} + 6H_2O_{(l)} + 8e^- \rightarrow CH_{4(g)} + 8OH^-$	−0.25
$2CO_{2(g)} + 12H^+ + 12e^- \rightarrow C_2H_{4(g)} + 4H_2O_{(l)}$	0.06
$2CO_{2(g)} + 8\ H_2O + 12e^- \rightarrow C_2H_{4(g)} + 12OH^-$	−0.34
$2CO_{2(g)} + 12H^+ + 12e^- \rightarrow CH_3CH_2OH_{(l)} + 3H_2O_{(l)}$	0.08
$2CO_{2(g)} + 9H_2O + 12e^- \rightarrow CH_3CH_2OH_{(l)} + 12OH^-$	−0.33

ILs are shown to lower the activation energy of CO_2^- formation[371] by co-catalyzing the reaction at the metal electrode surface, suppressing HER,[375,376] and increasing CO_2 solubility[377,378] with control over the reaction pathway.[379] An overview of the discussed reactions in the literature, as interpreted by us, are represented in Fig. 9. However, the exact mechanism by which ILs lower the overpotential (difference between the thermodynamic and experimental reduction potential) is unclear. Whether an inner sphere electron transfer[380] for surface adsorbed CO_2 or a carboxylated $[EMIM]^+$ promoted route[371] takes place is debated.

Briefly, Han-Scherer *et al.*[381] and Neyrizi *et al.*[382] reported the formation of an intermediate $[EMIM]^+$-CO_2^-, providing a low-energy pathway toward the conversion of CO_2 to CO on Ag

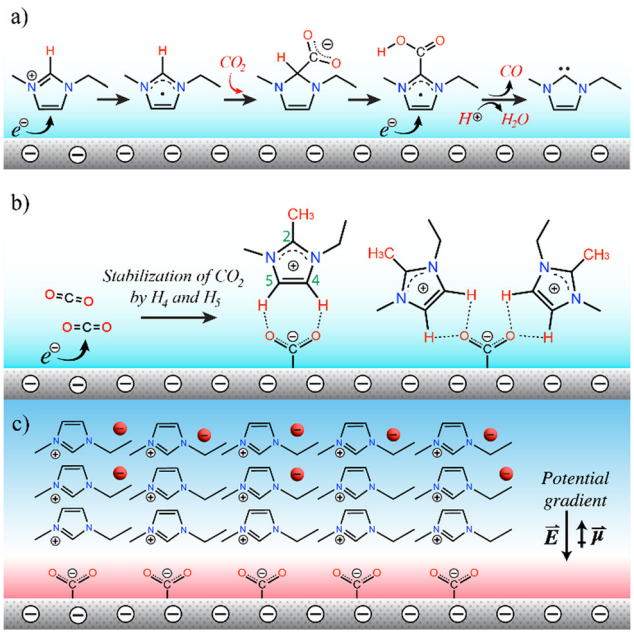

Fig. 9 Overview of the discussed reaction routes in the literature describing the co-catalytic role of $[EMIM]^+$ during CO_2 electrolysis.

Open Access Article. Published on 24 June 2024. Downloaded on 1/17/2026 6:47:09 PM. This article is licensed under a Creative Commons Attribution-NonCommercial 3.0 Unported Licence.

surfaces, as illustrated in Fig. 9a. Stabilization of the high-energy CO_2^- intermediate by hydrogen bonding through the C4–H or C5–H functionality of C2-substituted imidazolium cations are reported by Lau *et al.*,[383] as represented in Fig. 9b. Similarly to this study, Min *et al.*[384] also showed C4-H and C5-H promoted CO generation; however this was in parallel to C2-H promoted HER as the C2 was not substituted. Liu *et al.*[385] discussed the ionic screening effects on acceleration the CO generation through the first steps of CO_2RR. Recently, Noh *et al.*[386] reported that the imidazolium cations form an ordered structure at the electrode surface under negative applied potential, decreasing the entropy of activation, as represented in Fig. 9c. There are also few reports showing the importance of anion identity in tunning product selectivity.[387]

DES electrolytes are believed to play a similar role to ILs where increased Faradaic efficiencies towards CO production on Ag were reported,[388,389] compared to aqueous systems. Although studies with DESs are more scarce, the main challenge for both electrolytes for CO_2RR is their high viscosity and the related mass transport limitations that ultimately result in low current densities. Therefore, these solvents are often diluted with an appropriate solvent to tune viscosity and conductivity. In 2016, Kenis, Masel and coworkers reported[390] on the successful strategy of adding additional supporting salt (*e.g.*, KCl) in imidazolium chloride and DES based electrolytes in order to improve conductivity and therefore the current density. With these enhanced formulations, the question of course is whether the IL or the DES components function in the same way as they would without additional diluents or supporting salts. It is therefore important to develop a fundamental understanding of the effects of solvation, electric field, and surface adsorbed species on CO_2RR. While the physical models of the electrode–electrolyte interfaces with IL and DES based electrolytes are being developed to shed light to the CO_2RR mechanism, the reactive systems (*e.g.*, CO_2 chemisorbing ILs and DESs) bring more complexity to these models as the electron transfer reaction is accompanied by chemical reactions, and therefore present multiple scientific questions that are new and inherent to RCC. Before delving into the specific challenges of RCC with reactive electrolytes, we must first revisit CO_2RR with more traditional systems and outline how incorporation of ILs alters CO_2RR thermodynamics and kinetics. We can then begin to understand RCC with functionalized ILs and DESs.

4.1 State-of-art electrochemical CO_2 conversion

Since Hori's work,[369] published in the 1990s utilizing different metal electrodes for CO_2RR, considerable efforts have been dedicated to enhancing the performance of both metal and alloy electrodes. Achieving high selectivity in CO_2RR remains primary research focus due to close standard reduction potentials from CO and formic acid to multicarbon chemicals (C_{2+}). In 2017, Rossmeisl and co-workers[391] subsequently categorized metal electrodes into four groups: (i) Ti, Fe, Ni, Pd, Ga, and Pt electrodes primarily undergo the HER; (ii) Ag, Au, and Zn electrodes predominantly yield CO as the main reduction product; (iii) Cd, Hg, In, Tl, Sn, and Pb electrodes primarily generate formic acid/formate, and (iv) Cu which forms multicarbon products.

Cu-based materials demonstrate remarkable selectivity in catalyzing CO_2RR yielding a range of hydrocarbons and alcohols. Over the years, numerous strategies have been investigated to enhance the selectivity of hydrocarbons and alcohols over copper. These approaches include adjusting surface morphology, surface alloying, controlling oxidation states, and achieving atomic dispersion. These efforts have primarily focused on modulating binding energies of reaction intermediates and the electrode surface. For example, Gu *et al.*[392] reported 70% FE for ethanol and *n*-propanol over defect-site-rich Cu surfaces which enhances local CO production and, thereby, increase the surface *CO coverage and CO_2-to-alcohol selectivity in aqueous 0.1 M $KHCO_3$ electrolyte. Despite these advancements, the challenge persists in managing hydrogen production, which often competes with or exceeds the desired product yield. This is due to the aqueous nature of electrolytes, which necessitates precise control in adsorption of CO_2 or CO_2 intermediates on the catalyst active sites.[393]

Further, there are several material classes beyond transition metal monometallics that exhibit promise in CO_2 electrocatalysis, including metal alloys, carbon-based materials, transition metal chalcogenides, nanostructured materials, and single-atom catalysts. Despite the success demonstrated by a diverse range of material compositions and structures in aqueous CO_2RR conditions, their performance in IL electrolytes, which present unique advantages such as a broader electrochemical window and improved thermal stability, remains largely unexplored. Although these electrode materials have proven effective in aqueous CO_2RR, they still face limitations that is discussed herein.

4.1.1 Metal alloys. Metal alloys have emerged as promising catalysts for CO_2RR owing to their tunable material and surface properties, leading to enhanced catalytic activity and selectivity.[394,395] By altering adsorption energies of reaction intermediates, these alloys can promote specific CO_2RR pathways. For instance, Cu–In and Cu–Cd alloy catalysts have been shown to promote CO and formate products, respectively, while the Cu–Pd alloy exhibited enhanced selectivity towards CH_4.[396] There have also been studies on Cu alloys with Au,[397] Ag,[398] and Ga[399] all of which displayed increased selectivity towards C_{2+} alcohols including ethanol and methanol. Nevertheless, despite these achievements, a significant hurdle remains in terms of attaining precise control over alloy composition and structure to optimize catalytic performance, all while guaranteeing long-term stability. Another issue involves unintended phase nucleation or corrosion, impacting catalytic activity and selectivity adversely.[400] In particular with ILs and DESs, specific ion adsorption hence surface restructuring can occur besides corrosion. Therefore, surface and the organic ion behaviour needs to be characterized carefully with *in situ* techniques.

4.1.2 Carbon-based materials. Carbon-based electrodes, encompassing carbon nanotubes,[401] graphene,[402] graphite,[403] porous carbon,[404] and carbon-supported metal catalysts,[405] have garnered attention for CO_2RR due to their high surface area, conductivity, stability, and tunable chemistry. These materials, with their porous structures, elevate local CO_2 concentration, facilitating C–C coupling and C_{2+} product formation.[406] Moreover, they exhibit chemical stability across

 This journal is © The Royal Society of Chemistry 2024

Open Access Article. Published on 24 June 2024. Downloaded on 1/17/2026 6:47:09 PM. This article is licensed under a Creative Commons Attribution-NonCommercial 3.0 Unported Licence.

various pH conditions and can be tailored for enhanced conductivity, as demonstrated by Balamurugan *et al.* with a Cu complex on graphitized porous carbon achieving over 60% FE towards methane and ethylene.[407] However, low CO_2RR activity, competing reactions, mass transport limitations, and durability issues like surface fouling and catalyst leaching persist. Pure carbon electrodes often exhibit limited intrinsic activity towards CO_2 necessitating the incorporation of catalytic species to enhance reaction kinetics and lower overpotential. However, this leads to competing electrochemical reactions and increased HER reducing overall efficiency towards C_1/C_2 products. In addition, it has also been found that the material used for the doping of graphene is often inconsequential towards improving catalysis, necessitating the better mechanistic understanding on carbon-based supports to significantly move the field forward.[408]

4.1.3 Transition metal chalcogenides. Transition metal chalcogenides (TMCs) have emerged as promising catalysts for aqueous CO_2RR due to their unique surface properties facilitating the conversion of CO_2 into valuable products.[1] Examples like molybdenum sulfide (MoS_2),[409] copper oxide (CuO),[410] and tin sulfide (SnS)[411] exhibit remarkable catalytic activity, offering tunable surface chemistry, and electronic structure for precise control over product selectivity. These catalysts offer tunable surface chemistry and electronic structure allowing for precise control over product selectivity by adjusting catalyst composition, morphology, and properties. Their catalytic activity has been shown to be from active sites found in surface defects including edge sites and vacancies within terraces and controlling the population of these sites leads to better control of activity. Furthermore, TMCs have also shown improved charge transfer kinetics facilitating rapid electron transfer between the catalyst surface thus promoting CO_2 adsorption, activation, and subsequent reduction. In addition, facile synthesis protocols have been established to achieve low dimensionality including nanocrystals,[409] nanosheets,[412] and nanowires[413] all of which offer increased surface areas and modulation of surface active sites. There has been significant improvements reported in selectivity toward CO (with WSe_2),[414] CH_4 (with $MoTe_2$),[415] and CH_3OH ($Cu_{1.63}Se_{0.33}$)[416] when TMCs were used with ILs. The major role of the IL was discussed to be the local CO_2 enhancing. However, the specific interactions between the IL and the diverse catalytic sites remain unclear.

4.1.4 Nanostructured electrodes. Nanostructured electrodes, spanning metal/nonmetal nanoparticles,[417] metal chalcogenide nanocrystals,[409] carbon-based nanostructures,[418] and hybrid nanostructures,[419] exhibit enhanced CO_2RR efficiency compared to bulk materials, owing to their higher surface area and shortened diffusion pathways. These materials enable tailored reaction pathways and higher selectivity through tunable surface chemistry and catalytic species incorporation. For instance, Zhu *et al.* found that monodispersed gold nanoparticles exhibited increased FE to CO as well as a decrease in overpotential compared to a gold plate.[420] However, challenges persist in reproducible synthesis and scalability, corrosion-induced degradation, and limited mechanistic understanding at the atomic scale. Overcoming these hurdles requires advanced characterization techniques like scanning electrochemical sell microscopy (SECM) for operando local interrogation, yet further development is needed to fully unravel the complexities of nanostructured electrocatalysts and their microenvironment.[421] Achieving reproducible synthesis and scalability of these materials, understanding corrosion-induced degradation mechanisms, and elucidating atomic-scale mechanistic insights are critical for advancing nanostructured electrodes towards practical implementation in large-scale CO_2RR processes.

4.1.5 Single-atom electrodes. Single-atom electrodes, or single-atom catalysts (SACs), offer improved efficiency in CO_2RR compared to nanostructured materials due to precisely controlled dispersion of isolated metal atoms on support materials, providing a high density of active sites.[422] SACs exhibit enhanced CO_2 adsorption and controlled modulation of active sites, leading to accelerated reaction kinetics and tunable selectivity for valuable chemicals.[423] For example, Dai *et al.* manipulated the local coordination of a Cu SAC on a carbon support by doping with B and N and showed a 40% increase in FE towards CH_4 over its non-doped counterpart.[413] Additionally, their well-defined atomic structures allow for better understanding of reaction mechanisms and facilitate the development of highly efficient catalysts. However, the stability of these electrodes under IL/DES electrolytes remain unknown and needs to be examined for scalable RCC applications.

4.2 IL and DES electrolytes

Acknowledging the limitations of conventional aqueous electrolytes and saturation of the electrode materials research, recent efforts in CO_2RR has focused on electrolyte effects.[424–426] In particular, the challenges raised by the low solubility of CO_2, excessive HER, and the instability of metal and metal oxide catalysts in aqueous environments are the main motivators for electrolytes discovery and formulations. Due to the high CO_2 capacity of ILs and DESs, electrolytes based on these solvents have gained interest in CO_2RR and more recently in RCC. For example, electrode materials encountering low catalytic activity, ILs and DESs can alleviate these issues by providing a conductive environment and increasing CO_2 concentration at the electrode surface, enabling enhanced mass transport of reactants and intermediates to active sites within these electrode materials. Moreover, tuning solvent–solute interactions in ILs can stabilize catalytic active sites and inhibit undesirable side reactions, enhancing catalyst efficiency and selectivity. Overall, harnessing these benefits of IL and DES environments in CO_2RR and RCC holds promise in overcoming challenges such as stability, selectivity, and mass transport limitations.

ILs as electrolytes present wide electrochemical stability, high CO_2 solubility, negligible vapor pressures, and tunable physical properties.[381,427–429] The ionic DESs share similar properties to ILs and have been studied for CO_2RR in recent years. ILs are reported to activate CO_2, otherwise thermodynamically very stable, and accelerate its transport to the reaction interface, acting as ''co-catalysts''.[371] Analogous arguments can be envisioned for DESs; however, there are far fewer CO_2RR studies with both solvents, than for CO_2 capture. Furthermore, when it comes to RCC, there is scarcity in the literature.

Open Access Article. Published on 24 June 2024. Downloaded on 1/17/2026 6:47:09 PM.
This article is licensed under a Creative Commons Attribution-NonCommercial 3.0 Unported Licence.

Both CO_2RR and RCC studies to date including ILs have mostly involved the imidazolium cation and a variety of anions. While neat ILs demonstrate high CO_2 solubilities, they also present mass transfer limitations due to their high viscosities (*i.e.*, >15 cP at 25 °C). Functionalized ILs generally present even higher viscosities and may further increase in viscosity after saturation with CO_2 due to the increased hydrogen bonding as elaborated earlier. DESs are also viscous in nature as they are concentrated and involve an extensive hydrogen bonding network.[430] Therefore, CO_2RR and RCC studies to date examined ILs and DESs mostly in the presence of co-solvents such as water, acetonitrile, and dimethyl sulfoxide.

4.2.1 CO_2RR with ILs. The first study on IL electrolytes for CO_2RR was published by Zhao *et al.*[431] in 2004 where 1-*n*-butyl-3-methylimidazolium hexafluorophosphate ([BMIM][PF_6]) electrolyte saturated with water (3.5 wt% water) was shown to produce syngas (CO + H_2) on a Cu surface. Later in 2011, Rosen *et al.*[371] reported the use of the IL [EMIM][BF_4] as the supporting electrolyte in an aqueous solution (18 mol% IL) for the CO_2RR over an Ag electrode, achieving 96% Faradaic efficiency for conversion to CO at a lowered overpotential, due to the decrease in the free energy of the CO_2 reduction intermediate. Since then, several other non-functionalized imidazolium ILs with different anions such as $[BF_4]^-$,[432] dicyanamide ($[DCA]^-$),[432] hexafluorophosphate ($[PF_6]^-$),[433] trifluoromethylsulfonate ($[TfO]^-$),[434] and bis (trifluoromethylsulfonyl) imide ($[NTf_2]^-$),[379,380] have been studied to convert CO_2 into value-added products.

A review article published in 2024 summarizes the use of ILs and DESs for CO_2RR.[435] Accordingly, various heterogeneous metallic electrodes have been used in the presence of ILs in a variety of cell configurations for the production of many different CO_2 reduction products (*e.g.*, CO, HCOOH, CH_3OH, oxalate, polyethylene, *etc.*) as summarized in Table 6. The most relevant electrocatalytic performance metrics, including selectivity, current density and the main product faradaic efficiency, are included. Despite the controversy surrounding the hydrolytic decomposition of [EMIM][BF_4] through $[BF_4]^-$ hydrolysis to HF in the presence of water,[436] this IL has become famous for CO_2RR studies. In many cases, the introduction of an imidazolium-based IL, both in organic and aqueous solutions, has been found to significantly enhance catalytic activity and selectivity, promoting the reduction of CO_2 to CO and other valuable products while suppressing the HER. Apart from high selectivity for CO and HCOOH in IL based electrolytes on Ag and Pb, respectively, another interesting C1 product, methanol, was reported on atomically dispersed Sn catalysts on a defective CuO support.[437] This electrocatalyst showed remarkable selectivity of 88.6% for methanol production at a current density of 67.0 mA cm^{-2}. This study highlights the synergistic effect of catalyst design and the IL based electrolytes in achieving high selectivity and efficiency for methanol production.

Combining the non-functionalized ILs (*i.e.*, 0.5 M [BMIM][PF_6]/acetonitrile) with N,P-*co*-doped carbon aerogel (NPCA) electrolytes, one of the highest current densities in CO_2RR for CO generation was achieved with 99.1% FE and 143.6 mA cm^{-2} current

Table 6 Conventional ILs studied for CO_2RR with their experimental conditions, including working electrode (WE), onset potential, type of electrochemical cell, electrolysis potential (E_{ve}), total current density (CD_{total}), and Faradaic efficiency (FE) for the obtained products

IL	WE[Ref]	Catholyte	Anolyte	CO_2RR onset	Type of cell	E_{ve} (V)	CD_{total} (mA cm^{-2})	FE (%)
[EMIM][BF_4]	Ag NPs/GDE[376]	10.5 mol% IL in water	0.1 M H_2SO_4	−0.5 V *vs.* RHE	Flow	−0.7 V *vs.* SHE	—	∼100% (CO)
	MoS_2[438]	4 mol% IL in water	0.1 M H_2SO_4	−0.164 V *vs.* RHE	Two-compartment	−0.764 V *vs.* RHE	65	98% (CO)
	Ag[385]	0.9 M IL in acetonitrile with 0.1 M [TBA][BF_4]	—	−2.01 V *vs.* Ag/Ag^+	Two-compartment	−2.5 V *vs.* Ag/Ag^+	78.5	∼100% (CO)
	Ag-coated Al foam[439]	8 mol% IL in water	0.5 M H_2SO_4	−1.1 V *vs.* Pt	Flow	−1.8 V *vs.* Pt	36.6	75% (CO)
	Nanostructured Cu[440]	2–8 mol% IL in water	2–8 mol% IL in water	−1.2 V *vs.* Fc/Fc^+	Single-compartment	−1.55 V *vs.* Fc/Fc^+	—	83% (HCOOH)
	Ag[441]	0.7 M IL in acetonitrile	—	−1.9 V *vs.* Ag/Ag^+	Two-compartment	−2.5 V *vs.* Ag/Ag^+	∼40	80% (CO)
[EMIM][NTf_2]	Pb[379]	0.1 M IL in acetonitrile with 0.1 M TEAP	0.1 M IL in acetonitrile with 0.1 M TEAP	−2.12 V *vs.* Ag/Ag^+	Two-compartment	−2.40 V *vs.* Ag/Ag^+	—	40% (CO), 60% (carboxylate)
[BMIM][BF_4]	Sn dispersed CuO[437]	25 mol% IL in water		−1.9 V *vs.* Ag/Ag^+	Two-compartment	−2.0 V *vs.* Ag/Ag^+	67.0	88.6% (CH_3OH)
[BMIM][BF_4] [BMIM][OAc] [BMIM]-[CF_3SO_3]	Ag[442]	0.3 M IL in acetonitrile	0.1 M KOH	−2.0 to −1.88 V *vs.* Ag/Ag^+ depends on IL	Two-compartment cell	−1.65 V *vs.* Ag/Ag^+	−20	20–97% (CO) depending on the IL
[BMIM][Cl]	Ag[443]	IL with 20 wt% water	0.1 M H_2SO_4	−1.5 V *vs.* SCE	Two-compartment	—	−2.4	99% (CO)
[DMIM][BF_4]	Ag[444]	2 mM IL in acetonitrile with 0.1 M Bu_4NPF_6	2 mM IL in acetonitrile with 0.1 M Bu_4NPF_6	−2.28 V *vs.* Fc/Fc^+	Two-compartment	−2.3 V *vs.* Fc/Fc^+	—	45.1% (CO), 53.4% ($C_2O_4^{2-}$), 0.4% (HCO_2^-)
[MM][NTf_2]	Au[382]	0.5 mol% IL in acetonitrile	0.5 mol% IL in acetonitrile	−0.8 V *vs.* Ag/Ag^+	Single compartment	[a]	10	100% (CO)

[a] The bulk electrolysis was performed at constant current density at −10 mA cm^{-2} for 4.5 h.

 This journal is © The Royal Society of Chemistry 2024

Open Access Article. Published on 24 June 2024. Downloaded on 1/17/2026 6:47:09 PM. This article is licensed under a Creative Commons Attribution-NonCommercial 3.0 Unported Licence.

density.[445] This performance was attributed to the synergy between the electrode and the electrolyte, where the large electrochemically active surface area of the NPCA electrode and the improved electronic conductivity achieved by the N-/P-doping were complemented by high CO_2 availability at the electrode surface by the IL as well as the stabilization of the $[BMIM\text{-}CO_2]_{(ad)}$ complex that has a lower reaction barrier.

Apart from the bulk metals examined with IL electrolytes, electrocatalysis with MOFs also have interesting behavior in the presence of ILs. For example, Kang *et al.*[434] performed CO_2 electroreduction using a Zn-based MOF (Zn-1,3,5-benzenetricarboxylic acid metal–organic frameworks (Zn-BTC MOFs) deposited on carbon paper (CP)) in the neat imidazolium IL ([BMIM][BF_4]). They reported the adsorption of CO intermediate on the catalyst framework, stable enough to accommodate up to 6-electron transfers and the generation of CH_4 (80.1% FE at −2.2 V *vs.* Ag/Ag^+). The stabilization of the intermediate was believed to be due to the surface adsorbed layer of imidazolium cations on the surface after the Zn-BTC/CP cathode immersed in the IL electrolyte. The authors also performed CO_2, CO, and CH_4 adsorption experiments at 1 atm and 298 K on the Zn-BTC/CP. The obtained adsorption capacities showed stronger binding of CO_2 and CO over CH_4 on Zn-BTC/CP. Furthermore, electrolysis with bulk metal foils (Ag, Au, Fe, Pt, Cu, and Zn) produced very low CH_4 formation rates in comparison to Zn-BTC/CP under similar conditions, confirming the synergistic effects of the IL electrolyte and the MOF.

Similarly, Zhu *et al.*[446] reported an *in situ* electrosynthesized hollow copper metal–organic framework (Cu-MOF) that selectively produces formate ($FE_{formate}$ = 98.2%) with a very high current density of 102.1 mA cm^{-2} in a 0.5 M [BMIM][BF_4]/acetonitrile electrolyte containing 1.0 M water. To the best of our knowledge, this is the first report of such high current densities in a simple H-cell configuration. The authors ascribed this to the availability of abundant exposed edges, which offer more active sites for catalytic reactions, and the unique morphology facilitating direct contact between the catalyst and the substrate, favoring electron transfer. This facilitates efficient electron transfer from the inner metallic Cu-gauze to the outer shell of the Cu layer, and subsequently to the CO_2 substrate.

In the summary, significant progress has been observed in CO_2RR utilizing MOF-related electrocatalysts. However, achieving high selectivity and high current densities requires the dilution of IL with a suitable solvent, as it allows better transport of reactant to the electrode surface. The utilization of MOF structures in neat IL electrolyte may pose mass transfer limitations during CO_2RR, giving low current densities.[434] Therefore, a preferable strategy involves immobilizing IL on MOFs to serve as an electrocatalyst directly. This approach facilitates the study of functional IL, enabling selective CO_2 capture from dilute streams, followed by conversion.

From the studies thus far involving the imidazolium IL, it is inferred that the complex formation between the cation and CO_2 plays an important role in improving the CO_2RR efficiency and the thermodynamics.[447] While the formation of the imidazolium-CO_2 complex does not occur in the absence of the electric field with non-functionalized ILs (*e.g.*, [EMIM][BF_4] or [BMIM][PF_6] do not spontaneously chemisorb CO_2), it does with functionalized ILs involving basic anions. Therefore, exploring functional ILs with CO_2 chemisorption is gaining interest for RCC.

4.2.2 RCC with ILs. The underlying motivation for RCC with functionalized ILs and DESs is the utilization of the readily captured CO_2 as opposed to activating the physisorbed CO_2. However, the commercial availability of such tailored systems, in particular ILs, is limited. Further, the complexity of the reactions (both chemical and electrochemical) create a dynamic microenvironment during RCC. Hence, the mechanism, energetics, and kinetics associated with the reduction of the captured CO_2 has been difficult to probe. As a result, there have been very few reports in the literature regarding the utilization of functionalized ILs in RCC; Table 7 summarizes all of the reports to date.

To the best of our knowledge, the first report utilizing a functional IL for RCC was published in 2009 by Compton *et al.*[452] They examined neat [BMIM][OAc] with a CO_2 solubility of 1520 mM (at 1 bar and 25 °C) and reported reduction at −1.3 V *vs.* Ag wire on a Pt electrode at room temperature. While this study did not explain the reduction mechanism or report any specific products, they noted the irreversible nature of the reaction and that CO_2 complexes with the anion.

Later, Hollingsworth *et al.*[377] highlighted the superbasic tetraalkyl phosphonium IL, [P_{66614}][124-Trz], for RCC where CO_2 binds to the anion [124-Trz]$^-$. This interaction is said to enable the reduction of the chemisorbed CO_2 at −0.7 V *vs.* Ag/Ag^+

Table 7 Examples of functional ILs used for RCC with their experimental conditions: WE (working electrode; same as the electrocatalyst), onset potential, type of electrochemical cell, electrolysis potential (E_{ve}), total current density (CD_{total}), and faradaic efficiency (FE) for the obtained products

ILs	WE[Ref]	Catholyte	Anolyte	CO_2RR onset	Type of cell	E_{ve} (V)	CD_{total} (mA cm^{-2})	FE (%)
[P_{66614}][124-Trz]	Ag[377]	0.1 M IL in acetonitrile w/0.7 M H_2O	0.1 M IL in acetonitrile w/0.7 M H_2O	−0.90 V Ag/Ag^+	Two compartment cell	−0.7 V *vs.* Ag/Ag^+	—	95% ($HCOO^-$)
[BMIM][124-Trz]	Pb[448]	0.7 M IL in acetonitrile w/5 wt% H_2O	0.1 M H_2SO_4	−1.78 V Ag/Ag^+	Two compartment cell	−2.1 V *vs.* Ag/Ag^+	24.5	95.2% (HCOOH)
[P_{4444}][4-MF-PhO]	Pb[449]	0.5 M IL in acetonitrile	0.1 M H_2SO_4	−2.42 V Ag/Ag^+	Two compartment cell	−2.6 V *vs.* Ag/Ag^+	12.6	93.8% ($C_2O_4^{2-}$)
[EMIM][2-CNpyr]	Ag[450]	0.1 M IL in acetonitrile w/0.1 M TEAP	0.1 M IL in acetonitrile w/0.1 M TEAP	−1.92 V Ag/Ag^+	Single compartment cell	−2.1 V *vs.* Ag/Ag^+	6	94% (CO)
[EMIM][2-CNpyr]	Cu[451]	0.5 M IL in acetonitrile w/0.1 M TEAP	0.1 M H_2SO_4	−1.90 V Ag/Ag^+	Two compartment cell	−2.1 V *vs.* Ag/Ag^+	7.2	11% (Succinate)

Open Access Article. Published on 24 June 2024. Downloaded on 1/17/2026 6:47:09 PM.
This article is licensed under a Creative Commons Attribution-NonCommercial 3.0 Unported Licence.

on Ag. This potential is corresponding to applied overpotentials as low as 0.17 V, yielding formate as the primary product. The control experiments of the IL with a non-reactive anion ($[NTf_2]^-$) showed a selectivity towards CO production. This study points to the significance of reactive anions in providing alternative pathways with reduced activation energy for RCC. Nonetheless, the current density was limited, below 1 mA cm^{-2}, also pointing to the necessity for further tuning electrolyte formulations. Feng *et al.*[448] combined the favored imidazolium cation with the superbasic anion, 1-butyl-3-methylimidazolium 1,2,4-triazolide ([BMIM][124-Trz]), to further enhance the RCC performance. The FE and current density for formic acid, the only observed reaction product, reached 95.2% and 24.5 mA·cm^{-2}, respectively, on a Pb surface. The main explanation offered was that the CO_2 bound on the anion interacts closely with the C2 hydrogen of the imidazolium, thus lowering the energy barrier for generating formic acid. This was further supported by DFT calculations where the CO_2 in [124-Trz]-CO_2^- is mostly in an sp^2 hybridized state and more representative of that in formic acid. On the other hand, they also discussed the possible mechanism of imidazolium reduction followed by the electron transfer to CO_2 facilitated by this imidazolium radical, as with previous studies, where oxalate formation is prevented. However, the [124-Trz]-CO_2^- complex formation offers a lower-energy barrier for generating formic acid, and thus serves as the main mechanism for CO_2 reduction. These findings once again confirmed the importance of the ionic microhabitat in enhancing CO_2 reduction.

Another example of aprotic IL with a reactive anion, 4-(methoxycarbonyl) phenol, and phosphonium cation was reported to produce oxalate on a Pb electrode.[449] The IL, $[P_{4444}][4\text{-MF-PhO}]$, was diluted in acetonitrile (0.5 M) and oxalate was generated with 93.8% FE at −2.6 V *vs.* Ag/Ag^+. They attributed this outstanding selectivity to the effectiveness of $[P_{4444}][4\text{-MF-PhO}]$ in activating the CO_2 molecule through ester and phenoxy double active sites. Furthermore, the IL was discussed to tune the local electronic structure of Pb to facilitate CO_2 activation and dimerization of the surface adsorbed $CO_2^{\bullet-}$ to form $^*C_2O_4^{2-}$.

Recently, Gurkan and co-workers[450,451] have reported another functional IL with AHA and imidazolium cation, [EMIM][2-CNpyr], where they discussed the utilization of the CO_2 complexes with both the anion and the cation through the proposed mechanism shown in Fig. 10. They performed a systematic study where the anion and the cation were varied to investigate the effective role of the IL components. Accordingly, the pre-activation of CO_2 was achieved chemically through the carboxylate formation *via* the carbene intermediate of the $[EMIM]^+$ cation and the carbamate formation *via* binding to the nucleophilic $[2\text{-CNpyr}]^-$ anion. The carboxylic acid intermediate was confirmed by *in situ* surface enhanced Raman spectroscopy (SERS) and the organic radical formation, attributed to imidazolium, was further confirmed by electron paramagnetic resonance (EPR) spectroscopy. Specifically, the onset potential for RCC was observed to positively shifted by 240 mV when the IL was introduced to the acetonitrile-based electrolyte. The main product was CO, as seen on the surface by SERS and in the gas phase by (GC) with >94% FE at −2.1 V *vs.*

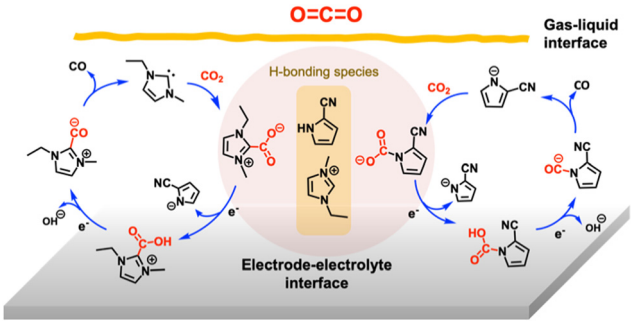

Fig. 10 The proposed CO_2 conversion reaction routes on Ag facilitated by the functionalized IL, [EMIM][2-CNpyr]. Reprinted with permission from ref. 450 Copyright 2023, American Chemical Society.

Ag/Ag^+ over a Ag electrode. In their follow up work, they reported the same IL on Cu where various C_{2+} products (~20% FE) including succinate were obtained.[451] This study specifically examined the electrode–electrolyte interface, highlighting the role of the HBD (protonated anion) that is generated *in situ* from CO_2 absorption for controlling the product selectivity. Interestingly, the ethane and ethylene formation were enhanced with an intentional increase in HBD concentration. This study suggests that the hydrogen bonding network offered by ILs and DESs within the interfacial region helps regulate RCC product selectivity and energetics in aprotic solvents.

From the above discussed studies, it can be concluded that CO_2 reduction onset potential shift positively with both the functionalized and non-functionalized ILs and produce similar products on the same electrodes; however, the mechanisms by which the electron transfer and the proton transfer differ. The main underlying reason is that the non-functional ILs are entirely composed of ions even after CO_2 exposure, while functional ILs contain an important proportion of neutral molecules (≥50 mol%) (potentially serving as native HBDs),[138,453] which directly impact the distribution of charged species and oriented dipoles at the electrode/solution interface. Therefore, it is critical to examine the electrode–electrolyte interfaces by *in situ* spectroscopy techniques complemented by first principle calculations to unravel roles of the individual components in facilitating RCC and governing selectivity.

4.2.3 CO_2RR and RCC with DESs. Similar to the functionalized ILs, the tunability of DESs through the appropriate choice of HBD and HBA components has received interest in CO_2RR research.[435,454] The charge delocalization achieved most commonly through the hydrogen bonding network is a mechanism for tuning physical properties, such as CO_2 solubility.[31,430] Specifically, when compared to ILs, DESs are simpler to prepare and purify. Therefore, DESs have been used as electrolyte components in both aqueous and non-aqueous CO_2RR. The first report of a DES electrolyte for CO_2RR in 2016 involved [Ch][Cl] : urea (1 : 2) DES (a.k.a, reline) for selective CO formation with Ag nanoparticles supported on a gas diffusion electrode.[390] The electrolyte composition was systematically varied from conventional (*i.e.*, KOH, $KHCO_3$, and KCl) to reline in an aqueous solution. The highest selectivity for CO (FE_{CO} = 94.1%) was observed with 2 M

 This journal is © The Royal Society of Chemistry 2024

Open Access Article. Published on 24 June 2024. Downloaded on 1/17/2026 6:47:09 PM.
This article is licensed under a Creative Commons Attribution-NonCommercial 3.0 Unported Licence.

[Ch][Cl]:urea/water at a total current density of 11.6 mA cm^{-2}. The authors explained the possibility of greater stabilization of the CO_2^- intermediate by the ammonium species, enabling high selectivity for CO compared to that of other conventional electrolytes. Furthermore, they highlighted the limitations of the DES electrolyte in achieving high current density due to its high viscosity and low conductivity. To improve the conductivity of the electrolyte, they introduced 1.5 M KCl to the 0.5 M DES/water mixture, which improved the electrolyte conductivity from 34.5 mS cm^{-1} to 131.4 mS cm^{-1}, thus achieving a two-fold increase in total current density (22.1 mA cm^{-2}) without appreciable change in CO selectivity at the same cell potential.

In a subsequent study in 2019, Garg *et al.*[388] conducted concentration-dependent CO selectivity investigations on Ag by varying the reline concentration from 50 to 70 wt% in water. At all tested reline concentrations, more than 95% FE_{CO} was observed at −0.884 V *vs.* the reversible hydrogen electrode (RHE). The authors attributed this high selectivity to reline-mediated interactions with the Ag surface, resulting in the restructuring of Ag with low-coordinated atoms and facilitating CO_2 reduction through choline and urea functionalities. Briefly, the elevated reline concentration was found to dissolve native Ag-oxide layers on the Ag foil, with the dissolved Ag-oxides subsequently being electrodeposited back onto the Ag foil during constant potential CO_2 electrolysis experiments (−1.084 V *vs.* RHE) as confirmed by the morphology analysis shown in Fig. 11a. This dissolution/deposition process resulted in low-coordinated silver atoms on the cathode surface, thereby increasing the surface area and promoting the adsorption of urea and choline cations. Consequently, this led to a significant reduction in HER and enhanced CO_2RR efficiency.

Further examples of DESs studied for CO_2RR and RCC are summarized in Table 8 where the reported CO_2 reduction onset potential, product selectivity, and the main experimental conditions are summarized. Most of the DESs reported present very low total current densities (in the range of 0.1 to 1 mA cm^{-2}). With the high viscosity of these electrolytes, the presence of a large hydrodynamic boundary layer at the catalyst surface is

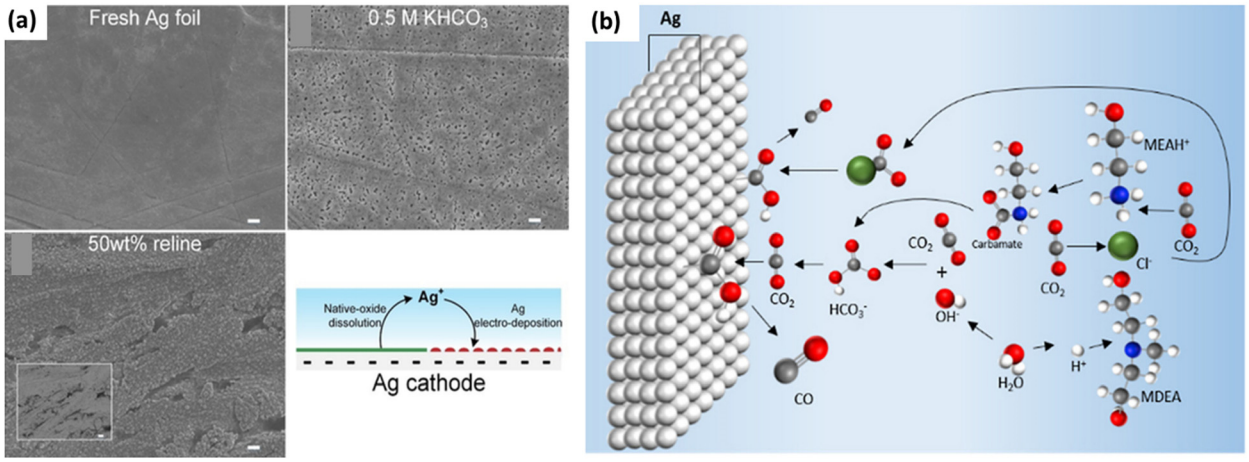

Fig. 11 (a) SEM images of fresh Ag foil and Ag foils after CO_2 electrolysis in 0.5 M $KHCO_3$ and 50 wt% reline; scale bar: 1 μm. (Top) Stability test over Ag foil in CO_2-saturated 50 wt% reline and 0.5 M $KHCO_3$ for 8 h at −0.984 V *vs.* RHE (bottom). Reprinted with permission from ref. 388. Copyright 2019, John Wiley and Sons. (b) Schematic representation of [MEAH][Cl]:MDEA DES mediated CO_2 reduction to CO on Ag surface. Reprinted with permission from ref. 455. Copyright 2021, Elsevier.

Table 8 Examples of DESs used for CO_2RR and RCC with their experimental conditions: working electrode (WE); same as the (electrocatalyst), onset potential, type of electrochemical cell, electrolysis potential (E_{ve}), total current density (CD_{total}), and Faradaic efficiency (FE) for the obtained products

DES	WE	Catholyte	Anolyte	CO_2RR onset	Type of cell	E_{ve} (V)	CD_{total} (mA cm^{-2})	FE_{CO} (%)
[Ch][Cl] : EG (1 : 2)	Au metal sheet[456]	Neat DES	1 M KOH	− 0.70 V *vs.* Ag/Ag^+	Two compartment	−1.60 V *vs.* Ag/Ag^+	1.1	81.8
[Ch][Cl] : urea (1 : 2)	Ag foil[389]	Neat DES	0.5 M H_2SO_4	−1.40 V *vs.* Ag/AgCl	Two compartment	−1.40 V *vs.* Ag/AgCl	0.1	15.8
[Ch][Cl] : EG (1 : 2)		Neat DES (1 : 2)		−1.43 V *vs.* Ag/AgCl		−1.43 V *vs.* Ag/AgCl	0.4	78
[Ch][Cl] : EG (1 : 2)		1 M DES in acetonitrile		−1.52 V *vs.* Ag/AgCl		−1.7 V *vs.* Ag/AgCl	20	98.8
[Ch][Cl] : urea (1 : 2)	Ag NPs/GDE[390]	2 M DES in H_2O	—	∼0.70 V *vs.* RHE	Flow	−0.83 V *vs.* RHE	11.6	94.1
[Ch][Cl] : EG (1 : 2)	$Cu_{0.3}Zn_{9.7}$ deposited on Cu foam[457]	1 M DES in propylene carbonate	0.1 M H_2SO_4	—	Two compartment	−1 V *vs.* RHE	∼16	94.9
[Ch][Cl] : urea (1 : 2)	Roughened Ag foil[388]	50 wt% DES in water	0.5 M H_2SO_4	—	Two compartment	−0.884 V *vs.* RHE	∼4.8	96
[MEAH][Cl] : MDEA (1 : 4)	Ag foil[455]	0.4 M DES in H_2O	0.1 M H_2SO_4	−0.80 V *vs.* RHE	Two compartment	−1.1 V *vs.* RHE	10.5	71

Open Access Article. Published on 24 June 2024. Downloaded on 1/17/2026 6:47:09 PM. This article is licensed under a Creative Commons Attribution-NonCommercial 3.0 Unported Licence.

very likely. Therefore, it is difficult for CO_2 to reach the electrode surface, thus yielding low current density. Therefore, most studies have included the addition of co-solvents to facilitate the CO_2 species transport to the electrode surface. Importantly, the nature of the solvent largely affects the electrolysis performance as recently highlighted by the study of Vasilyev *et al.*[389] where mixtures of [Ch][Cl] and ethylene glycol (1 : 2) DES (a.k.a, ethaline) with water, acetonitrile, propylene carbonate, and 2-(2-ethoxyethoxy)ethanol co-solvents were examined for CO_2RR on Ag electrodes. In particular, the viscosity was reduced from 1244 cP to 1.5 cP with the addition of water to DES (0.1 M DES in water), which led to an increas in total current density. However, the CO selectivity was only 23% since water encouraged the production of mainly H_2 at −1.6 V *vs.* Ag/AgCl. Further improvements in CO selectivity (>90%) and total current densities were observed by performing electrolysis in other aprotic solvents.

Amine-based DESs have been extensively studied for CO_2 capture owing to their remarkable CO_2 uptake capacities. However, their application in RCC is limited. To date, only one study, conducted by Ahmad *et al.*,[455] utilized an amine-based DES composed of monoethanolamine hydrochloride ([MEAH][Cl]) and methyldiethanolamine (MDEA) on Ag, Cu, and Zn surfaces. Consistent with previous research utilizing a 50 wt% reline/water electrolyte on Ag surfaces,[388] nano-sized agglomerates were observed with [MEAH][Cl] : MDEA (1 : 4) DES. Due to the enhanced surface area, remarkably high CO selectivity was obtained; 71% at −1.1 V *vs.* RHE in the aqueous solutions containing 0.4 M DES. The authors explained the stabilization of CO_2 species in the form of *COOH or *CHOO in the presence of protic species to selectively produce CO as shown in Fig. 11b. However, changing the molar ratio of [MEAH][Cl] : MDEA DES from 1 : 4 to 1 : 3, and 1 : 2 led to a decline in CO selectivity, from 71%, 43%, to 5%, respectively, alongside an increase in HER. This was attributed to the increased presence of protic species near the electrode while decreasing the HBD ratio, subsequently promoting greater H_2 production. Additionally, the authors mentioned the narrower potential windows accessible with the DES on Zn and Cu, compared to Ag. Notably, during electrolysis experiments with Cu surfaces, a color change was observed in the electrolyte, further confirming the instability of Cu in the presence of amine-based DESs.

Both IL and DES electrolytes are composed of a variety of charged species and display a complex electrical double-layer structure,[458] as evidenced by numerous probing techniques including advanced spectroscopy[459] and simulations.[460,461] Therefore, understanding the molecular-level RCC mechanism is crucial for enhancing the catalytic activity. The following sections summarize experimental and computational studies on the aspects of the surface species, double-layer structure, potential-dependent behavior of the electrode–electrolyte interface that controls the reaction energetics, kinetics, and product selectivity.

4.2.4 CO_2RR reaction thermodynamics and kinetic analysis. Thermodynamics offers a framework to determine reaction equilibria, primarily reflected in the equilibrium potentials of half-cell reactions which further determine the energy required to drive the redox reaction as in eqn (1):

$$\Delta G = -nFE \quad (1)$$

where G is the Gibbs free energy of the reaction, n is the number of electrons transferred per mole of reaction, F is Faraday's constant (96 485 C mol^{-1}) and E is the potential. The discrepancy between the actual potential applied (E) and the theoretical thermodynamic potential needed (E^0) for the electrochemical reaction is termed overpotential ($\eta = E - E^0$), indicating how far a reaction is from its equilibrium state on the Gibbs energy scale.

Experimentally observed overpotentials can arise from various distinct physical phenomena,[462] including activation overpotential (also called the charge-transfer overpotential, $\eta_{activation}$), concentration overpotential ($\eta_{mass\text{-}transport}$), and resistance overpotential, $\eta_{ohmic\text{-}drop}$, which can be significant for viscous electrolytes such as ILs and DESs. Accordingly, the overall overpotential is the sum of all:

$$\eta = \eta_{activation} + \eta_{mass\text{-}transport} + \eta_{ohmic\text{-}drop} \quad (2)$$

In the context of electrochemical CO_2 reduction, due to the high stability and inert nature of CO_2 molecules, the process of converting CO_2 requires a significant overpotential. From a thermodynamic perspective, multi-electron transfer reactions to yield products are more favorable than the direct one-electron reduction of CO_2 to form the radical anion,[463] CO_2^-, as shown in Table 5. Consequently, the primary factor in the total overpotential required for CO_2 conversion is the activation overpotential, $\eta_{activation}$.[464] Thus, the stabilization of the intermediate radical anion, which forms upon the initial electron transfer to CO_2, becomes a critical step especially in nonaqueous electrolytes.

The use of ILs as solvents or as electrolytes have generally led to anodic shifts in potential for non-catalytic and catalytic reductions *versus* the electrochemical reference. These milder potentials are often directly correlated to reductions in overpotential under equivalent conditions without ILs. However, ILs can modify the standard potential or the CO_2 reduction reaction. As a result, the magnitude of anodic shifts may not directly correlate to the magnitude in the overpotential reduction. Matsubara, Grills, and coworkers have provided valuable experimental data and analysis regarding the overpotential of solutions containing imidazolium cations as solvent or electrolyte in CH_3CN, particularly in the presence of CO_2 and with H_2O.[465,466] In presence of larger amount of water in an organic solvent and under CO_2, bicarbonate can form. Bicarbonate has a sufficiently similar pK_a to imidazolium that it can from an equilibrium between imidazolium carboxylate and water; effectively, the imidazolium can behave as a proton source during catalysis.

When ILs are used as electrolytes in organic or aqueous solvents, the catalytic activity can generally be determined using standard methods as the viscosity of the solution does not change significantly.[467] However, the diffusion constants of

 This journal is © The Royal Society of Chemistry 2024

Open Access Article. Published on 24 June 2024. Downloaded on 1/17/2026 6:47:09 PM.
This article is licensed under a Creative Commons Attribution-NonCommercial 3.0 Unported Licence.

both the catalyst and substrates is expected to be much lower due to the high viscosity, which leads to lower current responses. In order to more accurately determine rates, some studies have measured the diffusion constants, and determined that despite the lower catalytic currents, the second order rate constants for catalysis was improved by up to an order of magnitude.[468]

Overpotential, along with current density and FE represent the key metrics for evaluating the performance of an electrocatalytic process. These indices are closely linked to the kinetics of catalytic reactions, with current density being directly associated with the applied overpotential as expressed through the Butler–Volmer expression (eqn (3)):

$$j = j_0\left\{\exp\left(\frac{\alpha_a zF}{RT}\eta\right) - \exp\left(\frac{\alpha_c zF}{RT}\eta\right)\right\} \quad (3)$$

where j is electrode current density (A m^{-2}), j_0 is exchange current density (A m^{-2}), T is absolute temperature (K), z is the number of electrons involved in the electrode reaction, F is Faraday's constant, R is the universal gas constant, α is the charge transfer coefficient, and η is the overpotential applied. Tafel analysis has traditionally been used as a prevalent technique in electrocatalysis for quantifying how partial current density varies with applied potential (Tafel slope).[469] By comparing the experimentally obtained Tafel slopes against theoretical values predicted on a hypothesized mechanism, researchers have scrutinized the viability of a suggested reaction pathway.[470] Tafel analysis has not been without its drawbacks; for instance, it is unable to distinguish between two mechanisms that yield identical Tafel slopes, a common occurrence in reactions involving multiple electron and proton transfers,[471] and it is becoming more evident that it is limited to the analysis of kinetics for one-electron transfer processes.[472] Often times, it is the reactor kinetics in electrocatalysis that is measured by the traditional approaches and not the intrinsic reaction kinetics.[473] In complex reactions such as RCC, the measured Tafel slope represents the observed or apparent charge transfer coefficient rather than the actual. Since the measured kinetics depends on the electrochemical cell, it is imperative that we develop design equations for the processing of experimental data in the same way that we design equations for the extraction of intrinsic reaction constant for thermal catalysis carried out in batch, plug-flow, or continuously-stirred tank reactors. Moreover, implementing kinetic analysis in concentrated electrolytes like ILs and DESs presents further challenges due to the viscosity of these solvents and the unique double layer structures they form,[474] as discussed before. These factors can lead to findings of anomalously high charge transfer coefficients, attributed to adsorption–desorption phenomena.[475] Consequently, the relevance of the traditional Butler–Volmer relationship to concentrated electrolytes is questionable, prompting suggestions for modified equations.[476] Such revisions necessitate a comprehensive understanding of the electrolyte interfaces and the participating intermediates.

ILs have been said to co-catalyze CO_2RR since they helps overcome the activation overpotential by stabilizing the radical anion intermediate. Decreased overpotentials imply that the electrochemical reactions can proceed with less additional voltage, enhancing the energy efficiency and performance of CO_2 electrolyzers. Furthermore, ILs enhance CO_2 solubility, ensuring higher concentrations of CO_2 at the electrode surface and reducing concentration overpotentials. On the other hand, due to the high viscosity of ILs and DESs, they present significant ohmic overpotentials. Therefore, designing an electrochemical cell to minimize overpotentials due to ohmic drops and using a stable, well-defined reference electrode are crucial for consistent and comparative measurements in RCC.[467]

To quantitively compare CO_2 reduction in ILs and DESs *vs.* conventional aqueous and nonaqueous media, average turnover frequencies (TOF) are determined from the reported performances as shown in Fig. 12. TOF analysis provides an estimate of intrinsic reaction rates across different catalysts, reaction media, and products. This analysis provides a quantitative comparison of activity on a per active site, per time basis, which allows for a fair comparison of reaction kinetics between catalysts with different surface areas and structures. By plotting against overpotential, it becomes more facile to compare catalysts that may be measured with different electrode morphologies (*e.g.* metal foils, nanoparticles), reference electrodes, electrolyte environments, and apparent current densities.

TOF comparisons draw attention to the fact that transition metal dichalcogenides (TMDs, *i.e.* WSe_2 and $MoSe_2$) are typically highly active compared to pure metals in solutions containing ILs as shown in Fig. 12a. The large TOFs of WSe_2 and $MoSe_2$ at low overpotentials are especially notable considering that these materials are typically highly HER active and thus usually completely inactive for CO_2RR.[482,483] The compositional and faceting design space of TMDs could be especially promising for realizing high activity RCC at low overpotentials. Due to drastically differing active site densities, the apparent current densities observed in typical electrochemical scans comparing metals and TMDs is vastly different, and thus benefits from this careful TOF analysis.

These comparisons also make clear that onset overpotentials for CO_2 reduction in both dilute and concentrated ILs are typically on the order of $\sim$50–150 mV, much lower than similar catalysts measured in typical aqueous bicarbonate electrolytes. For example, CO_2 to HCOOH on Cu in [EMIM][BF_4]:H_2O (92 : 8 v-v) reaches a similar TOF ($\sim 10^{-1}$ s^{-1} $site^{-1}$) at a $\sim$270 mV lower overpotential than Cu measured in typical aqueous conditions as illustrated in Fig. 12b. Importantly, at similar TOFs, HCOOH represents over 60% of the FE over Cu in IL, whereas it represents $\sim$20% of the FE of Cu measured under conventional aqueous conditions, which is suggestive of the mechanistic changes between aqueous conditions and ILs. Due to the high intrinsic activity, using ILs could allow for low overpotential production of HCOOH without byproducts. This is also similar to the trend of CO production on Ag. This analysis again illustrates the role of the ILs in RCC.

For heterogeneous catalysts an estimation of the electrochemically active surface area (ECSA) and the density of active sites on the catalyst surface is required. Double layer capacitance

Open Access Article. Published on 24 June 2024. Downloaded on 1/17/2026 6:47:09 PM.
This article is licensed under a Creative Commons Attribution-NonCommercial 3.0 Unported Licence.

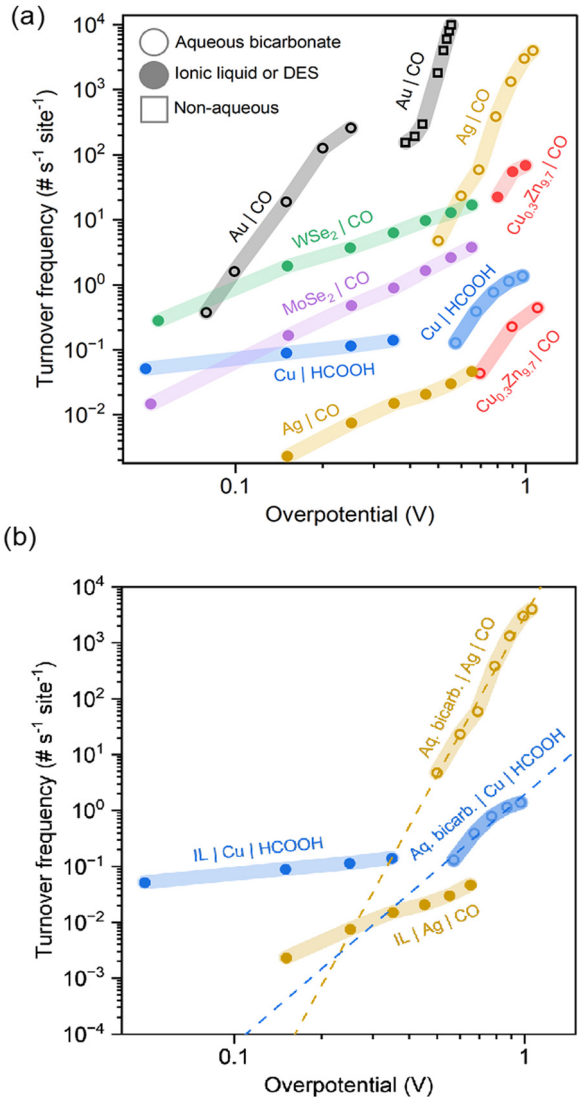

Fig. 12 (a) Calculated turnover frequency (TOF) of various catalysts in aqueous media,[457,477] non-aqueous media,[478] and ILs[414,440,457] plotted against the overpotential. The thermodynamic limiting potentials were taken as the standard values from aqueous media (−0.12 V *vs.* RHE for CO_2 to HCOOH and −0.10 V *vs.* RHE for CO_2 to CO) except in the case of Cu (in IL) where the value was taken as −1.32 V *vs.* Fc/Fc^+.[440] For WSe_2, $MoSe_2$, and Ag in IL, TOFs were previously reported based on roughness factors (determined by CV measurements) relative to reference samples. All other surface areas were converted to active site densities on an assumption of (111) facets, except for $Cu_{0.3}Zn_{9.7}$ which was converted assuming Zn(0001). For Cu in IL, the surface area was previously reported based on a measurement of ferricyanide reduction and use of Randles–Sevcik equation. For examples where ECSA was not previously reported, reported capacitance values were converted using a standard specific capacitance of 10 μF cm^{-2},[479] and 29 μF cm^{-2} for Cu.[480] (b) TOF of CO_2 to CO on Ag and CO_2 to HCOOH on Cu in ILs[414] and aqueous media[481] *vs.* potential replotted to highlight differences in slope and onset overpotential.

measurements are some of the most broadly used methods for assessing catalyst ECSAs as the capacitance is proportional to surface area. However, knowledge of the specific capacitance, an intrinsic material parameter, is needed for a quantitative conversion of the double layer capacitance to a catalyst surface area. Additionally, an assumption of the catalyst faceting (or characterization to elucidate the exposed facets) is necessary to estimate the density of exposed active sites, which is complex for typical polycrystalline catalysts. Since certain sites may be more active than others and even exhibit ensemble effects, normalizing to the total surface area provides a conservative lower bound for comparing the average TOFs of heterogeneous catalysts. Due to the high viscosity of ILs limiting mass transport, these measurements may reflect a mixed regime of mass transport and kinetic contributions, whereas many of the examples under aqueous conditions are more representative of intrinsic kinetics.

In general, catalysts measured in ILs seem to have larger Tafel slopes than catalysts measured in aqueous electrolytes. Since ILs are typically measured in small static electrochemical cells with poor convection, this could be reflective of mixed kinetic and mass transport contributions. Using forced convection strategies to alleviate mass transport limitations along with careful consideration of ECSA could be critical strategies to better understanding RCC in ILs. Alternatively, well-defined mass transport environments (*i.e.* rotating disk electrodes) could be used to better quantitatively account for these mass transport effects. Characterization of the catalyst faceting by imaging or diffraction could also allow for better active site quantification and may be aided by *in situ* studies to understand dynamic changes over catalysts in ILs that are distinct from aqueous environments. Specific capacitances for ECSA determination could also be determined under more uniform conditions, such as in a defined aprotic electrolyte.

4.2.5 Microenvironment constructed by ILs and DESs. In theory, employing IL and DES electrolytes should allow for the exploration of electrochemical reactions across a wide potential window without interference from electrolyte decomposition as in the case of aqueous systems due to their electrochemical stability. In practice, surface adsorption may occur or, depending on the electrode material, impurities may become reactive. The electrode–electrolyte interfaces with these electrolytes are not as well understood as with the aqueous systems where the classical double layer theories are useful in making accurate predictions.[458] The interface governs the potential distribution and the likelihood of a reaction happening. It is known that specific surface adsorption occurs with some of the commonly encountered organic or halide ions in ILs and DESs.[484,485] Further, the ions are not point charges and they undergo voltage-induced reorientations.[486–489]

Recently, Coskun *et al.*[451] studied the interfacial behavior of reactive IL ([EMIM][2-CNpyr]) on a Cu surface, where the IL can chemisorbed CO_2 and yield carboxylate ($[EMIM]^+$-CO_2^-) and carbamate ([2-CNpyr-COO]) adducts. The complex interfacial structure is probed with SERS as shown in Fig. 13a and b under N_2 and CO_2, respectively. Upon negative polarization of the electrode, there is increased interactions between $[EMIM]^+$ and the surface as evident from the increased intensity of 1347, 1380, and 1423 cm^{-1} peaks. With CO_2, these peaks experience a blue shift. Additionally, peaks at 1116, 1342, and 1380 cm^{-1} associated with C_4 and C_5 of $[EMIM]^+$ and N–CH_2 moiety of the ethyl group

 This journal is © The Royal Society of Chemistry 2024

Open Access Article. Published on 24 June 2024. Downloaded on 1/17/2026 6:47:09 PM.
This article is licensed under a Creative Commons Attribution-NonCommercial 3.0 Unported Licence.

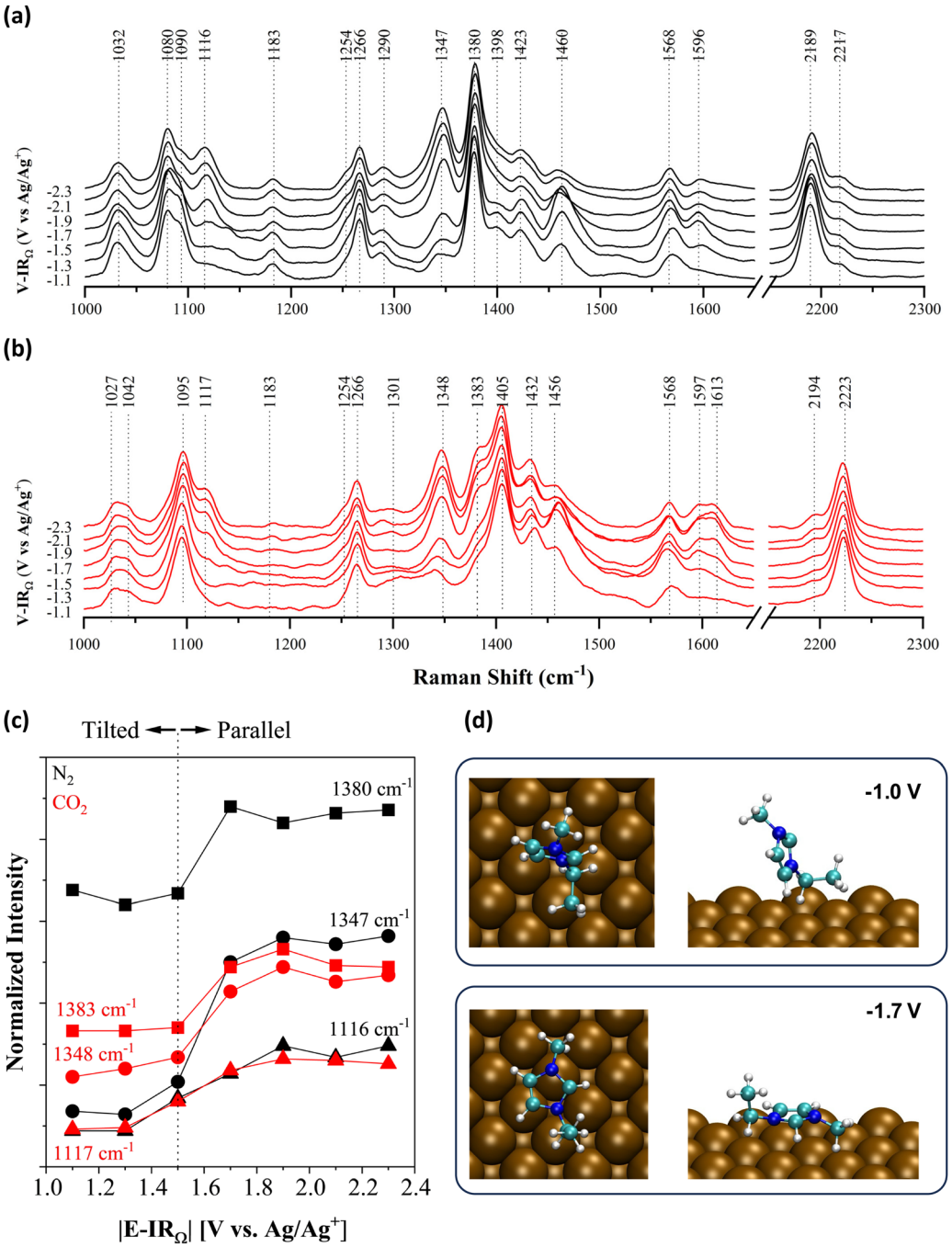

Fig. 13 Potential dependent SERS spectra of [EMIM][2-CNpyr] under (a) N_2 and (b) CO_2, (c) SERS peak intensity as a function of absolute applied potential (E-IR_Ω). The dotted line marks the potential of the change in the orientation of imidazolium species under N_2 (black) and CO_2 (red). Peaks: 1116 cm^{-1} (triangles) for $\delta(C_4C_5\text{-H})$; 1347 cm^{-1} for υ(Im-ring) + $\upsilon(CH_2(N))$ (circle); 1380 cm^{-1} for υ(Im-ring) + $\upsilon(CH_2(N))$ + $\upsilon(CH_3)$ (square). (d) Lowest energy geometries calculated for $[EMIM]^+$ at −1.0 and −1.7 V on Cu(100) (top and side views) indicating the preference of the parallel orientation at a more negative potential. Atom color code: blue = N; cyan = C; white = H. Reprinted with permission from ref. 451. Copyright 2023, John Wiley and Sons.

exhibit a relatively higher enhancement in intensity with polarization compared to other peaks, suggesting an orientation change of the cation evidenced at −1.5 V *vs.* Ag/Ag^+, as illustrated in Fig. 13c. This orientation was further supported by theoretical calculations as depicted in Fig. 13d. Simultaneously, the stretching of the $[2\text{-CNpyr}]^-$ ring at 1398 cm^{-1}, faintly observed under N_2, intensifies and shifts to 1405 cm^{-1} due to the closer proximity of the neutral 2-CNpyrH species formed *via* protonation of the anion upon CO_2 saturation. The presence of 2-CNpyrH upon exposure to CO_2 on the electrode surface is also confirmed by the shift in the –CN stretching vibration from 2189 cm^{-1} under N_2 to 2223 cm^{-1} under CO_2. Based on the findings from SERS analysis, the interfacial configuration was described as a layer rich in cations infiltrated with anions under N_2. However, under

Open Access Article. Published on 24 June 2024. Downloaded on 1/17/2026 6:47:09 PM. This article is licensed under a Creative Commons Attribution-NonCommercial 3.0 Unported Licence.

CO_2, the surface was predominantly characterized by $[EMIM]^+$, $[EMIM]^+$-CO_2^-, 2-CNpyrH, and fewer $[2\text{-CNpyr}]^-$ species. Notably, the presence of pyrrole species contributed to the creation of a distinct microenvironment by the reactive IL for RCC, as the anion forms complexes with CO_2 to generate carbamate adducts and can transport CO_2 to the electrode surface. Furthermore, the protonated anion, 2-CNpyrH, exhibits hydrogen bond donor properties which might also be the reason for the lowered overpotential. These unique interfacial configurations resulting from the reorientation of IL cations can influence the catalytic efficacy of electrochemical CO_2 utilization by modulating the electric field at the interface and facilitating CO_2 mass transport from the bulk to the electrode interface.

The extent of charge density and the hydrogen bonding between the ions impact how they structure near the electrode surface.[490] The interfacial structure in ILs are believed to be heterogenous and extend a few nanometers away from the electrode surface as examined by various techniques. Even when ILs are diluted with other solvents, they tend to crowd the surface with applied polarization. Therefore, their electric field effects can be significant. In the case of solutes undergoing electron transfer reactions in the presence of the IL or DES components, the reaction intermediates can present a varied levels of interaction with these components. Specifically, as the oxidation state changes, the solvent rearrangement may be significant thus impacting the reaction energy and the kinetics.

The earlier work with physisorbing imidazolium ILs reported decreased overpotentials for CO_2RR with the speculation that electrogenerated imidazolium carbene complexes with CO_2 at the C_2-position.[371] Although this complex formation has been reported also by others,[379,491] it was suggested that it served as a byproduct rather than an intermediate leading to the reduction of CO_2. The viewpoints presented in other studies[381] propose an alternative intermediate featuring a tetrahedral carbon at the C_2-position, while C_2–H is still present, resulting from coupling between the electrogenerated EMIM radical (as opposed to the carbene) and CO_2^-. By employing operando spectroscopy, Kemna *et al.*[459] reported the formation of the C_2-COOH (carboxylic acid) adduct, *via* the transient carbene intermediate, that is key to CO_2 conversion to CO and formate on Pt electrodes with the same $[EMIM][BF_4]$ IL as with the previous studies. Other researchers suggest that the interaction of the CO_2^- radical at the C_2-position of the imidazolium ring might not be the sole reason for the enhancements in the overpotentials reported. Lau *et al.*[383] investigated the structure–activity relationships of imidazolium salts featuring various substituents to probe the role of $C_{4,5}$-protons in co-catalyzing CO_2 reduction. They proposed that hydrogen bonding between these protons and adsorbed CO_2^- stabilizes the latter, potentially explaining the reduced overpotential. Tanner *et al.*[380] further claimed that the formation of the imidazolium–CO_2 complex is improbable to have a substantial impact on the overall reaction and the enhancement of CO_2RR facilitated by imidazolium cations is most pronounced for Ag, indicating a synergy between the electrode material and the co-catalyst. The suggested mechanism by the authors involves an initial chemical step, the desorption of IL cation, before an electron is transferred to CO_2. This proposed mechanism indicates that CO_2 directly receives the initial electron rather than the electron first being accepted by the $[EMIM]^+$ molecule to generate a cation radical that would then assist the bending of CO_2 and the stabilization of the radical anion of CO_2.

It should be noted that studies to date utilized different heterogenous catalysts (*e.g.*, working electrode), different reference electrodes, varying water content, and different supporting salts, which makes it difficult to develop a uniform understanding or make meaningful comparisons. Furthermore, it has been difficult to probe the dynamic electrode–electrolyte interfaces with evolving gases and speciation at different timescales. Sum frequency generation (SFG) is a useful method in probing surfaces and interfaces,[492] and it has been shown to complement surface enhanced spectroscopy techniques for CO_2RR mechanistic studies. Braunschweig *et al.*[493] provided evidence for an interfacial imidazolium-CO_2 adduct by utilizing SFG where a vibrational mode attributed to this adduct was observed at 2355 cm^{-1} (non-centrosymmetric CO_2 mode) at notably more positive potentials. Thus, they explained this complex lowering the potential barrier for CO_2 reduction in $[EMIM][BF_4]$ on Pt. Garcia Rey and Dlott[494] also utilized SFG to note a structural transition within the IL on Ag with $[EMIM][BF_4]$ (0.3 to 77 mol% water). A dip in the non-resonant SFG signal precisely at the onset potential, exhibiting distinct curvatures on either side, was evaluated by the authors as an indication of interfacial structure change. Furthermore, this dip coincided with a Stark shift of the CO product, hinting at a change in the interfacial electric field. Intriguingly, this structural transition occurred irrespective of CO_2 presence, suggesting an inherent property of the IL itself. Moreover, the same researchers observed a shift in the non-resonant SFG dip and the threshold potential for CO_2RR towards less negative potentials when the amount of water in the electrolyte was increased. In contrast to the mentioned SFG studies, Papasizza and Cuesta[495] could not observe any band attributable to the interfacial CO_2 or the imidazolium-CO_2 adduct by using an attenuated total reflection (ATR) surface-enhanced infrared absorption (SEIRA) on Au with $[EMIM][BF_4]$ (18 mol% in water). They revealed CO as the primary adsorbed product of CO_2RR under these conditions. The integrated absorbance of the band corresponding to solvated CO_2 mirrored the current.

Returning to the effect of water, numerous studies agree on the enhancement of CO_2RR with the presence of water in IL-based electrolytes.[376,496] This outcome is expected as CO_2RR necessitates both proton and electron transfers, and water serves as an effective proton donor. However, the notable drawback of introducing water into IL systems is the enhancement of HER. Nonetheless, some reports propose that imidazolium cations could mitigate HER, even at water concentrations as high as 90 mol%.[376] Conversely, in their ATR-SEIRAS study, Papasizza and Cuesta[495] documented significant HER with an 82 mol% water and 18 mol% $[EMIM][BF_4]$ mixture. Feaster *et al.*[497] observed that incorporating 0.1 M [EMIM][Cl] into acidic aqueous electrolyte curbed HER activity by 10–75% on transition metal catalysts, while no such suppression occurred in basic electrolyte. They argue that this phenomenon arises because $[EMIM]^+$ displaces

 This journal is © The Royal Society of Chemistry 2024

Open Access Article. Published on 24 June 2024. Downloaded on 1/17/2026 6:47:09 PM. This article is licensed under a Creative Commons Attribution-NonCommercial 3.0 Unported Licence.

interfacial H_3O^+, but not interfacial H_2O. The augmentation in CO_2RR may also stem from alterations in the product distribution with imidazolium reduction. For instance, it is reported[498] that the introduction of protons to pure [BMIM][NTf_2] skewed the equilibrium between the imidazolium radical and the carbene towards the former, potentially influencing the CO_2RR mechanism. Furthermore, Fortunati *et al.*[442] discusses that carbene can bind to active sites on the electrode and the basicity of the anion determines the equilibrium between $[EMIM]^+$ and its radical form.

Aside from experimental investigations, theoretical computations have sought to identify the pivotal intermediate involved in the CO_2RR within IL-based systems. Wang *et al.*[499] directed their attention to the electrochemical reduction of CO_2 in aqueous electrolytes of [EMIM][BF_4]. Employing the DFT method, they meticulously optimized all conceivable intermediate structures of $[EMIM]^+$-CO_2^- complexes at the C_2-position in the aqueous solutions, with the solvation environment addressed through an implicit water solvation model. Subsequently, they computed the Gibbs free energies of all intermediates and identified a thermodynamically favorable reaction pathway. In this pathway, $[EMIM]^+$ undergoes reduction before the formation of $[EMIM]^+$-CO_2^- complexes, with hydrogen at the C_2-position acting as the proton donor to yield the key intermediate, $[EMIM]^+$–COOH. However, despite the calculated redox potentials aligning with the thermodynamic pathways, achieving all steps in an exergonic manner necessitates an applied potential of −2.4 V *vs.* SHE, notably more negative than the experimental onset potentials (−0.25 V *vs.* SHE).[375] The authors attributed this disparity to the absence of the electrode surface in their calculations. In addition to the interactions between $[EMIM]^+$ and CO_2^-, the impacts of double layer effects on the CO_2RR are also noteworthy and can be explored through computational methodologies. Nørskov and co-workers[500,501] utilized DFT to examine the influence of the electric field on the CO_2RR at the interface. Their findings revealed that cations proximate to CO_2 exert a notable stabilizing influence on adsorbed CO_2 on weakly adsorbing metals like Ag, with this effect attributed not to specific chemical bonding but to the interfacial electric field.

Implicit solvent models may be insufficient to capture the non-covalent interactions present in the microenvironment formed by ILs/DESs. In an effort to explicitly model double layer effects, Lim *et al.*[502] devised a multiscale approach to focus on determining the free energies of adsorbed intermediates $*CO_2^-$, *COOH, and *CO in both aqueous solution and [EMIM][BF_4]–water mixtures. The results indicated a decrease in the overpotential for the CO_2 to CO conversion by 310 mV in the latter compared to the former. The primary distinction between the aqueous solution and the IL-containing solution is the robust electrostatic attraction between cations and anions, a microenvironment formed at the interface through non-covalent interactions among water, $[BF_4]^-$ and $[EMIM]^+$. This microenvironment facilitated stabilization of *COOH.

The mechanisms discussed above primarily apply to conventional ILs, where the CO_2 is only physically dissolved in the absence of an electric field, and the constructed electrochemical interface is simpler compared to CO_2-reactive ILs in RCC. For instance, one of the earlier examples of RCC utilized [P_{66614}][124-Trz][377] where basicity of the [124-Trz]$^-$ anion prompts its direct binding with CO_2 ([124-Trz]-CO_2^-) resulting in the formation of an additional CO_2-carrying species within the interface.[503] Thus, an alternative low-energy pathway for CO_2 conversion to formate was achieved. This phenomenon underscores the role of the CO_2-reactive, functionalized ILs, in lowering the reaction energy barrier in RCC. When such highly basic anions are combined with a cation like $[EMIM]^+$, a more complicated interplay emerges as discussed by the studies of Gurkan and co-workers.[450,451]

4.3 Electrolyzers for RCC

The electrolyzer design and cell configuration are important considerations in RCC. The electrolyzer architecture and the operating conditions (*e.g.*, temperature, pressure, applied potential, current) influence the transport of the active species and products between the bulk of the solvent and the electrode surface, as well as the temporal speciation of the capture agent and CO_2 adducts. The reactor and catalyst design also determines the rate of equilibration between the species in the gas and liquid phases. Recent studies on RCC have been carried out in different reactor designs which have different mass transport characteristics. The commonly used electrochemical reactors, the H-cell and the flow cell configuration, have also been used extensively for CO_2RR in the past and recent work has shown that hydrodynamics in the cell indeed determine the product distribution obtained.[473,504] To date, very few works have been reported for RCC, but it can be anticipated that the type of reactors used will also impact the product distribution. In some of the RCC systems discussed in this section, the membrane separating the cathode and anode compartments is used to control the generation and transport of protons that shift the equilibrium and release CO_2 in the proximity of the catalyst. Electrolyzer design is thus tightly tied to the performance of RCC systems and needs to be carefully studied.

4.3.1 Benchmarking. Electrolyzer design types that have been employed for fundamental RCC studies and activity benchmarking include the H-cell, compression cell, and rotating cylinder electrode (RCE) cell (Fig. 14). The H-cell is a typical membrane-separated, two-compartment electrochemical cell separating liquid anolyte from liquid catholyte under active bubbling of CO_2 (Fig. 14a). Leverick *et al.* investigated amines of varying pK_a and sterics and studied systematically the function of pH and temperature on the CO faradaic efficiency obtained on silver catalysts.[505] They observed that the partial current density of CO had a weak amine dependence but had a first order dependence with the partial pressure of CO_2 in the system, which suggested that the active species undergoing reduction is actually the dissolved CO_2 and not the amine.

Alternatively, a sandwich-type compression cell has advantages for activity benchmarking, including lower cell resistance with a short cathode to anode separation, and typically large electrode areas relative to a small volume of electrolyte to aid in the sensitivity of product detection (Fig. 14b).[506] Safipour *et al.*[508] investigated CO_2RR in the presence of MEA in a

Open Access Article. Published on 24 June 2024. Downloaded on 1/17/2026 6:47:09 PM.
This article is licensed under a Creative Commons Attribution-NonCommercial 3.0 Unported Licence.

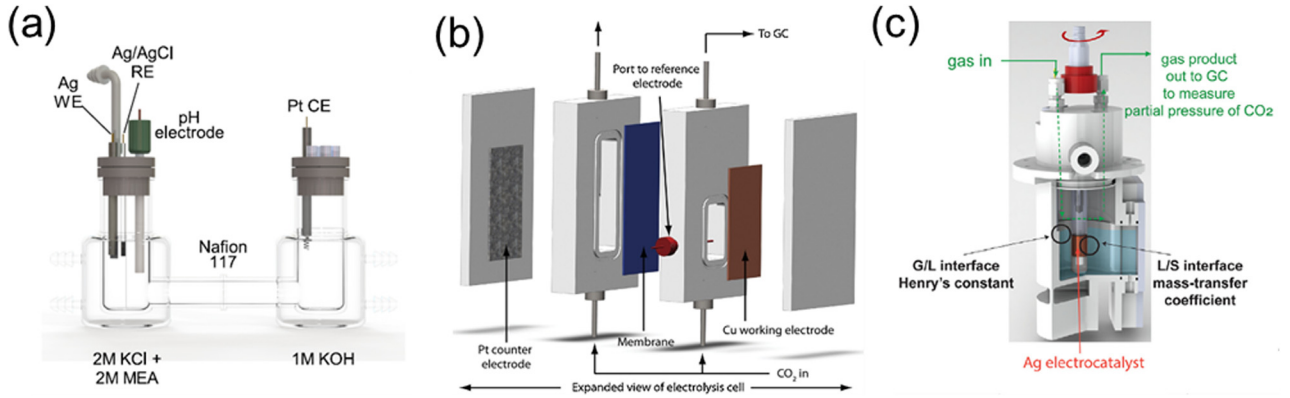

Fig. 14 Examples of electrolyzer designs for activity benchmarking. (a) The conventional H-type cell. Reprinted with permission from ref. 505. Copyright 2023, American Chemical Society. (b) The sandwich-type compression cell. Reprinted from ref. 506 with permission from the Royal Society of Chemistry. Copyright 2012. (c) The gas-tight rotating cylinder electrode cell. Reprinted with permission from ref. 507. Copyright 2023, Elsevier.

compression cell configuration and observed a maximum partial current density for CO of 5 mA cm^{-2}, which decreased with increasing MEA concentration. Compression cells are to a first approximation amenable to the modeling of transport in and out of the surface of the catalysts under the assumption of the absence of primary and secondary current distributions. With support of a 1D continuum reaction-transport model, Safipour *et al.*[508] concluded that the addition of MEA to the $KHCO_3$ electrolyte does not change HCO_3^- concentration, however, concentration of monoethanolammonium ($[MEAH]^+$) increases which acts as a proton source for H_2 and reduces the local CO_2 concentration, in turn decreasing the CO partial current density, with no evidence of any direct reduction of the carbamate.

RCE cells are particularly useful for benchmarking electrocatalytic activity because they can control mass transport by varying the rotation speed of the electrode, thus permitting a better analysis of the inherent kinetics at the WE. For instance, Shen *et al.* used an RCE cell to investigate RCC in bicarbonate and amine-based CO_2 capture solutions on Ag (Fig. 14c).[507] They studied different mass transport regimes by changing the rotation speed and observed different faradaic efficiencies and partial current densities for CO, ultimately concluding that the produced CO was primarily derived from the unbound dissolved CO_2 within the system while the bound CO_2-absorber species contributed only at highly negative potential.

The RCE cell system is unique in that it measures the partial pressure of CO_2 in the headspace of the cell, which is in a pseudo-equilibrium with the solution. The partial pressure of CO_2 can be used to estimate the amount of free and dissolved CO_2 in the bulk of the electrolyte and facilitates the discrimination between different carbon sources during RCC. Transport of mass, heat, and charge affect kinetics in RCC and thus needs to be considered while designing electrolyzers for this reaction. A cell design with a thick hydrodynamic layer, like the H-cell, could slow down the local mass transfer of the species resulting in lower faradaic efficiency.[509] Furthermore, cell resistance and uniform current distribution are some other factors that can potentially affect product distributions in electrochemical systems, especially for organic solvents with lower conductivity. The RCE cell provides an optimal balance for these concerns and is thus a state-of-the-art electrolyzer design for RCC activity benchmarking.

4.3.2 Advancing RCC to high performance electrolyzers. In order to transition fundamental research advances in integrated CO_2 capture and electrochemical conversion to a more mature commercial technology, the benchtop results need to be translated to a sophisticated electrolyzer specifically designed for reactive carbon capture at high performance conditions. Because electrochemical RCC as a field is still in its nascent stages, there have been limited reports of prototype electrolyzers designed to handle the challenges of integrated capture and conversion. Depending to an extent on the properties of the RCC solvent under consideration, many of the aspects of state-of-the-art aqueous-based CO_2RR electrolyzers discussed in the above section may or may not be desirable for a high-current, high-selectivity RCC device.

In any electrochemical CO_2 conversion reactor, some key criteria should be met for high performance: (1) a high mass flux of the reactant (*i.e.*, CO_2 or CO_2-adduct) to the cathode catalyst to ensure high product selectivity uninhibited by mass transfer limitations, (2) high catalyst activity and surface area to minimize the activation overpotential, (3) low ohmic losses in the form of solution, membrane, and electrode series resistance to keep the operating cell voltage low, (4) effective membrane separation of the cathode and anode to maintain low product crossover and back reactions,[510] and (5) stable system components under operating conditions to promote long-term device stability.[511,512] For electrolyzers under either gas-phase or liquid-phase cathode operation, flow cell design architectures have demonstrated the greatest success at achieving high-current–density, high-selectivity electrochemical CO_2 reduction.[513–515] In the best aqueous-based flow electrolyzers, current densities >1 A cm^{-2} have been achieved with sufficient CO_2 mass flux to even reach 90% FE for multicarbon C_{2+} products.[516–519] Similar current densities and FEs have been achieved in state-of-the-art flow electrolyzers designed for liquid-product formic acid production.[520–522] Several possible designs for different reactor types for integrated CO_2 capture and conversion are shown in Fig. 15, which will be referred to when

 This journal is © The Royal Society of Chemistry 2024

Open Access Article. Published on 24 June 2024. Downloaded on 1/17/2026 6:47:09 PM.
This article is licensed under a Creative Commons Attribution-NonCommercial 3.0 Unported Licence.

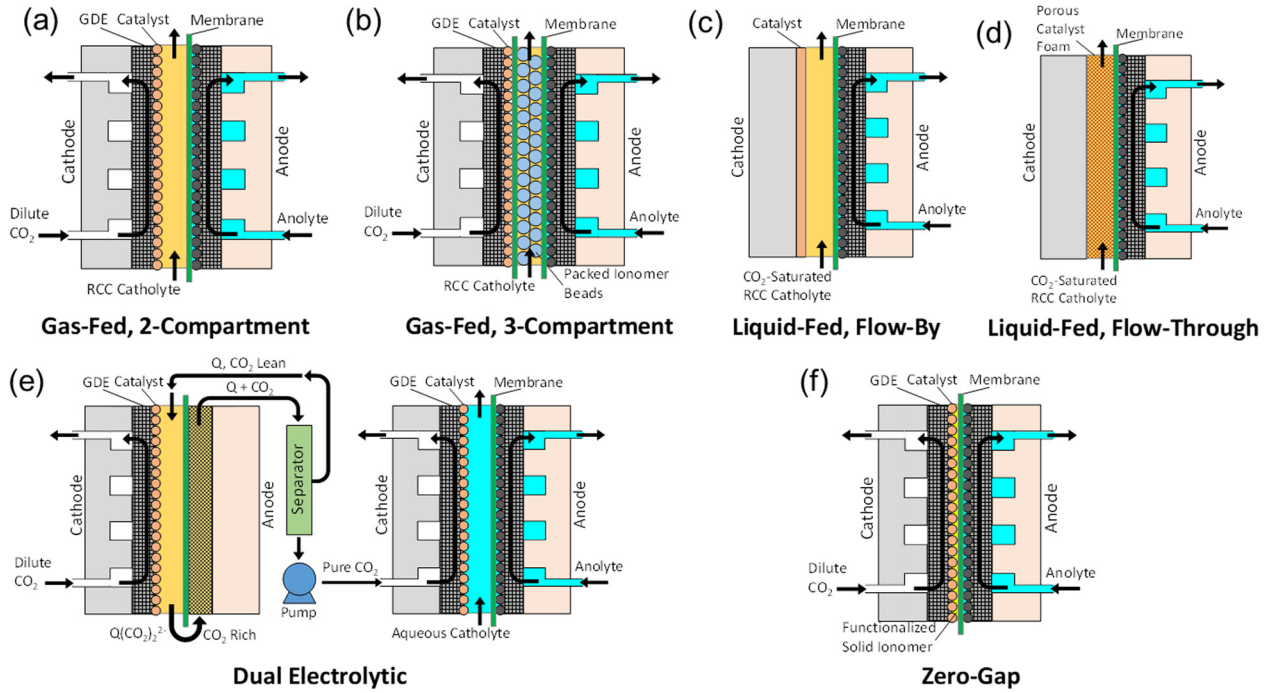

Fig. 15 Schematics of electrolyzer design concepts for high-performance integrated CO_2 capture and conversion. (a) Gas-fed, two-compartment GDE flow electrolyzer. (b) Gas-fed, three-compartment GDE flow electrolyzer. (c) Liquid-fed, flow-by electrolyzer. (d) Liquid-fed, flow-through electrolyzer. (e) Dual electrolytic cells. Q represents a generic CO_2 binding species, such as an organic quinone redox species. (f) Gas-fed, zero-gap flow electrolyzer.

discussing literature reports on electrolyzers for captured CO_2 conversion.

To achieve high CO_2 mass flux to the cathode, gas-fed flow electrolyzers typically rely on a gas diffusion electrode (GDE) with a conductive microporous structure to diffusively disperse reactant uniformly across the active catalytic area (Fig. 15a).[523,524] Moreover, the GDE interface is designed to be hydrophobic to prevent catholyte wetting of the pores, thus maintaining a high-surface–area catalyst/electrolyte/CO_2 triple-phase boundary for high CO_2 mass flux despite the relatively low solubility of CO_2 in water.[513] At present, it is unclear how effective the GDE reactor architecture could be for RCC systems. Functional solvents for carbon capture, including ILs and other non-aqueous media, complicate the interfacial interactions at the GDE. Organic solvents, in particular, are generally much lower in surface tension than water and can readily wet and subsequently flood most GDEs, thus impeding gaseous CO_2 mass transfer. Additionally, for an RCC mechanism involving the direct reduction of a CO_2-adduct, such as a bound CO_2–IL, liquid-phase mass transfer of the adduct species to the catalyst would still be a concern. Thus, liquid-phase reactor designs with sufficient sorbent species concentration to prevent mass transfer limitations of the CO_2-adduct to the cathode from inhibiting selectivity at high currents may be an important feature for RCC flow electrolyzer design. For instance, microfluidic electrolyzer designs have been demonstrated for aqueous CO_2RR in which the cathode and anode are separated by thin (<1 mm) electrolyte flow channels,[525–527] with one such microfluidic reactor reported to achieve >1 A cm^{-2} for CO_2RR.[518] These types of narrow-dimension liquid-phase catholyte flow reactors may be a suitable approach for RCC in functional solvents.

We must note here that the discussion in this section is descriptive of the state-of-the art in CO_2RR and RCC but that many knowledge gaps remain ahead in the path to understanding how to translate bench-scale catalysts to industrial scale RCC electrolyzers. For instance, we have indicated that using of organic solvents in GDEs is problematic because of flooding in CO_2RR applications. We have also indicated that ILs change in viscosity as these are loaded with CO_2. However, there could be a dynamic range where organic liquids and ILs mixtures can result in desirable properties for dynamic transport of CO_2 species within a pore while changing reaction energetics at the surface of the catalyst while preventing flooding. RCC systems are nonlinear systems and will require large experimental datasets that could eventually capture the full complexity of this reaction. As we develop a better understanding of the variables relevant to RCC performance, we anticipate that new electrolyzer concepts will be developed.

4.3.3 Ionic liquid flow electrolyzers. Despite the significant research literature to date on the application of ILs for CO_2RR, the large majority of reported studies have been laboratory-scale efforts with 3-electrode measurements, often in H-cell arrangements for fundamental studies.[528,529] There have been relatively few reports on electrolyzer designs for high-current CO_2 conversion using ILs and little effort directed toward scaling up this approach. There have, however, been key reports utilizing flow cell electrolyzers in combination with IL-mediated CO_2RR.[530] In one early instance, Rosen *et al.* used a Ag-nanoparticle-decorated GDE in flowing 18 mol% [EMIM][BF_4] in water separated from flowing aqueous H_2SO_4 by a Nafion membrane to achieve 96% FE for CO at cell voltages as low as 1.5 V.[371] The same group

Open Access Article. Published on 24 June 2024. Downloaded on 1/17/2026 6:47:09 PM. This article is licensed under a Creative Commons Attribution-NonCommercial 3.0 Unported Licence.

later used catholyte mixtures of varying concentrations of [EMIM][BF_4] in water with Ag in a flow electrolyzer, demonstrating nearly 100% FE for CO with as much as 89.5 mol% water due to the IL inhibition of HER.[376] Despite the high selectivity, this IL/water flow cell achieved relatively low currents, reaching only 10 mA on a 1.5 cm^2 cathode at a cell voltage of 2.5 V. In another example, cathodes catalyzed with varying sizes of Ag nanoparticles reached $\sim$4 mA cm^{-2} at a cell voltage of 3.25 V in a flow electrolyzer using pure [EMIM][BF_4] catholyte separated from 0.5 M aqueous H_2SO_4 anolyte by a Nafion membrane.[531] Another Ag-decorated GDE flow electrolyzer was reported using ILs of 0.6 mol% of 1,3-dialkyl- or 1,2,3-trialkyl-imidazolium cations with trifluoromethane–sulfonate (TfO) anions in water that was operated at high current densities but reached a maximum of 68% FE for CO at 50 mA cm^{-2}.[532] Each of these IL flow electrolyzers are examples of gas-fed, two-compartment GDE flow electrolyzers (Fig. 15a). A different IL flow electrolyzer design was presented by Miao *et al.* in which they used a membrane-free microscale-based electrochemical reactor flowing [BMIM[BF_4]] with only 0.5% w/v water pre-saturated with CO_2 in a narrow channel height of only 500 μm or less.[533] A mathematical model for the microscale IL flow electrolyzer was also described which matched well with experimental product concentration profiles *vs.* CO_2 residence time. Finally, one of the most effective IL flow electrolyzers demonstrated to date used a high flow rate (100 mL min^{-1}) of CO_2-saturated [EMIM][BF_4] (92 v/v%) in water to force convection through a Ag-nanoflower-coated Al foam 3D flow-through cathode, rather than gaseous CO_2 fed to a GDE, to maximize CO_2 mass transport in an IL electrolyte (Fig. 16a).[439] In this liquid-fed, flow-through cathode electrolyzer (Fig. 15d), performance at a cell voltage of 1.8 V increased from a CO partial current density of 0.5 mA cm^{-2} and FE_{CO} of 10% without flow to 36.6 mA cm^{-2} and 75% FE at 100 mL min^{-1}. This type of flow-through cathode electrolyzer thus holds promise as a strategy to mitigate mass transfer limitations in reactive CO_2 capture and conversion applications using functional solvents with CO_2-adduct species in the liquid phase.

There have also been a couple reports of investigations into larger size IL-based flow electrolyzers for CO_2 conversion. For instance, a 30 cm^2 Zn foil cathode was used with an ion exchange membrane in a pressurized flow cell using 1-ethyl-3-methylimidazolium trifluoromethanesulfonate ([EMIM][TfO]) in 90 wt% water acidified with H_2SO_4.[538] At a pressure of 30 bar, a CO selectivity of 82% FE was achieved at an applied current density of 3 mA cm^{-2}. Additionally, Yuan *et al.* reported an effort to scale up an IL-based liquid-fed, flow-by electrolyzer (Fig. 15c) for electrochemical CO_2RR.[534] This flow cell used CO_2-saturated [BMIM][BF_4] at an optimal concentration of 0.1 M in acetonitrile with 5 wt% water as catholyte separated by a Nafion membrane from aqueous 0.1 M H_2SO_4 anolyte. Acetonitrile solvent was used to reduce the IL viscosity, as the observed decline in CO_2RR performance at higher IL concentrations and

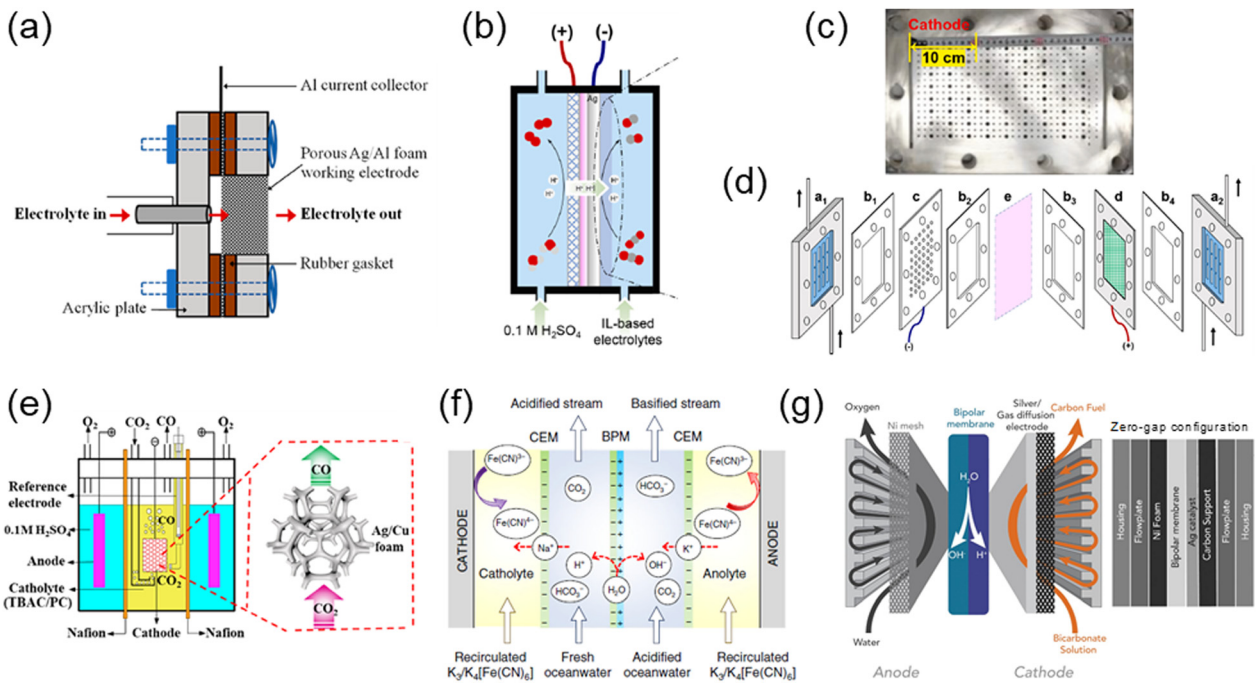

Fig. 16 Examples of electrolyzer device design for high performance RCC. (a) The cathode chamber of a CO_2-presaturated IL flow electrolyzer with a liquid-fed, flow-through porous cathode. Reprinted with permission from ref. 439 Copyright 2019, American Chemical Society. (b) A liquid-fed, flow-by IL electrolyzer and corresponding (c) image of a large perforated Ag plate cathode and (d) exploded view full cell schematic. Reprinted with permission from ref. 534 Copyright 2022, Elsevier. (e) A non-aqueous solvent porous flow-through cathode electrolyzer. Reprinted with permission from ref. 535 Copyright 2022, American Chemical Society. (f) A bipolar membrane electrodialysis cell for CO_2 separation from oceanwater and subsequent coupling in a dual electrolytic cell. Reprinted with permission from ref. 536 under CC-BY license. (g) Flow cell electrolyzer with a bipolar membrane in a zero-gap configuration for bicarbonate reduction. Adapted with permission from ref. 537 Copyright 2019, Elsevier.

 This journal is © The Royal Society of Chemistry 2024

Open Access Article. Published on 24 June 2024. Downloaded on 1/17/2026 6:47:09 PM.
This article is licensed under a Creative Commons Attribution-NonCommercial 3.0 Unported Licence.

flow rates were attributed to viscosity-related mass transfer limitations. A small amount of water was added as a proton source, which was also reported to enhance stability. The sizable electrolyzer used a perforated Ag plate cathode of 495 cm^2 (Fig. 16b–d). Under the optimal operating conditions, this large IL-based flow electrolyzer achieved a total current of 6.32 A (or 12.8 mA cm^{-2}) at 4.0 V with 83.9% FE for CO and $<2\%$ FE for H_2. Furthermore, it was demonstrated to be stable over 10 h and outperform an analogous aqueous 0.1 $KHCO_3$ flow electrolyzer in both stability and CO selectivity.[534] While better mass transfer and innovative flow-through cathode structuring may be needed to improve the current density, the strong performance of this scaled-up IL-based electrolyzer is encouraging for the prospects of commercially feasible reactive carbon capture.

4.3.4 Flow cell considerations for non-aqueous solvent. Many applications using ILs for CO_2 reduction have utilized non-aqueous solvents to reduce the viscosity or aprotic solvents such as acetonitrile, to inhibit competition from HER. In addition, some IL counterions, such as BF_4^-, are unstable in aqueous solvent and can undergo hydrolysis.[436] Thus, for ILs as well as some other functional solvents of interest for reactive carbon conversion, there may be a need to design electrolyzers for operation in non-aqueous solvent. Although the high surface tension of many organic solvents can lead to wetting and flooding of GDEs,[539] under some conditions a GDE flow cell can work with non-aqueous solvent. For instance, Pb-catalyzed CO_2 reduction to oxalate in acetonitrile in a GDE flow cell was reported at 80 mA cm^{-2} with no indication of cathode flooding.[540] In cases where the solvent leads to more pervasive GDE flooding issues or when the CO_2 is delivered in the liquid-phase only, alternative electrolyzer designs can accommodate non-aqueous electrolyte. Gas-fed, three-compartment GDE flow electrolyzers (Fig. 15b) using two-membranes with packed ionomer beads in the central compartment have been successful for CO_2RR to formate.[520,541] This three-compartment design was extended to non-aqueous catholyte, wherein the second membrane prevents GDE flooding, but with higher cell resistance due to ionomer dehydration in the non-aqueous solvent.[539] For non-aqueous electrolytes delivering CO_2 to the cathode in the liquid phase, flow cells using forced convection through porous electrodes have demonstrated effective performance (Fig. 15d). A flow cell with a homogeneous $[Ni(cyclam)]^{2+}$ electrocatalyst in acetonitrile achieved $>80\%$ FE for CO at up to 50 mA cm^{-2} by directing catholyte flow through porous graphite electrodes.[542] Similarly, in one of the highest performing CO_2 electrolyzers using an organic solvent, CO_2 was directed through a porous Ag-modified Cu foam cathode in 0.1 M tetrabutylammonium chloride (TBAC) in propylene carbonate (PC) catholyte separated by Nafion membranes from two anode chambers with aqueous 0.1 M H_2SO_4 (Fig. 16e).[535] With high CO_2 solubility in the organic solvent, minimized anode/cathode separation distance, and high mass transport through the porous flow-through cathode, this electrolyzer achieved 116.8 mA cm^{-2} with a CO FE of 92.2%, demonstrating the viability of high current performance with non-aqueous catholyte.

4.3.5 Dual electrolytic cells. Another electrolyzer design for integrated electrochemical CO_2 capture and conversion uses a dual electrolytic cell strategy. With this approach, the first electrochemical cell captures CO_2 at the cathode from a dilute source (*e.g.*, air, flue gas, *etc.*) and then releases it in a purified form at the anode. The first cell anode gaseous output is then coupled to the cathode of a second cell for optimized CO_2 flow electrolyzer conversion (Fig. 15e).[543,544] The dual electrolytic cell thus relies on a CO_2 catch-and-release strategy rather than the direct reactive capture and conversion of a CO_2-adduct species. CO_2RR can thus proceed efficiently from high CO_2 concentrations using dilute gas streams, with the tradeoff of needing additional energy input for the electrochemical purification step.

Few dual electrolytic systems have yet been reported for integrated CO_2 capture and conversion. Notably, Digdaya *et al.* demonstrated a directly coupled dual electrolytic system using a bipolar membrane electrodialysis cell and a vapor-fed CO_2RR cell to capture and convert CO_2 from ocean water (Fig. 16f).[536] The bipolar membrane cell used a reversible ferro/ferricyanide redox couple separated from the ocean water by cation exchange membranes to drive CO_2 release *via* the acidification of bicarbonate. The outlet CO_2 stream was then sent through tandem vapor-fed cells, first a pre-electrolysis oxygen reduction reaction cell to remove residual O_2 that would parasitically hurt CO_2RR performance, and then a subsequent GDE CO_2RR flow cell catalyzed by either Cu or Ag. The combined system led to a CO_2 capture efficiency of 71% with up to 95% FE to CO on Ag.

Although not many dual electrolytic cells have been characterized for integrated CO_2 capture and conversion in the literature, there are a several reported electrochemical CO_2 separation techniques that might be suitable for incorporation into a dual electrolytic system.[545,546] For instance, electrochemical cycling of organic quinone redox species in the presence of dilute CO_2 sources can selectively bind CO_2 during reduction and then oxidatively release it in a purified stream (Fig. 15e),[547] which was effectively demonstrated for 1,4-naphthoquinone in the ionic liquid [EMIM] tricyanomethanide, [TCM].[89] In another case, a liquid naphthoquinone sorbent was coupled to a ferrocene-derived counter electrolyte in a continuous electrochemical CO_2 capture and release system.[548] Quinones for CO_2 separation were also employed in a novel faradaic electro-swing reactive adsorption process in which a solid-state electrochemical cell with a polyanthraquinone–carbon nanotube electrode captured CO_2 upon reduction and subsequently released it during the anodic swing.[47] The electro-swing process was effectively demonstrated with CO_2 concentrations as low as 6000 ppm and at typical flue gas concentrations ($\sim$10%) with a CO_2 separation faradaic efficiency $>90\%$. Electrochemically mediated amine regeneration (EMAR) is another approach to CO_2 separation that may be amenable to dual electrolytic cell operation. In EMAR, CO_2 binds to an amine sorbent to form a carbamate, which is then electrochemically oxidized to release the CO_2 and subsequently reduced to regenerate the amine.[545] In one example of continuous EMAR, ethylene diamine sorbent was used in a Cu ion-mediated process to achieve a CO_2 separation efficiency $>80\%$ from flue gas.[549] In another, ethoxyethylamine in dimethyl sulfoxide was used in an electrochemical cation-swing process in which different Lewis acid cations entered the electrolyte depending on the direction of

Open Access Article. Published on 24 June 2024. Downloaded on 1/17/2026 6:47:09 PM.
This article is licensed under a Creative Commons Attribution-NonCommercial 3.0 Unported Licence.

current flow, and the cation identity led to a reversible carbamic acid-to-carbamate conversion that released purified CO_2.[550] These kinds of electrochemical CO_2 separation techniques could be designed for efficient coupling to optimized gas-fed CO_2RR reactors for a dual electrolytic integrated conversion of dilute CO_2 streams.

4.3.6 Zero-gap electrolyzers. Lastly, when considering the design of electrolyzers that promote CO_2 sorption and RCC, electrochemical engineers may also benefit from translating aspects of direct aqueous CO_2RR cells based on the zero-gap architecture. In a zero-gap electrolyzer, CO_2 is fed to a membrane electrode assembly in intimate contact with both electrodes, thus minimizing the ohmic resistance for ion exchange (Fig. 15f). RCC liquid-fed flow electrolyzers compatible with this configuration could similarly benefit from minimized cell resistance. For example, Li *et al.* demonstrated a bicarbonate flow electrolyzer in a zero-gap arrangement that used a bipolar membrane to supply protons to release CO_2 locally from the bicarbonate in the catholyte (Fig. 16g).[537] By releasing CO_2 *via* a local pH swing, CO_2RR can be promoted within the bicarbonate capture solution.[87] The acidic release of CO_2 at the bipolar membrane thus increased the reactant mass flux to the adjacent cathode surface in the zero-gap configuration, leading to high CO faradaic efficiency. The cell voltage required to reach 100 mA cm^{-2} was 4.4 V in this bicarbonate electrolyzer.[537]

As reported previously for IL-based CO_2RR, complexing of the imidazolium cations with CO_2 led to lower onset potentials and suppressed side reactions.[371] Researchers have sought to gain some of the benefits of functional solvent ILs while bypassing issues arising from the use of liquid electrolyte by incorporating imidazolium groups into solid polymer electrolyte membranes for use in zero-gap membrane electrode assembly electrolyzers. With a methylimidazolium-substituted styrene copolymer anion exchange membrane, a gas-fed CO_2RR electrolyzer was operated as high as 200 mA cm^{-2} at 3 V for 1000 h with >95% CO FE.[551,552] These imidazolium-functionalized membranes were trademarked as Sustainion™ and incorporated some of the functional characteristics of imidazolium-based ILs. More recently, benzimidazolium cations grafted onto alkaline polyelectrolytes enabled efficient CO_2RR conversion to ethylene over Cu catalyst at up to 331 mA cm^{-2}.[553] Similarly, EMIM-functionalized Mo_3P nanoparticles coated in anion exchange ionomer were reported to produce propane, a C_3 product, at 91% FE and a current density of 395 mA cm^{-2}.[554] In another, IL-MOF hybrid catalyst which immobilized 1-butyl-3-methylimidazolium hexafluorophosphate, [BMIM][PF_6], within the porous MOF achieved CO_2RR at >65% FE for CH_4.[555] Each of these examples highlights the feasibility of immobilizing functional IL or other sorbent groups at the ionomer and/or catalyst interface to enable some of the benefits of functional solvents in a zero-gap electrolyzer architecture.

4.4 Homogeneous CO_2 electrocatalysis

There is an extensive literature on the study of heterogeneous catalysts for CO_2RR in IL containing electrolytes. By comparison, there are far fewer studies that have examined the impact of IL salts as solvents or electrolyte for homogeneous catalysts. These studies have investigated catalysts that are already known for their selectivity towards CO_2 reduction in conventional solvents. They include catalysts selective towards CO production such as Fe(TPP)Cl,[556,557] *fac*-Re(bpy)$(CO)_3$Cl,[465,468,558] or Ni(cyclam)Cl_2,[559] and towards $HCOO^-$ production such as (Rh(bpy)(Cp*)Cl).[560] The molecular structures are shown in at the top of Fig. 17. The bottom shows catalysts that have incorporated imidazolium type functionalities in their secondary coordination sphere to enhance catalytic activity. A brief summary of electrocatalytic activity of the homogeneous catalyst for CO_2RR is given in Table 9.

These catalysts have been studied using ILs either as the primary solvent or as the electrolyte in organic/aqueous solvents. Additionally, there are two examples of catalysts that have been immobilized onto surfaces,[557,564] as well as modified molecular catalysts that incorporate IL cations in the secondary coordination sphere.[561–563] In all cases, the presence of small quantity

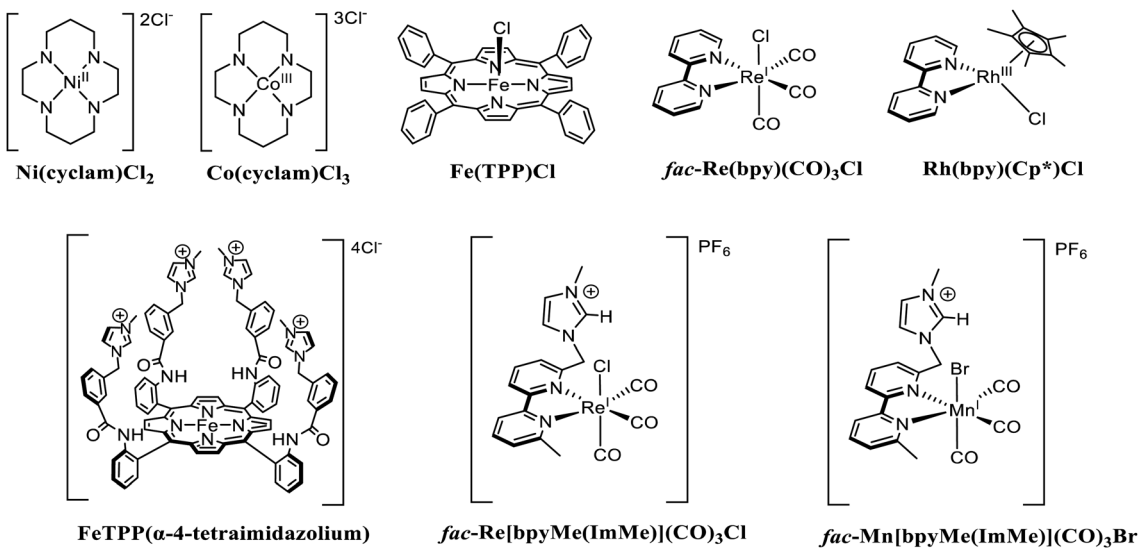

Fig. 17 Example structures of homogeneous electrocatalysts studied for CO_2RR in IL media.

 This journal is © The Royal Society of Chemistry 2024

Open Access Article. Published on 24 June 2024. Downloaded on 1/17/2026 6:47:09 PM. This article is licensed under a Creative Commons Attribution-NonCommercial 3.0 Unported Licence.

Table 9 Brief summary on homogeneous electrocatalysts studied for CO_2RR in ILs media with their experimental conditions (catholyte, electrolysis potential (E_{ve}), Faradaic efficiency (FE), turnover frequency (TOF), and turnover number (TON) for the obtained products)

Homogeneous catalyst[Ref] (concentration)	Catholyte	Proton source	E_{ve} (V)	FE % (product)	$TOF_{product}$	$TON_{product}$
$[Ni(cyclam)Cl_2]$[559] (80 mM)	Neat [BMIM][BF_4]	None added	−1.4 V *vs.* Ag/AgCl	95.2% (CO)	0.73 h^{-1}	2.19
	Neat [BMIM][NTf_2]	None added		75.1% (CO)	0.06 h^{-1}	0.17
$[Co(cyclam)Cl_3]$[559] (80 mM)	Neat [BMIM][BF_4]	None added		84.9% (CO)	0.08 h^{-1}	0.22
	Neat [BMIM][NTf_2]	None added		62% (CO)	0.04 h^{-1}	0.11
FeTPPCl[556] (0.5 mM)	0.3 M [BMIM][BF_4] in DMF with 0.1 M [TBA][PF_6]	1 M TFE	−1.56 V *vs.* NHE	93% (CO)	190 s^{-1}	27.4×10^5
[Rh(bpy)(Cp*)Cl]Cl[560] (1 mM)	0.5 M [EMIM][PF_6] in acetonitrile	5% v/v H_2O	−1.89 V *vs.* Fc^+/Fc	90% ($HCOO^-$), 9% (H_2)	—	—
			−1.83 V *vs.* Fc^+/Fc	91% ($HCOO^-$), 9% (H_2)	—	—
	0.1 M [EMIM][BF_6] in acetonitrile	0.1 M CH_3COOH	−0.9 V *vs.* Ag/AgCl	46% ($HCOO^-$), 40% (H_2)	—	—
$Re(bpy)(CO)_3Cl$[468] (0.5 mM)	Neat [EMIM][TCB]	50 mM H_2O	−1.8 V *vs.* Fc^+/Fc	88% (CO)	—	—
$Re(bpy)(CO)_3Cl$[558] (1 mM)	0.5 M [EMIM][PF_6] in acetonitrile	1.5 M TFE	−1.75 V *vs.* Fc^+/Fc	96% (CO), 1% (H_2)	—	—
			−2.05 V *vs.* Fc^+/Fc	77% (CO), 12% (H_2)	—	—
	0.5 M [BMPyrr][PF_6] in acetonitrile			80% (CO), 10% (H_2)	—	—
	0.5 M [EMIM][BF_4] in acetonitrile			71% (CO), 18% (H_2)	—	—
Homogeneous catalyst incorporated with imidazolium in the secondary coordination sphere						
FeTPP(α-4-tetraimidazolium)[561] (0.5 mM)	0.1 M KCl (aq.)	H_2O	−0.948 V *vs.* NHE	91% (CO)	14 986 s^{-1}	1.08×10^8
{Re[bpyMe(ImMe)]$(CO)_3Cl$}PF_6[562] (1 mM)	0.1 M [TBA][PF_6] in acetonitrile	9.4 M H_2O	−1.74 V *vs.* Fc^+/Fc	73% (CO)	—	—
{Mn[bpyMe(ImMe)]$(CO)_3Br$}PF_6[563] (1 mM)	0.1 M [TBA][PF_6] in acetonitrile	9.25 M H_2O	−1.56 V *vs.* Fc^+/Fc	77.7% (CO)	—	—
			−1.82 V *vs.* Fc^+/Fc	70.3% (CO)	—	—
Catalysts immobilized onto electrode surfaces						
$Re(bpy)(CO)_3Cl$@HPC[564]	[EMIM][BF_4] with H_2O (5% v/v)	H_2O	−1.75 V *vs.* Fc^+/Fc	79% (CO)	0.3 s^{-1}	260
			−2.05 V *vs.* Fc^+/Fc	76% ($HCOO^-$)	2.2 s^{-1}	1950
ZnTAPP@ITO[565]	Neat [BMIM][BF_4]	None added	−0.8 V *vs.* Ag/AgCl	14.5% (CO)	—	2.74
FeTAPP@ITO[565]				79.6% (CO)	—	9.18

(0.5–80 mM) of these homogeneous catalysts in neat IL or IL diluted in solvent result in anodic shifts of CO_2RR onset potential. These anodic potential shifts are generally larger than those observed in organic solvents saturated with non-IL electrolytes, indicating these changes are not solely due to the greater ionic strength of the ILs.[468,556] Studies that explored the effect of $[BF_4]^-$ *versus* $[PF_6]^-$ found minimal effects on the electrochemical and electrocatalytic response of *fac*-$Re(bpy)(CO)_3Cl$[558] and [Rh(bpy)-(Cp*)Cl].[560] $[TCB]^-$ and $[NTF_2]^-$ were both used as anions with $[EMIM]^+$ to study the electrocatalytic activity of *fac*-ReCl(bpy)-$(CO)_3$ and exhibited no significant differences.[468] However, $[NTF_2]^-$ was found to have an inhibitory effect on catalysis compared to $[BF_4]^-$ with [Ni(cyclam)Cl].[559]

Similarly, few studies have focused on the effect of different IL cations, either imidazolium ($[BMIM]^+$, $[EMIM]^+$) or pyrrolidiniums ($[BMPym]^+$, $[BMPyrr]^+$). One study with *fac*-$Re(bpy)(CO)_3Cl$ used the protic imidazolium cation $[DiMIM]^+$, but catalysis under CO_2 reduction conditions only resulted in hydrogen due to the acidity of the cation.[558] Under non-protic conditions with *fac*-$ReCl(bpy)(CO)_3Cl$ the imidazolium cations $[BMIM]^+$ and $[EMIM]^+$ led to greater anodic shifts than the pyrrolidinium cation,[558] $[BMPym]^+$ relative to ferrocene. The first reduction of *fac*-$ReCl(bpy)(CO)_3Cl$ is metal-based and leads to loss of the chloride ligand and is shifted anodically by ~80 mV. The second reduction is centered on the bpy ligand to form the anionic compound $[fac\text{-}Re(bpy)(CO)_3]^-$ and corresponds to the onset of electrocatalysis. The second reduction exhibits the largest anodic change (up to 450 mV) in potential under aprotic conditions. However, these changes to the reduction potential were minimized when the acid source trifluoroethanol was added to the IL. A computational study on this complex in ILs indicates the imidazolium cation stabilizes this anionic species through an electrostatic π^+–π interaction.[465] Adding of an external acid source, such as trifluoroethanol, is expected to minimize this electrostatic stabilization by protonating the reduced metal complex.[558] Despite the muted effect that the addition of an acid source had on the reduction potential, in all cases, the catalytic current with the imidazolium and pyrrolidinium cations was increased, indicating a beneficial effect on the catalytic rate. The rate enhancement is attributed to the imidazolium facilitating C–OH bond cleavage through a hydrogen-bonding interaction with CO_2 bound to the catalyst, which is believed to be the rate-determining step in catalysis.[465]

The impact of imidazolium-based and pyrrolidinium-based cations as electrolyte were also investigated with [Rh(bpy)(Cp*)-Cl]Cl, which catalyzes the reduction of CO_2 to $HCOO^-$.[560] In a mixed 95 : 5 acetonitrile : water solution, the presence of the IL cations results in a minimal change to the first reduction, which is metal-based. Like the prior example, $[fac\text{-}Re(bpy)(CO)_3]^-$, the second reduction occurs on the bpy ligand to generate the active catalyst and leads to the onset of catalysis. This reduction occurs at a more anodic potential (<100 mV) for both IL cations, with EMIM

Open Access Article. Published on 24 June 2024. Downloaded on 1/17/2026 6:47:09 PM. This article is licensed under a Creative Commons Attribution-NonCommercial 3.0 Unported Licence.

providing a larger effect. The EMIM cation also gives a greater current density than TBA, whereas BMIM results in a similar current density, and [BMPyrr] results in a lower current density. When acetic acid was used as an acid source, [EMIM][BF_4] resulted in almost double the faradaic efficiency (up to 66%) for formate compared to the non-IL electrolyte [TBA][BF_4]. The catalyst was also tested under aqueous conditions, where it displayed greater selectivity and more anodic catalytic onset potentials when [EMIM][BF_4] was the electrolyte compared to [TBA][PF_6]. Again, similar to [*fac*-Re(bpy)$(CO)_3$]$^-$, DFT calculations indicate that [EMIM]$^+$ stabilized the reduced species through π^+–π interactions, resulting in more anodic potentials. Furthermore, the computational studies suggest cations associated with the catalyst inhibit the HER *via* electrostatic interactions, resulting in improved selectivity for HCO_2^-.

As diffusion can slow the overall rate of catalysis due to the high viscosity of neat ILs, efforts have been made to immobilize molecular catalysts onto electrodes. These 'heterogenized' catalysts only require consideration of substrate diffusion to the electrode. *Fac*-Re(bpy)$(CO)_3$Cl catalyst was immobilized onto a conductive carbon porous material.[564] Interestingly, the catalyst selectivity changed with the applied catalytic potential. At the most anodic potentials, CO was the dominant product; however, at more cathodic potentials, formic acid was observed. The latter is not normally a product of CO_2 reduction with this catalyst when it is not immobilized and may be due to the local hydrophobic nature of the catalyst support. Formate was also observed as a product in another study under aqueous (non-IL) conditions where this catalyst was immobilized in Nafion.[557] The FE of H_2 also increases with greater concentrations of water. However, smaller amounts of water, down to 1%, led to lower current densities due to the higher viscosity of the solution. Thus, the ideal water content (5%) provided a good optimization between catalyst selectivity (75% FE for CO) and activity. Porphyrin-based catalysts containing Fe and Zn were immobilized onto indium tin oxide electrodes using in a conducting polymer.[565] With $BMImBF_4$ as the solvent under aprotic conditions, the Fe derivative demonstrated the highest faradaic efficiency for CO, with 79.6% and almost 10 TON, which are both higher than freely diffusing catalysts under the same conditions.

Another strategy to impart the positive local impact of imidazolium is to modify the ligand to contain these functionalities in the secondary coordination sphere. In the first study of this type, the bpy ligand in the selective CO_2 reduction catalysts [*fac*-Re(bpy)$(CO)_3$]$^-$ was modified to contain an imidazolium functionality near the bpy ligand.[562] Similar to these catalysts in IL solvents or when IL electrolytes are used, this complex demonstrated an increased catalytic activity and selectivity at more anodic potentials than the unfunctionalized complex. Furthermore, the synthesis of a variant with a methylated imidazolium complex did not demonstrate similar improvements in activity, indicating the acidic C–H is critical to the improved catalysis. DFT studies indicate the imidazolium facilitates the loss of Cl^- required to generate the active catalyst while not impacting the reductive properties of the bpy ligand, as well as facilitating the cleavage of the C–O bond to Re-bound CO_2. These studies were pursued further using imidazolium functionalized *fac*-Mn(bpy)$(CO)_3$ catalysts.[563] Similar to the Re analog, they found that the imidazolium functionalities enhance catalytic activity, resulting in the reduction of CO_2 to CO in the presence of H_2O at much more anodic potentials than the unfunctionalized congener. DFT studies indicated a synergistic interaction between the imidazolium and water molecules, likely due to the acidity of the C–H proton, which can participate in hydrogen-bonding interactions.

In another study, Fe(porphyrin) catalysts were modified to contain four pendant imidazolium cations.[561] In DMF : H_2O 9 : 1 mixture, the first reduction potential that corresponds to the Fe(III/II) reduction event is not impacted, indicating there is minimal inductive effect with the imidazolium functionalities. However, the next two reductive events, which have generally been assigned as ligand-based reductions,[566] exhibit anodic shifts of about 120 and 415 mV, respectively, with the larger shift associated with the third reduction corresponding to the catalytic wave. As a result, the catalytic wave was 375 mV more positive compared to unfunctionalized Fe(TPP)Cl. The placement of the imidazolium fragments on the ligand framework is also important; the addition of four 1-benzyl-3-methyl-imidazolium chlorides with Fe(TPP) exhibits no enhanced catalytic ability. In aqueous phosphate buffer, a higher current is observed despite the fact that CO_2 is only about one-third as soluble compared to DMF. Thus, pre-organizing the IL environment *via* incorporation into the second-coordination sphere leads to the same beneficial anodic shifts and enhanced catalytic activity.

Although studies with molecular catalysts in ILs are still nascent, the mechanisms by which these cations improve catalysis are likely different. For heterogeneous catalysts, imidazolium cations are believed to stabilize the formation of the CO_2 radical anion. However, the catalytic potentials for most homogeneous catalysts are positive of that required to form the radical. Instead, the cations are believed to stabilize the reduced forms of the catalysts through electrostatic interactions.

These stabilizing effects appear to be more pronounced at ligand-based reductions, which can result in π^+–π interactions. Enhanced catalytic rates have been attributed to hydrogen-bonding interactions between the imidazolium C–H and catalyst-carboxylate intermediates to facilitate bond cleavage or otherwise lower transition state structures. As the catalysts that have been studied typically have selectivity for CO_2 reduction in organic solvents, the IL cation's ability to suppress the hydrogen evolution has not been discussed extensively. However, the electrostatic impact of a closely associated imidazolium cation to the catalyst has been suggested as important to suppressing proton approach for hydrogen evolution. Homogeneous catalysts have also been immobilized onto electrode surfaces for use with ILs, although their resulting catalytic behavior may be due to both the IL and the local environment of the catalyst support. Additionally, studies using imidazolium functionalities incorporated into the secondary coordination sphere of molecular catalysts through ligand design demonstrate that the beneficial impacts on catalysis can be replicated through intramolecular interactions.

 This journal is © The Royal Society of Chemistry 2024

Open Access Article. Published on 24 June 2024. Downloaded on 1/17/2026 6:47:09 PM. This article is licensed under a Creative Commons Attribution-NonCommercial 3.0 Unported Licence.

4.5 Technoeconomic analysis

4.5.1 TEA for the CO_2 electrochemical conversion process. Techno-economic analysis (TEA) models have been instrumental in highlighting economically competitive pathways involving CO_2RR, which can then be deployed at an industrial scale to produce carbon-based commodities. In particular, these studies help to inform researchers which products have the most viable pathway to commercialization and what key performance targets must be achieved to enable parity with the present market price. To date, several studies are available on the economic feasibility of aqueous CO_2 electrolysis highlighting the importance of key experimental matrices such as current density, product selectivity, energy efficiency, and electrode stability. The studies specific to RCC are far less developed in comparison to CO_2RR, however, understanding of TEA findings with CO_2RR can provide insight into many of the same economic drivers (*e.g.*, electrolyzer capital expense, electricity costs, seperators, electrode materials, and electrolytes) that would be prominent for RCC.

4.5.2 TEA for single-step CO_2RR products. The simplest TEA assumes that products are made at the cathode in a single reaction step and that the water oxidation at the anode has no value-added anodic byproduct. The economic feasibility of CO_2RR depends on achieving high current density, high FE, and lower operational potential,[567] as examined through simulations (*e.g.*, formic acid as product).[568] The operational cost was found to be extremely sensitive to changes in electricity prices, with a 50% increase resulting in a 25% increase in the levelized cost for C_1 products and more than a 30% increase for C_2 products, respectively.[567] It has been recommended that current density and selectivity should be greater than 300 mA cm^{-2} and 80%, respectively, while keeping the cell voltage lower than 1.8 V. Based on the outcome of TEA studies and corresponding CO_2RR performance at the lab scale, Segets *et al.*[569] summarized key performance parameters and compared them to the current state-of-the-art for three CO_2RR products, *i.e.*, CO, HCOOH, and C_2H_4 (Table 10). The study determined that the achievable current densities and FEs for these products are higher than the minimum they calculated to be required for industrialization, *i.e.*, current density >0.2 A cm^{-2}, FE $>$ 80%. Also, the necessity of progress in the field of full cell potential, energy efficiency, stability, single-pass conversion efficiency, and cost of electricity have been highlighted.

Jouny *et al.*[570] used a TEA study to calculate the end-of-life net present value (NPV) of a generalized CO_2 electrolyzer system for the production of 100 tons/day of various CO_2 reduction products. The authors suggested that current density has a minimum impact on NPV after a threshold value of 200–400 mA cm^{-2} and that the required maximum cell voltage for profitable conditions can vary based on the desired product. In their review, Somoza-Tornos *et al.*[571] emphasized concerns related to the high variability in the CO_2RR product costs estimated *via* different TEA studies. This might be due to the variable input parameters (*e.g.*, price of CO_2 and electricity) and assumptions, and market values of different products during the period of studies.

Besides the economic feasibility of CO and HCOOH products, Shin *et al.*[572] and Gao *et al.*,[573] provided the roadmap for C_2 chemical production by a detailed TEA study. To achieve economic viability for these products, the cell performance required significant improvements to achieve targeted price of \$\$0.53 per kg. This assumed a further reduction in the electricity price to \$\$0.01 kW h^{-1} and improvements in the electrolyzer cost in addition to selling the hydrogen byproduct and using carbon credits. Considering the importance of energy consumption, Leonzio *et al.*[574] assessed that eliminating CO_2 crossover alone could drastically impact these estimations.

4.5.3 Coupling CO_2RR with valuable anodic reactions and tandem electrolysis. Another intriguing pathway to add economic value to the electrochemical CO_2RR is to couple it with other anodic processes besides water oxidation featuring lower standard thermodynamic cell potentials and yielding additional valuable products.[575] This coupling strategy offers a substantial decrease in energy consumption, while making additional marketable products with the same electricity, thereby enhancing the economic viability of CO_2RR. Notably, a study by Verma *et al.*[575] revealed that pairing CO_2RR with glycerol electro-oxidation can reduce energy consumption by up to 53% compared to coupling it with the OER. By employing glycerol electro-oxidation at the anode instead of OER, the onset cell potentials for CO_2 to HCOOH, C_2H_4, and C_2H_5OH production on a copper-coated gas diffusion layer (GDL) cathode were significantly lowered at -0.9, -0.95, and -1.3 V, respectively, compared to OER at the anode (*i.e.*, -1.75, -1.8, and -2.1 V, respectively). This innovative approach holds promise for improving the energetic efficiency and economic feasibility of CO_2RR processes.

Table 10 The key performance parameters based on TEA studies and state-of-the-art performance for the corresponding CO_2RR products (CO, HCOOH & C_2H_4) as extracted from ref. Segets *et al.*[569]

System metric	Key performance parameters	Current state-of-the-art
Current density	>0.2 A cm^{-2}	0.5–1.8 A cm^{-2}
Energy efficiency	$>50\%$	*ca.* 40%
Faradaic efficiency	$>80\%$	80–90%
Full cell potential @ 300 mA cm^{-2}	<3.0 V, better <2.5 V, ideally <2.0 V	2.7 V
Single pass conversion	$>50\%$	30–70%
System temperature	60–90 °C	40–80 °C
Additional notes and challenges:		
Stability	<10 μV h^{-1}	
Cost of electricity	<0.04 USD kW h^{-1}	

Open Access Article. Published on 24 June 2024. Downloaded on 1/17/2026 6:47:09 PM.
This article is licensed under a Creative Commons Attribution-NonCommercial 3.0 Unported Licence.

The CO_2RR can be coupled with numerous other organic oxidation reactions (OORs). Na *et al.*[576] performed a thorough study encompassing 132 768 process calculations to evaluate the economic feasibility of 295 electrochemical coproduction processes. The study indicates that coupling CO_2RR with OORs, mainly 2,5-furandicarboxylic acid (FDCA) and 2-furoic acid, results in making the production of every CO_2RR candidate economically feasible. It should be noted that the increased complexity of the OOR systems, particularly in comparison to the OER, requires intricate multistep separation processes and continuous monitoring of both anodic and cathodic products.[577]

Sisler *et al.*[578] reported a comparative TEA study for C_2H_4 production *via* a single-step CO_2 reduction in an alkaline flow cell, neutral MEA electrolyzers, and a CO_2–CO–C_2H_4 tandem electrolysis process. The TEA study suggested that the CO_2–CO–C_2H_4 tandem process required a significantly lower electrical energy efficiency (52% less) in comparison to the single-step process, and thus it was a more economically viable approach for C_2H_4 production. Similar to the use of multiple electrolyzers in tandem, TEA modeling has indicated that the use of stacked electrolyzers can be beneficial in comparison to a single chamber (SC) electrolyzer. For example, it was reported that an electro-stack electrolyzer achieved CO production at a significantly lower cost of $0.37 per kg compared to $0.41 per kg for the analogous SC electrolyzer.[579] The costs associated with MEA replacement and capital expenses were modestly lower for the stacked electrolyzer system.

4.5.4 Coupling electrochemical and non-electrochemical processes. Spurgeon and Kumar[580] conducted a comparative TEA study of competing CO_2RR routes aimed at producing liquid fuels. For the two-step CO_2 to CO, followed by Fischer–Tropsch synthesis (FTL) to convert syngas to diesel fuel (CO_2–CO–FTL) pathway, the base case levelized cost of fuel (LCF) for diesel fuel was determined to be $18.9 per gasoline gallon equivalent (gge) at the base case conditions, making it economically uncompetitive against the commercial diesel fuel price range of approximately $2.12–3.19 gge. However, optimistic performance parameters notably reduced the LCF to $4.4 gge. Furthermore, assuming a carbon emission offset credit of $100 per metric ton of CO_2, the LCF decreased to $3.5 gge. In a separate study,[581] four competing approaches to producing methyl formate ($HCOOCH_3$) from electrochemical CO_2RR to formic acid in methanol coupled with *in situ* non-electrochemical esterification were examined. These approaches involved different electrolyzers and CO_2 capture processes, showcasing the potential improvements in the levelized cost compared to commercially produced $HCOOCH_3$.

4.5.5 TEA analysis of CO_2 RCC. In a conventional gas electrolyzer, the modelled economic feasibility of CO_2RR products using either ILs or aqueous electrolytes is equivalent, with C1 products retaining profitability.[582] However, the integrated CO_2 capture and conversion process can offer greater benefits compared to involving separate CO_2 capture and conversion processes since the regeneration of the capture agent and release of molecular CO_2 can be bypassed, leading to enhanced energy efficiency and reduced capital costs for the industrialization process.[18] Gao *et al.*[583] have compared the TEA results for an integrated process for syngas production using 1-cyclohexylpiperidine as a CO_2 capture agent against a gas-fed electrolyzer similar to a PEM. The study indicates that RCC technology operated at 0.15 and 0.2 A cm^{-2} has competitive economic benefits due to lower capital cost and energy consumption relative to a GDE system.

In the TEA study conducted by Li *et al.*,[584] they aimed to gain insights into the energy dynamics of both sequential gas feed and integrated CO_2 capture and electrochemical conversion processes. According to their findings, in the base scenario (with CO FE of 70% and cell voltage of 4 V), assuming a 50% single-pass conversion efficiency, the integrated process shows marginal benefits over the sequential process due to the substantial energy demand for CO_2 electrolysis (Fig. 18a). However, under optimistic conditions (with CO FE of 90% and cell voltage of 3 V), and assuming similar CO_2 electrolysis efficiency in both scenarios, the integrated route demonstrates a significant 44% reduction in energy consumption compared to the sequential process. This reduction is primarily attributed to the decreased requirement for thermal energy associated with amine regeneration, as well as the reduced electricity needed for CO_2 compression and product purification (Fig. 18b). The integrated route presents a compelling advantage with a 22% reduction in energy costs compared to the sequential route (Fig. 18c). This significant decrease in energy consumption enhances the attractiveness of the integrated approach. The authors also compared

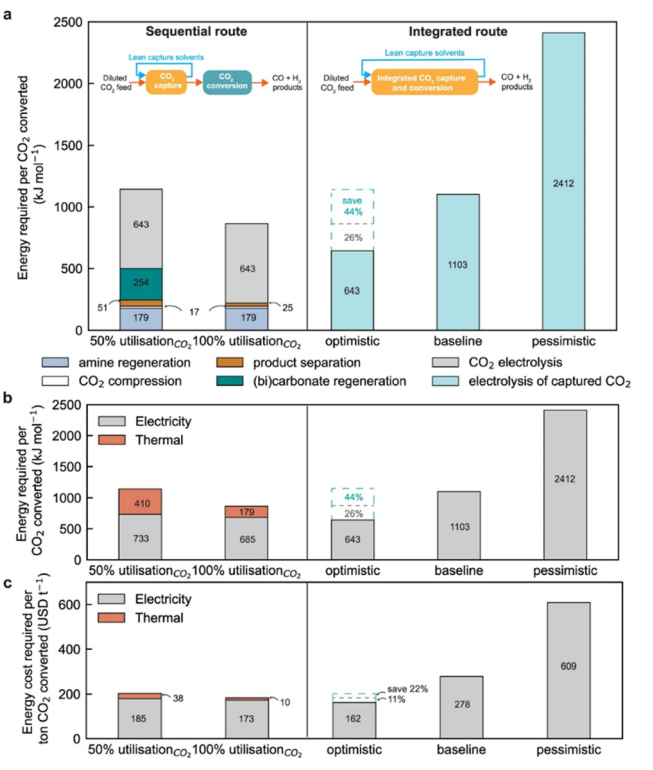

Fig. 18 Energy analysis for sequential and integrated CO_2RR: (a) overall energy consumption and energy requirements for various subprocesses, (b) the breakdown of thermal and electricity consumption, and (c) cost analysis of energy consumption in different scenarios. This data has been adapted with permission from ref. 584 under CC-BY 4.0 licence.

This journal is © The Royal Society of Chemistry 2024

Open Access Article. Published on 24 June 2024. Downloaded on 1/17/2026 6:47:09 PM. This article is licensed under a Creative Commons Attribution-NonCommercial 3.0 Unported Licence.

the energy consumption considering 100% single-pass conversion efficiency for sequential process and optimistic conditions for the integrated process (Fig. 18). Even in this scenario, the integrated approach retains a maximum overall energy advantage of 26% and an energy cost benefit of 11% (Fig. 18).

5. Critical properties for reactive capture and electrochemical conversion of CO_2

This section summarizes the IL/DES properties of interest for CCC, CO_2RR, and RCC, that are discussed at length in previous sections to provide a closure on the main discussions. Fig. 19 captures the critical points highlighted in this section.

5.1 Viscosity and conductivity

The high viscosity of ILs/DESs can hinder mass transfer, potentially limiting CO_2 uptake.[585] The high viscosity of IL/DES contributes to ohmic resistance and, therefore, can limit electrocatalytic CO_2 conversion. Such high viscosity (>100 cP at 25 °C) limits their realization as neat electrolytes for effective RCC.[91,586,587] In comparison, the viscosity of water is 1 cP.

Amine functionalized ILs demonstrate great absorption capacities compared to conventional ILs; however, the bulk viscosities of these ILs dramatically increase upon CO_2 absorption, resulting in a gel-like structure.[90,587,588] The reason behind the significant increase in the viscosity of these ILs following reaction with CO_2 has been extensively studied.[586,589] A detailed molecular dynamic simulation reveals that the substantial rise in viscosity is attributed to the establishment of robust and densely interconnected hydrogen-bonded networks between the zwitterion and di-cation species formed due to the CO_2 reaction with the amino-tailored cation.[94]

The experimental assessment of viscosity changes in amino-functionalized ILs, namely [aP_{4443}][Gly], [aP_{4443}][Ala], [aP_{4443}][Val], and [aP_{4443}][Leu], reveal a diminished CO_2 absorption for all of these ILs (less than 0.2 mol CO_2 per mol IL).[587] This outcome is attributed to an increase in viscosity, which notably reduces CO_2 diffusivity. The $[Ala]^-$ and $[Gly]^-$ anions have been further investigated in a different study paired with the phosphonium cation ($[P_{66614}]^+$), focusing on variations in viscosity following CO_2 absorption.[91] The findings indicated a substantial 48-fold and 117-fold escalation in viscosity at room temperature upon CO_2 absorption for [P_{66614}][Gly] and [P_{66614}][Ala], respectively. This phenomenon is ascribed to the development of hydrogen bond networks within the CO_2-complexed ILs.

Several studies attempted to reduce the viscosity of amino-functionalized ILs by substituting the cation with phosphonium and ammonium cations.[116,590] Despite observing a reduction in the bulk phase viscosity of the IL, the significant increase in viscosity upon CO_2 absorption remains unresolved. In other research, the pronounced increase in viscosity was addressed by strategically eliminating the hydrogen on the amine through anion-functionalization in AHA ILs.[126] This approach prevented

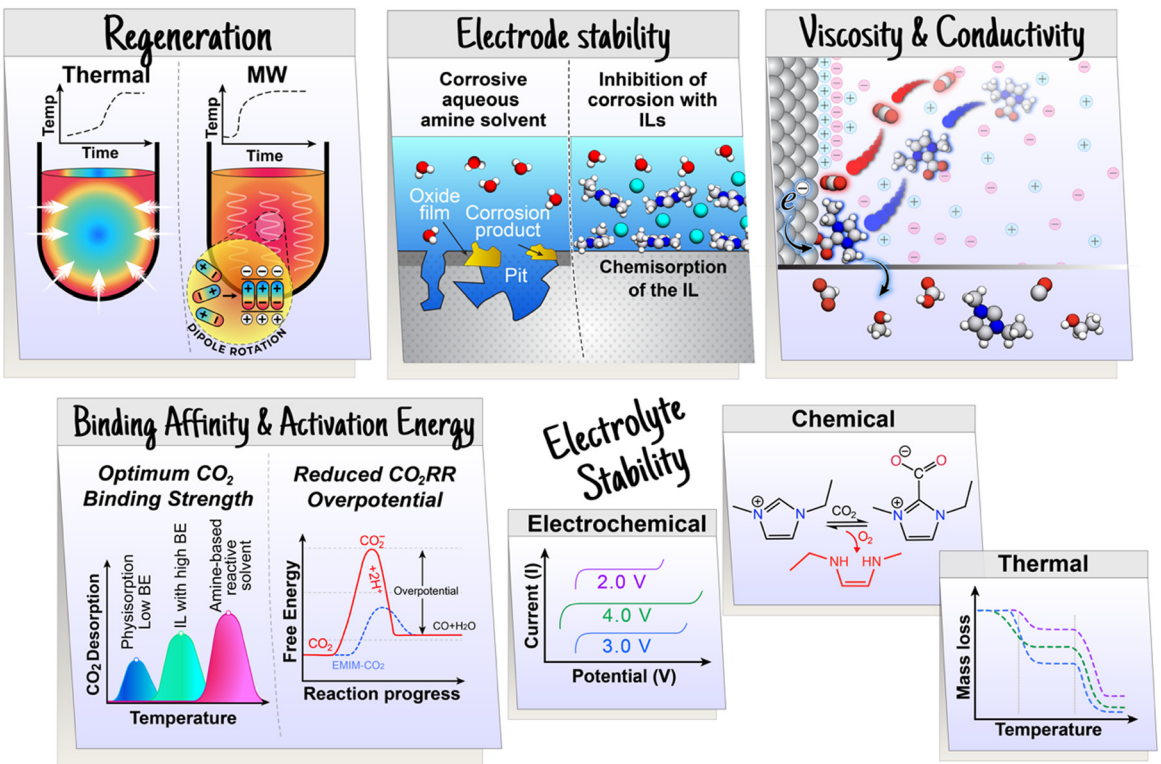

Fig. 19 Schematic illustration of critical properties for RCC.

Open Access Article. Published on 24 June 2024. Downloaded on 1/17/2026 6:47:09 PM.
This article is licensed under a Creative Commons Attribution-NonCommercial 3.0 Unported Licence.

the generation of an acidic proton during the CO_2 and IL reaction, thereby avoiding the formation of intermolecular hydrogen bonds. Despite the high viscosities of the demonstrated AHA ILs (*e.g.*, 370–500 cP at 25 °C), they did not exhibit further increase with CO_2 absorption. Solvents that have lower viscosity tend to be more favorable for CO_2 capture and utilization, as the mass transfer rate is generally higher and pumping costs are lower. In efforts to further reduce the viscosity and increase the gravimetric capacity, AHAs were later paired with smaller phosphonium and ammonium cations,[96] and the imidazolium cation.[453,591] Further, when imidazolium AHA IL was diluted with EG (IL : EG, 1 : 2 molar ratio), thus forming DES, as demonstrated by Lee *et al.*,[160] the viscosity was lowered from 70 to about 45 cP at 25 °C.

Despite these efforts, the viscosities of functionalized ILs and DESs remain high for RCC applications where the transport of CO_2-limiting conditions. Such viscosity-controlled energy losses due to mass transport overpotential and ohmic losses are not overcome by improved CO_2 concentration. Therefore, all of the electrolysis studies within RCC with ILs and DESs to date involve a co-solvent so that appreciable amounts of conversion products can be generated and quantified for reporting product distribution and faradaic efficiencies.

5.2 CO_2 binding affinity

Amine solutions, such as MEA, are used for industrial carbon capture, however, the regeneration of captured CO_2 requires a significant amount of energy input. The considerable energy demand associated with MEA can be largely ascribed to the substantial heat of reaction, reaching up to -85 kJ mol^{-1} of CO_2 at 40 °C.[64] Such high heat of reaction, along with heat losses from water vaporization in the stripper renders them interchangeable. Additional challenges include issues, such as corrosiveness, amine volatilization, and oxidative degradation of the amine.[592] In this regard, the potential of ILs emerges due to their elevated CO_2 capacity and lower enthalpies in comparison to the amine solvents commonly employed in industrial processes for CO_2 capture. The enthalpy associated with the physical absorption of CO_2 by ILs is approximately -20 kJ mol^{-1}. This energy suggests that the energy needed to release CO_2 physically absorbed by ILs during the regeneration step is only a quarter of that required in the amine solution method. Despite this efficiency, the CO_2 absorption capacity of these ILs is limited to around 3 mol% under atmospheric pressure.[593] Functionalizing ILs with CO_2-reactive chemisorption sites enhances the capture capacity of ILs, addressing limitations seen in the physical absorption process, as discussed earlier. Thus, TS-ILs are tailored with specific chemical properties to enhance the interaction and capture of CO_2 molecules, thereby increasing the affinity between the sorbent and CO_2. However, the functionalization of ILs with chemisorption sites significantly increases the heat of sorption (ΔH), resulting in higher energy consumption during regeneration phase.

For instance, the ΔH of two amino functionalized IL, $[P_{66614}][Pro]$ and $[P_{66614}][Met]$, were compared by using the same phosphonium cation.[74] The enthalpies of sorption between amino-functionalized ILs and CO_2 were experimentally measured to be -80 kJ mol^{-1} and -64 kJ mol^{-1} of CO_2, respectively, at 25 °C and 2–3 bar pressure. These results exhibit a noteworthy alignment with the calculated reaction energies for the gas-phase anions, demonstrating that the phosphonium cation has an insignificant effect on ΔH of CO_2 and the absorption of CO_2 is dominated by the anion of the ILs. Another study analyzed the enthalpy of carbamate formation on amino functionalized $[Pro]^-$ and $[Ala]^-$ anions with a different phosphonium cation upon CO_2 absorption.[594] The ΔH value for $[P_{4444}][Pro]$ was -52.8 kJ mol^{-1} compared to $[P_{4444}][Ala]$ at -75.3 kJ mol^{-1}. This difference suggests that the carbamic acid formation reaction is more favorable with $[Ala]^-$, despite $[Pro]^-$-based ILs exhibiting a higher CO_2 uptake. Carbamic acids displayed strong intramolecular hydrogen bonding, contributing to their stability. Additionally, intermolecular hydrogen bonds likely exist between carbamic acids, further enhancing their overall stability. The enthalpy associated with CO_2 absorption in carboxylate functionalized $[P_{66614}][OAc]$ was also determined in the same study through the analysis of the temperature-dependent variation in the natural logarithm of the equilibrium constant. The calculated enthalpy value is -37.6 kJ mol^{-1} between 20–40 °C under 5–30 kPa, indicating a chemical absorption process, yet the heat of absorption is significantly lower than amino functionalized ILs.

A similar calculation of CO_2 absorption enthalpy is conducted on an azolate functionalized IL, $[P_{66614}][2\text{-CNpyr}]$, over the temperature range of 22–55 °C *via* the temperature dependence of equilibrium constants and differential calorimeter.[126] The results were further verified by a first principles G3 calculation. The experimental reaction enthalpy is determined as -53 ± 5 kJ mol^{-1}, with -10 kJ mol^{-1} attributed to the enthalpy of physisorption, aligning with the enthalpy of non-functionalized ILs. The remaining enthalpy is associated with chemisorption facilitated by the functional group of the anion. The results further exhibited an excellent concordance with the G3-computed reaction energy of -49 kJ mol^{-1} for gas phase anion at 25 °C. A different approach is considered by investigating the CO_2 absorption enthalpy of another azolate functionalized IL, 1,1,3,3-tetramethylguanidinium imidazole ([TMG][Im]), at a CO_2 concentration of 15% to mimic the industrial process conditions.[128] The enthalpy of the reaction was determined by exploiting the temperature dependence of equilibrium constants within the range of 30 to 50 °C, yielding a value of -30.3 kJ mol^{-1}. Consequently, the captured CO_2 exhibits greater ease of release. A more comprehensive investigation is undertaken to explore the impact of various AHA anions, specifically indazolide, imidazolide, pyrrolide, pyrazolide, and triazolide, in ILs featuring the phosphonium cation $[P_{66614}]$, on the enthalpy of CO_2 absorption.[138] The reaction enthalpy of the $[Inda]^-$, $[BnIm]^-$, $[6\text{-BrBnIm}]^-$, $[2\text{-SCH}_3\text{BnIm}]^-$, $[2\text{-CNPyr}]^-$, $[3\text{-CF}_3\text{Pyra}]^-$, $[3\text{-CH}_3\text{-5-CF}_3\text{Pyra}]^-$, $[123\text{-Triz}]^-$, and $[124\text{-Trz}]^-$ anions were experimentally determined as -54, -52, -48, -41, -45, -44, -41, -37, and -42 kJ mol^{-1} CO_2 at 22 °C, respectively. It is found that while $[123\text{-Trz}]^-$ has the lowest reaction enthalpy, $[Inda]^-$ has the highest reaction enthalpy among all AHA anions. However, all the AHA ILs demonstrated a significantly lower absorption enthalpy compared to conventional amine solvents, such as MEA, and AEEA,

 This journal is © The Royal Society of Chemistry 2024

Open Access Article. Published on 24 June 2024. Downloaded on 1/17/2026 6:47:09 PM. This article is licensed under a Creative Commons Attribution-NonCommercial 3.0 Unported Licence.

reaching enthalpies of −80 kJ mol^{-1} CO_2 at 40 °C,[64] hence having a potential for CO_2 capture utilization with significantly lower regeneration energy requirement.

The enthalpy of the reaction between the IL and the CO_2 is the main driving force for the capture of CO_2. As a result, higher reaction enthalpies typically result in higher absorption. However, high absorption enthalpy results in challenging desorption along with elevated energy requirements for the regeneration step. Therefore, reducing the enthalpy of reactions on chemisorption dominated absorption is crucial to overcome these issues.

The effects of different substituents on the reaction enthalpy of CO_2 with the ILs having phenolic anions were investigated in a computational study.[143] The geometry and energy optimization of each anion, anion–CO_2 complexes, and gas CO_2 is calculated at the B3LYP/6-31++G(p,d) level. The results demonstrated that the addition of electron-withdrawing groups, such as Cl, to the structure of the phenolate anion decreased the reaction enthalpy. In contrast, addition of the electron-donating groups, such as Me, resulted in an increase in the reaction enthalpy. Hence, the reaction enthalpy of the [P_{66614}][3-Cl-PhO] is calculated as −31.4 kJ mol^{-1}. Conversely, [P_{66614}][4-MeO-PhO] had an enthalpy of −51.4 kJ mol^{-1}. The calculation of Mulliken atomic charge of the oxygen atom further revealed that as the substituent atoms gets more electron-withdrawing, the weaker the charge on the oxygen atom gets. In contrary, increase in the electron-donating ability of the groups leads to an increase in the charge of the oxygen atom of the phenolic anion. The comparison of the [4-Cl-PhO]$^-$, and [2,4,6-Cl-PhO]$^-$ anions show a significant change on the charge of the oxygen atom with the addition of Cl groups, from −0.6833 to −0.6270, respectively. The results observed on the change of reaction enthalpy and charge of oxygen atom showcased the roughly linear correlation between the Mulliken charge of the oxygen atom and enthalpy of CO_2 absorption. Among 13 ILs that were studied, [P_{66614}][4-MeO-PhO] had the highest enthalpy of −51.4 kJ mol^{-1} along with highest Mulliken charge of −0.7062 on the oxygen atom, whereas [P_{66614}][4-NO_2-PhO] had the lowest oxygen charge of −0.6187, therefore, the lowest reaction enthalpy with −17.1 kJ mol^{-1}. Hence, the effect of substituents plays a crucial role in designing ILs having low energy requirement for desorption.

A distinct methodology for fine-tuning the enthalpy and capacity of CO_2 absorption is proposed, involving the modulation of the basicity of ILs.[93] This approach integrates experimental and computational tools to systematically determine the optimum between absorption enthalpy and improved CO_2 capacity. ILs with various functionalization, utilizing the [P_{66614}] cation paired with eight different anions characterized by basicity between 8.2–19.8 pK_a, were investigated. An observable and noteworthy reduction in CO_2 capacity is noted, shifting from 1.02 mol CO_2 per mol IL in [P_{66614}][Pyr] to 0.08 mol CO_2 per mol IL in [P_{66614}][Tetz], correlated with a decline in the pK_a values of the respective weak proton donors in DMSO, dropping from 19.8 to 8.2, respectively. The effect of basicity on the CO_2 absorption enthalpy of ILs is further investigated by calculation of gas-phase reaction energetics at the B3LYP/6-31++G(p,d) level. Comparison of absorption enthalpy between the most and least basic ILs demonstrated a significant difference, with [P_{66614}][Pyr] having −91.0 kJ mol^{-1}, whereas [P_{66614}][Tetz] having −19.1 kJ mol^{-1}, which is in the range of physisorption.[593] However, a decrease in pK_a from 18.6 for [P_{66614}][Im] to 13.9 for [P_{66614}][134-Trz] resulted in only a 5% decrease in CO_2 capacity preserving almost equimolar absorption ability, although a substantial decrease in enthalpy of CO_2 absorption was observed from −89.9 kJ mol^{-1} to −56.4 kJ mol^{-1}. Therefore, the enthalpy of CO_2 absorption in these basic ILs can be systematically adjusted by manipulating their basicity while preserving their absorption capacity. However, steric effects can also be important impacting binding affinity.

A study underscored the significance of considering entropy variations arising from structural differences in anion functionalized ILs.[595] Methylbenzolate-based ILs were synthesized having amino groups both in *ortho*- and *para*-positions. The results indicated that [P_{66614}][*p*-AA] exhibited a CO_2 absorption capacity of 0.94 mole of CO_2 per mole of IL, while [P_{66614}][*o*-AA] showed a lower capacity of 0.60 mole of CO_2 per mole of IL at 30 °C. Notably, the Mulliken charge analysis of the N atom in these ILs revealed that [*o*-AA] had a stronger interaction with CO_2 (Mulliken charge: −0.584) compared to [*p*-AA] (Mulliken charge: −0.529), suggesting higher absorption enthalpy. However, the unexpected increase in CO_2 absorption capacity from [P_{66614}][*o*-AA] to [P_{66614}][*p*-AA] was attributed to the entropic effect, challenging the conventional enthalpy-driven perspective in CO_2 capture. The computation of the enthalpy of CO_2 absorption in these ILs indicated that the IL with the amino group in the *para*-position exhibited an enthalpy of −41 kJ mol^{-1}. This value marked a notable decrease from −56 kJ mol^{-1} observed when the amino group was positioned *ortho*-, all while maintaining its equimolar CO_2 absorption capacity. Therefore, the higher CO_2 capacity and the lower enthalpy of the [P_{66614}][*p*-AA] is attributed to the difference in the formation of intermolecular hydrogen bonding as a result of entropic differences. These differences emphasize the importance of considering both enthalpy and entropy in the Gibbs free energy calculation for a more comprehensive understanding of CO_2 capture mechanisms.

The importance of hydrogen bonding and the proton activity in DESs (Section 2.4) was also highlighted in a series of publications by the Gurkan group.[149,160,165,166] Similar to ILs, basicity and steric effects are both at play in governing the CO_2 absorption strength in DESs, which ultimately impact the regeneration energy in CO_2 capture. This, again, is an important concept for RCC since the CO_2 bound on an IL ion or DES component in the electrolyte needs to be released at the electrode surface for hydrogenation and C–C coupling without the consumption of the IL/DES.

In summary, although functionalized ILs offers significant enhancements to the CO_2 absorption capacity compared to the conventional ILs, the increase in enthalpy of the CO_2 absorption can be very drastic due to the high exothermic effect of chemisorption of CO_2 on the reactive functionalized sites, reaching enthalpies as high as −80 to 90 kJ mol^{-1}.[74] Modifications such as addition of substituent groups, changing the

Open Access Article. Published on 24 June 2024. Downloaded on 1/17/2026 6:47:09 PM. This article is licensed under a Creative Commons Attribution-NonCommercial 3.0 Unported Licence.

basicity, and consideration of entropic effects, are pivotal in fine-tuning the enthalpy of CO_2 absorption when designing high capacity ILs/DESs for CO_2 absorption, facilitating the ease of regeneration as well as recovery in RCC.

5.3 Regeneration energy and other factors impacting cyclability

The primary determinants of the effectiveness of absorbents include the CO_2 capacities and regenerability. An absorbent exhibiting a substantial heat of reaction implies a correspondingly significant energy requirement for its decomplexation during regeneration. However, the heat of reaction, or enthalpy of reaction, is linked to CO_2 capacity, as indicated by the equation $\ln(K) = -\Delta G/RT$, where K represents the equilibrium constant for the complexation reaction, and ΔG denotes the Gibbs free energy change. The relationship is further delineated by $\Delta G = \Delta H - T\Delta S$ where ΔH is the CO_2 absorption enthalpy, ΔS is the change in entropy associated with CO_2 absorption, and T is the temperature. Consequently, a trade-off arises between the desire for enhanced CO_2 capacity at a specific temperature and the preference to minimize the heat required for reversing the reaction. Hence, evaluation of regeneration performance of functionalized ILs is critical, given their higher reaction enthalpies compared to conventional ILs. The same thermodynamic principles apply to DESs. In both cases, functionalization leads to a higher thermal energy requirement for regeneration of the sorbents.

The regeneration of an amino-functionalized IL, [BMIM][Gly], is assessed through the measurement of CO_2 sorption at 25 °C and 0.9 bar, followed by vacuum treatment for 1 hour at 25 °C in each of 5 consecutive cycles.[115] The results indicated that [BMIM][Gly] could be desorbed effectively within 1 hour under the conditions tested and the CO_2 absorption capacity exhibited no significant variations across five consecutive cycles (retained capacity of 95.4% after the fifth cycle). The slight decrease in the capacity was attributed to the marginally imperfect desorption of CO_2 under the tested conditions. In another study, the regeneration performance of the amino-functionalized IL, 1-aminoethyl-2,3-dimethylimidazolium taurine ([AEMMIM][Tau]) was assessed over six consecutive absorption–desorption cycles.[596] The findings revealed an approximate 5% reduction in the absorption capacity of the IL when desorption occurred at 80 °C under 20 Pa, indicating the regenerability of the IL, particularly under slightly elevated temperatures.

A more comprehensive investigation of the effect of temperature on the regeneration on amino functionalized [APMIM][Lys] was conducted by changing the regeneration temperature between 90 and 120 °C.[597] It was found that the reabsorption loading increased with higher regeneration temperatures. The regeneration efficiency fluctuated between 79.0 and 84.4% as the temperature was increased from 90 to 110 °C, suggesting incomplete regeneration. However, [APmim][Lys] achieved a regeneration efficiency of 99.6% at 120 °C, establishing it as the optimal regeneration temperature. Subsequently, the results of five absorption–desorption cycle at 120 °C illustrated the regeneration efficiency of CO_2 in the saturated [APMIM][Lys] solution, which ranged between 99.1 and 100%. The regeneration performance of [APMIM][Lys] is compared with the widely used amine solvent MEA over 5 cycles. MEA, in contrast, could only preserve 81% of its initial absorption capacity (0.46 mol of CO_2 per mol of MEA),[598] highlighting the potential of [APMIM][Lys] as an absorbent for repetitive cycles.

The regeneration of carboxylate-functionalized ILs was investigated utilizing a 1:1 $[P_{4444}][HCO_2]/H_2O$ and $[P_{2228}][CH_3CO_2]/H_2O$ mixture as CO_2 capture media.[599] The IL/H_2O mixtures underwent regeneration at 70 °C by flowing dry N_2 or air through a stirred liquid mixture for 15 minutes. The results demonstrated complete regeneration (100%) for the $[P_{4444}][HCO_2]$ system and 90% regeneration for the $[P_{2228}][CH_3CO_2]$ system after two absorption–desorption cycles.

A comprehensive analysis of the regeneration process for an azolate-functionalized ionic liquid, [TMG][Im], was conducted using IR spectroscopy.[128] IR spectra were obtained for CO_2-flowed [TMG][Im] at 35 °C for 40 minutes, and N_2-bubbled [TMG][Im] at 65 °C for 30 minutes following absorption. The CO_2-free [TMG][Im] and regenerated [TMG][Im] did not exhibit any differences in their IR spectra, while additional carbonyl peaks were observed in the CO_2-absorbed [TMG][Im]. Furthermore, a five-cycle absorption–desorption process resulted in a ±5% change in the CO_2 capture capacity of [TMG][Im], indicating the successful regeneration of the IL.

Co-absorption of water and other impurities from CO_2 sources such as oxygen in DAC applications, can alter the reaction mechanism in functionalized ILs and DESs, and hence the regeneration energy and absorption–desorption cyclability. In fact, there are very few studies that demonstrate cycling beyond 5 to 10. Further, the side reactions leading to thermal and oxidative degradation in ILs/DESs are not well understood. The side reactions can be accelerated during regeneration with the elevation of temperature and co-adsorption of water, O_2, and other gases. Oxidative degradation has been reported for amine functionalized adsorbents, such as aminosilane.[600] Further, poly(ethylenimine) is reported to readily oxidize with increased temperature due to the presence of secondary amines.[601] Recently, the role of water on the oxidative degradation of solid amine sorbents including supported poly(ethylenimine) has recently been reported by Jones and colleagues.[602] They report a radical mediated autooxidative degradation mechanism that is accelerated by water. DES and IL solvents share common structural motifs to these previously studied amines and therefore similar oxidation mechanisms may occur. Lee *et al.* reported radical and S_N2 side reactions that occur in functionalized IL [EMIM][2-CNpyr], due primarily to the nucleophilic anion, that degrade the sorbent to lose 50% of its CO_2 capacity after exposure to oxygen at 80 °C continuously for a week.[51] Despite the reported loss in capacity, the functionalized IL demonstrate superior stability compared to the solid amines where CO_2 capacity loss in the orders of 80% and 61% have been reported under dry air at 120 °C[71] and 80 °C[72] for 7 days, respectively.

Most DESs and ILs are hygroscopic, similar to salts. While the absorbed water improves transport and CO_2 uptake

 This journal is © The Royal Society of Chemistry 2024

Open Access Article. Published on 24 June 2024. Downloaded on 1/17/2026 6:47:09 PM.
This article is licensed under a Creative Commons Attribution-NonCommercial 3.0 Unported Licence.

capacity, it is not desirable from the point of view of thermal regeneration and the energy cost. For instance, absorbed water reacts with CO_2 in the presence of a base such as in the functionalized systems, thus forming bicarbonate, which is energetically less favorable to release CO_2 compared to CO_2-IL complexes. Lee *et al.*[263] measured the CO_2 capacity of the reactive IL, [EMIM][2-CNpyr], as a function of CO_2 feed and relative humidity. While the viscosity was seen to decrease, CO_2 capacity increased slightly with increasing relative humidity hence the increasing water content. The increase in capacity is due to the additional CO_2 absorbed by the water. Similar chemistry occurs in an amine functionalized DESs.[160] The common DES ethaline absorbs about 6 wt% water when exposed to air[603] and maintains its H-bonding network up to 30 wt% water,[604] beyond which it becomes a simple solution. The reactive IL, [EMIM][2-CNpyr], was mixed with ethylene glycol to achieve a functionalized DES, in another study by Lee *et al.*[160] The authors reported induced electrostatics as a result of H-bonding, as demonstrates by DFT calculations of the reaction pathways where the CO_2 binding energies were reduced, compared to the IL itself, thereby enabling regeneration at 40 °C after absorption at 25 °C. On the other hand, these types of DESs present lower thermal stabilities, compared to ILs, as the volatile component evaporates at elevated temperatures. Further, the amount of sorbed water can influence the phase behavior in addition to the transport properties and the CO_2 capacities.

Considering the high heat capacity of water, it is desirable to eliminate its co-absorption with CO_2 sorbents through the inclusion of hydrophobic moieties in reactive solvents and hydrophobic film barriers or supports in composites for RCC. In fact, the presence of water is detrimental for most solid sorbents such as zeolites and MOFs, thus necessitating a pre-absorption column to first remove water from the gas mixture. On the other hand, water is tolerable with ILs, DESs, and their composites where the reaction mechanism, absorption capacity, transport properties, and regeneration temperature may be affected without loss of performance. Lee *et al.*[190] demonstrated a one-to-one comparison of the breakthrough performance of an encapsulated reactive IL (an example of an ENIL) and zeolite 13× where the zeolite lost its CO_2 selectivity completely with co-absorption of water and the ENIL demonstrated maintained selectivity accompanied with improved CO_2 capacity. However, the mass transfer limitation in ENIL breakthrough curves was apparent in the presence of water in addition to the need for increasing the regeneration temperature from 40 to 90 °C.

In contrast to the notion of molecular and composite designs for increased hydrophobicity to suppress water effects, Lackner and colleagues[13,43,44] demonstrated a moisture-swing regeneration that is based on quaternary ammonium hydroxide resins where the CO_2 is absorbed under water-lean conditions and released under water-rich conditions. Further, they coupled this approach with the conventional thermal-swing regeneration in an effort to minimize the regeneration energetics and improve the CO_2 desorption rates.

The issue of high energy consumption during thermal solvent regeneration may also be circumvented by dielectric heating by irradiation instead of conventional thermal heating by convection. A faster CO_2 release was reported in aqueous amines by the use of microwaves.[49] Microwave regeneration of dry alkanolamines is reported to decrease the energy requirement by 10-fold.[50] Similarly, the dielectric response was increased with the number of amine functional groups in mesoporous silica which resulted in 4-fold increase in adsorbent regeneration rate.[605] The proof of concept on the utility of dielectric heating for solvent regeneration was recently demonstrated for functionalized ILs and DESs.[51,165] In particular, the absorption–desorption cyclability of [EMIM][2-CNpyr] up to 10 cycles was possible with microwaves.[51] The authors reported improved cycling efficiency in comparison to conventional thermal heating. They also noted the prospects of improved stability since the exposure to elevated temperatures that accelerate degradation kinetics are suppressed with the dielectric heating approach.

In summary, functionalized ILs and DESs demand more energy-intensive regeneration processes, primarily attributed to their high level of chemisorption from reactive functional groups, as compared to conventional ILs and DESs. However, in contrast to conventional amine solvents like MEA, functionalized ILs/DESs exhibit superior regenerability across repetitive absorption–desorption cycles. Nevertheless, it is noteworthy that amine-functionalized ILs/DESs necessitate more energy-intensive regeneration steps compared to carboxylate and azolate functionalized ones, primarily due to their higher enthalpy of reaction. Therefore, there is a tradeoff between high CO_2 capacity/selectivity and the required regeneration energy. As a result, sorbents for applications such as DAC where very high CO_2 capacities and selectivities are needed. Key performance indicators will be the ease of regeneration with a maintained working capacity, stability, and cyclability. The sorbent regeneration step contributes the most to the operating cost of CO_2 removal processes, and thus further optimization of the capture and regeneration energetics of the chemically and thermally stable ILs and DESs must be pursued.

5.4 Stability of functional electrolytes during RCC

The stability of the functional electrolyte in RCC signifies that performance indicators (*e.g.*, CO_2 uptake, solvent regeneration, mass transfer, faradaic efficiency, current density, conversion, and energy efficiency) must be preserved during long-term operation without significant decay. Better stability corresponds to lower maintenance and replacement costs associated with the consumption of catalysts, electrodes, exchange membranes, and electrolytes. In this subsection, the stability issues of functional solvents/electrolytes, both chemical and electrochemical, are reviewed under RCC conditions.

The main sources of industrial CO_2, such as power plants and petroleum industries, contain impurities. The flue gas from typical coal-fired power plants consists of 13% CO_2, 68% N_2, 16% water, 3% O_2, and other residuals such as hydrocarbons, NO_x, SO_x, H_2S, particulates, mercury, and chlorides.[606] The exposure of small amount of O_2, water, NO_x, SO_x, and H_2S has significant impact on the stability of functional CO_2 capture solvents. Some of these impurities strongly bind with the functional solvents and poison the catalyst with preferential

Open Access Article. Published on 24 June 2024. Downloaded on 1/17/2026 6:47:09 PM. This article is licensed under a Creative Commons Attribution-NonCommercial 3.0 Unported Licence.

adsorption. ILs with fluorine-containing anions (*e.g.*, $[BF_4]^-$, $[PF_6]^-$) have been very popular for CO_2RR studies in the last few years; however, such anions may undergo hydrolysis, forming hydrofluoric acid,[607] which is highly corrosive. This reactivity is particularly inconvenient for treating exhaust gases arising from combustion processes, which can contain as much as 10% water. As a result, utilizing anions that are hydrogen-bond acceptors thus strongly interacting with water can result in weakened cation–anion interactions in imidazolium-based ILs.[132] These intermolecular changes influence the RCC reaction mechanism, CO_2 uptake capacity, and CO_2 binding mechanism and strength. In addition, higher amounts of water in ILs also favor the formation of H_2 over the reduction of CO_2 species, highlighting the multiple effects of water on the stability and performance of ILs for RCC.

Imidazolium based ILs are considered co-catalysts for CO_2 electrolysis, however, reactions involving imidazolium cations can impede RCC. Under moderately basic conditions, imidazolium can undergo deprotonation at the weakly acidic C2 position and the generated nucleophilic N-heterocyclic carbenes can react with aldehydes, sulfur, H_2S, and CO_2.[608] This reactivity is also true under the negative applied potentials since imidazolium is reduced to form a carbene with a an electron transfer reaction, which then combines with CO_2 available in the bulk and generates $[EMIM]^+$-CO_2^- complex. This complex is reported as an inactive CO_2RR byproduct due to the strong energy requirements to break $[EMIM]^+$-CO_2^- bonds. However, the presence of some water can reactivate $[EMIM]^+$-CO_2^- complexes during RCC to dramatically increase CO_2 reduction rates.[432]

Further, the presence of sulfur impurities in the CO_2-stream has the capacity to chemically interact with the n-heterocyclic carbene generated by a single electron reduction of imidazolium and form imidazole-2-thiones.[609] The sulfur-containing complexes have been shown to cause significant metal surface poisoning which would negatively impact on the RCC performance. However, most of the existing RCC studies is centered on CO_2 capture from the pure CO_2 stream or CO_2 diluted in inert gas and their subsequent conversion, and almost no studies have considered SO_2 or similar acidic gases potentially present in real flue gas. Therefore, additional studies are required to evaluate the potential effects of these impurities during the electrolysis step.

Aside from the chemical side reactions, the electrochemical stability window (the difference in voltage between the onset potentials of oxidation and reduction reactions of the electrolyte itself) is a critical property. The electrochemical stability window of ILs depends not only on the chemical structure, but also on the electrode materials. The exact determination of the stability window is also dependent on the sweep rate of the potential, temperature, atmosphere, and impurities. In general, ILs are reported to have high electrochemical stability compared to that of conventional solvents. However, the presence of trace amounts of unavoidable impurities limit their electrochemical windows.[610] Most of the literature reports IL stability using an inert glassy carbon electrode. However, for electrocatalysis, active metal or metal oxide electrodes are more relevant to consider. For instance, Dongare *et al.*[467] observed earlier cathodic degradation of [EMIM][2-CNpyr] on Ag (−2.3 V *vs.* Ag/Ag^+), Au (−2.1 V *vs.* Ag/Ag^+), Sn (−2.05 V *vs.* Ag/Ag^+), in comparison to glassy carbon (−2.45 V *vs.* Ag/Ag^+). The anodic degradation was observed to start from 0.5 V *vs.* Ag/Ag^+ on an Ag surface. Additionally, they confirmed the anodic degradation of [EMIM][2-CNpyr] on Pt and carbon rod, noting a color change of IL from light yellow to dark brown during the bulk electrolysis experiment conducted at −2.1 V *vs.* Ag/Ag^+. Such degradation products could crossover during the RCC; hence, ILs with nucleophilic anions should be avoided in the anolyte. Furthermore, authors also reported increased HER when the aqueous anolyte was used with the non-aqueous catholyte containing the CO_2-reactive IL. The increase in HER current was attributed to the crossover of H^+ from the anolyte to the catholyte. To address these issues, the strategy of integrated electrolysis (coupled/paired electrolysis or co-electrolysis) has emerged in recent years, where the aqueous electrolytes at the anode side is replaced with other oxidation reactions such as electrooxidation of glycerol[611] or methanol.[612]

Further, CO_2 electroreduction takes place at potentials that are very close to the cathodic limit of most ILs. Therefore, qualitative and quantitative in-depth investigations of the cathodic stability of ILs are necessary. Recently, Michez *et al.*[491] reported the stability of $[BMIM][NTf_2]$ by studying its reductive decomposition on Au electrodes. Using NMR and gas chromatography, they confirmed the formation of the neutral dimers by recombination of two imidazole-2-yl radicals (generated by $1e^-$ transfer to imidazolium cation) with >80% FE at −2.5 V *vs.* Fc^+/Fc. Despite the general recognition of ILs as highly stable electrolytes, the cathodic limit is relevant to examine as it can significantly impact the performance of CO_2 electrolysis.

5.5. Electrode stability

Various materials ranging from pure metals to SACs are being explored for their potential use in RCC systems, each offering distinct advantages. However, their long term thermal and electrochemical stability must also be considered for practical implementation. Electrodes used in CO_2RR undergo various stability issues including corrosion, surface passivation, and catalyst deactivation due to chemical reactions with CO_2, water, and electrolyte salts, which degrade the electrode surface and diminish performance overtime. In the context of stability challenges present in aqueous electrolytes, ILs offer improved durability and composition control by mitigating surface restructuring and corrosion that would occur at more negative potentials and higher temperatures. For example, the work by Parada *et al.*, demonstrated corrosion resistance properties of imidazolium based ILs through a process called 'solid catalyst ionic liquid layer' that shielded electrodes from degradation by forming stable passivation layers on the surface.[613] For electrode materials encountering low catalytic activity, ILs can alleviate these issues by providing a conductive environment and increasing CO_2 concentration at the electrode surface. Moreover, tailored solvent–solute interactions in ILs can stabilize catalytic active sites and inhibit undesirable side reactions, enhancing catalyst efficiency and selectivity.

 This journal is © The Royal Society of Chemistry 2024

Open Access Article. Published on 24 June 2024. Downloaded on 1/17/2026 6:47:09 PM. This article is licensed under a Creative Commons Attribution-NonCommercial 3.0 Unported Licence.

6. Conclusions and outlook

This review summarizes the recent advancements and offers a perspective in the reactive capture and thermal and electrochemical conversion of CO_2, with a specific focus on the roles of the functional ILs and DESs as the capture agents as well as the catalysts and the electrolyte media. Specific advantages of these solvents according to their molecular design are discussed in the context of the state-of-the-art CO_2 capture figures of merit. While there has been significant progress in improving the CO_2 capacity of ILs and DESs for separations and conversion by thermal catalysis, utilization of these solvents for RCC is relatively recent. Therefore, there is still a need to pursue research on the specific reaction mechanisms and the compatibility of ILs and DESs with the electrode materials in terms of understanding stability, interfacial structure, and surface adsorption as they relate to the thermodynamics and kinetics of RCC. These studies will assist in advancing functional electrolytes and electrolyzer design simultaneously.

As most ILs and DESs demonstrate increased viscosity with CO_2 saturation, thus limiting the mass transfer processes, they are commonly supported through porous materials to increase gas–liquid surface area and improve transport properties without compromising the CO_2 capacities. Among the various support structures investigated for CO_2 capture with ILs, MOFs have been of interest also as an active material for tuning the CO_2RR selectivity with high current densities. To date, a few of the MOFs, mostly those with Cu and Zn,[446,614] have been investigated due to the availability of multiple active sites exposed for CO_2 binding. Furthermore, when these MOFs are wetted by IL electrolytes, there is believed to be increased availability of CO_2 and longer residence time for reaction intermediates on the surface, thus enabling multi electron transfer reactions. Therefore, these types of materials could be interesting to further explore as catalysts in RCC.

Despite advancement in ILs, DESs, and composites based on these liquids with porous supports, the current state of the CO_2 capture field necessitates improved solvents/sorbents for simultaneous achievement of high CO_2 capacities, fast transport, non-thermal or low energy for regeneration, and long-term stability under high oxygen and humidity conditions, as underscored by the 2019 NASEM report on NET and Reliable Sequestration.[615] To advance the discoveries toward this goal, besides the simulations and ML approaches, the characterization of the gas–liquid, gas–solid, and liquid–solid interfaces as well as temporal changes in these interfaces are quite important. For the composites, the interactions taking place between the IL molecules and the surface of porous material are critical factors governing affinity-based capture and CO_2 transport. The presence of the IL can alter several characteristics of the support material, such as morphology, surface area, pore volume, and thermal stability. Concomitantly, when the IL coating on the porous material is thin, the properties of the liquid layer might be significantly different compared to the bulk. The structural changes in the IL associated with the presence of a surface and surface-specific interactions can further result in kinetic effects. For example, the confinement of ILs,[616] has been discussed to impact liquid structure and dynamics where deviations from the bulk have been reported, such as faster molecular motion near walls.[617] Usually, confinement is defined by the relative size of the confining structure with respect to the molecular dimension of the liquid. ILs with approximately 1 nm ion size are said to be confined when they are in a 10 nm-sized pore. The examination of such buried interfaces in these length-scales with nm-scale resolution is often difficult, especially as they evolve during absorption–desorption events, thus necessitating the utilization of advanced *in situ* characterization techniques. Furthermore, most experimental research on IL/DES based hybrid materials has been directed towards enhancing CO_2 capture and separation performance in pure gas composition under dry conditions; however, practical applications involve gas mixtures with N_2, O_2, and moisture, which significantly impact the material's overall performance and stability. Future efforts need to prioritize testing with multi-component gas mixtures, reflecting real-world conditions, and incorporate moisture to understand how water impacts both CO_2 capture efficiency, potential regeneration processes, and the corresponding lifetime of the material under operation conditions. These assessments are also relevant for RCC processes as direct utilization of CO_2 from the capture media present the possibility of co-absorbed impurities from the CO_2 source and their side reactions.

Regarding the use of ILs and DESs for the thermal conversion of CO_2 into valuable products, determination of the structural factors controlling the thermal stability limits is crucial. These limits can largely deviate from those of the bulk liquids when there are direct interactions with the surface of the support. Concomitantly, these interactions become even more significant in the presence of a metal complex or a metal nanoparticle in the catalyst structure. In such cases, ILs and DESs can substantially alter the electronic structure on the active metal centers. Hence, the research should be directed towards elucidating these interactions and their consequences on the catalytic properties.

In review of the electrocatalytic conversion of CO_2 using functional ILs and DESs, the most critical challenge is the high viscosity of these liquids as electrolytes. While high faradaic efficiencies and lower overpotentials were possible under controlled experimental conditions, the obtained current densities have been typically very low (<25 mA cm^{-2}), therefore, the overall performance still needs improvements to be industrially relevant. The high viscosities impede mass transport of CO_2 or the CO_2 carrying specie to the electrode surface. ILs, even in dilution, present interfacial structuring that increases resistance. Therefore, there is an interplay between the increased IL concentration for increased CO_2 availability and the increased interfacial resistance due to IL ion accumulation in controlling the current density and CO_2 conversion rates. Additionally, in cases where CO_2 is captured in carboxylate form, it is not electrochemically active, hence the utilization of the captured CO_2 remains limited. As a result, further studies are needed to investigate the behavior of carboxylate adducts at the interface and develop solutions to unlock their electrochemical utilization. Some of the transport challenges can also be

Open Access Article. Published on 24 June 2024. Downloaded on 1/17/2026 6:47:09 PM. This article is licensed under a Creative Commons Attribution-NonCommercial 3.0 Unported Licence.

addressed through the RCC electrolyzer design, aiming for high liquid-phase CO_2-adduct species mass flux to the active catalyst by forced convection through highly porous foam cathodes to enable operation at simultaneously high current density and selectivity. The electrolyte stability, evolution in interfacial resistance, and the cross-over through the separator are critical parameters to examine further for practical RCC electrolyzers.

Returning back to the fundamental aspects, answers to several scientific questions remain incomplete: How do ILs and DESs alter the interfacial microenvironment? What are the critical elements of the microenvironment that enables the capture CO_2 to be reduced at potentials and rates that are feasible for scalable RCC? How does the hydrogen bonding in the electrolyte affect the CO_2 reduction energetics and mechanisms? How can the change in the interfacial pH in the presence of ILs and DESs be assessed? How do ILs/DESs influence the electric field on the electrode surface? The answers to these questions will help advance the state of functional electrolytes for RCC.

Author contributions

S. D. and B. G. created the outline of this review, wrote the original draft, and edited; B. G. managed the project. A. S. A., S. F. K. O., S. K., and A. U., contributed to Sections 2.1–2.3 (CO_2 capture) and led Section 3 (thermal conversion). M. Z. wrote Section 2.5 (composites), contributed to Section 5 (sorbent properties), and oversaw the discussions and editing in Section 2 (CO_2 capture). R. D. wrote Sections 2.4 and 2.5 and constructed tables (CO_2 capture with DESs); O. K. C wrote Section 4.2.4 (thermodynamics & kinetics) and 4.2.5 (microenvironments); M. M. contributed to Section 5 (electrolyte properties) and created all of the original graphics. A. B., M. G. C. G. M.-G., and J. M. S. wrote Section 4.3 (electrolyzers). R. D. R. and C. H. contributed to Section 4.2.4 (Tafel slope and turn over frequencies); J. S. S. and J. Y. Y. wrote Section 4.4 (homogenous catalysts); R. S. B. and J. M. V. wrote Section 4.1 (electrodes) and 5.5 (electrode stability); R. L. S. contributed to editing of the manuscript. B. M. and B. K. wrote Section 4.5 (technoeconomic analysis) with contributions from J. M. S. All authors discussed, edited, and reviewed the manuscript before submission.

List of abbreviations

AFIL	1-(3-Aminopropl)-3-methylimidazolium chloride
Ag NPs	Silver nanoparticles
Ag/Ag^+	Silver/silver nitrate reference electrode
AHA	Aprotic heterocyclic anions
AMP	2-Amino-2-methyl-1-propanol
CCC	CO_2 capture and concentration
CD	Current density
CDR	CO_2 removal
$*C_2O_4^{2-}$	Adsorbed oxalate
*CO	Adsorbed CO
$CO_2^{\bullet-}$	CO_2 anion radical
CO_2RR	Electrolytic CO_2 reduction reactions
CO_3^{2-}	Carbonate anion
COFs	Covalent organic frameworks
CP	Carbon paper
CuO	Cupric oxide
DAC	Direct air capture
DBU	1,8-Diazabicyclo[5.4.0]undec-7-ene
DES	Deep eutectic solvents
DETA	Diethylenetriamine
DFT	Density functional theory
DMSO	Dimethyl sulphoxide
eCCC	Electrochemical CO_2 capture and concentration
ECSA	Electrochemical active surface area
EDA	Electron donor–acceptor
EG	Ethylene glycol
Eim	1-Ethylimidazole
ENILs	Encapsulated ionic liquids
E_{ve}	Electrolysis potential/actual potential applied
E^0_{ve}	Theoretical thermodynamic potential
Fc/Fc^+	Ferrocenium/ferrocene reference potential
FE	Faradaic efficiency
FTIR	Fourier-transform infrared spectroscopy
GCMC	Grand Canonical Monte Carlo
GDE	Gas diffusion electrode
HBA	Hydrogen bond acceptor
HBD	Hydrogen bond donor
HCO_3^-	Bicarbonate anion
$HCOO^-$	Formate
HCOOH	Formic acid
HER	Hydrogen evaluation reaction
HNIW	2,4,6,8,10,12-Hexanitro-2,4,6,8,10,12-hexaazaisowurtzitane
HRMAS NMR	High resolution magic angle spinning nuclear magnetic resonance
ILPMs	Ionic liquid polymer membranes
ILs	Ionic liquids
KCl	Potassium chloride
$KHCO_3$	Potassium bicarbonate
KOH	Potassium hydroxide
LTTMs	Low-transition-temperature mixtures
MEA	Monoethanolamine
MMMs	Mixed matrix membranes
MOFs	Metal–organic frameworks
MoS_2	Molybdenum disulfide
NH_3	Ammonia
NH_4HCO_3	Ammonium bicarbonate
NHE	Normal hydrogen electrode
NPCA	N,P-Co-doped carbon aerogel
OH^-	Hydroxide ions
PEI	Poly(ethylenimine)
P-ILs	Protic ionic liquids
PMMA	Poly(methyl methacrylate)

 This journal is © The Royal Society of Chemistry 2024

Open Access Article. Published on 24 June 2024. Downloaded on 1/17/2026 6:47:09 PM. This article is licensed under a Creative Commons Attribution-NonCommercial 3.0 Unported Licence.

PSA	Pressure-swing adsorption/absorption
RCC	Reactive capture and conversion
RCE	Rotating cylinder electrode
reline	DES formed by choline chloride and urea
rGA	Reduced graphene aerogel
RWGS	Rreverse water gas shift reaction
SFG	Sum frequency generation
SHE	Standard hydrogen electrode
SILMs	Supported ionic liquid membranes
SILP	Supported ionic liquid phase
SPS-IL	Switchable polarity ionic liquids
TEAP	Tetraethylammonium perchlorate
TFE	Trifluoroethanol
TNT	2,4,6-Trinitrotoluene
TOF	Turnover frequencies
TSA	Temperature-swing adsorption/ absorption
TS-IL	Task-specific ionic liquid
VFT	Vogel–Fulcher–Tammann
WE	Working electrode
ZIF	Zeolitic imidazolate frameworks
Zn–BTC	Zn-1,3,5-benzenetricarboxylic acid
[124-Trz]-CO_2^-	CO_2 bind to 124-triazole anion to form carbamate
[123-Trz]$^-$	123-Triazolate
[2-CNpyr]$^-$	2-Cyanopyrrolide anion
[Ala]$^-$	Alaninate
[AEMMIM][Tau]	1-Aminoethyl-2, 3-dimethylimidazolium taurine
[aP_{4443}][Ala]	(3-Aminopropyl)tributylphosphonium l-α-aminopropionic acid
[aP_{4443}][Gly]	(3-Aminopropyl)tributylphosphonium aminoethanoic acid
[aP_{4443}][Leu]	(3-Aminopropyl)tributylphosphonium l-α-amino-4-methylvaleric acid
[aP_{4443}][Val]	(3-Aminopropyl)tributylphosphonium l-α-aminoisovaleric acid
[APBIM][BF_4]	1-Propylamide-3-butyl imidazolium tetrafluoroborate
[APMIM][Lys]	1-Aminopropyl-3-methylimidazolium lysine
[BF_4]$^-$	Tetrafluoroborate
[BMIM][124-Trz]	1-Butyl-3-methylimidazolium 1,2,4-triazolide
[BMIM][Ala]	1-Butyl-3-methylimidazolium alaninate
[BMIM][BF_4]	1-*n*-Butyl-3-methylimidazolium tetrafluoroborate
[BMIM][CF_3SO_3]	1-*n*-Butyl-3-methylimidazolium trifluoromethanesulfonate
[BMIM][Cl]	1-*n*-Butyl-3-methylimidazolium chloride
[BMIM][DCA]	1-*n*-Butyl-3-methylimidazolium dicyanamide
[BMIM][$FeCl_4$]	1-Butyl-3-methylimidazolium tetrachloroferrate
[BMIM][Gly]	1-Butyl-3-methylimidazolium glycinate
[BMIM][HSO_4]	1-*n*-butyl-3-methylimidazolium hydrogen sulfate
[BMIM][$MeSO_3$]	1-*n*-Butyl-3-methylimidazolium methanesulfonate
[BMIM][NO_3]	1-*n*-Butyl-3-methylimidazolium nitrate
[BMIM][NTf_2]	1-Butyl-3-methylimidazolium bis(trifluoromethylsulfonyl)imide
[BMIM][OAc]	1-Butyl-3-methylimidazolium acetate
[BMIM][$OcSO_4$]	1-*n*-Butyl-3-methylimidazolium octyl sulfate
[BMIM][PF_6]	1-*n*-Butyl-3-methylimidazolium hexafluorophosphate
[BMIM][SbF_6]	1-*n*-Butyl-3-methylimidazolium hexafluoroantimonate
[BMIM][SCN]	1-*n*-Butyl-3-methylimidazolium thiocyanate
[BMIM][Val]	1-Butyl-3-methylimidazolium valinate
[BMIM]$^+$	1-*n*-Butyl-3-methylimidazolium
[BMMIM][OAc]	1,2-Dimethyl-3-butylimidazolium acetate
[BMMIM][PF_6]	1-*n*-Butyl-2,3-dimethylimidazolium hexafluorophosphate
[BMPyr][DCA]	1-*n*-Butyl-1-methylpyrrolidinium dicyanamide
[BMPyr][PF_6]	1-*n*-Butyl-1-methylpyrrolidinium hexafluorophosphate
[C_{10}MIM][NTf_2]	1-Decyl-3-methylimidazolium bis(trifluoromethyl)sulfonylimide
[C_2OHMIM][Lys]	1-Hydroxyethyl-3-methylimidazolium lysine
[C_2OHMIM][NTf_2]	1-(2-Hydroxyethyl)-3-methylimidazolium bis(trifluoromethyl)sulfonylimide
[C_6MIM][$C(CN)_3$]	1-Hexyl-3-methylimidazolium tricyanomethanide
[C_6MIM][Cl]	1-Hexyl-3-methylimidazolium chloride
[C_6MIM][DCA]	1-Hexyl-3-methylimidazolium tricyanomethanide
[C_8MIM][NfO]	1-Octyl-3-methylimidazolim perfluorobutanesulfonate
[C_8MIM][NTf_2]	1-Octyl-3-methylimidazolium bistrifluoromethanesulfonylimide
[Car]$^-$	Carvacrol
[Ch]$^+$	Choline
[Ch][Cl]	Choline chloride
[Cl]$^-$	Chloride
[DAMT][BF_4]	3,5-Diamino-1-methyl-1,2,4-triazolium tetrafluoroborate
[DBUH][4-F-PhO]	IL Formed by 1,8-diazabicyclo[5.4.0]-undecane-7-ene (DBU) and 4-fluoro-phenol (4-F-PhOH)
[DCA]$^-$	Dicyanamide
[DETA][OAc]	Diethylenetriamine acetate
[DMIM][BF_4]	1-Decyl-3-methylimidazolium tetrafluoroborate
[Eaca]$^-$	6-Aminocaproicate
[EMIM][2-CNpyr]	1-Ethyl-3-methylimidazolium 2-cyanopyrrolide

Open Access Article. Published on 24 June 2024. Downloaded on 1/17/2026 6:47:09 PM.
This article is licensed under a Creative Commons Attribution-NonCommercial 3.0 Unported Licence.

[EMIM][BF_4]	1-Ethyl-3-methylimidazolium tetrafluoroborate
[EMIM][Cl]	1-Ethyl-3-methylimidazolium chloride
[EMIM][DEP]	1-Ethyl-3-methylimidazolium diethyl phosphate
[EMIM][NTf_2]	1-Ethyl-3-methylimidazolium bis(trifluoromethylsulfonyl)imide
[EMIM][OAc]	1-Ethyl-3-methylimidazolium acetate
[EMIM][TfO]	1-Ethyl-3-methylimidazolium trifluoromethanesulfonate
$[EMIM]^+$	1-Ethyl-3-methylimidazolium
$[EMIM]^+$-CO_2^-	1-Ethyl-3-methylimidazolium carboxylate
$[Gaba]^-$	γ-Aminobutyricate
$[Gly]^-$	Glycinate
$[HDBU]^+$	1,8-Diazabicyclo[5,4,0]undec-7-ene imidazole
[HEMIM][DCA]	1-(2-Hydroxyethyl)-3-methylimidazolium dicyanamide
[HeMOEim][Br]	1-(2-Hydroxyl-ethyl)-3-methoxyethyl-imidazolium bromide
$[His]^-$	Histidine
$[In]^-$	Indole
$[Im]^-$	Imidazole
$[Maba]^-$	*n*-Methyl-4-aminobutyricate
$[MEAH]^+$	Monoethanolamine
[MEAH][Cl]:MDEA	DES formed with monoethanolamine hydrochloride ([meah][cl]) and methyl-diethanolamine (mdea)
[MM][NTf_2]	1,3-Dimethylimidazolium
[MPPyr][DCA]	1-Methyl-1-propyl pyrrolidinium dicyanamide
$[N_{1111}]^-$	Tetramethylammonium anion
[N_{2222}][Ala]	Tetraethylammonium α-alaninate
[N_{2222}][4-PyO]	Tetraethylamminonium 4-hydroxypyridine
[N_{2222}][$CH(CN)_2$]	Tetraethylamminonium malononitrile
[N_{2222}][Gly]	Tetraethylammonium glycinate
[N_{2222}][β-Ala]	Tetraethylammonium β-alaninate
[N_{2224}][Ala]	Triethylbutylammonium α-alaninate
[NAIm][Br]	1-(3-Aminopropyl)-3-(2-bromoethyl)imidazole
$[NTf_2]^-$	Bis(trifluoromethylsulfonyl) imide
$[NTf_2]^-$	Bis(trifluoromethylsulfonyl) imide
$[OAc]^-$	Acetate
$[Oxa]^-$	Oxazole
[P1444][NTf_2]	Tributylmethyl-phosphonium bis(trifuoromethylsulfonyl)imid
[P2222][BnIm]	Triethylphosphonium benzimidazolate
[P2228][2-CNPyr]	Triethyloctylphosphonium 2-cyanopyrrolide
[P_{4442}][DAA]	Tributylethylphosphonium diacetamide
[P_{4442}][Suc]	Tributylethylphosphonium succinimide
[P_{4444}][2-Op]	Tetrabutylphosphonium 2-hydroxylpyridium
[P_{4444}][4-MF-PhO]	Tetrabutylphosphonium 4-(methoxycarbonyl) phenol
[P_{4444}][Ala]	Tetrabutylphosphonium α-alaninate
[P_{4444}][Gly]	Ttetrabutylphosphonium glycinate
[P_{4444}][HCO_2]	Tetrabutylphosphonium methanoate
[P_{4444}][Lys]	Tetrabutylphosphonium lysinate
[P_{4444}][OAc]	Tetrabutylphosphonium acetate
[P_{4444}][Pro]	Tetrabutylphosphonium prolinate
[P_{4444}][Ser]	Tetrabutylphosphonium serinate
[P_{4444}][β-Ala]	Tetrabutylphosphonium β-alaninate
$[P_{4444}]^+$	Tetrabutylphosphonium
[P_{66614}][123-Trz]	Trihetyl(tetradecyl)phosphonium 1,2,3-triazolide
[P_{66614}][124-Trz]	Trihexyltetradecylphosphonium 1,2,4-triazolide
[P_{66614}][134-Trz]	Trihexy(tetradecyl)phosphonium 1,3,4-trizolate
[P_{66614}][2-CNpyr]	Trihetyl(tetradecyl)phosphonium 2-cyanopyrrolide
[P_{66614}][2-Op]	Trihetyl(tetradecyl)phosphonium 2-hydroxylpyridium
[P_{66614}][2-SCH_3BnIm]	Trihetyl(tetradecyl)phosphonium 2-methlythio-benzimidazolide
[P_{66614}][3-CF_3Pyra]	Trihetyl(tetradecyl)phosphonium 3-trifluoromethyl-pyrazolide
[P_{66614}][3-CH_3-5-CF_3Pyra]	Trihetyl(tetradecyl)phosphonium 3-methly-5-trifluoromethyl-pyrazolide
[P_{66614}][3-Cl-PhO]	Trihexyl(tetradecyl)phosphonium o-chlorophenolate
[P_{66614}][3-Op]	Trihetyl(tetradecyl)phosphonium 3-hydroxylpyridium
[P_{66614}][4-MeO-PhO]	Trihexyl(tetradecyl)phosphonium *p*-methoxyphenolate
[P_{66614}][4-NO_2-PhO]	Trihexyl(tetradecyl)phosphonium *p*-nitrophenolate
[P_{66614}][4-Op]	Trihetyl(tetradecyl)phosphonium 4-hydroxylpyridium
[P_{66614}][6-BrBnIm]	Trihetyl(tetradecyl)phosphonium 6-bromo-benzimidazolide
[P_{66614}][Ala]	Trihetyl(tetradecyl)phosphonium α-alaninate
[P_{66614}][BnIm]	Trihetyl(tetradecyl)phosphonium benzimidazolide
[P_{66614}][Gly]	Trihetyl(tetradecyl)phosphonium glycinate
[P_{66614}][Im]	Trihexyl(tetradecyl)phosphonium imidazole
[P_{66614}][Inda]	Trihetyl(tetradecyl)phosphonium indazolide
[P_{66614}][Iso]	Trihexyl(tetradecyl)-phosphonium isoleucinate
[P_{66614}][Met]	Trihetyl(tetradecyl)phosphonium methioninate
[P_{66614}][MN]	Trihetyl(tetradecyl)phosphonium malononitrile
[P_{66614}][NTf_2]	Trihexyl(tetradecyl)phosphonium bis(trifluoromethyl)sulfonylimide

This journal is © The Royal Society of Chemistry 2024

Open Access Article. Published on 24 June 2024. Downloaded on 1/17/2026 6:47:09 PM.
This article is licensed under a Creative Commons Attribution-NonCommercial 3.0 Unported Licence.

$[P_{66614}][OAc]$	Trihetyl(tetradecyl)phosphonium acetate
$[P_{66614}][Pro]$	Trihetyl(tetradecyl)phosphonium prolinate
$[P_{66614}][Pyr]$	Trihexyl(tetradecyl)phosphonium pyrazole
$[P_{66614}][Tetz]$	Trihexyl(tetradecyl)phosphonium tetrazole
$[PF_6]^-$	Hexafluorophosphate
$[Phe]^-$	Phenylalaninate
$[PhO]^-$	Phenolate
$[Pro]^-$	Prolinate
$[PMIM][NTf_2]$	1-Propyl-3-methylimidazoliumbis-(trifluoro-methylsulfonyl)imide
[Tea][Tau]	Tetra-ethylalkylammonium taurinate
$[TEPA][NO_3]$	Tetraethylenepentammonium nitrate
$[TETA][NO_3]$	Triethylenetetrammonium nitrate
$[TfO]^-$	Trifluoromethylsulfonate anion
$[Thy]^-$	Thymol
[TMG][Im]	1,1,3,3-Tetramethylguanidinium imidazole
[Vbtma][gly]	Dimethylethylenediammonium propanoate
Fe(TPP)Cl	Iron tetraphenylporphyrin chloride
fac-Re(bpy)$(CO)_3$Cl	Dicationic Re bipyridine-type complex, *fac*-Re(6,6′-(2-((trimethylammonio)-methyl)phenyl)-2,2′-bipyridine) $(CO)_3$Cl hexafluorophosphate (12+)
$Ni(cyclam)Cl_2$	Ni-Cyclam complex
Rh(bpy)(Cp*)Cl	[Rh(bpy)(Cp*)Cl]Cl complex where bpy = 2,2′-bipyridine and Cp* = pentamethylcyclopentadienyl
Zn(TPP)Cl	Zinc tetraphenylporphyrin chloride
$Co(cyclam)Cl_3$	Co-Cyclam complex

Conflicts of interest

There are no conflicts to declare.

Acknowledgements

This work was supported by the Center for Closing the Carbon Cycle, an Energy Frontier Research Center funded by the U.S. Department of Energy (DOE), Office of Science, Basic Energy Sciences (BES), under Award Number DE-SC0023427 (electrochemical conversion; S. D., A. B., M. G., R. D. R., J. S., R. S. B., J. M. V., J. Y. Y., C. H., C. G. M.-G., J. M. S., B. G.), Basic Energy Sciences, award # DE-SC0022214 (sorbents for CO_2 capture; M. Z., R. D., B. G.), Breakthrough Electrolytes for Energy Storage (BEES2) under award # DE-SC0019409 (electrolyte properties; M. M., B. G.), and National Science Foundation Career award # 2045111 from the Division of Chemical, Bioengineering, Environmental and Transport Systems (interfacial analysis of ionic liquid electrolytes; O. K. C., B. G.). A. U. thanks the Fulbright Türkiye's Visiting Scholar Program, the Koç University Visiting Scholar Program, and the Scientific and Technological Research Council of Türkiye (TUBITAK) 2219 Program. B. K.'s efforts were supported by the Department of Energy, National Nuclear Security Administration (NNSA) grants (DE-NA0004112 and DE-NA0004007).

References

1 E. S. Sanz-Pérez, C. R. Murdock, S. A. Didas and C. W. Jones, *Chem. Rev.*, 2016, **116**, 11840–11876.
2 W. Wang, S. P. Wang, X. B. Ma and J. L. Gong, *Chem. Soc. Rev.*, 2011, **40**, 3703–3727.
3 National Academies of Sciences Engineering and Medicine (U.S.). Committee on a Research Agenda for a New Era in Separation Science, A research agenda for transforming separation science, 2019.
4 M. Bui, C. S. Adjiman, A. Bardow, E. J. Anthony, A. Boston, S. Brown, P. S. Fennell, S. Fuss, A. Galindo, L. A. Hackett, J. P. Hallett, H. J. Herzog, G. Jackson, J. Kemper, S. Krevor, G. C. Maitland, M. Matuszewski, I. S. Metcalfe, C. Petit, G. Puxty, J. Reimer, D. M. Reiner, E. S. Rubin, S. A. Scott, N. Shah, B. Smit, J. P. M. Trusler, P. Webley, J. Wilcox and N. Mac Dowell, *Energy Environ. Sci.*, 2018, **11**, 1062–1176.
5 S. Choi, J. H. Drese and C. W. Jones, *ChemSusChem*, 2009, **2**, 796–854.
6 Y. S. Bae and R. Q. Snurr, *Angew. Chem., Int. Ed.*, 2011, **50**, 11586–11596.
7 Z.-Z. Yang, Y.-N. Zhao and L.-N. He, *RSC Adv.*, 2011, **1**, 545–567.
8 C. Finn, S. Schnittger, L. J. Yellowlees and J. B. Love, *Chem. Commun.*, 2012, **48**, 1392–1399.
9 H. R. Jhong, S. C. Ma and P. J. A. Kenis, *Curr. Opin. Chem. Eng.*, 2013, **2**, 191–199.
10 A. Calbry-Muzyka, H. Madi, F. Rüsch-Pfund, M. Gandiglio and S. Biollaz, *Renewable Energy*, 2022, **181**, 1000–1007.
11 R. W. Baker, B. Freeman, J. Kniep, Y. I. Huang and T. C. Merkel, *Ind. Eng. Chem. Res.*, 2018, **57**, 15963–15970.
12 D. O. E. DOE/NETL Advanced Carbon Dioxide Capture R&D Program: Technology Update, NETL, Eds., Department of Energy: Morgantown, WV, 2010.
13 X. Y. Shi, H. Xiao, H. Azarabadi, J. Z. Song, X. L. Wu, X. Chen and K. S. Lackner, *Angew. Chem., Int. Ed.*, 2020, **59**, 6984–7006.
14 F. Zeman, *Environ. Sci. Technol.*, 2007, **41**, 7558–7563.
15 R. Baciocchi, G. Storti and M. Mazzotti, *Chem. Eng. Process.*, 2006, **45**, 1047–1058.
16 S. Chatterjee and K.-W. Huang, *Nat. Commun.*, 2020, **11**, 3287.
17 G. Realmonte, L. Drouet, A. Gambhir, J. Glynn, A. Hawkes, A. C. Köberle and M. Tavoni, *Nat. Commun.*, 2019, **10**, 3277.
18 M. C. Freyman, Z. Huang, D. Ravikumar, E. B. Duoss, Y. Li, S. E. Baker, S. H. Pang and J. A. Schaidle, *Joule*, 2023, **7**, 631–651.
19 D. J. Heldebrant, J. Kothandaraman, N. M. Dowell and L. Brickett, *Chem. Sci.*, 2022, **13**, 6445–6456.
20 A. M. Zito, L. E. Clarke, J. M. Barlow, D. Bím, Z. Zhang, K. M. Ripley, C. J. Li, A. Kummeth, M. E. Leonard, A. N. Alexandrova, F. R. Brushett and J. Y. Yang, *Chem. Rev.*, 2023, **123**, 8069–8098.
21 J. S. Wilkes, *Green Chem.*, 2002, **4**, 73–80.
22 T. Welton, *Chem. Rev.*, 1999, **99**, 2071–2083.
23 N. V. Plechkova and K. R. Seddon, *Chem. Soc. Rev.*, 2008, **37**, 123–150.

Open Access Article. Published on 24 June 2024. Downloaded on 1/17/2026 6:47:09 PM. This article is licensed under a Creative Commons Attribution-NonCommercial 3.0 Unported Licence.

24 P. Wasserscheid and W. Keim, *Angew. Chem., Int. Ed.*, 2000, **39**, 3772–3789.
25 T. L. Greaves and C. J. Drummond, *Chem. Rev.*, 2008, **108**, 206–237.
26 R. Sheldon, *Chem. Commun.*, 2001, 2399–2407, DOI: **10.1039/b107270f**.
27 M. Armand, F. Endres, D. R. MacFarlane, H. Ohno and B. Scrosati, *Nat. Mater.*, 2009, **8**, 621–629.
28 K. S. Egorova, E. G. Gordeev and V. P. Ananikov, *Chem. Rev.*, 2017, **117**, 7132–7189.
29 B. B. Hansen, S. Spittle, B. Chen, D. Poe, Y. Zhang, J. M. Klein, A. Horton, L. Adhikari, T. Zelovich, B. W. Doherty, B. Gurkan, E. J. Maginn, A. Ragauskas, M. Dadmun, T. A. Zawodzinski, G. A. Baker, M. E. Tuckerman, R. F. Savinell and J. R. Sangoro, *Chem. Rev.*, 2021, **121**, 1232–1285.
30 A. P. Abbott, D. Boothby, G. Capper, D. L. Davies and R. K. Rasheed, *J. Am. Chem. Soc.*, 2004, **126**, 9142–9147.
31 E. L. Smith, A. P. Abbott and K. S. Ryder, *Chem. Rev.*, 2014, **114**, 11060–11082.
32 G. García, S. Aparicio, R. Ullah and M. Atilhan, *Energy Fuels*, 2015, **29**, 2616–2644.
33 M. A. R. Martins, S. P. Pinho and J. A. P. Coutinho, *J. Solution Chem.*, 2019, **48**, 962–982.
34 M. Francisco, A. van den Bruinhorst and M. C. Kroon, *Angew. Chem., Int. Ed.*, 2013, **52**, 3074–3085.
35 R. Ghahremani, R. F. Savinell and B. Gurkan, *J. Electrochem. Soc.*, 2022, **169**, 030520.
36 X. Li, S. Wang and C. Chen, *Energy Procedia*, 2013, **37**, 1836–1843.
37 R.-T. Guo, G.-Y. Li, Y. Liu and W.-G. Pan, *Energy Fuels*, 2023, **37**, 15429–15452.
38 K. Sumida, D. L. Rogow, J. A. Mason, T. M. McDonald, E. D. Bloch, Z. R. Herm, T.-H. Bae and J. R. Long, *Chem. Rev.*, 2012, **112**, 724–781.
39 S. Mahajan and M. Lahtinen, *J. Environ. Chem. Eng.*, 2022, **10**, 108930.
40 D. G. Boer, J. Langerak and P. P. Pescarmona, *ACS Appl. Mater. Interfaces*, 2023, **6**, 2634–2656.
41 A. E. Creamer and B. Gao, *Environ. Sci. Technol.*, 2016, **50**, 7276–7289.
42 M. Pardakhti, T. Jafari, Z. Tobin, B. Dutta, E. Moharreri, N. S. Shemshaki, S. Suib and R. Srivastava, *ACS Appl. Mater. Interfaces*, 2019, **11**, 34533–34559.
43 K. S. Lackner, *Eur. Phys. J.: Spec. Top.*, 2009, **176**, 93–106.
44 T. Wang, K. S. Lackner and A. Wright, *Environ. Sci. Technol.*, 2011, **45**, 6670–6675.
45 X. Shi, H. Xiao, H. Azarabadi, J. Song, X. Wu, X. Chen and K. S. Lackner, *Angew. Chem., Int. Ed.*, 2020, **59**, 6984–7006.
46 M. C. Stern and T. A. Hatton, *RSC Adv.*, 2014, **4**, 5906–5914.
47 S. Voskian and T. A. Hatton, *Energy Environ. Sci.*, 2019, **12**, 3530–3547.
48 M. Rahimi, G. Catalini, S. Hariharan, M. Wang, M. Puccini and T. A. Hatton, *Cell Rep. Phys. Sci.*, 2020, **1**, 100033.
49 S. Tsubaki, K. Furusawa, H. Yamada, T. Kato, T. Higashii, S. Fujii and Y. Wada, *ACS Sustainable Chem. Eng.*, 2020, **8**, 13593–13599.
50 J. Yang, H. Y. Tan, Q. X. Low, B. P. Binks and J. M. Chin, *J. Mater. Chem. A*, 2015, **3**, 6440–6446.
51 Y.-Y. Lee, E. Cagli, A. Klemm, Y. Park, R. Dikki, M. K. Kidder and B. Gurkan, *ChemSusChem*, 2023, **16**, e202300118.
52 S.-M. Kim, K.-M. Kim, B.-K. Choi, J.-H. Mun, B.-J. Shin, U. Lee, C.-H. Shin, J. Choi, B.-M. Min and U. Lee, *Chem. Eng. J.*, 2022, **428**, 132044.
53 S. Chen, X. Han, X. Sun, X. Luo and Z. Liang, *Chem. Eng. J.*, 2020, **386**, 121295.
54 R. Zhang, X. He, T. Liu, C. E. Li, M. Xiao, H. Ling, X. Hu, X. Zhang, F. Tang and H. A. Luo, *Sep. Purif. Technol.*, 2022, **295**, 121292.
55 M. Xiao, D. Cui, Q. Yang, Z. Liang, G. Puxty, H. Yu, L. Li, W. Conway and P. Feron, *Chem. Eng. Sci.*, 2021, **229**, 116009.
56 N. E. L. Hadri, D. V. Quang and M. R. M. Abu-Zahra, *Energy Proc.*, 2015, **75**, 2268–2286.
57 A. C. Forse and P. J. Milner, *Chem. Sci.*, 2021, **12**, 508–516.
58 J. Xiang, D. Wei, W. Mao, T. Liu, Q. Luo, Y. Huang, Z. Liang and X. Luo, *Sep. Purif. Technol.*, 2024, **330**, 125310.
59 G. T. Rochelle, *Science*, 2009, **325**, 1652–1654.
60 G. F. Versteeg, L. A. J. Van Dijck and W. P. M. Van Swaaij, *Chem. Eng. Commun.*, 1996, **144**, 113–158.
61 C. H. Yu, C. H. Huang and C. S. Tan, *Aerosol Air Qual. Res.*, 2012, **12**, 745–769.
62 P. Singh, D. W. F. Brilman and M. J. Groeneveld, *Int. J. Greenhouse Gas Control*, 2011, **5**, 61–68.
63 N. El Hadri, D. V. Quang, E. L. V. Goetheer and M. R. M. Abu Zahra, *Appl. Energy*, 2017, **185**, 1433–1449.
64 I. Kim and H. F. Svendsen, *Ind. Eng. Chem. Res.*, 2007, **46**, 5803–5809.
65 T. Nguyen, M. Hilliard and G. T. Rochelle, *Int. J. Greenhouse Gas Control*, 2010, **4**, 707–715.
66 E. Pérez-Gallent, C. Vankani, C. Sánchez-Martínez, A. Anastasopol and E. Goetheer, *Ind. Eng. Chem. Res.*, 2021, **60**, 4269–4278.
67 S. Kar, A. Goeppert and G. K. S. Prakash, *Acc. Chem. Res.*, 2019, **52**, 2892–2903.
68 M. Abdinejad, Z. Mirza, X.-A. Zhang and H.-B. Kraatz, *ACS Sustainable Chem. Eng.*, 2020, **8**, 1715–1720.
69 M. Li, K. Yang, M. Abdinejad, C. Zhao and T. Burdyny, *Nanoscale*, 2022, **14**, 11892–11908.
70 L. Chen, F. Li, Y. Zhang, C. L. Bentley, M. Horne, A. M. Bond and J. Zhang, *ChemSusChem*, 2017, **10**, 4109–4118.
71 D. Filotás, T. Nagy, L. Nagy, P. Mizsey and G. Nagy, *Electroanalysis*, 2018, **30**, 690–697.
72 J. C. S. Choi, A. Banerjee, R. L. Sacci, G. M. Veith and C. Stieber, *et al.*, *ChemRxiv*, 2024, DOI: **10.26434/chemrxiv-2024-5xsp5** This content is a preprint and has not been peer-reviewed.
73 Y. Wu, J. Xu, K. Mumford, G. W. Stevens, W. Fei and Y. Wang, *Green Chem. Eng.*, 2020, **1**, 16–32.
74 B. E. Gurkan, J. C. de la Fuente, E. M. Mindrup, L. E. Ficke, B. F. Goodrich, E. A. Price, W. F. Schneider and J. F. Brennecke, *J. Am. Chem. Soc.*, 2010, **132**, 2116–2117.
75 J.-F. Pérez-Calvo, D. Sutter, M. Gazzani and M. Mazzotti, *Sep. Purif. Technol.*, 2021, **274**, 118959.

 This journal is © The Royal Society of Chemistry 2024

Open Access Article. Published on 24 June 2024. Downloaded on 1/17/2026 6:47:09 PM. This article is licensed under a Creative Commons Attribution-NonCommercial 3.0 Unported Licence.

76 F. O. Ochedi, J. Yu, H. Yu, Y. Liu and A. Hussain, *Environ. Chem. Lett.*, 2021, **19**, 77–109.
77 F. Wang, J. Zhao, H. Miao, J. Zhao, H. Zhang, J. Yuan and J. Yan, *Appl. Energy*, 2018, **230**, 734–749.
78 K. Jiao, X. Chen, X. Bie, D. Liu, M. Qiu and S. Ma, *Sci. Rep.*, 2021, **11**, 10457.
79 D. Bonalumi and A. Giuffrida, *Energy*, 2016, **117**, 439–449.
80 H. Liu, Y. Chen, J. Lee, S. Gu and W. Li, *ACS Energy Lett.*, 2022, **7**, 4483–4489.
81 H. Li, J. Gao, Q. Du, J. Shan, Y. Zhang, S. Wu and Z. Wang, *Energy*, 2021, **216**, 119250.
82 J. Li and N. Kornienko, *Chem. Sci.*, 2022, **13**, 3957–3964.
83 U. K. Ghosh, S. E. Kentish and G. W. Stevens, *Energy Proc.*, 2009, **1**, 1075–1081.
84 R. Ramezani and R. Di Felice, *Green Energy Environ.*, 2021, **6**, 83–90.
85 V. Sang Sefidi and P. Luis, *Ind. Eng. Chem. Res.*, 2019, **58**, 20181–20194.
86 U. E. Aronu, A. F. Ciftja, I. Kim and A. Hartono, *Energy Proc.*, 2013, **37**, 233–240.
87 E. W. Lees, M. Goldman, A. G. Fink, D. J. Dvorak, D. A. Salvatore, Z. Zhang, N. W. X. Loo and C. P. Berlinguette, *ACS Energy Lett.*, 2020, **5**, 2165–2173.
88 M. Ramdin, T. W. de Loos and T. J. H. Vlugt, *Ind. Eng. Chem. Res.*, 2012, **51**, 8149–8177.
89 B. Gurkan, F. Simeon and T. A. Hatton, *ACS Sustainable Chem. Eng.*, 2015, **3**, 1394–1405.
90 E. D. Bates, R. D. Mayton, I. Ntai and J. H. Davis, *J. Am. Chem. Soc.*, 2002, **124**, 926–927.
91 B. F. Goodrich, J. C. De La Fuente, B. E. Gurkan, D. J. Zadigian, E. A. Price, Y. Huang and J. F. Brennecke, *Ind. Eng. Chem. Res.*, 2011, **50**, 111–118.
92 H. Ohno and K. Fukumoto, *Acc. Chem. Res.*, 2007, **40**, 1122–1129.
93 C. Wang, X. Luo, H. Luo, D.-E. Jiang, H. Li and S. Dai, *Angew. Chem., Int. Ed.*, 2011, **50**, 4918–4922.
94 K. E. Gutowski and E. J. Maginn, *J. Am. Chem. Soc.*, 2008, **130**, 14690–14704.
95 X. Zhang, X. Zhang, H. Dong, Z. Zhao, S. Zhang and Y. Huang, *Energy Environ. Sci.*, 2012, **5**, 6668–6681.
96 P. Brown, B. E. Gurkan and T. A. Hatton, *AIChE J.*, 2015, **61**, 2280–2285.
97 X. Zhu, M. Song and Y. Xu, *ACS Sustainable Chem. Eng.*, 2017, **5**, 8192–8198.
98 N. Noorani and A. Mehrdad, *J. Mol. Liq.*, 2022, **357**, 119078.
99 R. Giernoth, *Angew. Chem., Int. Ed.*, 2010, **49**, 2834–2839.
100 Z. M. Memon, E. Yilmaz and M. Soylak, *J. Mol. Liq.*, 2017, **229**, 459–464.
101 A. Brzęczek-Szafran, P. Więcek, M. Guzik and A. Chrobok, *RSC Adv.*, 2020, **10**, 18355–18359.
102 W. Qian, J. Texter and F. Yan, *Chem. Soc. Rev.*, 2017, **46**, 1124–1159.
103 Q. Zhang and J. n M. Shreeve, *Chem. Rev.*, 2014, **114**, 10527–10574.
104 S. K. Singh and A. W. Savoy, *J. Mol. Liq.*, 2020, **297**, 112038.
105 S. K. Singh and P. L. Dhepe, *Green Chem.*, 2016, **18**, 4098–4108.
106 I. J. Lin and C. S. Vasam, *J. Organomet. Chem.*, 2005, **690**, 3498–3512.
107 R. D. Rogers and K. R. Seddon, *Science*, 2003, **302**, 792–793.
108 Y. Wang, C. Zheng, Y. Wang, H. Chen and Y. Xu, *J. Environ. Chem. Eng.*, 2019, **7**, 102774.
109 S. Kang, Y. G. Chung, J. H. Kang and H. Song, *J. Mol. Liq.*, 2020, **297**, 111825.
110 X. Luo, Y. Guo, F. Ding, H. Zhao, G. Cui, H. Li and C. Wang, *Angew. Chem., Int. Ed.*, 2014, **126**, 7173–7177.
111 X. Gao, X. Liu, A. Mariani, G. A. Elia, M. Lechner, C. Streb and S. Passerini, *Energy Environ. Sci.*, 2020, **13**, 2559–2569.
112 G. Shi, R. Zhai, H. Li and C. Wang, *Green Chem.*, 2021, **23**, 592–596.
113 Q. R. Sheridan, W. F. Schneider and E. J. Maginn, *Chem. Rev.*, 2018, **118**, 5242–5260.
114 R. Zhang, Q. Ke, Z. Zhang, B. Zhou, G. Cui and H. Lu, *Int. J. Mol. Sci.*, 2022, **23**, 11401.
115 N. Noorani and A. Mehrdad, *Fluid Phase Equilib.*, 2020, **517**, 112591.
116 Y.-Y. Jiang, G.-N. Wang, Z. Zhou, Y.-T. Wu, J. Geng and Z.-B. Zhang, *Chem. Commun.*, 2008, 505–507.
117 H. Yu, Y.-T. Wu, Y.-Y. Jiang, Z. Zhou and Z.-B. Zhang, *New J. Chem.*, 2009, **33**, 2385–2390.
118 M. B. Shiflett, D. J. Kasprzak, C. P. Junk and A. Yokozeki, *J. Chem. Thermodyn.*, 2008, **40**, 25–31.
119 M. B. Shiflett, B. A. Elliott, S. R. Lustig, S. Sabesan, M. S. Kelkar and A. Yokozeki, *ChemPhysChem*, 2012, **13**, 1806–1817.
120 E. J. Maginn, Design and evaluation of ionic liquids as novel CO_2 absorbents, University of Notre Dame (US), 2004.
121 G. Gurau, H. Rodríguez, S. P. Kelley, P. Janiczek, R. S. Kalb and R. D. Rogers, *Angew. Chem., Int. Ed.*, 2011, **50**, 12024–12026.
122 P. J. Carvalho and J. A. Coutinho, *J. Phys. Chem. Lett.*, 2010, **1**, 774–780.
123 P. J. Carvalho, V. H. Álvarez, B. Schröder, A. M. Gil, I. M. Marrucho, M. Aznar, L. M. Santos and J. A. Coutinho, *J. Phys. Chem. B*, 2009, **113**, 6803–6812.
124 P. Raveendran and S. L. Wallen, *J. Am. Chem. Soc.*, 2002, **124**, 12590–12599.
125 M. Mei, X. Hu, Z. Song, L. Chen, L. Deng and Z. Qi, *J. Mol. Liq.*, 2022, **348**, 118036.
126 B. Gurkan, B. Goodrich, E. Mindrup, L. Ficke, M. Massel, S. Seo, T. Senftle, H. Wu, M. Glaser and J. Shah, *J. Phys. Chem. Lett.*, 2010, **1**, 3494–3499.
127 G. Cui, N. Zhao, J. Wang and C. Wang, *Chem. – Asian J.*, 2017, **12**, 2863–2872.
128 X. Lei, Y. Xu, L. Zhu and X. Wang, *RSC Adv.*, 2014, **4**, 7052–7057.
129 F. Li, Y. Bai, S. Zeng, X. Liang, H. Wang, F. Huo and X. Zhang, *Int. J. Greenhouse Gas Control*, 2019, **90**, 102801.
130 X. Zhang, W. Xiong, L. Peng, Y. Wu and X. Hu, *AIChE J.*, 2020, **66**, e16936.
131 X. Zhu, M. Song, B. Ling, S. Wang and X. Luo, *J. Solution Chem.*, 2020, **49**, 257–271.
132 S. Oh, O. Morales-Collazo and J. F. Brennecke, *J. Phys. Chem. B*, 2019, **123**, 8274–8284.

Open Access Article. Published on 24 June 2024. Downloaded on 1/17/2026 6:47:09 PM. This article is licensed under a Creative Commons Attribution-NonCommercial 3.0 Unported Licence.

133 J. Hu, L. Chen, M. Shi and C. Zhang, *Fluid Phase Equilib.*, 2018, **459**, 208–218.
134 K. Mei, X. He, K. Chen, X. Zhou, H. Li and C. Wang, *Ind. Eng. Chem. Res.*, 2017, **56**, 8066–8072.
135 T. R. Gohndrone, T. Song, M. A. DeSilva and J. F. Brennecke, *J. Phys. Chem. B*, 2021, **125**, 6649–6657.
136 G. M. Avelar Bonilla, O. Morales-Collazo and J. F. Brennecke, *ACS Sustainable Chem. Eng.*, 2019, **7**, 16858–16869.
137 D. V. Quang, A. Dindi, A. V. Rayer, N. E. Hadri, A. Abdulkadir and M. R. M. Abu-Zahra, *Greenhouse Gases: Sci. Technol.*, 2015, **5**, 91–101.
138 S. Seo, M. Quiroz-Guzman, M. A. DeSilva, T. B. Lee, Y. Huang, B. F. Goodrich, W. F. Schneider and J. F. Brennecke, *J. Phys. Chem. B*, 2014, **118**, 5740–5751.
139 S. Oh, O. Morales-Collazo, A. N. Keller and J. F. Brennecke, *J. Phys. Chem. B*, 2020, **124**, 8877–8887.
140 V. V. Chaban and N. A. Andreeva, *J. Ionic Liq.*, 2023, **3**, 100068.
141 D. W. Keith, G. Holmes, D. S. Angelo and K. Heidel, *Joule*, 2018, **2**, 1573–1594.
142 A. Sodiq, Y. Abdullatif, B. Aissa, A. Ostovar, N. Nassar, M. El-Naas and A. Amhamed, *Environ. Technol. Innovation*, 2023, **29**, 102991.
143 C. Wang, H. Luo, H. Li, X. Zhu, B. Yu and S. Dai, *Chem. – Eur. J.*, 2012, **18**, 2153–2160.
144 F. Ding, X. He, X. Luo, W. Lin, K. Chen, H. Li and C. Wang, *Chem. Commun.*, 2014, **50**, 15041–15044.
145 X.-M. Zhang, K. Huang, S. Xia, Y.-L. Chen, Y.-T. Wu and X.-B. Hu, *Chem. Eng. J.*, 2015, **274**, 30–38.
146 T. Zhao, X. Zhang, Z. Tu, Y. Wu and X. Hu, *J. Mol. Liq.*, 2018, **268**, 617–624.
147 Y. Huang, G. Cui, Y. Zhao, H. Wang, Z. Li, S. Dai and J. Wang, *Angew. Chem., Int. Ed.*, 2017, **56**, 13293–13297.
148 X. An, X. Du, D. Duan, L. Shi, X. Hao, H. Lu, G. Guan and C. Peng, *Phys. Chem. Chem. Phys.*, 2017, **19**, 1134–1142.
149 A. Klemm, S. P. Vicchio, S. Bhattacharjee, E. Cagli, Y. Park, M. Zeeshan, R. Dikki, H. Liu, M. K. Kidder, R. B. Getman and B. Gurkan, *ACS Sustainable Chem. Eng.*, 2023, **11**, 3740–3749.
150 H. Yan, L. Zhao, Y. Bai, F. Li, H. Dong, H. Wang, X. Zhang and S. Zeng, *ACS Sustainable Chem. Eng.*, 2020, **8**, 2523–2530.
151 W. Xiong, M. Shi, L. Peng, X. Zhang, X. Hu and Y. Wu, *Sep. Purif. Technol.*, 2021, **263**, 118417.
152 F.-F. Chen, K. Huang, J.-P. Fan and D.-J. Tao, *AIChE J.*, 2018, **64**, 632–639.
153 L. Qiu, Y. Fu, Z. Yang, A. C. Johnson, C.-L. Do-Thanh, B. P. Thapaliya, S. M. Mahurin, L.-N. He, D.-E. Jiang and S. Dai, *ChemSusChem*, 2024, **17**, e202301329.
154 S. Wen, T. Wang, X. Zhang, W. Xu, X. Hu and Y. Wu, *AIChE J.*, 2023, **69**, e18206.
155 X. Suo, Y. Fu, C.-L. Do-Thanh, L.-Q. Qiu, D.-E. Jiang, S. M. Mahurin, Z. Yang and S. Dai, *J. Am. Chem. Soc.*, 2022, **144**, 21658–21663.
156 R. B. Leron and M.-H. Li, *J. Chem. Thermodyn.*, 2013, **57**, 131–136.
157 R. B. Leron and M.-H. Li, *Thermochim. Acta*, 2013, **551**, 14–19.
158 V. Alizadeh, L. Esser and B. Kirchner, *J. Chem. Phys.*, 2021, **154**, 094503.
159 G. Cui, M. Lv and D. Yang, *Chem. Commun.*, 2019, **55**, 1426–1429.
160 Y.-Y. Lee, D. Penley, A. Klemm, W. Dean and B. Gurkan, *ACS Sustainable Chem. Eng.*, 2021, **9**, 1090–1098.
161 J. Ruan, X. Ye, R. Wang, L. Chen, L. Deng and Z. Qi, *Fuel*, 2023, **334**, 126709.
162 Bhawna, A. Pandey and S. Pandey, *ChemistrySelect*, 2017, **2**, 11422–11430.
163 Z. Wang, C. Wu, Z. Wang, S. Zhang and D. Yang, *Chem. Commun.*, 2022, **58**, 7376–7379.
164 Z. Wang, Z. Wang, J. Chen, C. Wu and D. Yang, *Molecules*, 2021, **26**, 7167.
165 R. Dikki, E. Cagli, D. Penley, M. Karayilan and B. Gurkan, *Chem. Commun.*, 2023, **59**, 12027–12030.
166 R. Dikki, V. Khokhar, M. Zeeshan, S. Bhattacharjee, O. K. Coskun, R. Getman and B. Gurkan, *Green Chem.*, 2024, **26**, 3441.
167 Y. Gu, Y. Hou, S. Ren, Y. Sun and W. Wu, *ACS Omega*, 2020, **5**, 6809–6816.
168 X. Liu, Q. Ao, S. Shi and S. Li, *Mater. Res. Express*, 2022, **9**, 015504.
169 Z. Wang, Z. Wang, X. Huang, D. Yang, C. Wu and J. Chen, *Chem. Commun.*, 2022, **58**, 2160–2163.
170 N. Ahmad, X. Lin, X. Wang, J. Xu and X. Xu, *Fuel*, 2021, **293**, 120466.
171 Z. Wang, M. Chen, B. Lu, S. Zhang and D. Yang, *ACS Sustainable Chem. Eng.*, 2023, **11**, 6272–6279.
172 G. Cui, Y. Xu, D. Hu, Y. Zhou, C. Ge, H. Liu, W. Fan, Z. Zhang, B. Chen, Q. Ke, Y. Chen, B. Zhou, W. Zhang, R. Zhang and H. Lu, *Chem. Eng. J.*, 2023, **469**, 143991.
173 M. Chen, W. Xiong, W. Chen, S. Li, F. Zhang and Y. Wu, *AIChE J.*, 2024, **70**, e18319.
174 F. F. Chen, K. Huang, Y. Zhou, Z. Q. Tian, X. Zhu, D. J. Tao, D. E. Jiang and S. Dai, *Angew. Chem., Int. Ed.*, 2016, **55**, 7166–7170.
175 S. Zheng, S. Zeng, Y. Li, L. Bai, Y. Bai, X. Zhang, X. Liang and S. Zhang, *AIChE J.*, 2021, **68**, e17500.
176 T. Zhou, C. Gui, L. Sun, Y. Hu, H. Lyu, Z. Wang, Z. Song and G. Yu, *Chem. Rev.*, 2023, **123**, 12170–12253.
177 B. Koyuturk, C. Altintas, F. P. Kinik, S. Keskin and A. Uzun, *J. Phys. Chem. C*, 2017, **121**, 10370–10381.
178 V. Nozari, S. Keskin and A. Uzun, *ACS Omega*, 2017, **2**, 6613–6618.
179 I. Cota and F. F. Martinez, *Coord. Chem. Rev.*, 2017, **351**, 189–204.
180 X. Li, K. Chen, R. Guo and Z. Wei, *Chem. Rev.*, 2023, **123**, 10432–10467.
181 A. H. Ab Rahim, N. M. Yunus and M. A. Bustam, *Molecules*, 2023, **28**, 7091.
182 Y. Zhang, M. X. Wu, G. Zhou, X. H. Wang and X. Liu, *Adv. Funct. Mater.*, 2021, **31**, 2104996.
183 M. Yin, L. Wang and S. Tang, *ACS Appl. Mater. Interfaces*, 2022, **14**, 55674–55685.
184 H. P. Caglayan, U. Unal, S. Keskin and A. Uzun, *ACS Appl. Nano Mater.*, 2023, **6**, 2203–2217.

 This journal is © The Royal Society of Chemistry 2024

Open Access Article. Published on 24 June 2024. Downloaded on 1/17/2026 6:47:09 PM. This article is licensed under a Creative Commons Attribution-NonCommercial 3.0 Unported Licence.

185 O. Durak, M. Zeeshan, S. Keskin and A. Uzun, *Chem. Eng. J.*, 2022, **437**, 135436.
186 M. Zeeshan, K. Yalcin, F. E. Sarac Oztuna, U. Unal, S. Keskin and A. Uzun, *Carbon*, 2021, **171**, 79–87.
187 M. S. Raja Shahrom, A. R. Nordin and C. D. Wilfred, *J. Environ. Chem. Eng.*, 2019, **7**, 103319.
188 X. He, J. Zhu, H. Wang, M. Zhou and S. Zhang, *Coatings*, 2019, **9**, 590.
189 Y. Yu, J. Mai, L. Huang, L. Wang and X. Li, *RSC Adv.*, 2014, **4**, 12756.
190 Y. Y. Lee, K. Edgehouse, A. Klemm, H. Mao, E. Pentzer and B. Gurkan, *ACS Appl. Mater. Interfaces*, 2020, **12**, 19184–19193.
191 S. Chen, Y. Chao, J. Wu, H. Ye, X. Luo and Z. Liang, *Ind. Eng. Chem. Res.*, 2022, **61**, 11953–11963.
192 Y. Xu, Y. Zhou, J. Liu and L. Sun, *J. Energy Chem.*, 2017, **26**, 1026–1029.
193 Y. Zhou, J. Liu, M. Xiao, Y. Meng and L. Sun, *ACS Appl. Mater. Interfaces*, 2016, **8**, 5547–5555.
194 M. Mirzaei, B. Mokhtarani, A. Badiei and A. Sharifi, *Chem. Eng. Technol.*, 2018, **41**, 1272–1281.
195 M. Balsamo, A. Erto, A. Lancia, G. Totarella, F. Montagnaro and R. Turco, *Fuel*, 2018, **218**, 155–161.
196 S. Yoshida, K. Takahashi, S. Kudo, S. Iwamura, I. Ogino and S. R. Mukai, *Ind. Eng. Chem. Res.*, 2017, **56**, 2834–2839.
197 J. Wu, Z. Yang, J. Xie, P. Zhu, J. Wei, R. Jin and H. Yang, *Langmuir*, 2023, **39**, 2729–2738.
198 Y. Uehara, D. Karami and N. Mahinpey, *Energy Fuels*, 2018, **32**, 5345–5354.
199 D. N. Lapshin, M. Jorge, E. E. B. Campbell and L. Sarkisov, *J. Mater. Chem. A*, 2020, **8**, 11781–11799.
200 I. H. Arellano, J. Huang and P. Pendleton, *Chem. Eng. J.*, 2015, **281**, 119–125.
201 M. Zhao, Y. Ban and W. Yang, *Chem. Eng. J.*, 2022, **439**, 135650.
202 M. Zeeshan, V. Nozari, M. B. Yagci, T. Isık, U. Unal, V. Ortalan, S. Keskin and A. Uzun, *J. Am. Chem. Soc.*, 2018, **140**, 10113–10116.
203 M. Zeeshan, S. Keskin and A. Uzun, *Polyhedron*, 2018, **155**, 485–492.
204 F. P. Kinik, C. Altintas, V. Balci, B. Koyuturk, A. Uzun and S. Keskin, *ACS Appl. Mater. Interfaces*, 2016, **8**, 30992–31005.
205 M. Mohamedali, H. Ibrahim and A. Henni, *Chem. Eng. J.*, 2018, **334**, 817–828.
206 M. Zeeshan, H. Kulak, S. Kavak, H. M. Polat, O. Durak, S. Keskin and A. Uzun, *Microporous Mesoporous Mater.*, 2020, **306**, 110446.
207 T. J. Ferreira, R. P. P. L. Ribeiro, J. P. B. Mota, L. P. N. Rebelo, J. M. S. S. Esperança and I. A. A. C. Esteves, *ACS Appl. Nano Mater.*, 2019, **2**, 7933–7950.
208 T. J. Ferreira, A. T. Vera, B. A. de Moura, L. M. Esteves, M. Tariq, J. M. S. S. Esperança and I. A. A. C. Esteves, *Front. Chem.*, 2020, **8**, 590191.
209 M. Mohamedali, A. Henni and H. Ibrahim, *Microporous Mesoporous Mater.*, 2019, **284**, 98–110.
210 G. Yang, J. Yu, S. Peng, K. Sheng and H. Zhang, *Polymers*, 2020, **12**, 370.
211 C. Chen, N. Feng, Q. Guo, Z. Li, X. Li, J. Ding, L. Wang, H. Wan and G. Guan, *J. Colloid Interface Sci.*, 2018, **521**, 91–101.
212 J. Yang, M. Tong, G. Han, M. Chang, T. Yan, Y. Ying, Q. Yang and D. Liu, *Adv. Funct. Mater.*, 2023, **33**, 2213743.
213 Y. Zhang, Y. Huang, S. Chen, L. Shi, J. Wang, Q. Yi and F. Pei, *Chem. Eng. J.*, 2023, **471**, 144580.
214 L. Qiu, L. Peng, D. Moitra, H. Liu, Y. Fu, Z. Dong, W. Hu, M. Lei, D.-E. Jiang, H. Lin, J. Hu, K. A. McGarry, I. Popovs, M. Li, A. S. Ivanov, Z. Yang and S. Dai, *Small*, 2023, **19**, 2370338.
215 B. B. Polesso, F. L. Bernard, H. Z. Ferrari, E. A. Duarte, F. D. Vecchia and S. Einloft, *Heliyon*, 2019, **5**, e02183.
216 B. B. Polesso, R. Duczinski, F. L. Bernard, H. Z. Ferrari, M. da Luz, F. Dalla Vecchia, S. M. C. de Menezes and S. Einloft, *Am. J. Mater. Sci.*, 2019, **22**, e20180810.
217 H. Kulak, H. M. Polat, S. Kavak, S. Keskin and A. Uzun, *Energy Technol.*, 2019, **7**, 1900157.
218 W. Zhang, E. Gao, Y. Li, M. T. Bernards, Y. Li, G. Cao, Y. He and Y. Shi, *Energy Fuels*, 2019, **33**, 8967–8975.
219 J.-Z. Yin, M.-Y. Zhen, P. Cai, D. Zhou, Z.-J. Li, H.-Y. Zhu and Q.-Q. Xu, *Mater. Res. Express*, 2018, **5**, 065060.
220 F. Liu, K. Huang and L. Jiang, *AIChE J.*, 2018, **64**, 3671–3680.
221 M. Mohamedali, A. Henni and H. Ibrahim, *Adsorption*, 2019, **25**, 675–692.
222 A. Erto, A. Silvestre-Albero, J. Silvestre-Albero, F. Rodríguez-Reinoso, M. Balsamo, A. Lancia and F. Montagnaro, *J. Colloid Interface Sci.*, 2015, **448**, 41–50.
223 J. Ren, Z. Li, Y. Chen, Z. Yang and X. Lu, *Chin. J. Chem. Eng.*, 2018, **26**, 2377–2384.
224 Y. Uehara, D. Karami and N. Mahinpey, *Ind. Eng. Chem. Res.*, 2017, **56**, 14316–14323.
225 Y. Uehara, D. Karami and N. Mahinpey, *Adsorption*, 2019, **25**, 703–716.
226 K. N. Ruckart, R. A. O'Brien, S. M. Woodard, K. N. West and T. G. Glover, *J. Phys. Chem. C*, 2015, **119**, 20681–20697.
227 C. Xue, L. Feng, Q. Zhang, R. Huang, Y. Hao, X. Ma, G. Liu, K. Li and X. Hao, *Int. J. Greenhouse Gas Control*, 2019, **84**, 111–120.
228 J. Cheng, Y. Li, L. Hu, J. Liu, J. Zhou and K. Cen, *Fuel Process. Technol.*, 2018, **172**, 216–224.
229 J. M. Zhu, F. Xin, Y. C. Sun and X. C. Dong, *Theor. Found. Chem. Eng.*, 2014, **48**, 787–792.
230 V. Hiremath, A. H. Jadhav, H. Lee, S. Kwon and J. G. Seo, *Chem. Eng. J.*, 2016, **287**, 602–617.
231 P. Tamilarasan and S. Ramaprabhu, *RSC Adv.*, 2016, **6**, 3032–3040.
232 X. Song, J. Yu, M. Wei, R. Li, X. Pan, G. Yang and H. Tang, *Materials*, 2019, **12**, 2361.
233 B. Dong, L. Wang, S. Zhao, R. Ge, X. Song, Y. Wang and Y. Gao, *Chem. Commun.*, 2016, **52**, 7082–7085.
234 N. Z. Zulkurnai, U. F. Md Ali, N. Ibrahim and N. S. Abdul Manan, *IOP Conf. Ser.: Mater. Sci. Eng.*, 2017, **206**, 012001.
235 Z. Ghazali, N. Suhaili, M. N. A. Tahari, M. A. Yarmo, N. H. Hassan and R. Othaman, *J. Mater. Res. Technol.*, 2020, **9**, 3249–3260.

Open Access Article. Published on 24 June 2024. Downloaded on 1/17/2026 6:47:09 PM. This article is licensed under a Creative Commons Attribution-NonCommercial 3.0 Unported Licence.

236 N. Noorani and A. Mehrdad, *Sci. Rep.*, 2023, **13**, 13012.
237 O. Durak, M. Zeeshan, N. Habib, H. C. Gulbalkan, A. A. A. M. Alsuhile, H. P. Caglayan, S. F. Kurtoğlu-Öztulum, Y. Zhao, Z. P. Haslak, A. Uzun and S. Keskin, *Microporous Mesoporous Mater.*, 2022, **332**, 111703.
238 M. Zeeshan, V. Nozari, S. Keskin and A. Uzun, *Ind. Eng. Chem. Res.*, 2019, **58**, 14124–14138.
239 O. Durak, H. Kulak, S. Kavak, H. M. Polat, S. Keskin and A. Uzun, *J. Phys.: Condens. Matter*, 2020, **32**, 484001.
240 S. F. Kurtoğlu-Öztulum, A. Jalal and A. Uzun, *J. Mol. Liq.*, 2022, **363**, 119804.
241 M. Babucci, A. Akcay, V. Balci and A. Uzun, *Langmuir*, 2015, **31**, 9163–9176.
242 K. B. Sezginel, S. Keskin and A. Uzun, *Langmuir*, 2016, **32**, 1139–1147.
243 V. Nozari, M. Zeeshan, S. Keskin and A. Uzun, *CrystEngComm*, 2018, **20**, 7137–7143.
244 M. Mirzaei, A. R. Badiei, B. Mokhtarani and A. Sharifi, *J. Mol. Liq.*, 2017, **232**, 462–470.
245 Y. Cheng, S. Zhou, P. Hu, G. Zhao, Y. Li, X. Zhang and W. Han, *Sci. Rep.*, 2017, **7**, 1439.
246 S. Kavak, H. M. Polat, H. Kulak, S. Keskin and A. Uzun, *Chem. – Asian J.*, 2019, **14**, 3655–3667.
247 R. Duczinski, F. Bernard, M. Rojas, E. Duarte, V. Chaban, F. D. Vecchia, S. Menezes and S. Einloft, *J. Nat. Gas Sci. Eng.*, 2018, **54**, 54–64.
248 F. W. M. d Silva, G. M. Magalhães, E. O. Jardim, J. Silvestre-Albero, A. Sepúlveda-Escribano, D. C. S. de Azevedo and S. M. P. de Lucena, *Adsorpt. Sci. Technol.*, 2015, **33**, 223–242.
249 N. Habib, O. Durak, H. C. Gulbalkan, A. S. Aydogdu, S. Keskin and A. Uzun, *ACS Appl. Eng. Mater.*, 2023, **1**, 1473–1481.
250 M. Zeeshan, H. C. Gulbalkan, Z. P. Haslak, S. Keskin and A. Uzun, *Microporous Mesoporous Mater.*, 2021, **316**, 110947.
251 R. Santiago, J. Lemus, D. Hospital-Benito, C. Moya, J. Bedia, N. Alonso-Morales, J. J. Rodriguez and J. Palomar, *ACS Sustainable Chem. Eng.*, 2019, **7**, 13089–13097.
252 W. Zhang, E. Gao, Y. Li, M. T. Bernards, Y. He and Y. Shi, *J. CO2 Util.*, 2019, **34**, 606–615.
253 S. Zheng, S. Zeng, G. Li, X. Yao, Z. Li and X. Zhang, *Chem. Eng. J.*, 2023, **451**, 138736.
254 Z. Li, W. Sun, C. Chen, Q. Guo, X. Li, M. Gu, N. Feng, J. Ding, H. Wan and G. Guan, *Appl. Surf. Sci.*, 2019, **480**, 770–778.
255 T. Ariyanto, K. Masruroh, G. Y. S. Pambayun, N. I. F. Mukti, R. B. Cahyono, A. Prasetya and I. Prasetyo, *ACS Omega*, 2021, **6**, 19194–19201.
256 Z. Huang, M. Mohamedali, D. Karami and N. Mahinpey, *Fuel*, 2022, **310**, 122284.
257 I. H. Arellano, J. Huang and P. Pendleton, *RSC Adv.*, 2015, **5**, 65074–65083.
258 I. H. Arellano, S. H. Madani, J. Huang and P. Pendleton, *Chem. Eng. J.*, 2016, **283**, 692–702.
259 N. I. F. Mukti, T. Ariyanto, W. B. Sediawan and I. Prasetyo, *RSC Adv.*, 2023, **13**, 23158–23168.
260 F. Hussin, M. K. Aroua and R. Yusoff, *J. Environ. Chem. Eng.*, 2021, **9**, 105333.
261 N. Hussain Solangi, F. Hussin, A. Anjum, N. Sabzoi, S. Ali Mazari, N. M. Mubarak, M. Kheireddine Aroua, M. T. H. Siddiqui and S. Saeed Qureshi, *J. Mol. Liq.*, 2023, **374**, 121266.
262 X. Li, D. Wang, Z. He, F. Su, N. Zhang, Y. Xin, H. Wang, X. Tian, Y. Zheng and D. Yao, *Chem. Eng. J.*, 2021, **417**, 129239.
263 Y.-Y. Lee and B. Gurkan, *J. Membr. Sci.*, 2021, **638**, 119652.
264 Y.-Y. Lee, N. P. Wickramasinghe, R. Dikki, D. L. Jan and B. Gurkan, *Nanoscale*, 2022, **14**, 12638–12650.
265 N. O'Reilly, N. Giri and S. L. James, *Chem. – Eur. J.*, 2007, **13**, 3020–3025.
266 M. Z. Ahmad and A. Fuoco, *Curr. Res. Green Sustainable Chem.*, 2021, **4**, 100070.
267 B. D. Egleston, A. Mroz, K. E. Jelfs and R. L. Greenaway, *Chem. Sci.*, 2022, **13**, 5042–5054.
268 S. Zhang, K. Dokko and M. Watanabe, *Chem. Sci.*, 2015, **6**, 3684–3691.
269 J. Avila, C. Červinka, P. Y. Dugas, A. A. Pádua and M. Costa Gomes, *Adv. Mater. Interfaces*, 2021, **8**, 2001982.
270 J. Avila, L. F. Lepre, C. C. Santini, M. Tiano, S. Denis-Quanquin, K. Chung Szeto, A. A. Padua and M. Costa Gomes, *Angew. Chem., Int. Ed.*, 2021, **133**, 12986–12992.
271 W. Shan, P. F. Fulvio, L. Kong, J. A. Schott, C.-L. Do-Thanh, T. Tian, X. Hu, S. M. Mahurin, H. Xing and S. Dai, *ACS Appl. Mater. Interfaces*, 2018, **10**, 32–36.
272 P. Scovazzo, A. E. Visser, J. H. DavisJr, R. D. Rogers, C. A. Koval, D. L. DuBois and R. D. Noble, *Ionic Liquids*, American Chemical Society, 2002, ch. 6, vol. 18, pp. 69–87.
273 N. N. R. Ahmad, C. P. Leo, A. W. Mohammad, N. Shaari and W. L. Ang, *Int. J. Energy Res.*, 2021, **45**, 9800–9830.
274 W. Luo, C. Wang, M. Jin, F. Li, H. Li, Z. Zhang, X. Zhang, Y. Liang, G. Huang and T. Zhou, *Sep. Purif. Technol.*, 2024, **330**, 125406.
275 N. Habib, Ö. Durak, A. Uzun and S. Keskin, *Sep. Purif. Technol.*, 2023, **312**, 123346.
276 R. Mahboubi, E. Joudaki, R. M. Behbahani and N. Azizi, *Mater. Today Commun.*, 2023, **36**, 106542.
277 C. R. Groom, I. J. Bruno, M. P. Lightfoot and S. C. Ward, *Acta Crystallogr., Sect. B: Struct. Sci., Cryst. Eng. Mater.*, 2016, **72**, 171–179.
278 I. J. Bruno, J. C. Cole, P. R. Edgington, M. Kessler, C. F. Macrae, P. McCabe, J. Pearson and R. Taylor, *Acta Crystallogr., Sect. B: Struct. Sci., Cryst. Eng. Mater.*, 2002, **58**, 389–397.
279 M. Mohan, O. Demerdash, B. A. Simmons, J. C. Smith, M. K. Kidder and S. Singh, *Green Chem.*, 2023, **25**, 3475–3492.
280 M. Mohan, K. S. Jetti, M. D. Demerdash, M. O. Kidder and J. C. Smith, *J. Chem. Theory Comput.*, 2024, **12**(18), 7040–7054.
281 H. M. Polat, M. Zeeshan, A. Uzun and S. Keskin, *Chem. Eng. J.*, 2019, **373**, 1179–1189.
282 H. M. Polat, S. Kavak, H. Kulak, A. Uzun and S. Keskin, *Chem. Eng. J.*, 2020, **394**, 124916.

 This journal is © The Royal Society of Chemistry 2024

Open Access Article. Published on 24 June 2024. Downloaded on 1/17/2026 6:47:09 PM. This article is licensed under a Creative Commons Attribution-NonCommercial 3.0 Unported Licence.

283 H. C. Gulbalkan, Z. P. Haslak, C. Altintas, A. Uzun and S. Keskin, *Sep. Purif. Technol.*, 2022, **287**, 120578.
284 T. Yan, M. Tong, D. Liu, Q. Yang and C. Zhong, *J. Mater. Chem. A*, 2023, **11**, 14911–14920.
285 M. Zeeshan, H. C. Gulbalkan, O. Durak, Z. P. Haslak, U. Unal, S. Keskin and A. Uzun, *Adv. Funct. Mater.*, 2022, **32**, 2204149.
286 Y. Chen and T. Mu, *Green Chem.*, 2019, **21**, 2544–2574.
287 A. Velty and A. Corma, *Chem. Soc. Rev.*, 2023, **52**, 1773–1946.
288 Z. Xie, M. Zhu, A. Nambo, J. B. Jasinski and M. A. Carreon, *Dalton Trans.*, 2013, **42**, 6732–6735.
289 B. Kumar, M. Asadi, D. Pisasale, S. Sinha-Ray, B. A. Rosen, R. Haasch, J. Abiade, A. L. Yarin and A. Salehi-Khojin, *Nat. Commun.*, 2013, **4**, 2819.
290 M. I. Qadir and J. Dupont, *Angew. Chem., Int. Ed.*, 2023, **62**, e202301497.
291 Z. J. Li, J. F. Sun, Q. Q. Xu and J. Z. Yin, *ChemCatChem*, 2021, **13**, 1848–1866.
292 Y. He, D. Jiang, X. Li, J. Ding, H. Li, H. Wan and G. Guan, *J. CO2 Util.*, 2021, **44**, 101427.
293 T. Chen, Y. Guo and Y. Xu, *Chem. Commun.*, 2023, **59**, 12282–12285.
294 X. Gao, J. Zhao, Y. Gao, Y. Deng, Y. Shi, J. He and Y. Li, *New J. Chem.*, 2023, **47**, 17449–17455.
295 M. Liu, X. Wang, Y. Jiang, J. Sun and M. Arai, *Catal. Rev.*, 2018, **61**, 214–269.
296 Y. Xie, Q. Sun, Y. Fu, L. Song, J. Liang, X. Xu, H. Wang, J. Li, S. Tu, X. Lu and J. Li, *J. Mater. Chem. A*, 2017, **5**, 25594–25600.
297 P. Migowski, P. Lozano and J. Dupont, *Green Chem.*, 2023, **25**, 1237–1260.
298 J. Peng and Y. Deng, *New J. Chem.*, 2001, **25**, 639–641.
299 H. Kawanami, A. Sasaki, K. Matsui and Y. Ikushima, *Chem. Commun.*, 2003, 896–897, DOI: **10.1039/b212823c**.
300 J. Byun and K. A. I. Zhang, *ChemCatChem*, 2018, **10**, 4610–4616.
301 Á. Mesías-Salazar, R. S. Rojas, F. Carrillo-Hermosilla, J. Martínez, A. Antiñolo, O. S. Trofymchuk, F. M. Nachtigall, L. S. Santos and C. G. Daniliuc, *New J. Chem.*, 2024, **48**, 105–111.
302 F. Norouzi and A. Abdolmaleki, *Fuel*, 2023, 334.
303 L. Xiao, D. Su, C. Yue and W. Wu, *J. CO2 Util.*, 2014, **6**, 1–6.
304 Z. Zhang, F. Fan, H. Xing, Q. Yang, Z. Bao and Q. Ren, *ACS Sustainable Chem. Eng.*, 2017, **5**, 2841–2846.
305 X. Meng, Z. Ju, S. Zhang, X. Liang, N. von Solms, X. Zhang and X. Zhang, *Green Chem.*, 2019, **21**, 3456–3463.
306 C. Luo, J. Wang, H. Lu, K. Wu, Y. Liu, Y. Zhu, B. Wang and B. Liang, *Green Chem.*, 2022, **24**, 8292–8301.
307 Q. Yi, T. Liu, X. Wang, Y. Shan, X. Li, M. Ding, L. Shi, H. Zeng and Y. Wu, *Appl. Catal., B*, 2021, **283**, 119620.
308 Y. Zhang, M. Qiu, J. Li, H. Wu, L. Shi and Q. Yi, *Fuel*, 2023, **332**, 126191.
309 B. Chen, S. Zhang and Y. Zhang, *Green Chem.*, 2023, **25**, 7743–7755.
310 A. Dani, E. Groppo, C. Barolo, J. G. Vitillo and S. Bordiga, *J. Mater. Chem. A*, 2015, **3**, 8508–8518.
311 J. D. Ndayambaje, I. Shabbir, Q. Zhao, L. Dong, Q. Su and W. Cheng, *Catal. Sci. Technol.*, 2024, **14**, 293–305.
312 Y. Qu, Y. Chen and J. Sun, *J. CO2 Util.*, 2022, **56**, 101840.
313 Y. Qu, J. Lan, Y. Chen and J. Sun, *Sustainable Energy Fuels*, 2021, **5**, 2494–2503.
314 G. Chen, J. Zhang, X. Cheng, X. Tan, J. Shi, D. Tan, B. Zhang, Q. Wan, F. Zhang, L. Liu, B. Han and G. Yang, *ChemCatChem*, 2020, **12**, 1963–1967.
315 Y. Toda, Y. Komiyama, A. Kikuchi and H. Suga, *ACS Catal.*, 2016, **6**, 6906–6910.
316 J. Steinbauer, L. Longwitz, M. Frank, J. Epping, U. Kragl and T. Werner, *Green Chem.*, 2017, **19**, 4435–4445.
317 J. Sun, L. Han, W. Cheng, J. Wang, X. Zhang and S. Zhang, *ChemSusChem*, 2011, **4**, 502–507.
318 X. Meng, H. He, Y. Nie, X. Zhang, S. Zhang and J. Wang, *ACS Sustainable Chem. Eng.*, 2017, **5**, 3081–3086.
319 S. Yue, P. Wang and X. Hao, *Fuel*, 2019, **251**, 233–241.
320 Á. F. Arruda da Mata, N. Glanzmann, P. H. Fazza Stroppa, F. Terra Martins, R. P. das Chagas, A. D. da Silva and J. L. S. Milani, *New J. Chem.*, 2022, **46**, 12237–12243.
321 Y. Zou, Y. Ge, Q. Zhang, W. Liu, X. Li, G. Cheng and H. Ke, *Catal. Sci. Technol.*, 2022, **12**, 273–281.
322 P. Wang, Q. Lv, Y. Tao, L. Cheng, R. Li, Y. Jiao, C. Fang, H. Li, C. Geng, C. Sun, J. Ding, H. Wan and G. Guan, *Mol. Catal.*, 2023, **544**, 113157.
323 C. Li, F. Liu, T. Zhao, J. Gu, P. Chen and T. Chen, *Mol. Catal.*, 2021, **511**, 111756.
324 Y. Fu, Y. Xu, Z. Zeng, A.-R. Ibrahim, J. Yang, S. Yang, Y. Xie, Y. Hong, Y. Su, H. Wang, Y. Wang, L. Peng, J. Li and W. L. Queen, *Green Energy Environ.*, 2023, **8**, 478–486.
325 A. Zhang, C. Chen, C. Zuo, X. Xu, T. Cai, X. Li, Y. Yuan, H. Yang and G. Meng, *Green Chem.*, 2022, **24**, 7194–7207.
326 D. Dong, X. Zhao, C. Pu, Y. Yao, B. Zhao, G. Tian, G. Chang and X. Yang, *Inorg. Chem.*, 2023, **62**, 20528–20536.
327 Y. Sun, H. Huang, H. Vardhan, B. Aguila, C. Zhong, J. A. Perman, A. M. Al-Enizi, A. Nafady and S. Ma, *ACS Appl. Mater. Interfaces*, 2018, **10**, 27124–27130.
328 V. K. Tomazett, G. Chacon, G. Marin, M. V. Castegnaro, R. P. das Chagas, L. M. Lião, J. Dupont and M. I. Qadir, *J. CO2 Util.*, 2023, **69**, 102400.
329 N. Wu, Y. Zou, R. Xu, J. Zhong and J. Li, *J. CO2 Util.*, 2021, **52**, 101702.
330 J. Sun, Z. Li, X. Li, M. Xue and J. Yin, *Catal. Lett.*, 2021, **152**, 2669–2677.
331 Q. Su, Y. Qi, X. Yao, W. Cheng, L. Dong, S. Chen and S. Zhang, *Green Chem.*, 2018, **20**, 3232–3241.
332 L. Sun, M. Yin and S. Tang, *J. Environ. Chem. Eng.*, 2023, **11**(5), 110843.
333 Z. Shi, Q. Su, T. Ying, X. Tan, L. Deng, L. Dong and W. Cheng, *J. CO2 Util.*, 2020, **39**, 101162.
334 Y. He, X. Li, W. Cai, H. Lu, J. Ding, H. Li, H. Wan and G. Guan, *ACS Sustainable Chem. Eng.*, 2021, **9**, 7074–7085.
335 J. Ding, P. Wang, Y. He, L. Cheng, X. Li, C. Fang, H. Li, H. Wan and G. Guan, *Appl. Catal., B*, 2023, **324**, 122278.
336 M. D. Porosoff, B. Yan and J. G. Chen, *Energy Environ. Sci.*, 2016, **9**, 62–73.

Open Access Article. Published on 24 June 2024. Downloaded on 1/17/2026 6:47:09 PM. This article is licensed under a Creative Commons Attribution-NonCommercial 3.0 Unported Licence.

337 T. Sasaki, *Curr. Opin. Green Sustainable Chem.*, 2022, **36**, 100633.
338 S. J. Louis Anandaraj, L. Kang, S. DeBeer, A. Bordet and W. Leitner, *Small*, 2023, **19**, 2206806.
339 C. I. Melo, A. Szczepanska, E. Bogel-Lukasik, M. Nunes da Ponte and L. C. Branco, *ChemSusChem*, 2016, **9**, 1081–1084.
340 C. I. Melo, D. Rente, M. Nunes da Ponte, E. Bogel-Łukasik and L. C. Branco, *ACS Sustainable Chem. Eng.*, 2019, **7**(14), 11963–11969.
341 R. Wang, Y.-R. Du, G.-R. Ding, R. Zhang, P.-X. Guan and B.-H. Xu, *ACS Sustainable Chem. Eng.*, 2022, **10**, 5363–5373.
342 M. I. Qadir, A. Weilhard, J. A. Fernandes, I. de Pedro, B. J. C. Vieira, J. C. Waerenborgh and J. Dupont, *ACS Catal.*, 2018, **8**, 1621–1627.
343 M. I. Qadir, F. Bernardi, J. D. Scholten, D. L. Baptista and J. Dupont, *Appl. Catal., B*, 2019, **252**, 10–17.
344 M. F. Santos, M. L. Alcantara, C. A. O. Nascimento, G. S. Bassani and R. M. B. Alves, *Clean Technol. Environ. Policy*, 2024, **26**, 11–29.
345 J. Klankermayer, S. Wesselbaum, K. Beydoun and W. Leitner, *Angew. Chem., Int. Ed.*, 2016, **55**, 7296–7343.
346 A. Weilhard, S. P. Argent and V. Sans, *Nat. Commun.*, 2021, **12**, 231.
347 L. Piccirilli, B. Rabell, R. Padilla, A. Riisager, S. Das and M. Nielsen, *J. Am. Chem. Soc.*, 2023, **145**, 5655–5663.
348 W. Ma, J. Hu, L. Zhou, Y. Wu, J. Geng and X. Hu, *Green Chem.*, 2022, **24**, 6727–6732.
349 R. Webber, M. I. Qadir, E. Sola, M. Martín, E. Suárez and J. Dupont, *Catal. Commun.*, 2020, **146**, 106125.
350 R. Kanega, M. Z. Ertem, N. Onishi, D. J. Szalda, E. Fujita and Y. Himeda, *Organometallics*, 2020, **39**, 1519–1531.
351 Q. Li, T. Huang, Z. Zhang, M. Xiao, H. Gai, Y. Zhou and H. Song, *Mol. Catal.*, 2021, **509**, 111644.
352 B. Feng, Z. Zhang, J. Wang, D. Yang, Q. Li, Y. Liu, H. Gai, T. Huang and H. Song, *Fuel*, 2022, **325**, 124853.
353 S. J. Louis Anandaraj, L. Kang, S. DeBeer, A. Bordet and W. Leitner, *Small*, 2023, **19**, e2206806.
354 P. Schwiderowski, H. Ruland and M. Muhler, *Curr. Opin. Green Sustainable Chem.*, 2022, **38**, 100688.
355 F. S. Zebarjad, S. Hu, Z. Li and T. T. Tsotsis, *Ind. Eng. Chem. Res.*, 2019, **58**, 11811–11820.
356 F. S. Zebarjad, Z. Wang, H. Li, S. Hu, Y. Tang and T. T. Tsotsis, *Chem. Eng. Sci.*, 2021, **242**, 116722.
357 J. Reichert, S. Maerten, K. Meltzer, A. Tremel, M. Baldauf, P. Wasserscheid and J. Albert, *Sustainable Energy Fuels*, 2019, **3**, 3399–3405.
358 M. Babucci, C.-Y. Fang, A. S. Hoffman, S. R. Bare, B. C. Gates and A. Uzun, *ACS Catal.*, 2017, **7**, 6969–6972.
359 M. Babucci, C.-Y. Fang, J. E. Perez-Aguilar, A. S. Hoffman, A. Boubnov, E. Guan, S. R. Bare, B. C. Gates and A. Uzun, *Chem. Sci.*, 2019, **10**, 2623–2632.
360 A. Jalal and A. Uzun, *J. Catal.*, 2017, **350**, 86–96.
361 M. E. Royer and C. R. Hebd, *Acad. Sci., Ser. D*, 1870, **70**, 731.
362 P. G. Russell, N. Kovac, S. Srinivasan and M. Steinberg, *J. Electrochem. Soc.*, 1977, **124**, 1329–1338.
363 M. Gattrell, N. Gupta and A. Co, *J. Electroanal. Chem.*, 2006, **594**, 1–19.
364 Y. Hori, in *Modern Aspects of Electrochemistry*, ed.C. G. Vayenas, R. E. White and M. E. Gamboa-Aldeco, Springer, New York, New York, NY, 2008, pp. 89–189, DOI: 10.1007/978-0-387-49489-0_3.
365 C. Shi, K. Chan, J. S. Yoo and J. K. Nørskov, *Org. Process Res. Dev.*, 2016, **20**, 1424–1430.
366 S. Ringe, C. G. Morales-Guio, L. D. Chen, M. Fields, T. F. Jaramillo, C. Hahn and K. Chan, *Nat. Commun.*, 2020, **11**, 33.
367 C. Hahn and T. F. Jaramillo, *Joule*, 2020, **4**, 292–294.
368 J. T. Feaster, C. Shi, E. R. Cave, T. T. Hatsukade, D. N. Abram, K. P. Kuhl, C. Hahn, J. K. Norskov and T. F. Jaramillo, *ACS Catal.*, 2017, **7**, 4822–4827.
369 Y. Hori, A. Murata and R. Takahashi, *J. Chem. Soc., Faraday Trans. 1*, 1989, **85**, 2309–2326.
370 N. S. Spinner, J. A. Vega and W. E. Mustain, *Catal. Sci. Technol.*, 2012, **2**, 19–28.
371 B. A. Rosen, A. Salehi-Khojin, M. R. Thorson, W. Zhu, D. T. Whipple, P. J. A. Kenis and R. I. Masel, *Science*, 2011, **334**, 643–644.
372 D. Wakerley, S. Lamaison, J. Wicks, A. Clemens, J. Feaster, D. Corral, S. A. Jaffer, A. Sarkar, M. Fontecave, E. B. Duoss, S. Baker, E. H. Sargent, T. F. Jaramillo and C. Hahn, *Nat. Energy*, 2022, **7**, 130–143.
373 M. Ma, E. L. Clark, K. T. Therkildsen, S. Dalsgaard, I. Chorkendorff and B. Seger, *Energy Environ. Sci.*, 2020, **13**, 977–985.
374 A. Bard, *Standard potentials in aqueous solution*, Routledge, 2017.
375 B. A. Rosen, J. L. Haan, P. Mukherjee, B. Braunschweig, W. Zhu, A. Salehi-Khojin, D. D. Dlott and R. I. Masel, *J. Phys. Chem. C*, 2012, **116**, 15307–15312.
376 B. A. Rosen, W. Zhu, G. Kaul, A. Salehi-Khojin and R. I. Masel, *J. Electrochem. Soc.*, 2013, **160**, H138.
377 N. Hollingsworth, S. F. R. Taylor, M. T. Galante, J. Jacquemin, C. Longo, K. B. Holt, N. H. de Leeuw and C. Hardacre, *Angew. Chem., Int. Ed.*, 2015, **54**, 14164–14168.
378 L. Chen, S.-X. Guo, F. Li, C. Bentley, M. Horne, A. M. Bond and J. Zhang, *ChemSusChem*, 2016, **9**, 1271–1278.
379 L. Sun, G. K. Ramesha, P. V. Kamat and J. F. J. L. Brennecke, *Langmuir*, 2014, **30**, 6302–6308.
380 E. E. L. Tanner, C. Batchelor-McAuley and R. G. Compton, *J. Phys. Chem. C*, 2016, **120**, 26442–26447.
381 F. A. Hanc-Scherer, M. A. Montiel, V. Montiel, E. Herrero and C. M. Sanchez-Sanchez, *Phys. Chem. Chem. Phys.*, 2015, **17**, 23909–23916.
382 S. Neyrizi, J. Kiewiet, M. A. Hempenius and G. Mul, *ACS Energy Lett.*, 2022, **7**, 3439–3446.
383 G. P. S. Lau, M. Schreier, D. Vasilyev, R. Scopelliti, M. Grätzel and P. J. Dyson, *J. Am. Chem. Soc.*, 2016, **138**, 7820–7823.
384 Z. Min, B. Chang, C. Shao, X. Su, N. Wang, Z. Li, H. Wang, Y. Zhao, M. Fan and J. Wang, *Appl. Catal., B*, 2023, **326**, 122185.
385 B. Liu, W. Guo and M. A. Gebbie, *ACS Catal.*, 2022, **12**, 9706–9716.

 This journal is © The Royal Society of Chemistry 2024

Open Access Article. Published on 24 June 2024. Downloaded on 1/17/2026 6:47:09 PM. This article is licensed under a Creative Commons Attribution-NonCommercial 3.0 Unported Licence.

386 S. Noh, Y. J. Cho, G. Zhang and M. Schreier, *J. Am. Chem. Soc.*, 2023, **145**, 27657–27663.
387 S. Sharifi Golru and E. J. Biddinger, *Electrochim. Acta*, 2020, **361**, 136787.
388 S. Garg, M. Li, T. E. Rufford, L. Ge, V. Rudolph, R. Knibbe, M. Konarova and G. G. X. Wang, *ChemSusChem*, 2020, **13**, 304–311.
389 D. V. Vasilyev, A. V. Rudnev, P. Broekmann and P. J. Dyson, *ChemSusChem*, 2019, **12**, 1635–1639.
390 S. Verma, X. Lu, S. C. Ma, R. I. Masel and P. J. A. Kenis, *Phys. Chem. Chem. Phys.*, 2016, **18**, 7075–7084.
391 A. Bagger, W. Ju, A. S. Varela, P. Strasser and J. Rossmeisl, *ChemPhysChem*, 2017, **18**, 3266–3273.
392 Z. Gu, H. Shen, Z. Chen, Y. Yang, C. Yang, Y. Ji, Y. Wang, C. Zhu, J. Liu, J. Li, T.-K. Sham, X. Xu and G. Zheng, *Joule*, 2021, **5**, 429–440.
393 Z. Lin, C. Han, G. E. P. O'Connell and X. Lu, *Angew. Chem., Int. Ed.*, 2023, **62**, e202301435.
394 D. Kim, J. Resasco, Y. Yu, A. M. Asiri and P. Yang, *Nat. Commun.*, 2014, **5**, 4948.
395 E. L. Clark, R. Nielsen, J. E. Sørensen, J. L. Needham, B. Seger and I. Chorkendorff, *ACS Energy Lett.*, 2023, **8**, 4414–4420.
396 W. Zhu, L. Zhang, P. Yang, X. Chang, H. Dong, A. Li, C. Hu, Z. Huang, Z.-J. Zhao and J. Gong, *Small*, 2018, **14**, 1703314.
397 C. G. Morales-Guio, E. R. Cave, S. A. Nitopi, J. T. Feaster, L. Wang, K. P. Kuhl, A. Jackson, N. C. Johnson, D. N. Abram, T. Hatsukade, C. Hahn and T. F. Jaramillo, *Nat. Catal.*, 2018, **1**, 764–771.
398 J. Park, C. Jeong, M. Na, Y. Oh, K.-S. Lee, Y. Yang and H. R. Byon, *ACS Catal.*, 2024, **14**, 3198–3207.
399 D. Bagchi, J. Raj, A. K. Singh, A. Cherevotan, S. Roy, K. S. Manoj, C. P. Vinod and S. C. Peter, *Adv. Mater.*, 2022, **34**, 2109426.
400 M. Ding, Z. Chen, C. Liu, Y. Wang, C. Li, X. Li, T. Zheng, Q. Jiang and C. Xia, *Mater. Rep.: Energy*, 2023, **3**, 100175.
401 J. Wu, R. M. Yadav, M. Liu, P. P. Sharma, C. S. Tiwary, L. Ma, X. Zou, X.-D. Zhou, B. I. Yakobson, J. Lou and P. M. Ajayan, *ACS Nano*, 2015, **9**, 5364–5371.
402 A. Hasani, M. A. Teklagne, H. H. Do, S. H. Hong, Q. Van Le, S. H. Ahn and S. Y. Kim, *Carbon Energy*, 2020, **2**, 158–175.
403 S. Oh, J. R. Gallagher, J. T. Miller and Y. Surendranath, *J. Am. Chem. Soc.*, 2016, **138**, 1820–1823.
404 L. Ye, Y. Ying, D. Sun, Z. Zhang, L. Fei, Z. Wen, J. Qiao and H. Huang, *Angew. Chem., Int. Ed.*, 2020, **59**, 3244–3251.
405 Y. Zhu, X. Yang, C. Peng, C. Priest, Y. Mei and G. Wu, *Small*, 2021, **17**, 2005148.
406 K. Zhao and X. Quan, *ACS Catal.*, 2021, **11**, 2076–2097.
407 M. Balamurugan, H.-Y. Jeong, V. S. K. Choutipalli, J. S. Hong, H. Seo, N. Saravanan, J. H. Jang, K.-G. Lee, Y. H. Lee, S. W. Im, V. Subramanian, S. H. Kim and K. T. Nam, *Small*, 2020, **16**, 2000955.
408 L. Wang, Z. Sofer and M. Pumera, *ACS Nano*, 2020, **14**, 21–25.
409 S. Palchoudhury, K. Ramasamy, J. Han, P. Chen and A. Gupta, *Nanoscale Adv.*, 2023, **5**, 2724–2742.
410 A. Zahid, A. Shah and I. Shah, *Nanomaterials*, 2022, **12**, 1380.
411 X. Zheng, P. De Luna, F. P. García de Arquer, B. Zhang, N. Becknell, M. B. Ross, Y. Li, M. N. Banis, Y. Li, M. Liu, O. Voznyy, C. T. Dinh, T. Zhuang, P. Stadler, Y. Cui, X. Du, P. Yang and E. H. Sargent, *Joule*, 2017, **1**, 794–805.
412 M. Chhowalla, H. S. Shin, G. Eda, L.-J. Li, K. P. Loh and H. Zhang, *Nat. Chem.*, 2013, **5**, 263–275.
413 M. Dai and R. Wang, *Small*, 2021, **17**, 2006813.
414 M. Asadi, K. Kim, C. Liu, A. V. Addepalli, P. Abbasi, P. Yasaei, P. Phillips, A. Behranginia, J. M. Cerrato, R. Haasch, P. Zapol, B. Kumar, R. F. Klie, J. Abiade, L. A. Curtiss and A. Salehi-Khojin, *Science*, 2016, **353**, 467–470.
415 X. Liu, H. Yang, J. He, H. Liu, L. Song, L. Li and J. Luo, *Small*, 2018, **14**, 1704049.
416 D. Yang, Q. Zhu, C. Chen, H. Liu, Z. Liu, Z. Zhao, X. Zhang, S. Liu and B. Han, *Nat. Commun.*, 2019, **10**, 677.
417 E. Sedano Varo, R. Egeberg Tankard, J. Kryger-Baggesen, J. Jinschek, S. Helveg, I. Chorkendorff, C. D. Damsgaard and J. Kibsgaard, *J. Am. Chem. Soc.*, 2024, **146**, 2015–2023.
418 A. Vasileff, Y. Zheng and S. Z. Qiao, *Adv. Energy Mater.*, 2017, **7**, 1700759.
419 J. K. Stolarczyk, S. Bhattacharyya, L. Polavarapu and J. Feldmann, *ACS Catal.*, 2018, **8**, 3602–3635.
420 W. Zhu, R. Michalsky, Ö. Metin, H. Lv, S. Guo, C. J. Wright, X. Sun, A. A. Peterson and S. Sun, *J. Am. Chem. Soc.*, 2013, **135**, 16833–16836.
421 A. Asserghine, A. Baby, E. Gao, H. Zhao and J. Rodríguez-López, *Electrochim. Acta*, 2024, **475**, 143620.
422 L. Liu, M. Li, F. Chen and H. Huang, *Small Struct.*, 2023, **4**, 2200188.
423 Y. Cheng, S. Yang, S. P. Jiang and S. Wang, *Small Methods*, 2019, **3**, 1800440.
424 D. F. Gao, R. M. Arán-Ais, H. S. Jeon and B. Roldan Cuenya, *Nat. Catal.*, 2019, **2**, 198–210.
425 B. Deng, M. Huang, X. Zhao, S. Mou and F. Dong, *ACS Catal.*, 2022, **12**, 331–362.
426 G. Marcandalli, M. C. O. Monteiro, A. Goyal and M. T. M. Koper, *Acc. Chem. Res.*, 2022, **55**, 1900–1911.
427 Y. Matsubara, D. C. Grills and Y. J. A. C. Kuwahara, *Journal*, 2015, **5**, 6440–6452.
428 X. Tan, X. Sun and B. J. N. S. R. Han, *Natl. Sci. Rev.*, 2022, **9**, nwab022.
429 L. M. Welch, M. Vijayaraghavan, F. Greenwell, J. Satherley and A. J. Cowan, *Faraday Discuss.*, 2021, **230**, 331–343.
430 S. Spittle, D. Poe, B. Doherty, C. Kolodziej, L. Heroux, M. A. Haque, H. Squire, T. Cosby, Y. Zhang, C. Fraenza, S. Bhattacharyya, M. Tyagi, J. Peng, R. A. Elgammal, T. Zawodzinski, M. Tuckerman, S. Greenbaum, B. Gurkan, C. Burda, M. Dadmun, E. J. Maginn and J. Sangoro, *Nat. Commun.*, 2022, **13**, 219.
431 G. Zhao, T. Jiang, B. Han, Z. Li, J. Zhang, Z. Liu, J. He and W. Wu, *J. Supercrit. Fluids*, 2004, **32**, 287–291.
432 B. Ratschmeier, A. Kemna and B. Braunschweig, *Chem-ElectroChem*, 2020, **7**, 1765–1774.
433 A. Atifi, D. W. Boyce, J. L. DiMeglio and J. Rosenthal, *ACS Catal.*, 2018, **8**, 2857–2863.

Open Access Article. Published on 24 June 2024. Downloaded on 1/17/2026 6:47:09 PM. This article is licensed under a Creative Commons Attribution-NonCommercial 3.0 Unported Licence.

434 X. Kang, Q. Zhu, X. Sun, J. Hu, J. Zhang, Z. Liu and B. Han, *Chem. Sci.*, 2016, **7**, 266–273.
435 A. Leal-Duaso, Y. Adjez and C. M. Sánchez-Sánchez, *ChemElectroChem*, 2024, **11**, e202300771.
436 M. G. Freire, C. M. S. S. Neves, I. M. Marrucho, J. A. P. Coutinho and A. M. Fernandes, *J. Phys. Chem. A*, 2010, **114**, 3744–3749.
437 W. Guo, S. Liu, X. Tan, R. Wu, X. Yan, C. Chen, Q. Zhu, L. Zheng, J. Ma, J. Zhang, Y. Huang, X. Sun and B. Han, *Angew. Chem., Int. Ed.*, 2021, **60**, 21979–21987.
438 M. Asadi, B. Kumar, A. Behranginia, B. A. Rosen, A. Baskin, N. Repnin, D. Pisasale, P. Phillips, W. Zhu, R. Haasch, R. F. Klie, P. Král, J. Abiade and A. Salehi-Khojin, *Nat. Commun.*, 2014, **5**, 4470.
439 V. Vedharathinam, Z. Qi, C. Horwood, B. Bourcier, M. Stadermann, J. Biener and M. Biener, *ACS Catal.*, 2019, **9**, 10605–10611.
440 T. N. Huan, P. Simon, G. Rousse, I. Génois, V. Artero and M. Fontecave, *Chem. Sci.*, 2017, **8**, 742–747.
441 W. Guo, B. Liu and M. A. Gebbie, *J. Phys. Chem. C*, 2023, **127**, 14243–14254.
442 A. Fortunati, F. Risplendi, M. Re Fiorentin, G. Cicero, E. Parisi, M. Castellino, E. Simone, B. Iliev, T. J. S. Schubert, N. Russo and S. Hernández, *Commun. Chem.*, 2023, **6**, 84.
443 F. Zhou, S. Liu, B. Yang, P. Wang, A. S. Alshammari and Y. Deng, *Electrochem. Commun.*, 2014, **46**, 103–106.
444 S.-F. Zhao, M. Horne, A. M. Bond and J. Zhang, *J. Phys. Chem. C*, 2016, **120**, 23989–24001.
445 C. Chen, X. Sun, X. Yan, Y. Wu, H. Liu, Q. Zhu, B. B. A. Bediako and B. Han, *Angew. Chem., Int. Ed.*, 2020, **59**, 11123–11129.
446 Q. Zhu, D. Yang, H. Liu, X. Sun, C. Chen, J. Bi, J. Liu, H. Wu and B. Han, *Angew. Chem., Int. Ed.*, 2020, **59**, 8896–8901.
447 M. Aghaie, N. Rezaei and S. Zendehboudi, *Renewable Sustainable Energy Rev.*, 2018, **96**, 502–525.
448 J. Feng, S. Zeng, H. Liu, J. Feng, H. Gao, L. Bai, H. Dong, S. Zhang and X. Zhang, *ChemSusChem*, 2018, **11**, 3191–3197.
449 C. Jiang, S. Zeng, X. Ma, J. Feng, G. Li, L. Bai, F. Li, X. Ji and X. Zhang, *AIChE J.*, 2023, **69**, e17859.
450 S. Dongare, O. K. Coskun, E. Cagli, K. Y. C. Lee, G. Rao, R. D. Britt, L. A. Berben and B. Gurkan, *ACS Catal.*, 2023, **13**, 7812–7821.
451 O. K. Coskun, S. Dongare, B. Doherty, A. Klemm, M. Tuckerman and B. Gurkan, *Angew. Chem., Int. Ed.*, 2024, **63**, e202312163.
452 L. E. Barrosse-Antle and R. G. Compton, *Chem. Commun.*, 2009, 3744–3746, DOI: **10.1039/B906320J**.
453 S. Seo, M. A. DeSilva and J. F. Brennecke, *J. Phys. Chem. B*, 2014, **118**, 14870–14879.
454 D. V. Vasilyev and P. J. Dyson, *ACS Catal.*, 2021, **11**, 1392–1405.
455 N. Ahmad, X. Wang, P. Sun, Y. Chen, F. Rehman, J. Xu and X. Xu, *Renewable Energy*, 2021, **177**, 23–33.
456 S. Imteyaz, C. M. Suresh, T. Kausar and P. P. Ingole, *J. CO2 Util.*, 2023, **68**, 102349.
457 Z. Zhang, S. Li, Y. Rao, L. Yang, W. Yan and H. Xu, *Chem. Eng. J.*, 2024, **479**, 147376.
458 O. K. Coskun, M. Muñoz, S. Dongare, W. Dean and B. E. Gurkan, *Langmuir*, 2024, **40**, 3283–3300.
459 A. Kemna, N. García Rey and B. Braunschweig, *ACS Catal.*, 2019, **9**, 6284–6292.
460 D. V. Vasilyev, S. Shyshkanov, E. Shirzadi, S. A. Katsyuba, M. K. Nazeeruddin and P. J. Dyson, *ACS Appl. Energy Mater.*, 2020, **3**, 4690–4698.
461 G. Li, C. Jiang, S. Zeng, K. Peng, L. Yuan, J. Chu and X. Zhang, *J. Mol. Liq.*, 2023, **375**, 121392.
462 A. J. Bard, L. R. Faulkner and H. S. White, *Electrochemical methods: fundamentals and applications*, John Wiley & Sons, 2022.
463 A. W. B. Aylmer-Kelly, A. Bewick, P. R. Cantrill and A. M. Tuxford, *Faraday Discuss. Chem. Soc.*, 1973, **56**, 96–107.
464 X. Liu, J. Xiao, H. Peng, X. Hong, K. Chan and J. K. Nørskov, *Nat. Commun.*, 2017, **8**, 15438.
465 Y. Matsubara, D. C. Grills and Y. Kuwahara, *ACS Catal.*, 2015, **5**, 6440–6452.
466 Y. Matsubara, D. C. Grills and Y. Koide, *ACS Omega*, 2016, **1**, 1393–1411.
467 S. Dongare, O. K. Coskun, E. Cagli, J. S. Stanley, A. Q. Mir, R. S. Brower, J. M. Velázquez, J. Y. Yang, R. L. Sacci and B. Gurkan, *Langmuir*, 2024, **40**, 9426–9438.
468 D. C. Grills, Y. Matsubara, Y. Kuwahara, S. R. Golisz, D. A. Kurtz and B. A. Mello, *J. Phys. Chem. Lett.*, 2014, **5**, 2033–2038.
469 M. Dunwell, W. Luc, Y. Yan, F. Jiao and B. Xu, *ACS Catal.*, 2018, **8**, 8121–8129.
470 T. Shinagawa, A. T. Garcia-Esparza and K. Takanabe, *Sci. Rep.*, 2015, **5**, 13801.
471 A. R. Woldu, Z. Huang, P. Zhao, L. Hu and D. Astruc, *Coord. Chem. Rev.*, 2022, **454**, 214340.
472 J. Newman and N. P. Balsara, *Electrochemical systems*, John Wiley & Sons, 2021.
473 N. B. Watkins, Z. J. Schiffer, Y. Lai, C. B. Musgrave, III, H. A. Atwater, W. A. Goddard, III, T. Agapie, J. C. Peters and J. M. Gregoire, *ACS Energy Lett.*, 2023, **8**, 2185–2192.
474 M. V. Fedorov and A. A. Kornyshev, *Chem. Rev.*, 2014, **114**, 2978–3036.
475 N. A. Shaheen, M. Ijjada, M. B. Vukmirovic and R. Akolkar, *J. Electrochem. Soc.*, 2020, **167**, 143505.
476 X. Shen, N. Sinclair, J. Wainright and R. F. Savinell, *J. Electrochem. Soc.*, 2021, **168**, 056520.
477 M. Liu, Y. Pang, B. Zhang, P. De Luna, O. Voznyy, J. Xu, X. Zheng, C. T. Dinh, F. Fan, C. Cao, F. P. G. de Arquer, T. S. Safaei, A. Mepham, A. Klinkova, E. Kumacheva, T. Filleter, D. Sinton, S. O. Kelley and E. H. Sargent, *Nature*, 2016, **537**, 382–386.
478 A. T. Chu, O. Jung, W. L. Toh and Y. Surendranath, *J. Am. Chem. Soc.*, 2023, **145**, 9617–9623.
479 C. Wei, S. Sun, D. Mandler, X. Wang, S. Z. Qiao and Z. J. Xu, *Chem. Soc. Rev.*, 2019, **48**, 2518–2534.
480 Z. Zhou, X. Hu, J. Li, H. Xie and L. Wen, *Adv. Sci.*, 2024, **11**, 2309963.
481 A. Thevenon, A. Rosas-Hernández, A. M. Fontani Herreros, T. Agapie and J. C. Peters, *ACS Catal.*, 2021, **11**, 4530–4537.
482 G. Shi, L. Yu, X. Ba, X. Zhang, J. Zhou and Y. Yu, *Dalton Trans.*, 2017, **46**, 10569–10577.

 This journal is © The Royal Society of Chemistry 2024

Open Access Article. Published on 24 June 2024. Downloaded on 1/17/2026 6:47:09 PM. This article is licensed under a Creative Commons Attribution-NonCommercial 3.0 Unported Licence.

483 L. Yu, Y. Xie, J. Zhou, Y. Li, Y. Yu and Z. Ren, *J. Mater. Chem. A*, 2018, **6**, 4706–4713.
484 W. Dean, J. Klein and B. Gurkan, *J. Electrochem. Soc.*, 2021, **168**, 026503.
485 Q. Zhang, Y. Han, Y. Wang, S. Ye and T. Yan, *Electrochem. Commun.*, 2014, **38**, 44–46.
486 S. Baldelli, *Acc. Chem. Res.*, 2008, **41**, 421–431.
487 V. O. Santos, M. B. Alves, M. S. Carvalho, P. A. Z. Suarez and J. C. Rubim, *J. Phys. Chem. B*, 2006, **110**, 20379–20385.
488 J.-Y. Fu, X.-C. Li, Z. Yu, X.-N. Huang-Fu, J.-A. Fan, Z.-Q. Zhang, S. Huang, J.-F. Zheng, Y.-H. Wang and X.-S. Zhou, *Langmuir*, 2022, **38**, 6209–6216.
489 J. M. Klein, H. Squire and B. Gurkan, *J. Phys. Chem. C*, 2020, **124**, 5613–5623.
490 W. Dean, D. Penley, Y.-Y. Lee, R. Ghahremani, S. Dongare and B. Gurkan, *J. Phys. Chem. C*, 2022, **126**, 14598–14610.
491 R. Michez, T. Doneux, C. Buess-Herman and M. Luhmer, *ChemPhysChem*, 2017, **18**, 2208–2216.
492 N. G. Rey and D. D. Dlott, *J. Electroanal. Chem.*, 2017, **800**, 114–125.
493 B. Braunschweig, P. Mukherjee, J. L. Haan and D. D. Dlott, *J. Electroanal. Chem.*, 2017, **800**, 144–150.
494 N. García Rey and D. D. Dlott, *Phys. Chem. Chem. Phys.*, 2017, **19**, 10491–10501.
495 M. Papasizza and A. Cuesta, *ACS Catal.*, 2018, **8**, 6345–6352.
496 D. Vasilyev, E. Shirzadi, A. V. Rudnev, P. Broekmann and P. J. Dyson, *ACS Appl. Energy Mater.*, 2018, **1**, 5124–5128.
497 J. T. Feaster, A. L. Jongerius, X. Liu, M. Urushihara, S. A. Nitopi, C. Hahn, K. Chan, J. K. Nørskov and T. F. Jaramillo, *Langmuir*, 2017, **33**, 9464–9471.
498 R. Michez, J. Vander Steen, T. Doneux, M. Luhmer and C. Buess-Herman, *Electrochim. Acta*, 2018, **270**, 434–439.
499 Y. Wang, M. Hatakeyama, K. Ogata, M. Wakabayashi, F. Jin and S. Nakamura, *Phys. Chem. Chem. Phys.*, 2015, **17**, 23521–23531.
500 L. D. Chen, M. Urushihara, K. Chan and J. K. Nørskov, *ACS Catal.*, 2016, **6**, 7133–7139.
501 M. Urushihara, K. Chan, C. Shi and J. K. Nørskov, *J. Phys. Chem. C*, 2015, **119**, 20023–20029.
502 H.-K. Lim, Y. Kwon, H. S. Kim, J. Jeon, Y.-H. Kim, J.-A. Lim, B.-S. Kim, J. Choi and H. Kim, *ACS Catal.*, 2018, **8**, 2420–2427.
503 Y. Hu, J. Feng, X. Zhang, H. Gao, S. Jin, L. Liu and W. Shen, *ChemistrySelect*, 2021, **6**, 9873–9879.
504 J. Jang, M. Rüscher, M. Winzely and C. G. Morales-Guio, *AIChE J.*, 2022, **68**, e17605.
505 G. Leverick, E. M. Bernhardt, A. I. Ismail, J. H. Law, A. Arifutzzaman, M. K. Aroua and B. M. Gallant, *ACS Catal.*, 2023, **13**, 12322–12337.
506 K. P. Kuhl, E. R. Cave, D. N. Abram and T. F. Jaramillo, *Energy Environ. Sci.*, 2012, **5**, 7050–7059.
507 K. Shen, D. Cheng, E. Reyes-Lopez, J. Jang, P. Sautet and C. G. Morales-Guio, *Joule*, 2023, **7**, 1260–1276.
508 J. Safipour, A. Z. Weber and A. T. Bell, *ACS Energy Lett.*, 2023, **8**, 5012–5017.
509 L.-C. Weng, A. T. Bell and A. Z. Weber, *Phys. Chem. Chem. Phys.*, 2018, **20**, 16973–16984.
510 Q. Xu, S. Liu, F. Longhin, G. Kastlunger, I. Chorkendorff and B. Seger, *Adv. Mater.*, 2024, **36**, 2306741.
511 Z. Wang, Y. Zhou, P. Qiu, C. Xia, W. Fang, J. Jin, L. Huang, P. Deng, Y. Su, R. Crespo-Otero, X. Tian, B. You, W. Guo, D. Di Tommaso, Y. Pang, S. Ding and B. Y. Xia, *Adv. Mater.*, 2023, **35**, 2303052.
512 H. Shen, Z. Gu and G. Zheng, *Sci. Bull.*, 2019, **64**, 1805–1816.
513 D. Ma, T. Jin, K. Xie and H. Huang, *J. Mater. Chem. A*, 2021, **9**, 20897–20918.
514 D. M. Weekes, D. A. Salvatore, A. Reyes, A. Huang and C. P. Berlinguette, *Acc. Chem. Res.*, 2018, **51**, 910–918.
515 Y. J. Sa, C. W. Lee, S. Y. Lee, J. Na, U. Lee and Y. J. Hwang, *Chem. Soc. Rev.*, 2020, **49**, 6632–6665.
516 Q. Chen, X. Wang, Y. Zhou, Y. Tan, H. Li, J. Fu and M. Liu, *Adv. Mater.*, 2024, **36**, 2303902.
517 Y. Cao, Z. Chen, P. Li, A. Ozden, P. Ou, W. Ni, J. Abed, E. Shirzadi, J. Zhang, D. Sinton, J. Ge and E. H. Sargent, *Nat. Commun.*, 2023, **14**, 2387.
518 J. E. Huang, F. Li, A. Ozden, A. Sedighian Rasouli, F. P. García de Arquer, S. Liu, S. Zhang, M. Luo, X. Wang, Y. Lum, Y. Xu, K. Bertens, R. K. Miao, C.-T. Dinh, D. Sinton and E. H. Sargent, *Science*, 2021, **372**, 1074–1078.
519 F. P. García de Arquer, C.-T. Dinh, A. Ozden, J. Wicks, C. McCallum, A. R. Kirmani, D.-H. Nam, C. Gabardo, A. Seifitokaldani, X. Wang, Y. C. Li, F. Li, J. Edwards, L. J. Richter, S. J. Thorpe, D. Sinton and E. H. Sargent, *Science*, 2020, **367**, 661–666.
520 K. Fernández-Caso, G. Díaz-Sainz, M. Alvarez-Guerra and A. Irabien, *ACS Energy Lett.*, 2023, **8**, 1992–2024.
521 T. Fan, W. Ma, M. Xie, H. Liu, J. Zhang, S. Yang, P. Huang, Y. Dong, Z. Chen and X. Yi, *Cell Rep. Phys. Sci.*, 2021, **2**, 100353.
522 I. Grigioni, L. K. Sagar, Y. C. Li, G. Lee, Y. Yan, K. Bertens, R. K. Miao, X. Wang, J. Abed, D. H. Won, F. P. García de Arquer, A. H. Ip, D. Sinton and E. H. Sargent, *ACS Energy Lett.*, 2021, **6**, 79–84.
523 Y. Luo, K. Zhang, Y. Li and Y. Wang, *InfoMat*, 2021, **3**, 1313–1332.
524 E. W. Lees, B. A. W. Mowbray, F. G. L. Parlane and C. P. Berlinguette, *Nat. Rev. Mater.*, 2022, **7**, 55–64.
525 D. T. Whipple, E. C. Finke and P. J. A. Kenis, *Electrochem. Solid-State Lett.*, 2010, **13**, B109.
526 S. Ma, M. Sadakiyo, R. Luo, M. Heima, M. Yamauchi and P. J. A. Kenis, *J. Power Sources*, 2016, **301**, 219–228.
527 B. Endrődi, G. Bencsik, F. Darvas, R. Jones, K. Rajeshwar and C. Janáky, *Prog. Energy Combust. Sci.*, 2017, **62**, 133–154.
528 M. Alvarez-Guerra, J. Albo, E. Alvarez-Guerra and A. Irabien, *Energy Environ. Sci.*, 2015, **8**, 2574–2599.
529 M. König, J. Vaes, E. Klemm and D. Pant, *iScience*, 2019, **19**, 135–160.
530 D. Yang, Q. Zhu and B. Han, *Innovation*, 2020, **1**, 100016.
531 A. Salehi-Khojin, H.-R. M. Jhong, B. A. Rosen, W. Zhu, S. Ma, P. J. A. Kenis and R. I. Masel, *J. Phys. Chem. C*, 2013, **117**, 1627–1632.
532 S. S. Neubauer, B. Schmid, C. Reller, D. M. Guldi and G. Schmid, *ChemElectroChem*, 2017, **4**, 160–167.

Open Access Article. Published on 24 June 2024. Downloaded on 1/17/2026 6:47:09 PM. This article is licensed under a Creative Commons Attribution-NonCommercial 3.0 Unported Licence.

533 Y. Miao, N. Siri-Nguan, T. Sornchamni, G. N. Jovanovic and A. F. Yokochi, *Chem. Eng. J.*, 2018, **333**, 300–309.
534 L. Yuan, L. Zhang, J. Feng, C. Jiang, J. Feng, C. Li, S. Zeng and X. Zhang, *Chem. Eng. J.*, 2022, **450**, 138378.
535 S. Wu, Y. Hua, J. Zhang, F. Shen, W. Song, X. Zhang, J. Liu, B. Yang, Y. Dai and J. Shi, *Energy Fuels*, 2022, **36**, 3771–3777.
536 I. A. Digdaya, I. Sullivan, M. Lin, L. Han, W.-H. Cheng, H. A. Atwater and C. Xiang, *Nat. Commun.*, 2020, **11**, 4412.
537 T. Li, E. W. Lees, M. Goldman, D. A. Salvatore, D. M. Weekes and C. P. Berlinguette, *Joule*, 2019, **3**, 1487–1497.
538 S. Messias, M. M. Sousa, M. Nunes da Ponte, C. M. Rangel, T. Pardal and A. S. Reis Machado, *React. Chem. Eng.*, 2019, **4**, 1982–1990.
539 M. Gautam, F. Nkurunziza, M. C. Mulvehill, S. S. Uttarwar, D. T. Hofsommer, C. A. Grapperhaus and J. M. Spurgeon, *ChemSusChem*, 2023, e202301337.
540 M. König, S.-H. Lin, J. Vaes, D. Pant and E. Klemm, *Faraday Discuss.*, 2021, **230**, 360–374.
541 H. Yang, J. J. Kaczur, S. D. Sajjad and R. I. Masel, *ECS Trans.*, 2017, **77**, 1425.
542 C. Jiang, A. W. Nichols, J. F. Walzer and C. W. Machan, *Inorg. Chem.*, 2020, **59**, 1883–1892.
543 Q. Xia, K. Zhang, T. Zheng, L. An, C. Xia and X. Zhang, *ACS Energy Lett.*, 2023, **8**, 2840–2857.
544 I. Sullivan, A. Goryachev, I. A. Digdaya, X. Li, H. A. Atwater, D. A. Vermaas and C. Xiang, *Nat. Catal.*, 2021, **4**, 952–958.
545 K. M. Diederichsen, R. Sharifian, J. S. Kang, Y. Liu, S. Kim, B. M. Gallant, D. Vermaas and T. A. Hatton, *Nat. Rev. Methods Primers*, 2022, **2**, 68.
546 J. H. Rheinhardt, P. Singh, P. Tarakeshwar and D. A. Buttry, *ACS Energy Lett.*, 2017, **2**, 454–461.
547 F. Simeon, M. C. Stern, K. M. Diederichsen, Y. Liu, H. J. Herzog and T. A. Hatton, *J. Phys. Chem. C*, 2022, **126**, 1389–1399.
548 K. M. Diederichsen, Y. Liu, N. Ozbek, H. Seo and T. A. Hatton, *Joule*, 2022, **6**, 221–239.
549 M. Wang, M. Rahimi, A. Kumar, S. Hariharan, W. Choi and T. A. Hatton, *Appl. Energy*, 2019, **255**, 113879.
550 F.-Y. Kuo, S. E. Jerng and B. M. Gallant, *ACS Cent. Sci.*, 2023, **9**, 1750–1757.
551 R. B. Kutz, Q. Chen, H. Yang, S. D. Sajjad, Z. Liu and I. R. Masel, *Energy Technol.*, 2017, **5**, 929–936.
552 M. Pellerite, M. Kaplun, C. Hartmann-Thompson, K. A. Lewinski, N. Kunz, T. Gregar, J. Baetzold, D. Lutz, M. Quast, Z. Liu, H. Yang, S. D. Sajjad, Y. Gao and R. Masel, *ECS Trans.*, 2017, **80**, 945.
553 L. Xue, Z. Gao, T. Ning, W. Li, J. Li, J. Yin, L. Xiao, G. Wang and L. Zhuang, *Angew. Chem., Int. Ed.*, 2023, **62**, e202309519.
554 M. Esmaeilirad, Z. Jiang, A. M. Harzandi, A. Kondori, M. Tamadoni Saray, C. U. Segre, R. Shahbazian-Yassar, A. M. Rappe and M. Asadi, *Nat. Energy*, 2023, **8**, 891–900.
555 E. P. Delmo, Y. Wang, J. Wang, S. Zhu, T. Li, X. Qin, Y. Tian, Q. Zhao, J. Jang, Y. Wang, M. Gu, L. Zhang and M. Shao, *Chin. J. Catal.*, 2022, **43**, 1687–1696.
556 J. Choi, T. M. Benedetti, R. Jalili, A. Walker, G. G. Wallace and D. L. Officer, *Chem. – Eur. J.*, 2016, **22**, 14158–14161.
557 T. Yoshida, K. Tsutsumida, S. Teratani, K. Yasufuku and M. Kaneko, *J. Chem. Soc., Chem. Commun.*, 1993, 631–633, DOI: 10.1039/C39930000631.
558 E. Vichou, Y. Li, M. Gomez-Mingot, M. Fontecave and C. M. Sánchez-Sánchez, *J. Phys. Chem. C*, 2020, **124**, 23764–23772.
559 J. Honores, D. Quezada, M. García, K. Calfumán, J. P. Muena, M. J. Aguirre, M. C. Arévalo and M. Isaacs, *Green Chem.*, 2017, **19**, 1155–1162.
560 E. Vichou, A. Solé-Daura, C. Mellot-Draznieks, Y. Li, M. Gomez-Mingot, M. Fontecave and C. M. Sánchez-Sánchez, *ChemSusChem*, 2022, **15**, e202201566.
561 A. Khadhraoui, P. Gotico, B. Boitrel, W. Leibl, Z. Halime and A. Aukauloo, *Chem. Commun.*, 2018, **54**, 11630–11633.
562 S. Sung, D. Kumar, M. Gil-Sepulcre and M. Nippe, *J. Am. Chem. Soc.*, 2017, **139**, 13993–13996.
563 S. Sung, X. Li, L. M. Wolf, J. R. Meeder, N. S. Bhuvanesh, K. A. Grice, J. A. Panetier and M. Nippe, *J. Am. Chem. Soc.*, 2019, **141**, 6569–6582.
564 D. Grammatico, H. N. Tran, Y. Li, S. Pugliese, L. Billon, B.-L. Su and M. Fontecave, *ChemSusChem*, 2020, **13**, 6418–6425.
565 D. Quezada, J. Honores, M. J. Aguirre and M. Isaacs, *J. Coord. Chem.*, 2014, **67**, 4090–4100.
566 C. Römelt, J. Song, M. Tarrago, J. A. Rees, M. van Gastel, T. Weyhermüller, S. DeBeer, E. Bill, F. Neese and S. Ye, *Inorg. Chem.*, 2017, **56**, 4745–4750.
567 M. G. Kibria, J. P. Edwards, C. M. Gabardo, C.-T. Dinh, A. Seifitokaldani, D. Sinton and E. H. Sargent, *Adv. Mater.*, 2019, **31**, 1807166.
568 M. Pérez-Fortes, J. C. Schöneberger, A. Boulamanti, G. Harrison and E. Tzimas, *Int. J. Hydrogen Energy*, 2016, **41**, 16444–16462.
569 D. Segets, C. Andronescu and U.-P. Apfel, *Nat. Commun.*, 2023, **14**, 7950.
570 M. Jouny, W. Luc and F. Jiao, *Ind. Eng. Chem. Res.*, 2020, **59**, 8121–8123.
571 A. Somoza-Tornos, O. J. Guerra, A. M. Crow, W. A. Smith and B.-M. Hodge, *iScience*, 2021, **24**, 102813.
572 H. Shin, K. U. Hansen and F. Jiao, *Nat. Sustainable*, 2021, **4**, 911–919.
573 T. Gao, B. Xia, K. Yang, D. Li, T. Shao, S. Chen, Q. Li and J. Duan, *Energy Fuels*, 2023, **37**, 17997–18008.
574 G. Leonzio, B. Chachuat and N. Shah, *Sustain. Prod. Consum.*, 2023, **43**, 124–139.
575 S. Verma, S. Lu and P. J. A. Kenis, *Nat. Energy*, 2019, **4**, 466–474.
576 J. Na, B. Seo, J. Kim, C. W. Lee, H. Lee, Y. J. Hwang, B. K. Min, D. K. Lee, H.-S. Oh and U. Lee, *Nat. Commun.*, 2019, **10**, 5193.
577 Á. Vass, B. Endrődi and C. Janáky, *Curr. Opin. Electrochem.*, 2021, **25**, 100621.
578 J. Sisler, S. Khan, A. H. Ip, M. W. Schreiber, S. A. Jaffer, E. R. Bobicki, C.-T. Dinh and E. H. Sargent, *ACS Energy Lett.*, 2021, **6**, 997–1002.
579 J. W. Sun, H. Q. Fu, P. F. Liu, A. Chen, P. Liu, H. G. Yang and H. Zhao, *EES Catal.*, 2023, **1**, 934–949.
580 J. M. Spurgeon and B. Kumar, *Energy Environ. Sci.*, 2018, **11**, 1536–1551.

 This journal is © The Royal Society of Chemistry 2024

Open Access Article. Published on 24 June 2024. Downloaded on 1/17/2026 6:47:09 PM. This article is licensed under a Creative Commons Attribution-NonCommercial 3.0 Unported Licence.

581 J. M. Spurgeon, N. Theaker, C. A. Phipps, S. S. Uttarwar and C. A. Grapperhaus, *ACS Sustainable Chem. Eng.*, 2022, **10**, 12882–12894.
582 Y. Li, F. Li, A. Laaksonen, C. Wang, P. Cobden, P. Boden, Y. Liu, X. Zhang and X. Ji, *Ind. Chem. Mater.*, 2023, **1**, 410–430.
583 N. Gao, C. Quiroz-Arita, L. A. Diaz and T. E. Lister, *J. CO2 Util.*, 2021, **43**, 101365.
584 M. Li, E. Irtem, H.-P. Iglesias van Montfort, M. Abdinejad and T. Burdyny, *Nat. Commun.*, 2022, **13**, 5398.
585 H. Weingärtner, *Angew. Chem., Int. Ed.*, 2008, **47**, 654–670.
586 M. D. Soutullo, C. I. Odom, B. F. Wicker, C. N. Henderson, A. C. Stenson and J. H. Davis, *Chem. Mater.*, 2007, **19**, 3581–3583.
587 Y. Zhang, S. Zhang, X. Lu, Q. Zhou, W. Fan and X. Zhang, *Chem. – Eur. J.*, 2009, **15**, 3003–3011.
588 X. Li, M. Hou, Z. Zhang, B. Han, G. Yang, X. Wang and L. Zou, *Green Chem.*, 2008, **10**, 879–884.
589 G. Yu, S. Zhang, G. Zhou, X. Liu and X. Chen, *AIChE J.*, 2007, **53**, 3210–3221.
590 J. Kagimoto, K. Noguchi, K. Murata, K. Fukumoto, N. Nakamura and H. Ohno, *Chem. Lett.*, 2008, **37**, 1026–1027.
591 Y.-Y. Lee, K. Edgehouse, A. Klemm, H. Mao, E. Pentzer and B. Gurkan, *ACS Appl. Mater. Interfaces*, 2020, **12**, 19184–19193.
592 R. E. Siegel, S. Pattanayak and L. A. Berben, *ACS Catal.*, 2023, **13**, 766–784.
593 J. Huang and T. Rüther, *Aust. J. Chem.*, 2009, **62**, 298–308.
594 Q. Yang, Z. Wang, Z. Bao, Z. Zhang, Y. Yang, Q. Ren, H. Xing and S. Dai, *ChemSusChem*, 2016, **9**, 806–812.
595 X. Y. Luo, F. Ding, W. J. Lin, Y. Q. Qi, H. R. Li and C. M. Wang, *J. Phys. Chem. Lett.*, 2014, **5**, 381–386.
596 Z. Xue, Z. Zhang, J. Han, Y. Chen and T. Mu, *Int. J. Greenhouse Gas Control*, 2011, **5**, 628–633.
597 Z. Zhou, X. Zhou, G. Jing and B. Lv, *Energy Fuels*, 2016, **30**, 7489–7495.
598 B. Lv, Y. Shi, C. Sun, N. Liu, W. Li and S. Li, *Chem. Eng. J.*, 2015, **270**, 372–377.
599 K. Anderson, M. P. Atkins, J. Estager, Y. Kuah, S. Ng, A. A. Oliferenko, N. V. Plechkova, A. V. Puga, K. R. Seddon and D. F. Wassell, *Green Chem.*, 2015, **17**, 4340–4354.
600 C.-J. Yoo, S. J. Park and C. W. Jones, *Ind. Eng. Chem. Res.*, 2020, **59**, 7061–7071.
601 P. Bollini, S. Choi, J. H. Drese and C. W. Jones, *Energy Fuels*, 2011, **25**, 2416–2425.
602 J. S. A. Carneiro, G. Innocenti, H. J. Moon, Y. Guta, L. Proaño, C. Sievers, M. A. Sakwa-Novak, E. W. Ping and C. W. Jones, *Angew. Chem., Int. Ed.*, 2023, **62**, e202302887.
603 Y. Chen, D. Yu, W. Chen, L. Fu and T. Mu, *Phys. Chem. Chem. Phys.*, 2019, **21**, 2601–2610.
604 T. Zhekenov, N. Toksanbayev, Z. Kazakbayeva, D. Shah and F. S. Mjalli, *Fluid Phase Equilib.*, 2017, **441**, 43–48.
605 H. Nigar, B. Garcia-Baños, F. L. Peñaranda-Foix, J. M. Catalá-Civera, R. Mallada and J. Santamaría, *AIChE J.*, 2016, **62**, 547–555.
606 J. F. Brennecke and B. E. Gurkan, *J. Phys. Chem. Lett.*, 2010, **1**, 3459–3464.
607 R. P. Swatloski, J. D. Holbrey and R. D. Rogers, *Green Chem.*, 2003, **5**, 361–363.
608 B. Wang, L. Qin, T. Mu, Z. Xue and G. Gao, *Chem. Rev.*, 2017, **117**, 7113–7131.
609 M. Feroci, M. Orsini and A. Inesi, *Adv. Synth. Catal.*, 2009, **351**, 2067–2070.
610 S. Doblinger, T. J. Donati and D. S. Silvester, *J. Phys. Chem. C*, 2020, **124**, 20309–20319.
611 M. S. E. Houache, R. Safari, U. O. Nwabara, T. Rafaïdeen, G. A. Botton, P. J. A. Kenis, S. Baranton, C. Coutanceau and E. A. Baranova, *ACS Appl. Energy Mater.*, 2020, **3**, 8725–8738.
612 X. Wei, Y. Li, L. Chen and J. Shi, *Angew. Chem., Int. Ed.*, 2021, **60**, 3148–3155.
613 W. A. Parada, D. V. Vasilyev, K. J. J. Mayrhofer and I. Katsounaros, *ACS Appl. Mater. Interfaces*, 2022, **14**, 14193–14201.
614 J. H. Cho, C. Lee, S. H. Hong, H. Y. Jang, S. Back, M.-G. Seo, M. Lee, H.-K. Min, Y. Choi, Y. J. Jang, S. H. Ahn, H. W. Jang and S. Y. Kim, *Adv. Mater.*, 2023, **35**, 2208224.
615 National Academies of Sciences, Division on Earth, Life Studies, Ocean Studies Board, Board on Chemical Sciences, Board on Earth Sciences, Board on Energy *et al.* Negative emissions technologies and reliable sequestration: a research agenda. (2019).
616 S. Perkin, *Phys. Chem. Chem. Phys.*, 2012, **14**, 5052–5062.
617 C. Pinilla, M. G. Del Pópolo, R. M. Lynden-Bell and J. Kohanoff, *J. Phys. Chem. B*, 2005, **109**, 17922–17927.